

Electrostatic powder charging phenomena and their utilization in a novel powder application method for powder bed fusion of polymers

Elektrostatische Pulveraufladungsphänomene und ihre Nutzung in einem neuartigen Pulverauftragsverfahren für die pulverbettbasierte Additive Fertigung von Polymeren

Der Technischen Fakultät
der Friedrich-Alexander-Universität
Erlangen-Nürnberg

zur
Erlangung des Doktorgrades Dr.-Ing.

vorgelegt von

Sebastian-Paul Kopp, M.Sc.

aus Amberg

Als Dissertation genehmigt
von der Technischen Fakultät
der Friedrich-Alexander-Universität Erlangen-Nürnberg

Tag der mündlichen
Prüfung: 25.04.2024

Gutachter: Prof. Dr.-Ing. Michael Schmidt
Prof. Dr.-Ing. Volker Schöppner, Universität
Paderborn

Preface

Die vorliegende Dissertation entstand im Wesentlichen im Rahmen meiner Tätigkeit als wissenschaftlicher Mitarbeiter am Bayerischen Laserzentrum (blz) in Erlangen. Die Inhalte sind schwerpunktmäßig im Kontext des Teilprojekts B6 des Sonderforschungsbereichs 814 (SFB 814) – Additive Fertigung entstanden. Aus diesem Grund gilt mein Dank der Deutschen Forschungsgemeinschaft (DFG) für die Finanzierung des SFB 814 – Additive Fertigung. Ferner danke ich der Erlangen Graduate School in Advanced Optical Technologies (SAOT) für die Unterstützung.

Mein ganz besonderer Dank gilt meinem Doktorvater Herrn Prof. Dr.-Ing. Michael Schmidt, dem Ordinarius des Lehrstuhls für Photonische Technologien (LPT), der mir durch das entgegengebrachte Vertrauen die eigenverantwortliche Bearbeitung meines Forschungsprojektes ermöglichte. Durch die wissenschaftlichen Diskussionen und Anregungen förderte er mich stets in meiner wissenschaftlichen Ausbildung und Weiterentwicklung. Herrn Prof. Dr.-Ing. Volker Schöppner, Leiter der Kunststofftechnik an der Universität Paderborn (KTP), danke ich für die wissenschaftliche Betreuung als Zweitgutachter. Mein weiterer Dank gilt Herrn Prof. Dr.-Ing. Nico Hanenkamp für die Übernahme des Prüfungsvorsitzes und Herrn Prof. Dr.-Ing. Andreas Bück als fachfremder Gutachter.

Den Geschäftsführern des blz, Herrn Prof. Dr.-Ing. Michael Schmidt und Herrn Dr.-Ing. Stephan Roth, danke ich für das in mich gesetzte Vertrauen als Mitarbeiter und Gruppenleiter der Fachgruppe „Prozesstechnik Kunststoffe“ sowie zuletzt als Leiter des Geschäftsbereichs „Nichtmetalle und Präzisionsbearbeitung“. Durch die Vielzahl an Möglichkeiten zur selbständigen Bearbeitung verschiedenster wissenschaftlicher und industrieller Fragestellungen konnte ich mich fachlich wie auch persönlich weiterentwickeln.

Mein herzlicher Dank gilt auch meinen Kolleginnen und Kollegen am blz und LPT für die vielen fachlichen Diskussionen, die freundliche Arbeitsatmosphäre und die stetige Unterstützung. Insbesondere danke ich den Technikern Ali Sahin, Torsten Zimmermann, Udo Müller, Peter Holik, Benjamin Steffan sowie den weiteren Technikern des LPT für die überaus wichtige und erfolgreiche Unterstützung beim Aufbau des ersten Prototypen. Darüber hinaus danke ich meiner alten Fachgruppe „Prozesstechnik Kunststoffe“, insbesondere Maximilian Marschall, Vadim Medvedev, sowie den

ehemaligen Mitgliedern Dr. rer. nat. Thomas Stichel und Thomas Schuffenhauer, für die freundschaftliche Atmosphäre, die unzähligen fachlichen Diskussionen und den ausgesprochen wertvollen, nicht-fachlichen Ausgleich. Ebenso möchte ich mich bei den ehemaligen Gruppen „Prozesstechnik Metalle“, „Systemtechnik & Kurzpulsprozesse“ sowie „Services“ für den guten prozess- und werkstoffübergreifenden Austausch bedanken. Mein herzlicher Dank für die freundliche, angenehme und oft auch amüsante Arbeitsatmosphäre gilt darüber hinaus Vanessa Möritz, Dominic Bartels, Lisa Ackermann, Alexander Wittmann, Magdalena Kestler, Johannes Vetter, Michelle Trbic sowie der Buchhaltung des blz.

Besonders bedanken möchte ich mich auch bei einer Vielzahl an motivierten sowie begabten Studierenden. Hervorzuheben sind Benedikt Schmaus, Cindy Ly Huynh, Pius Marcellinus Eshun, Natalie Wöltinger und Niklas Ebert.

Nicht zuletzt danke ich auch für äußerst wertvolle wissenschaftliche Kooperationen außerhalb des blz. Mein Dank gilt Björn Düsenberg und Dr. rer. nat. Jochen Schmidt vom Lehrstuhl für Feststoff- und Grenzflächenverfahrenstechnik (LFG), Andreas Jaksch, dem Geschäftsführer des SFB 814, Dr.-Ing. Sandra Greiner vom Lehrstuhl für Kunststofftechnik (LKT) und Prof. Dr.-Ing. Katrin Wudy von der TU München. Zudem danke ich meinen langjährigen Freunden Dr. rer. nat. Fabian Graßl vom Department Chemie und Pharmazie sowie Maximilian Weißflog, mit dem ich gemeinsam die Polarlichter im hohen Norden Schwedens bestaunen durfte. Außerdem danke ich Dr. rer. nat. Max Gmelch von der SAOT für seine erstklassigen Outreach-Aktivitäten.

Mein allergrößter Dank gebührt meiner Familie, die mich bei all meinen Entscheidungen unterstützt und auf meinem Weg stets gefördert hat und immer einen wertvollen Ausgleich sowie Rückhalt für mich darstellt. Abschließend danke ich von Herzen meiner Partnerin Teresa, die mir immer mit Rat und Tat zur Seite steht und mich in so manch stressiger Zeit an die schönen Dinge im Leben erinnert.

Fürth, im November 2023

Sebastian-Paul Kopp

Table of Contents

List of Symbols and Abbreviations	vi
List of Figures	x
List of Tables.....	xii
1 Introduction	1
2 State of the Art.....	3
2.1 Laser-Based Powder Bed Fusion of Polymers (PBF-LB/P).....	3
2.1.1 Fundamentals of the PBF-LB/P Process	5
2.1.2 Conventional Powder Application Methods for PBF-LB/P	10
2.1.3 New Approaches for Powder Application Methods in PBF-LB/P.....	16
2.2 Electrophotographic Powder Application (EPA)	22
2.2.1 Physical Principles of Electrophotography.....	23
2.2.2 First Applications in Powder Bed Fusion and Current Limitations.....	33
3 Objective and Methodology.....	37
4 Requirements for Substituting Conventional Powder Application Methods of PBF-LB/P by EPA	41
4.1 Achieving a Suitable Particle Charging	41
4.2 Enhancing Powder Deposition Efficiency by Reducing Interparticle Attraction Forces	58
4.3 Forming of the Electric Deposition Field	66
4.4 Compensation of Charge Accumulation	74
5 Application potentials of EPA for PBF-LB/P in Pharmaceutical 3D Printing.....	85
6 Conclusion.....	105
7 Zusammenfassung.....	107
Appendix.....	109
Bibliography	113

List of Symbols and Abbreviations

<i>Abbreviation</i>	<i>Description</i>
2D	Two-dimensional
3D	Three-dimensional
AC	Alternating current
AM	Additive manufacturing
ASTM	American Society for Testing and Materials
BJT	Binder jetting
CAD	Computer aided design
CAD	Charged area development
CCA	Charge control agent
CGM	Charge generation material
CO	Carbon monoxide
CO ₂	Carbon dioxide
CTL	Charge transport layer
DAD	Discharged area development
DED	Directed energy deposition
DIN	Deutsches Institut für Normung e. V.
DLP	Digital light processing
dpi	Dots per inch
DSC	Differential scanning calorimetry
EN	Europäische Norm
EPA	Electrophotographic powder application
EPA-PBF-LB/P	Laser-based powder bed fusion of polymers using electrophotographic powder application with contactless powder deposition
ETM	Electron transport material
HTM	Hole transport material
IR	Infrared

<i>Abbreviation</i>	<i>Description</i>
ISO	International Organization for Standardization
LS	Laser sintering
MEX	Material extrusion
MJT	Material jetting
MRL	Manufacturing readiness level
NIR	Near infrared
OPC	Organic photoconductor
PA11	Polyamide 11
PA12	Polyamide 12
PBF	Powder bed fusion
PBF-LB	Powder bed fusion – laser beam or laser-based powder bed fusion
PBF-LB/M	Powder bed fusion – laser beam of metals or laser-based powder bed fusion of metals
PBF-LB/P	Powder bed fusion – laser beam of polymers or laser-based powder bed fusion of polymers
PC	Polycarbonate
PP	Polypropylene
PS	Polystyrene
PSD	Particle size distribution
SHL	Sheet lamination
SLM	Selective laser melting
SLS	Selective laser sintering
STEP	Selective thermoplastic electrophotographic process
STL	Standard tessellation language
TRL	Technology readiness level
UCL	Undercoat layer
VPP	Vat polymerization

Symbol	Unit	Description
A	m^2	Area
d_c	m	Distance to the corona wire
$d_{\text{corona wire}}$	m	Diameter of the corona wire
d_p	m	Thickness of the photoconductor
d_{pixel}	m	Pixel size
$d_{\text{pixel 300dpi}}$	m	Pixel size for a resolution of 300 dpi
$d_{\text{pixel 1200dpi}}$	m	Pixel size for a resolution of 1200 dpi
$d\vec{S}$	-	Vector pointing in the direction of an outward normal to the area A
\vec{E}	$V m^{-1}$	Electric field
e	C	Elementary charge
E_c	$V m^{-1}$	Electric field strength of the field surrounding a corona wire
E_p	$V m^{-1}$	Electric field strength inside a photoconductor
$E_{\text{Pasch min}}$	$V m^{-1}$	Minimum electric field strength required for Paschen's breakdown to occur
\vec{F}_{el}	N	Electric field force
ΔH_c	J	Crystallization enthalpy
ΔH_m	J	Melting enthalpy
H_r	-	Hausner ratio
h_s	m	Hatching distance
h_{1-3}	m	Thicknesses of the deposited powder layers 1-3
K_p	-	Dielectric constant of the photoconductor
N_b	-	Number of charges per unit volume in the bulk
P_L	W	Laser power
q	C	Electric charge of a point charge
q_{particle}	C	Electric charge of a particle
r	m	Radius

<i>Symbol</i>	<i>Unit</i>	<i>Description</i>
T_B	°C	Required build chamber temperature
$T_{c\ on}$	°C	Crystallization onset temperature
$T_{c\ peak}$	°C	Crystallization peak temperature
$T_{degrad\ polymer\ B}$	°C	Degradation temperature of polymer B
T_g	°C	Glass transition temperature
$T_{g\ polymer\ A}$	°C	Glass transition temperature of polymer A
$T_{m\ on}$	°C	Melting onset temperature
$T_{m\ peak}$	°C	Melting peak temperature
U_c	V	Potential of the corona wire
U_p	V	Surface potential of a photoconductor
U_r	V	Residual potential inside a photoconductor
v	$m\ s^{-1}$	Translational velocity
v_s	$m\ s^{-1}$	Scanning velocity
ϵ_0	$F\ m^{-1}$	Permittivity of free space
ϵ_p	$F\ m^{-1}$	Permittivity of the photoconductor
γ	$N\ m^{-1}$	Surface tension
η	Pa s	Melt viscosity
ρ_b	$kg\ m^{-3}$	Bulk density
ρ_{tap}	$kg\ m^{-3}$	Tap density
σ_p	$C\ m^{-2}$	Charge per unit area on a photoconductor
Φ_E	$N\ m^2\ C^{-1}$	Electric flux
ω	s^{-1}	Rotational velocity

List of Figures

Figure 1: Seven divisions of AM according to DIN EN ISO/ASTM 52900:2022-03 [22–24].	4
Figure 2: Schematic overview of a PBF-LB/P machine, based on [30,35]. ...	5
Figure 3: Schematic DSC curve of a semi-crystalline polymer with process-relevant temperatures, based on [56,59].	8
Figure 4: Schematic illustration of PBF-LB/P consolidation depths and layer thicknesses h_1 , h_2 and h_3 for printing the first three layers, based on [73].	10
Figure 5: Overview of conventional powder application methods, v – translational velocity, ω – rotational velocity; a) doctor blade, b) counterclockwise rotating roller, c) clockwise rotating roller.....	11
Figure 6: Overview of three categories of new powder application methods; a) area-based with a multi-chambered coater, b) line-based and c) mask-based powder application.	17
Figure 7: Overview of the Manufacturing Readiness Level (MRL), based on [164,165]; the detailed guideline for the evaluation of the MRL according to the Department of Defense of the United States of America is available under [166].	22
Figure 8: Schematic representation of gas discharge-based charging of a photoconductor to a negative surface potential $-U_p$ using a corotron device, consisting of a grounded shielding with a corona emitting wire inside; U_c – potential of the corona wire, d_p – thickness of the photoconductor, σ_p – charge per unit area on photoconductor, E_p – electric field strength inside photoconductor; based on [169].	26
Figure 9: Schematic representation of gas discharge-based charging of a photoconductor to a negative surface potential $-U_p$ using a scorotron device, consisting of a grounded support plate and corona emitting wires and a meshed screen underneath; U_c – potential of the corona wire, U_s – potential of the screen, d_p – thickness of the photoconductor, σ_p – charge per unit area on photoconductor, E_p – electric field inside photoconductor; based on [169].	27

Figure 10: Visualization of the effect of incident electromagnetic radiation on the layers of a negatively charged organic photoconductor, based on [171]. 29

Figure 11: Visualization of the effect of incident electromagnetic radiation on the combined charge transport and charge generation layer of a positively charged organic photoconductor, based on [171]. 30

Figure 12: Bottom-up approach for identifying and understanding the requirements for the utilization of electrophotography in the context of PBF-LB/P..... 38

Figure 13: Key research questions and associated sections within this thesis to identify and understand the requirements for the successful substitution of conventional powder application for PBF-LB/P methods with EPA..... 40

Figure 14: Triboelectric charge control of polymer particles, transforming the natural bimodal particle charging (left) to monomodal charging (right) suitable for EPA-PBF-LB/P..... 41

Figure 15: Influence of vibration excitation on the powder deposition result in EPA-PBF-LB/P. 58

Figure 16: Tailored electric deposition field by using a transfer frame. 66

Figure 17: a) Applied charge compensation strategy for limiting the surface potential of the part generated by EPA-PBF-LB/P; b) graded material transition showing the potential of selective multi-material powder deposition by EPA; c) parts manufactured by EPA-PBF-LB/P consisting of a polypropylene (PP) powder which cannot be processed in conventional PBF-LB/P due to poor powder flowability..... 74

Figure 18: Manufacturing multi-material pharmaceutical parts by EPA-PBF-LB/P..... 85

List of Tables

Table 1: Influence of geometrical aspects of conventional powder application mechanisms on the resulting quality of the applied powder layer in terms of homogeneity and density for PBF-LB/P.	12
Table 2: Influence of characteristics of the conventional powder application process on the resulting quality of the applied powder layer in terms of homogeneity and density for PBF-LB/P.	14
Table 3: Influence of powder properties on the resulting quality of the conventionally applied powder layer in terms of homogeneity and density for PBF-LB/P.	15
Table 4: Classification of the flow properties of polymer powders, based on [35,132].	16
Table 5: Comparison of conventional powder application methods and new powder application approaches for PBF-LB/P, based on studies reported to date [133]; the new approaches are highlighted in light blue.	21
Table 6: Process steps of EPA, based on [169].	23
Table 7: Comparison between the contacting and contactless strategy for using EPA in AM.	35

1 Introduction

The utilization of electrostatics in the context of photographic copies dates back to 1939, when Chester F. Carlson has patented a process [1] and one year later an apparatus [2] for electrophotography. Five years later, research activities on this new process, often also referred to as xerography, started to accelerate [3]. The invention of electrophotography, which is the basis for every laser printer, has revolutionized the printing industry. In contrast to former photographic printing technologies, which were based on chemical processes like the cyanotype process [4], electrophotography allowed dry and non-chemical printing for the first time.

Although today's hot topics such as resource efficiency and sustainability were of subordinate importance back then, electrophotography has substantially increased both. Based purely on attractive and repulsive electrostatic interaction forces between powder particles and the latent charge pattern on a photoconductive surface, it allowed photographic prints and graphic reproductions to be generated economically. Time- and material-intensive chemical reactions associated with risks to health were not necessary anymore. Furthermore, the ability of the latent charge pattern to be varied rapidly by selective illumination of the photoconductive layer made electrophotography a highly flexible printing process [3]. From today's perspective of additive manufacturing (AM), the selective deposition of powder particles onto a substrate – usually a piece of paper – followed by a fusion step can be interpreted as a first powder-based single layer quasi-AM process for generating letters or images. In the following, this is referred to as two-dimensional (2D) printing.

Initial approaches for generating three-dimensional (3D) solid objects by means of AM emerged as early as the late 1960s. Based on photosensitive resins cured by exposure to ultraviolet (UV) electromagnetic radiation, a first apparatus for 3D printing by means of stereolithography (SLA) was patented in 1986. Starting in the 1990s, multiple other AM processes [5], including powder-based ones [6], were invented. Especially powder-based AM, often referred to as powder bed fusion (PBF) [7], offers the capability to generate complex parts for high-performance applications [8], e.g., in aerospace [9], automotive [10] and medical [11] industries. Recently, PBF has also become increasingly important in pharmaceutical applications [12] to meet the growing demand for personalized medicine [13].

In state-of-the-art laser-based PBF (PBF-LB), with conventional doctor blade- or roller-based powder application methods, geometrical flexibility for generating parts is purely realized via selective laser irradiation and thus selective powder fusion [14]. However, this inherently involves a complete filling of the build chamber with powder material and the need to recycle unused powder, the so-called partcake material [15].

Moreover, conventional powder application methods do not allow to tailor the material composition within a powder layer. Thus, they inhibit the fabrication of multi-material parts or parts with locally adjusted material distributions and therefore tailored functional properties by means of PBF-LB.

Substituting conventional powder application methods for PBF-LB by electrophotographic powder application (EPA) offers the possibility to overcome these limitations. First approaches for transferring electrophotography from 2D to 3D printing date back to 1990 [16] and 1992 [17], respectively. However, as will be discussed in detail in 2.2.2, successful implementation of EPA to PBF-LB, especially in case of polymer powders (PBF-LB/P), has not been possible so far.

2 State of the Art

In the following, first PBF-LB/P as a powder-based AM technology is discussed. The focus is on state-of-the-art powder application strategies as well as on new approaches and their deficiencies. Finally, the fundamentals of EPA are discussed pointing out current shortcomings, which render the successful utilization of EPA as powder application method for PBF-LB/P impossible so far.

2.1 Laser-Based Powder Bed Fusion of Polymers (PBF-LB/P)

Additive manufacturing (AM) is a primary forming process for generating parts from three-dimensional (3D) model data [18]. The main distinguishing feature of AM compared to conventional manufacturing processes is the computer-driven, layer-by-layer generation of parts [19], accomplished without the need for part-specific tooling [18]. The standards ISO 17296 (International Organization for Standardization) [20] and ASTM F2792 (American Society for Testing and Materials) [21] with its successor ISO/ASTM 52900 [22] specify that AM encompasses seven areas, one of which is powder bed fusion [23]. The different areas are determined based on the binding mechanism utilized and the morphology or delivery characteristics of the feedstock [18]. Figure 1 gives an overview of the seven divisions of AM based on DIN EN ISO/ASTM 52900:2022-03.

<p>Binder jetting (BJT)</p> <p>Selective deposition of a liquid bonding agent for joining powder materials</p>	<p>Directed energy deposition (DED)</p> <p>Usage of focused thermal energy to fuse materials by melting during their deposition; energy sources:</p> <ul style="list-style-type: none"> • Laser (DED-LB) • Electron beam (DED-EB) • Plasma arc 	<p>Material extrusion (MEX)</p> <p>Selective dispensing of materials by usage of a nozzle or an orifice</p> <ul style="list-style-type: none"> • Fused deposition modeling (FDM) • Fused filament fabrication (FFF) 	<p>Material jetting (MJT)</p> <p>Selective deposition of droplets of a feedstock material, cured by:</p> <ul style="list-style-type: none"> • Ultraviolet (UV) radiation • Heat • Reaction during droplet mixing
<p>Powder bed fusion (PBF)</p> <p>Selective fusion of regions of a powder bed by thermal energy; energy sources:</p> <ul style="list-style-type: none"> • Laser (LBF-LB) • Electron beam (PBF-EB) 	<p>Sheet lamination (SHL)</p> <p>Bonding of sheets of material</p>	<p>Vat polymerization (VPP)</p> <p>Selective curing of a liquid photopolymer in a vat by light-activated polymerization</p> <ul style="list-style-type: none"> • Stereolithography (SLA) • Digital light processing (DLP) 	

Figure 1: Seven divisions of AM according to DIN EN ISO/ASTM 52900:2022-03 [22–24].

Powder bed fusion – laser beam (PBF-LB), often referred to as laser-based powder bed fusion, laser sintering (LS) or formerly as selective laser sintering (SLS), is capable of processing a wide range of materials [25]. While the term SLS was rather related to polymers, selective laser melting (SLM) was used in the context of metals [23]. However, following the latest standardization efforts by ISO/ASTM [22], the term PBF-LB should be used. The two most commonly utilized materials in PBF-LB are metals (PBF-LB/M) [26] and polymers (PBF-LB/P) [27]. Additionally, ceramics are also suitable for this process, although they present challenges in direct processing [28]. This is mainly due to thermal stress-induced cracks and low absorptance of ceramic powder materials at visible and near infrared laser wavelengths [29].

2.1.1 Fundamentals of the PBF-LB/P Process

The PBF-LB/P process can be divided into three recurring main process steps [30]: powder application, irradiation, and consolidation. Beforehand, the build job is prepared by supplying a computer aided design (CAD) data set containing the geometry information of the parts to be generated [31]. In this context, the most common file format is the standard tessellation language (STL), which represents the surface of 3D objects as a collection of triangles. It is widely supported by most machine-specific control software [32]. Additionally, for preparing the build job, powder is filled into the powder hopper. In order to increase process reliability, a thermal insulation layer consisting of the powder for the respective build job is created on the build platform. In general, powder efficiency in PBF-LB/P is relatively low [33]. Studies have shown that the nesting efficiency, which relates the weight of the parts produced to the weight of the total powder used to produce the parts, is significantly less than 20% [34]. Thus, powder portions, which are not processed into the actual part – the so-called partcake material, or powder from the overflow containers (see Figure 2) – need to be refreshed with virgin powder, usually in a mixing ratio of 1:1 [35]. Refreshing with virgin powder is necessary to compensate for the physical and chemical aging effects of the partcake and overflow material caused by exposure to high temperatures inside the build chamber and powder section [36]. Figure 2 gives a schematic overview of the key parts of a PBF-LB/P machine. Depending on the machine manufacturer, the individual implementation of the functional elements can vary considerably.

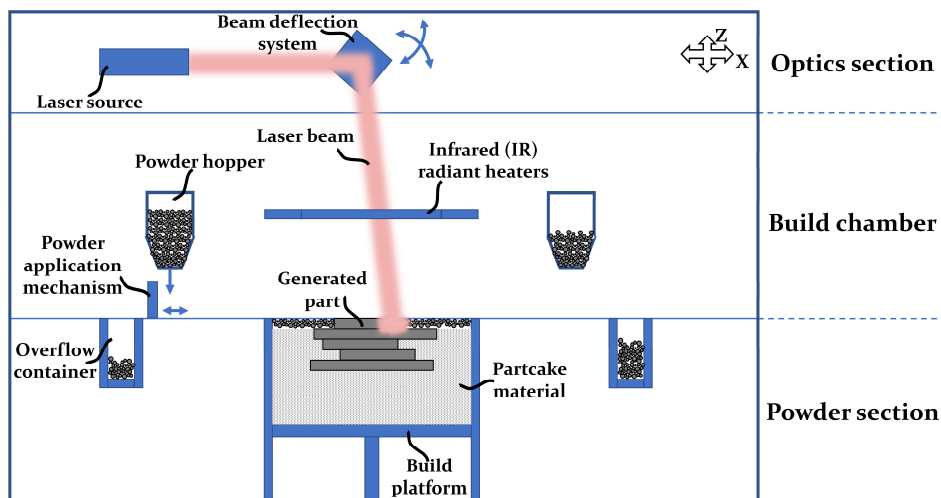


Figure 2: Schematic overview of a PBF-LB/P machine, based on [30,35].

In general, three sections can be distinguished – optics section, build chamber and powder section [35]. The optics section contains the laser source and a beam deflection system composed of mirrors and a galvanometer scanner to ensure the process-specific high laser scanning velocities of several m/s.

Laser sources for PBF-LB/P

Since most polymers exhibit suitable absorption properties at a laser wavelength of 10.6 μm , carbon dioxide (CO_2) lasers emitting at this wavelength are still the most common laser sources for PBF-LB/P [37]. The reason for the generally high absorption of laser radiation at a wavelength of 10.6 μm in polymers is mainly due to the excitation of molecular vibrations [38]. Hence, the high absorption of electromagnetic radiation at a wavelength of 10.6 μm in polyamide 12 (PA12), which is the most commonly used polymer in PBF-LB/P [39], can be attributed to the excitation of a stretching vibration between the carbon atoms of the main chain and the carbonyl groups as side chains [40]. However, recent trends in this area suggest a growing preference for shorter wavelengths such as 5.5 μm , as shown by the use of carbon monoxide (CO) lasers [41]. The primary reason for this trend is the enhanced detail resolution made possible by the smaller achievable spot sizes of laser radiation at shorter wavelengths [42]. In addition, diode lasers that emit in the near-infrared (NIR) range are becoming increasingly important. These diode lasers offer advantages such as compact dimensions, which allow the development of small desktop devices [43], and high throughputs when used in diode laser arrays [44]. However, the absorption of polymer powders in the NIR is only around 10 %, whereas the absorption at 10.6 μm is usually > 70 % [6]. This requires the usage of additives such as dyes or carbon particles [45] to achieve sufficient absorption [46]. In pharmaceutical PBF-LB/P [47], the use of CO_2 lasers is not possible because the energy input to achieve sufficient interlayer connection is too high [48] and exceeds the thermal degradation threshold of the drugs [49]. Therefore, dyes in combination with diode lasers [50] are used to target the absorption of laser energy to prevent thermal damage [51].

Process cycle

3D parts are generated by iteratively applying the main process steps powder application, irradiation, and consolidation in the build chamber (see Figure 2) [52]. The build chamber is preheated to a material dependent temperature via radiant heaters emitting in the infrared (IR) spectrum. A doctor blade- or roller-based powder application mechanism is utilized to homogeneously spread a powder layer with a thickness between 80 μm and

150 μm . Mostly, a layer thickness of 100 μm is used [30]. For powder application, the build platform is lowered by a distance corresponding to the desired layer thickness before a new powder layer is applied by the powder application mechanism (see 2.1.2). In order to reduce the cooling of the irradiated and consolidated cross-sectional area of the generated part by the new powder layer, the powder is preheated before application. The layer thickness of the applied powder layer strongly depends on the particle size distribution (PSD) and flowability of the powder and correlates with the achievable print resolution of the part in height direction (z-direction) and the resulting process time. By applying a special powder fractioning process for polyamide 11 (PA11), layer thicknesses of down to 40 μm can currently be achieved [41]. However, especially the fine particle fractions with diameters < 40 μm cannot be processed in PBF-LB/P due to strong interparticle attraction forces [14]. They reduce the powder flowability and thus need to be strained out, negatively impacting the environmental footprint of this technology [34].

Materials for PBF-LB/P

PBF-LB/P requires the use of thermoplastic polymers, i.e., polymers which undergo a transition from a hard structure to a softer one and finally end up as a viscous melt when heated [53]. Especially in the early days, amorphous polymers, such as polycarbonate (PC) or polystyrene (PS) were used for PBF-LB/P – mainly due to their low shrinkage. Since they show inferior flowability compared to semi-crystalline polymers, the corresponding parts had a higher porosity and thus limited mechanical resistance. For this reason and because of a growing understanding for suitable process windows for processing semi-crystalline polymers in PBF-LB/P [54], amorphous polymers became less important [55]. According to the model of quasi-isothermal laser sintering [56], a semi-crystalline polymer exhibits a temperature level at which both the solid and molten states can exist simultaneously. This implies that semi-crystalline polymers suitable for PBF-LB/P must show a hysteresis between melting and crystallization [57]. Figure 3 presents a schematic differential scanning calorimetry (DSC) curve of a semi-crystalline polymer. It is important to note that heating and cooling rates for DSC measurements in the context of PBF-LB/P are typically in the range of 10 – 20 K/min. In contrast, the laser-induced heating and subsequent cooling rates during PBF-LB/P lie in the range of 10^6 K/min [58].

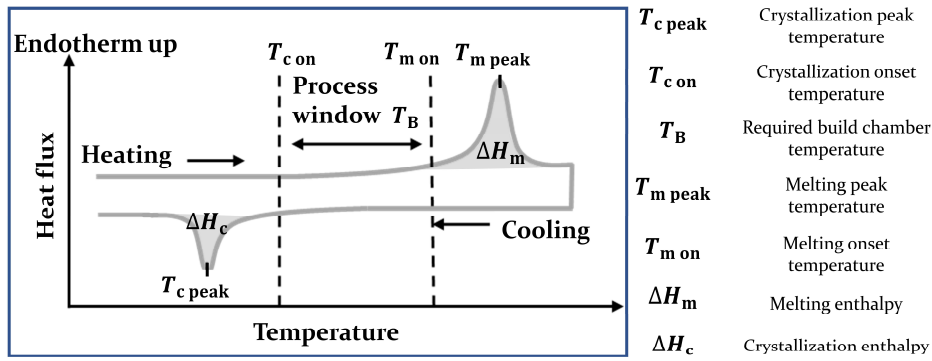


Figure 3: Schematic DSC curve of a semi-crystalline polymer with process-relevant temperatures, based on [56,59].

Despite this significant difference in heating and cooling rates between a DSC measurement and the real PBF-LB/P process, DSC curves provide valuable information about the material-specific process window of semi-crystalline polymers. The process window and therefore the required build chamber temperature T_B are defined as temperature range between the crystallization onset temperature $T_{c \text{ on}}$ and the melting onset temperature $T_{m \text{ on}}$ of the polymer. In this temperature range, both solid and molten states can be present [60]. According to the model of quasi-isothermal laser sintering, only the melting enthalpy ΔH_m required for phase transition between the solid and the molten state has to be supplied by laser radiation [57]. By selectively scanning the desired geometry on the powder surface with the laser radiation applying a specific irradiation strategy, e.g., a meander pattern [61], a cross-sectional area of the part is created [62]. Important process parameters are the laser power P_L , the distance between the individual paths of the scanned laser radiation, the so-called hatching distance h_s and the scanning velocity v_s . If the build chamber temperature T_B is too low, premature crystallization may occur, accompanied by thermal and crystallization-induced shrinkage processes, leading to the parasitic effect of curling [63]. These shrinkage processes cause the more rapidly cooling edge regions of the laser-irradiated cross-sectional area to bulge upward due to thermal stresses. Since the curled areas are prone to adhere to the powder application mechanism (see Figure 2) during powder spreading, this usually leads to an abortion of the build job [64]. Conversely, if the build chamber temperature is too high, it can have a negative effect on the dimensional accuracy and surface quality of the manufactured parts. This is because the excessive temperature can cause powder particles to adhere to the outer contour of the part in an uncontrolled manner, resulting in undesirable surface roughness and impaired dimensional accuracy [37].

The parasitic effects resulting from inappropriate build chamber temperatures suggest that polymers with a high temperature delta between T_{con} and $T_{\text{m on}}$ are desirable, as the large delta correlates with a large process window.

Model of quasi-isothermal sintering

The model of quasi-isothermal laser sintering assumes that the molten powder does not crystallize in the build chamber until the parts are finally generated and the subsequent cooling phase has begun [57]. However, the general validity of this assumption has been challenged in recent years [65]. It was found that in deeper layers of the manufactured part – under near-isothermal conditions with cooling rates significantly below 1 K/min – isothermal crystallization already occurs during the PBF-LB/P process [66]. This was attributed to the heating and cooling rate dependence of the crystallization of polymers [67]. Semi-crystalline polymers crystallize significantly earlier at lower cooling rates [68], i.e., at higher temperature levels [35]. This contradicts the original model of quasi-isothermal laser sintering. Recent findings indicate that crystallization, associated with a transition from the molten to the solid state, already occurs during the PBF-LB/P buildup process [69]. Based on these findings, a defined temperature gradient in z-direction can be applied by taking advantage of the already ongoing isothermal crystallization during the building process. Thus, a more efficient cooling phase and furthermore an enhanced reproducibility of part properties due to a homogenized thermal history of the parts can be achieved [69].

Consolidation

The final step of the three iterative main process steps after powder application and irradiation is the consolidation step. Depending on the polymer type, essentially two different consolidation mechanisms can occur: liquid phase sintering and partial melting on the one hand, and full melting on the other [70]. In rare cases, a third mechanism, chemical consolidation, e.g., by partial cross linking, may take place [55]. In contrast to molding processes, there is no mechanical pressure involved in PBF-LB/P. Thus, the driving forces for consolidation in PBF-LB/P purely arise from temperature effects, gravity and capillary forces. This requires the use of materials that have a melt viscosity η below a certain critical value in accordance with the respective surface tension driving force γ to obtain parts with low porosity [71]. As described in [72], there is a strong correlation between consolidation and powder application. This results in a dependence of the consolidation depth [73] on the number of layers already additively generated. In

case of the first laser-irradiated powder layer, the consolidation process can develop freely into the underlying powder bed, resulting in a higher consolidation depth and thus layer thickness (see Figure 4).

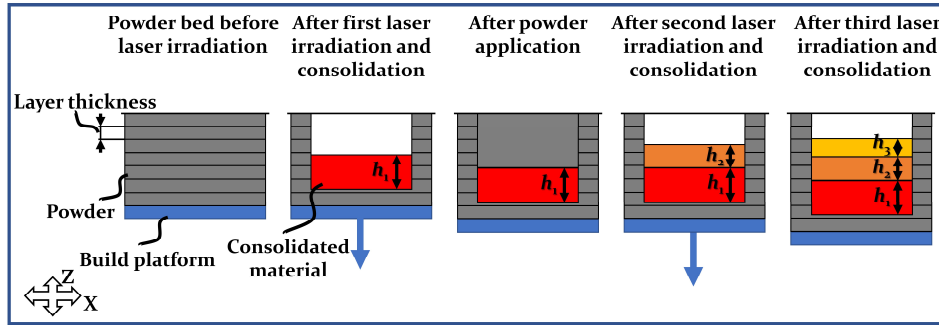


Figure 4: Schematic illustration of PBF-LB/P consolidation depths and layer thicknesses h_1 , h_2 and h_3 for printing the first three layers, based on [73].

Only after a certain number of additively generated layers, according to [73] after approximately ten layers, steady state conditions with constant consolidation depths and therefore layer thicknesses are achieved. Thus, for printing the first layers, significantly more powder must be applied than is required for the desired layer thickness. In order to maintain constant part properties in each layer, the laser energy input must be adjusted according to the amount of powder that needs to be consolidated [74].

2.1.2 Conventional Powder Application Methods for PBF-LB/P

The powder application step, often also referred to as powder spreading or coating, provides the powder material required to build up a layer of the 3D part. In general, two different mechanisms can be distinguished for conventional powder application: doctor blade (Figure 5 a)) and roller application mechanisms. The latter can rotate counterclockwise (Figure 5 b)) or clockwise (Figure 5 c)). Doctor blades, which are often also referred to as wipers or squeegees [75], can have a variety of different geometries [76], from flat (Figure 5 a)) to rounded, angled or with a sharp knife [77]. As described in [78], combinations of doctor blade and roller application mechanisms were also employed, which increased the powder bed density [79]. Moreover, in [80] the spreading mechanisms were mechanically stimulated to induce vibrational modes. This also enhanced the packing density of the applied powder layer [81].

Prior to the actual powder application step, the feed powder must be supplied to the application mechanism. For this purpose, hopper- (see Figure 2) or piston-based systems are commonly used [78]. In case of piston-based systems, a feedstock platform containing the feed powder is installed instead of the powder hopper visible in Figure 2.

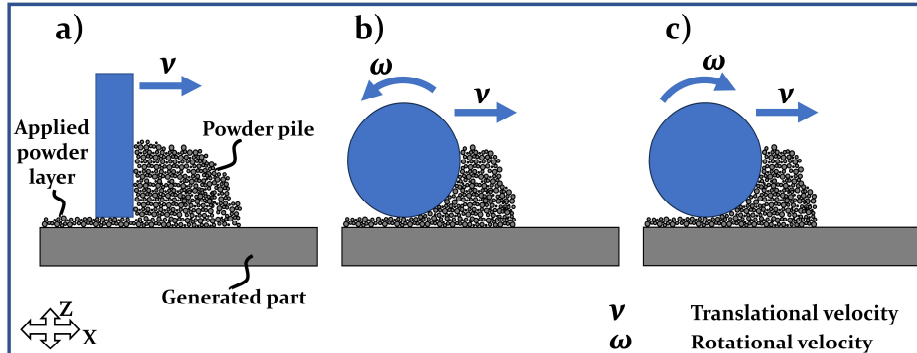


Figure 5: Overview of conventional powder application methods, v – translational velocity, ω – rotational velocity; a) doctor blade, b) counterclockwise rotating roller, c) clockwise rotating roller.

The platform containing the feedstock material is lifted prior to powder application to provide the required powder. To avoid undercooling of the irradiated and consolidated areas during subsequent powder application, the feed powder must be preheated to a temperature corresponding to the process window of the polymer (see Figure 3). However, according to [82], the application of a fresh powder layer using conventional powder application methods inevitably leads to undercooling of the powder bed surface - potentially to temperatures below the process window [83]. As described in 2.1.1.1, this can cause premature crystallization associated with the parasitic effect of curling and consequently the abortion of the build job. The reason for the inevitable undercooling is an insufficient preheating of the feed powder before and during application. This effect can be particularly challenging when processing polymer powders with a small processing window. In this case, increasing the preheating time of the feed powder and reducing the translational velocity v of the powder application mechanism are possible compensation strategies [84]. However, these strategies extend process times and therefore diminish the productivity of the PBF-LB/P process. Even with a preheated doctor blade or roller, the limited heat conductivity of polymers does not allow sufficient heating of the entire fresh powder layer.

As powder application sets the starting conditions for the subsequent PBF-LB process steps (see 2.1.1) [85], it plays a key role in determining the final part quality [86]. The aim is to reproducibly achieve a homogeneous and dense powder layer [87], resulting in a dense powder bed [88]. In particular, the packing density, which is closely related to the presence and distribution of pores within the powder layer, is critical to the PBF-LB process [89]. A high and uniform packing density of the applied powder layer enhances the absorption of laser energy [90], the surface finish [91], and the density and thus mechanical properties [92] of the final solidified part [93]. While in PBF-LB/M a higher packing density of the applied layer [94] additionally leads to an improved melt pool shape [95], in PBF-LB/P the heat conductivity of the powder layer can be increased [35]. As shown in [96], this reduces curling due to faster through-heating of the applied powder layer.

Essentially, three main influencing factors determine the resulting quality of the conventionally applied powder layer in terms of homogeneity and density. In Table 1, the influence of the utilized powder application mechanism itself is examined. The influence of crucial parameters of the powder application process is summarized in Table 2. Finally, the influence of powder properties on the homogeneity and density of the applied powder layer is presented in Table 3.

Table 1: Influence of geometrical aspects of conventional powder application mechanisms on the resulting quality of the applied powder layer in terms of homogeneity and density for PBF-LB/P.

Application mechanism and key geometrical aspects	Effect on powder bed quality
Doctor blade: <ul style="list-style-type: none"> • Width and height [97] • Inclination angle [77] • Tip roundness [98] 	<ul style="list-style-type: none"> ➤ Higher powder bed density with round tip [97] and increasing width [98] ➤ More homogeneous powder layer with flat doctor blade (see Figure 5 a) [75]
Roller: <ul style="list-style-type: none"> • Diameter [99] • Surface texture [100] 	<ul style="list-style-type: none"> ➤ Higher powder bed density with larger diameter [99] ➤ Higher powder bed density with smooth instead of textured roller [100]
Generally: Highest powder bed density achievable with counterclockwise rotating roller (see Figure 5 b)) [101]	

The effects of the powder application mechanism itself on the resulting layer quality, summarized in Table 1, suggest that a counterclockwise rotating roller with a smooth surface and a large diameter is favorable for achieving a homogeneous and dense powder layer. As already mentioned, a greater compaction and therefore higher powder bed density increases heat conductivity and thus reduces curling. For this reason, counterclockwise rotating rollers are favorable for testing new powder materials for PBF-LB/P with not fully known process windows and for manufacturing materials with small process windows that are prone to curling [102]. However, as demonstrated in [103], counterclockwise rotating rollers lead to pronounced particle movement within the powder pile (see Figure 5). This involves significantly higher particle velocities than in case of doctor blade-based powder application. According to [104], there is a strong correlation between the impact velocity of polymer particles and the resulting triboelectric charging. Electrostatic interaction forces [105] affect powder flowability [106] and therefore directly influence the quality of the applied powder layer (cf. Table 3) [107]. Thus, the pronounced particle movement [108] induced by counterclockwise rotating rollers is a stronger limiting factor on the maximum translational velocity than is the case with doctor blades. Electrostatic interaction between powder particles is discussed in detail in section 4.1.

Table 2: Influence of characteristics of the conventional powder application process on the resulting quality of the applied powder layer in terms of homogeneity and density for PBF-LB/P.

Key process characteristics	Effect on powder bed quality
Layer thickness [109]	<ul style="list-style-type: none"> ➤ No clear trend with respect to powder bed density deducible [110,111] ➤ More homogeneous powder layer with larger layer thickness [112]
Translational velocity [113]	<ul style="list-style-type: none"> ➤ No clear trend with respect to powder bed density deducible [113] ➤ Less homogeneous powder layer with higher translational velocity [87]
Rotational velocity and direction [98]: <ul style="list-style-type: none"> ➤ Counterclockwise [98] ➤ Clockwise [102] 	Counterclockwise: <ul style="list-style-type: none"> ➤ No clear trend of rotational velocity with respect to powder bed density deducible [98] ➤ Material-dependent effect of rotational velocity on powder bed homogeneity [98] Clockwise: <ul style="list-style-type: none"> ➤ Higher powder bed density with higher rotational velocity [79] ➤ Significantly more defects [79] and thus less homogeneous powder layer with higher rotational velocity [102]
Vibrational frequency and amplitude in case of mechanical stimulation [114]	<ul style="list-style-type: none"> ➤ Higher powder bed density with larger amplitude and frequency, especially close to resonance frequencies of the mechanical system [114] ➤ Generally negative impact on layer homogeneity due to possible formation of ridges or distortions [114]

Table 3: Influence of powder properties on the resulting quality of the conventionally applied powder layer in terms of homogeneity and density for PBF-LB/P.

Powder properties	Effect on powder bed quality
Particle size and particle size distribution [115]	<ul style="list-style-type: none"> ➤ Generally lower powder bed density and less homogeneous layer with finer powder due to strong interparticle cohesive / adhesive forces [116](van der Waals [117], liquid bridges [118,119], electrostatic interactions [120] or, more rarely, magnetic dipole-interactions) [121] ➤ Higher powder bed density [122] and more homogeneous layer with multimodal powders [123] having a properly adjusted mixing ratio between finer and coarser fractions [124]
Particle shape [86]	<ul style="list-style-type: none"> ➤ Especially for doctor blade-based powder application higher powder bed density with spherical powder particles [86] ➤ Less pronounced dependence of powder bed density on particle shape for counterclockwise rotating roller [86] ➤ Higher powder bed density by adding fibers with properly adjusted length to powder particles [125]
Influence of aging effects, moisture and temperature on powder flowability [126]	<p>Aging effects:</p> <ul style="list-style-type: none"> ➤ Negative influence on powder bed density and layer homogeneity due to enhanced electrostatic interaction associated with aging powders [105] <p>Moisture and temperature of the powder:</p> <ul style="list-style-type: none"> ➤ Decreasing Young's modulus with increasing temperature of polymers leads to an enlarged contact surface between particles and thus enhanced friction forces and triboelectric charging [127] ➤ Additionally: Significantly increasing cohesive / adhesive forces between polymer particles [128] with increasing temperature, but subordinate effect of powder moisture on flowability [129] ➤ Summarizing: Overall improving powder bed quality with increasing temperature due to improved powder flowability with a Hausner ratio $H_r < 1.25$ due to the complex interaction of the two effects described above [126]

The large number of different effects summarized in Table 1, Table 2 and Table 3, determining the quality of the applied powder layer, particularly

those related to powder properties (see Table 3), severely limits the availability of suitable powder materials for PBF-LB/P [130]. Especially by reducing the dependence of the powder layer quality on powder properties, the variety of polymer materials suitable for PBF-LB/P could be drastically increased. While thousands of different feedstock materials are available for traditional polymer processing techniques such as injection molding or extrusion, only a few formulations are currently available for PBF-LB/P [130].

The Hausner ratio H_r is used to evaluate the flowability of powders [131]. It relates the tap density ρ_{tap} to the bulk density ρ_b and is calculated as follows [132]:

$$H_r = \frac{\rho_{\text{tap}}}{\rho_b} \geq 1 \quad (1)$$

According to [132], the flowability of polymer powders is classified as summarized in Table 4.

Table 4: Classification of the flow properties of polymer powders, based on [35,132].

Hausner ratio H_r	Flow property
$1.00 < H_r \leq 1.25$	Free flowing
$1.25 < H_r \leq 1.40$	Free flowing to cohesive
$H_r > 1.40$	Cohesive

Beyond the strong dependence on powder flowability, a major limiting factor of conventional powder application methods, which decisively restricts the versatility of PBF-LB/P, is the limited number of materials that can be processed simultaneously. Doctor blade- or roller-based powder application methods only allow one material to be applied at a time [133]. As a result, multi-material parts or parts with locally tailored material compositions and thus functional properties cannot be generated by PBF-LB/P with conventional powder application methods [134].

2.1.3 New Approaches for Powder Application Methods in PBF-LB/P

The shortcomings of conventional powder application methods explained in section 2.1.2 highlight the need for improved application strategies for PBF-LB/P. As discussed in section 2.1.2, a major drawback of conventional powder application methods is their strong dependence on the powder flowability and thus the limited number of suitable powder materials [133].

In addition, the increased parasitic electrostatic charging of powder particles at higher powder application velocities limits productivity. Also, the inevitable latency time until a freshly applied powder layer is through heated to decrease undercooling of the previously irradiated and consolidated regions reduces productivity of the PBF-LB/P process [69]. Finally, with conventional doctor blade- or roller-based powder application methods only one material can be applied simultaneously [134].

All new approaches for powder application focus on overcoming the latter limitation of only being able to apply one material at a time. As shown in Figure 6, the new approaches can be divided into three categories according to their powder deposition modality.

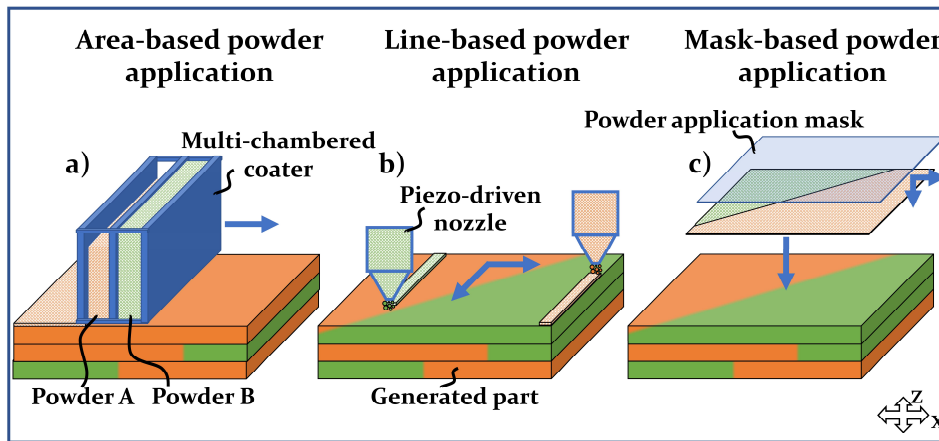


Figure 6: Overview of three categories of new powder application methods; a) area-based with a multi-chambered coater, b) line-based and c) mask-based powder application.

In the case of area-based powder application (see Figure 6 a)), the new layer is deposited over the entire powder bed, similar to the conventional doctor blade mechanism (see Figure 5 a)) [135]. For this purpose, the conventional doctor blade-based application mechanism was developed further to a multi-chambered coater, often also referred to as multi-chambered recoater [136]. Typically, two chambers containing two different powder materials are employed. The chambers can be aligned either perpendicularly (as shown in Figure 6 a)) or parallelly with respect to the application direction [137]. For the perpendicular alignment, flexible locking mechanisms are necessary to only deposit one powder at a time [134].

There are various possibilities to achieve multi-material layers with a multi-chambered coater. In case of the parallel configuration, two or more areas consisting of the respective powder materials can be applied, whereby the

individual areas lie next to each other with distinct boundary lines [135]. However, this does not allow to flexibly tailor the material composition within a layer or from layer to layer. Additionally, a sharp separation zone is created, which is also susceptible to stresses and delamination effects after consolidation and solidification due to the abrupt material change [138]. The difficulties associated with the sharp separation zone can be partially compensated for dual chambered coaters by using powder mixtures of both materials [139]. Nevertheless, the ability of area-based powder application using a multi-chambered coater in parallel configuration to generate tailored multi-material parts is severely limited [140].

In contrast, the perpendicular configuration provides a further degree of freedom by allowing different powders to be applied alternately [137]. In addition, a flexible suction unit can be employed [141] to remove unconsolidated material so that a different powder can be applied to the same layer without lowering the build platform [142]. However, this concept is prone to cross-contamination between the different material areas, either related to leakage of the locking mechanism, or during suction and re-application of a different powder to the same layer [134]. In summary, apart from some limited possibilities to achieve multi-material parts by PBF-LB/P, this new approach for powder application still suffers from similar drawbacks to the conventional doctor blade-based method.

The second category of new powder application methods for PBF-LB/P is the line-based approach (see Figure 6 b)). Unlike the first approach, line-based powder application is highly selective, depositing powder line-by-line only where it is needed to create the part. First approaches of vibration nozzle-based powder application, often also referred to as dispenser-based application, were already shown in [143]. Essentially, this method is based on the formation of particle bridges between the particles inside the powder nozzle due to interparticle forces, in particular van der Waals forces. If the powder flowability, which is influenced by the powder properties summarized in Table 3, is properly matched to the nozzle used, powder deposition will only occur by breaking the powder bridges with a vibratory stimulus [144]. In addition to powder flowability, nozzle geometry [145], powder moisture, powder temperature and, finally, the frequency and amplitude of vibration excitation all have a significant impact on line-based powder application [146]. Typically, a piezoelectric actuator is utilized to mechanically excite the nozzle. The piezoelectric excitation generates the required vibrational stimulus, which increases the mean distance between the powder particles, thereby reducing the interparticle attraction forces. The effect

of reducing interparticle forces by piezoelectric excitation is discussed in detail in section 4.2.

Ideally, powder bridges form back again without external vibrational stimulus, ensuring a precise start-stop functionality of the line-based powder application approach [147]. To increase productivity, the powder nozzles containing the different materials to be applied can be arranged in arrays [148]. However, due to the line-by-line deposition modality with line widths in the range of several hundred μm , layer preparation times can easily be in the order of minutes [144]. In contrast, the deposition of a powder layer using conventional powder application methods (see 2.1.2), takes less than half a minute, including the latency to preheat the freshly applied powder [69]. Although this comparison is between a laboratory-scale nozzle-based application mechanism and an industrial machine, the cycle time to prepare a powder layer remains a major limiting factor of the line-based approach. Therefore, in [149] a combination of conventional and nozzle-based powder application is suggested. This is particularly beneficial for reducing cycle time when only small amounts of powder need to be applied through the nozzle [150], e.g., filler particles or fibers to locally tailor the properties of the part [146]. However, if not only filler particles to modify the properties of the part need to be applied through the nozzle, but also a fraction of the total powder layer, a suction unit is required to locally remove the conventionally applied powder [151]. The cavities created in this way can be filled with a different material using the line-based application mechanism [151]. As the additional process step of selective powder removal is required in this case, the total cycle time increases again significantly.

In contrast to the area-based powder application approach (see Figure 6 a)), line-based powder application (see Figure 6 b)) allows highly selective deposition of different materials for PBF-LB/P. As a result, the material composition can be adjusted both within a layer and from layer to layer, offering the potential to increase the flexibility of PBF-LB/P for generating multi-material parts. Nevertheless, line-based powder application also has some drawbacks. As mentioned above, the long cycle time required to apply a powder layer is a major disadvantage of this approach. In addition, line-by-line powder deposition inevitably results in poor layer homogeneity due to grooves [145]. This suggests that line-based powder application is particularly suited to the selective deposition of filler particles or fibers, rather than the creation of entire layers. These filler particles, such as silver, copper or carbon black, or fibers can be used to locally tailor the chemical, electrical or mechanical properties of the PBF-LB/P part in situ [152]. Another major drawback is the strong dependence of the line-based approach

on powder flowability. Even a small mismatch between nozzle geometry, piezoelectric excitation parameters and powder flowability can result in undesired or uncontrolled powder deposition or nozzle blockage. Due to the strong dependence on powder flowability, the variety of suitable powder materials is still limited, comparable to conventional powder application methods (see 2.1.2). However, the ability to selectively deposit different materials makes line-based approaches a promising extension of conventional powder application methods.

Finally, the third category of new powder application methods for PBF-LB/P is the mask-based approach (see Figure 6 c)). At first glance, the mask-based application looks similar to the area-based approach (see Figure 6 a)) as in both cases powder is deposited across the entire powder bed, rather than line-by-line as in the line-based approach shown in Figure 6 b)). However, the key difference between the mask-based and area-based approaches is that mask-based application does not require the lateral movement of an application device, such as a doctor blade, roller or coater, across the powder bed. Instead, the entire new powder layer is applied at once. As the term mask implies, the powder layer can be flexibly shaped in the x-y plane, allowing for a high degree of selectivity.

There are essentially two different concepts for this approach. According to [153], one is based on negative pressure, which selectively attracts powder particles to a cylindrical drum. This drum consists of a fine mesh with a mesh size smaller than the diameter of the smallest particles of the powder to be applied. A matrix of valves can relieve the negative pressure locally, allowing the powder to fall from the sieve drum onto the build platform [133]. However, apart from patents [153,154] and demonstration videos [155], there is no scientific research on the pressure-based concept [133].

The second concept for mask-based powder application utilizes electrostatic attraction and repulsion forces between powder particles and a selectively dischargeable photoconductor to deposit a powder layer. The origins of this technology lie in laser printing of toner particles onto paper, which has revolutionized the printing industry [3]. Details of this technology, known as electrophotography, electrophotographic powder application (EPA) or xerography, can be found in section 2.2.

EPA [156] provides the ability to selectively apply powder based purely on electrostatic forces [157]. This can be used to significantly reduce the dependence of powder application on powder flowability, which is a major drawback of both the conventional application methods (see 2.1.2) as well as the area- and line-based approach (see Figure 6 a) and b)) [158]. As

shown in [159], the shape of the powder pattern can be tailored almost arbitrarily, depending mainly on the latent charge pattern on the photoconductor. However, as shown in a number of studies [145,156–158,160–163], only the general proof of concept for the use of EPA in PBF-LB on a single-layer basis has been demonstrated to date. The current state of the art of substituting conventional powder application methods by EPA in PBF-LB/P is discussed in detail in section 2.2.2.

Table 5 compares the conventional powder application methods (see 2.1.2) and the new powder application approaches (see 2.1.3) in terms of their ability to overcome crucial limitations of the conventional methods.

Table 5: Comparison of conventional powder application methods and new powder application approaches for PBF-LB/P, based on studies reported to date [133]; the new approaches are highlighted in light blue.

	Conventional	Area-based	Line-based	Mask-based	
				Air pressure	Electrostatics
Multi-material capabilities	-	Poor	Good	Good	Good
Selectivity	-	-	High	High	High
Dependence on powder flowability	High	High	High	Unknown	Low
Coating rate [133]	240 to 560 mm ³ /s	40 to 140 mm ³ /s	0.4 to 4.1 mm ³ /s	130 to 290 mm ³ /s	130 to 290 mm ³ /s
Resolution of applied powder layer / pattern [133]	X	-	0.09 to 1.3 mm	0.8 to 1.6 mm	0.8 to 1.6 mm
	Y	-	0.09 to 1.3 mm	0.8 to 1.6 mm	0.8 to 1.6 mm
	Z	-	0.1 to 0.15 mm	Unknown	Unknown
Manufacturing readiness level (MRL) [133]	10	4 to 5	4 to 5	3 to 4	2

Therefore, the ability of each application method to create multi-material powder layers is evaluated. The achievable selectivity is further assessed as a measure of the potential to tailor the material composition within a layer and from layer to layer. The dependence on the powder flowability gives an

estimation of the powder application method to increase the number of suitable powder materials for PBF-LB/P. To get a rough estimate of the achievable productivity of the powder application method, the coating rate is given based on [133]. To evaluate the geometrical accuracy of the application method, the resolution of the applied powder layer or pattern is also adapted from [133]. Finally, similar to [133], the maturity of the technology is assessed on the basis of the Manufacturing Readiness Level (MRL), which extends the Technology Readiness Level (TRL) by incorporating producibility issues relevant to the manufacturing environment (cf. Figure 7) [164].

Manufacturing Readiness Level (MRL)		
Phase	MRL	Maturity of the manufacturing technology
Phase 3: Production implementation	10	Full rate production demonstrated and lean production processes prepared
	9	Low rate production demonstrated and capability to start full rate production prepared
	8	Pilot line capability demonstrated and capability to start full rate production prepared
	7	Advanced capabilities demonstrated in a production representative environment
Phase 2: Pre-production	6	Advanced capabilities demonstrated in a production relevant environment
	5	Basic capability demonstrated in a production relevant environment
Phase 1: Technology assessment and proof of concept	4	Basic capability demonstrated in a laboratory environment
	3	Experimental proof of concept completed
	2	Proposed concept applied and validated
	1	Concept proposed with fundamental scientific validation

Figure 7: Overview of the Manufacturing Readiness Level (MRL), based on [164,165]; the detailed guideline for the evaluation of the MRL according to the Department of Defense of the United States of America is available under [166].

2.2 Electrophotographic Powder Application (EPA)

As shown in section 2.1.3, electrophotography is a promising approach to surmount the shortcomings of conventional powder application methods in PBF-LB/P. The aim of this section is to provide a basic understanding of the key aspects of EPA relevant to the implementation of this technology in PBF-LB/P. In particular, current limitations, which account for the low MRL of 2 (see Table 5) and thus inhibit a successful utilization of EPA, are emphasized in section 2.2.2.

2.2.1 Physical Principles of Electrophotography

The full electrophotographic printing process, as used in conventional 2D office laser printers [167] with toner particles [168], consists of six steps, which are summarized in Table 6.

Table 6: Process steps of EPA, based on [169].

Step number	Step name	Description
1	Charge	Charging of photoconductor and powder
2	Expose	Selective exposure of photoconductor to electromagnetic radiation to create latent charge pattern
3	Develop	Attraction of powder particles to the surface of the photoconductor by using the latent charge pattern to create a powder pattern
4	Transfer	Moving of the powder pattern from the development area to the actual fusion area and powder deposition
5	Fuse	Consolidation of the deposited powder
6	Clean	Removing of residual material and charges from the photoconductor

In electrophotography, charges are generated by either gas discharge or triboelectric charging. To charge the photoconductor, gas discharge-based charging is used, often referred to as corona charging due to the underlying physical effect of corona emission. A corotron (see Figure 8) or scorotron (see Figure 9) can be employed for this charging method. In order to achieve sufficient particle attraction and thus successful powder development in step 3, a surface potential U_p in the range of $U_p \approx \pm 600 \text{ V}$ is needed at the surface of the photoconductor [169].

The fundamental description of the relationship between the flux of an electric field Φ_E through an area A and the source for that flux, which is the charge, is formulated in Gauss's Law [170].

For a closed area A placed in an arbitrary electric field \vec{E} , the flux Φ_E through A is given by [170]:

$$\Phi_E = \oiint_A \vec{E} \cdot d\vec{S} \quad (2)$$

with a vector $d\vec{S}$ pointing in the direction of an outward normal to the closed area A . It is important to note that in case there are no sinks or sources of \vec{E} within A , the net flux Φ_E through this surface is zero. However,

to include the case of an internal sink or source, a spherical surface of radius r centered on and surrounding a positive point charge q . in vacuum is now considered. The electric field is everywhere outwardly radial, and at any distance r it is completely perpendicular to the surface of the point charge q ., which leads to:

$$E = E_{\perp} \quad (3)$$

Thus, (2) can be rewritten as follows [169-171]:

$$\Phi_E = \oiint_A E_{\perp} dS = \oiint_A E dS \quad (4)$$

Due to the fact that E is constant over the surface of the sphere, it can be written in front of the integral. Furthermore, the surface integral of a sphere is known to be $4\pi r^2$. Thus, (4) can be given as follows:

$$\Phi_E = E \oiint_A dS = E 4\pi r^2 \quad (5)$$

According to Coulomb's Law, the electric field of the point charge q . is given by [170]:

$$E = \frac{1}{4\pi\epsilon_0} \frac{q}{r^2} \quad (6)$$

Subsequently, inserting (6) into (5) results in:

$$\Phi_E = \frac{q}{\epsilon_0} \quad (7)$$

The relation given in (7) describes the electric flux associated with a single point charge q . within a closed surface A . Due to the fact that all charge distributions essentially consist of a sum of point charges, the net charge flux within any closed area is given by [171]:

$$\Phi_E = \frac{1}{\epsilon_0} \sum q. \quad (8)$$

Finally, combining (2) and (8) yields Gauss's Law in its general representation:

$$\oiint_A \vec{E} \cdot d\vec{S} = \frac{1}{\epsilon_0} \sum q. \quad (9)$$

Applying Gauss's Law [170], the required charge per unit area σ_p , which has to be obtained on the photoconductor to achieve a certain surface potential U_p , can be calculated as follows [171]:

$$\frac{1}{\epsilon_0} \sigma_p d_p = E_p d_p = U_p \quad (10)$$

Moreover, the relationship between the permittivity of free space ϵ_0 , the permittivity of the photoconductor ϵ_p and the dielectric constant of the photoconductor K_p is given as follows [170]:

$$\epsilon_0 = \frac{\epsilon_p}{K_p} \quad (11)$$

Using (11), equation (10) can be written in the following way:

$$U_p = E_p d_p = \frac{\sigma_p}{\epsilon_p} K_p d_p \quad (12)$$

with the surface potential of the photoconductor U_p , the electric field strength inside the photoconductor E_p , the thickness of the photoconductor d_p , the permittivity of the photoconductor ϵ_p , and the dielectric constant of the photoconductor K_p . For organic photoconductors, the dielectric constant is in the range of $K_p \approx 3$.

A corotron (see Figure 8) is a device used to apply the required charge per unit area σ_p (cf. equation (10)) to the photoconductor [172] to achieve the surface potential needed for subsequent powder development [169]. At sufficiently high corona voltages U_c applied to a fine wire of diameter $d_{\text{corona wire}}$, which is placed close to a grounded shielding, the air surrounding the wire is ionized [173]. Due to the repulsive forces between the equally charged wire and ions, the ions are accelerated both towards the grounded shielding and towards the surface of the photoconductor. Finally, the ions reaching the photoconductor, are responsible for σ_p and hence the surface potential U_p , whereas the ions reaching the grounded shielding give rise to a shielding current [174]. Although this shielding current is a source of inefficiency [175], it stabilizes the corona effect by promoting a balance between the ions generated and those surrounding the wire [176].

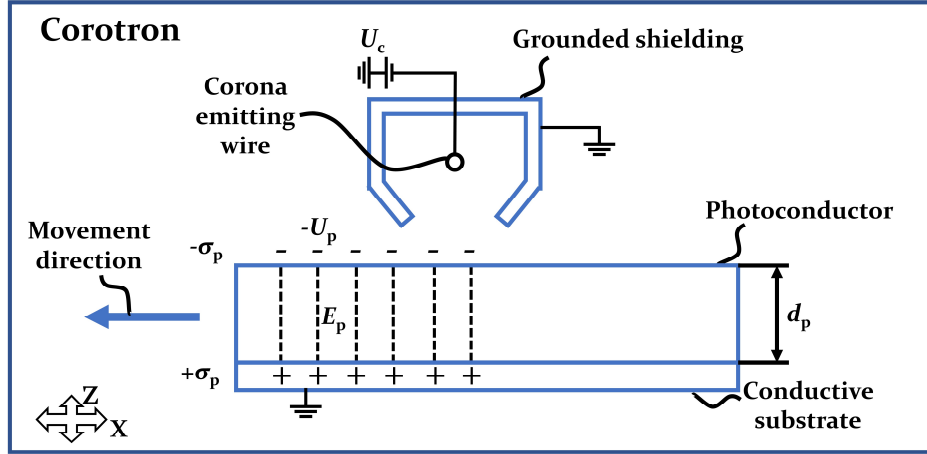


Figure 8: Schematic representation of gas discharge-based charging of a photoconductor to a negative surface potential $-U_p$ using a corotron device, consisting of a grounded shielding with a corona emitting wire inside; U_c – potential of the corona wire, d_p – thickness of the photoconductor, σ_p – charge per unit area on photoconductor, E_p – electric field strength inside photoconductor; based on [169].

Depending on the polarity and the surrounding atmospheric conditions, in particular humidity and pressure [177], different types of ions are generated by the corona effect. At a positive corona voltage U_c , mainly $(\text{H}_2\text{O})_n\text{H}^+$ and $(\text{H}_2\text{O})_n\text{NO}^+$ are formed, whereas at a negative corona voltage, mainly CO_3^- and $(\text{H}_2\text{O})_n\text{CO}_3^-$ are formed [178].

In order to accelerate electrons to sufficiently high velocities to ionize air molecules, a certain field strength E_c of the electric field surrounding the corona wire is required. It can be calculated as follows:

$$E_c = \frac{U_c}{d_c} \quad (13)$$

where U_c is the voltage applied to the corona wire and d_c is the distance to it. As long as the condition $E_c \geq E_{\text{Pasch min}}$ is fulfilled, i.e., the electric field strength E_c is above the minimum electric field strength $E_{\text{Pasch min}}$ required for Paschen's breakdown to occur, air molecules are ionized. $E_{\text{Pasch min}}$ is a function of the ambient conditions around the corona wire [179], in particular the humidity and temperature of the surrounding atmosphere [180]. As an example, a corona wire with a diameter of $d_{\text{corona wire}} = 50 \mu\text{m}$, a distance of $d_c = 1 \text{ cm}$ between the photoconductor and the wire, and a voltage applied to the corona wire of $U_c = +8000 \text{ V}$, can sufficiently charge the photoconductor to a voltage of $U_p \approx +600 \text{ V}$ at a lateral speed between the corotron and the photoconductor of 5 cm/s [169].

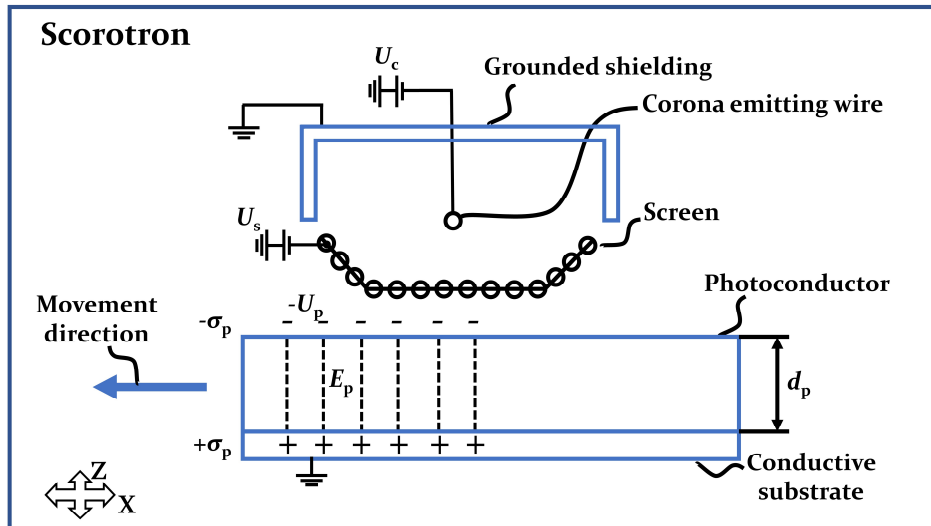


Figure 9: Schematic representation of gas discharge-based charging of a photoconductor to a negative surface potential $-U_p$ using a scorotron device, consisting of a grounded support plate and corona emitting wires and a meshed screen underneath; U_c – potential of the corona wire, U_s – potential of the screen, d_p – thickness of the photoconductor, σ_p – charge per unit area on photoconductor, E_p – electric field inside photoconductor; based on [169].

However, corona charging is susceptible to some significant non-uniformities [181] that cause inconsistent charging results [182]. As the charging of the photoconductor in process step 1 (see Table 6) forms the basis for the subsequent process steps of electrophotography, these non-uniformities are a major issue for the process reliability of this technology. According to [174], there are essentially two main causes of non-uniformity associated with corona charging. The first one is based on current avalanches which are caused by different velocities of the ions generated by the corona effect [169]. These avalanches lead to a non-uniform deposition of ions towards the photoconductor [182]. The second cause of inhomogeneous corona charging is contamination of the corona wire with toner or dust particles, which necessitates regular cleaning of the fine and fragile corona wire [169]. Often, a scorotron (see Figure 9) is used instead of a corotron to compensate for the charging irregularities [183]. It is equipped with a screen with a certain screen potential U_s , which is placed between the corona wire and the surface to be charged. This allows to determine the approximate surface potential of the photoconductor U_p by the applied screen potential U_s . Since the screen acts as a mediator for the ions generated by the high voltage applied to the corona wire [184], the charging is more homogeneous [176].

However, it is important to note that corona charging generates a significant amount of corrosive ions and reactive neutral species that are harmful to both the corona wire and the photoconductor [185]. In addition, ozone is produced and therefore adequate exhaust ventilation and occupational safety measures are required due to the safety hazards associated with ozone [186].

Besides homogeneous charging of the photoconductor, homogeneous charging of the toner powder is also an integral part of process step 1 (see Table 6). This is due to the fact that the dominant force which is responsible for development in step 3 is the electric field force \vec{F}_{el} . It is defined as follows [187]:

$$\vec{F}_{el} = q_{\text{particle}} \cdot \vec{E} \quad (14)$$

with the charge q_{particle} of the powder particle and the field strength \vec{E} of the surrounding electric field. As can be seen from (14), the particle charge directly influences the force acting on a powder particle, which dominantly determines the movement of the powder particle during development [188]. This directly affects the homogeneity, thickness and geometric accuracy of a developed powder layer.

The most common method for charging toner is triboelectric charging, which is based on tribological contact between toner particles or toner and carrier particles [189]. Toner particles are composed of an agglomerate of a polymer, a pigment and at least one charge control agent (CCA), with a particle size distribution between 6 and 20 μm [190]. In most cases, thermoplastic polymers are used [191]. Carriers typically consist of ferritic particles and CCAs added to their surface [192]. Unlike the gas discharge effect of corona charging, triboelectric powder charging generates charges by charge separation [193]. This effect is studied in detail in section 4.1.

In general, triboelectric charging of insulators such as toner particles, is poorly understood [194]. The bimodal triboelectric charge distribution of polymers is a major concern with this charging method [105]. Triboelectrically charged polymers have an integral charge close to zero. As a result, they appear almost neutral overall, although the individual particles within the powder bulk are highly charged [105]. As examined in detail in section 4.1, a neutral overall charge distribution is highly unfavorable for electrophotography. To compensate for this effect in common 2D laser printing technology, manufacturers have developed numerous different toner formulations and triboelectric charging strategies, such as single and dual

component development [195], powder cloud development [187] or magnetic brush development [196]. Although the combinations of toner polymers, CCAs, carrier particles with their CCAs and the technical implementation vary between different development methods [197], they all have in common the need for controlled tribological contact for charge separation. However, while triboelectric charging is the standard powder charging method for 2D laser printing, it has not yet been applied to electrophotography for PBF-LB/P (cf. section 2.2.2).

Having sufficiently charged the powder and photoconductor (step 1), a latent charge pattern must be created on the photoconductor by selective exposure to electromagnetic radiation of an appropriate wavelength in step 2. For this purpose, negative (see Figure 10) or positive (see Figure 11) charging organic photoconductors (OPCs) are utilized [198–200]. Apart from OPCs, they also can consist of amorphous selenium evaporated onto a metallic substrate [169]. For exposure, either lasers or diodes, which can either be scanned across the photoconductor surface or formed into a mask by a digital light processing (DLP) projector, are used.

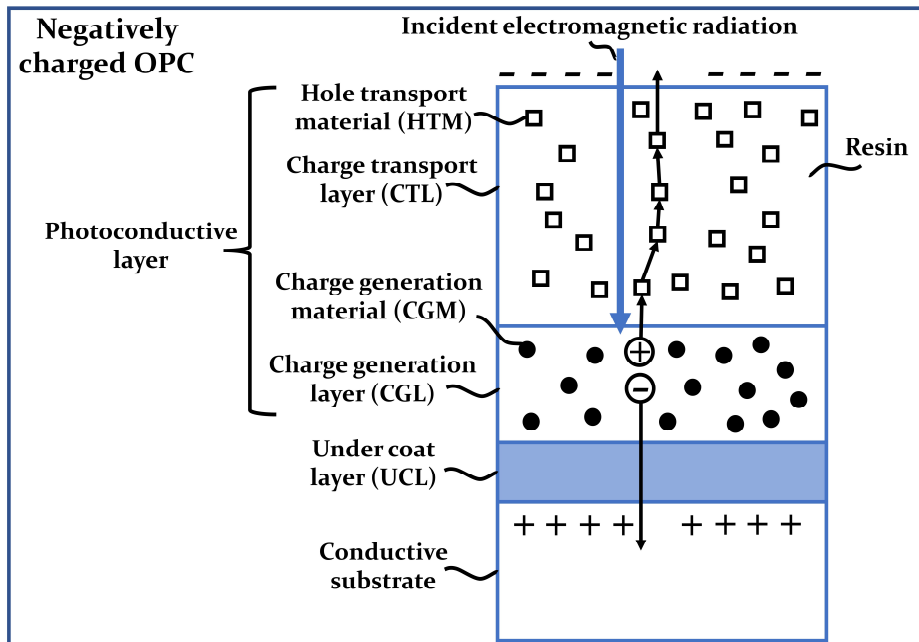


Figure 10: Visualization of the effect of incident electromagnetic radiation on the layers of a negatively charged organic photoconductor, based on [171].

In 2D electrophotographic devices, the photoconductor is typically implemented as a rotatable photoconductor drum that is brought into close

proximity to the charged powder for powder development in step 3 (cf. Table 6).

The primary function of the conductive substrate, typically an aluminum substrate, is to provide an electrical path to ground. The under coat layer (UCL) consists of a binder resin [201] that only allows negative charges to pass through due to a high electron mobility and affinity [202]. UCLs are mainly made of metal oxides anodized with a polyamide, polyester, or melamine coating [171]. The charge generation layer (CGL) is typically only 0.1 to 1.0 μm thick and generates an electron-hole pair when exposed to electromagnetic radiation, more specifically the photons of this radiation [202]. The incident photons must have a sufficiently high energy to create the electron-hole pairs through the underlying physical internal photoelectric effect [203]. A high quantum efficiency of the material is essential for an efficient conversion of the incident photons into electron-hole pairs. In Figure 10 and Figure 11, the electrons are visualized as circles with a minus sign, while the holes are visualized as circles with a plus sign inside.

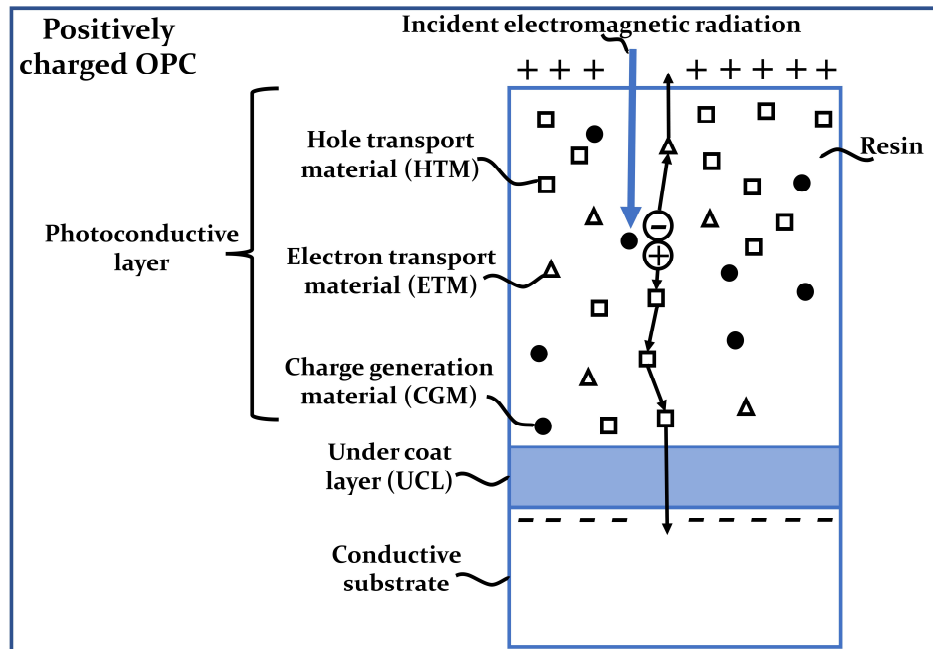


Figure 11: Visualization of the effect of incident electromagnetic radiation on the combined charge transport and charge generation layer of a positively charged organic photoconductor, based on [171].

The electron-hole pairs separate due to the electric field between the charges applied to the surface of the photoconductor by previous corona

charging and the conductive substrate. Depending on their charge, the pairs then separate, either migrating into the grounded substrate or via the charge transport layer (CTL), neutralizing charges at the photoconductor surface [203]. The CTL of negative charging OPCs (see Figure 10), which is typically 20 to 30 μm thick, consists of a hole transport material (HTM), often arylamide or benzidine, within a protective polycarbonate or polyester film [204,205]. Due to the continuous physical contact of this layer with toner, paper, the cleaning device in step 6, ozone, and other corrosive ions and reactive neutral species, the CTL is also made of a resistive polymer resin. Wear resistance against the influences mentioned above is critical to the achievable lifetime of an electrophotographic device [169].

Unlike negative charging OPCs, where the photoconductive layer is composed of the CGL and the CTL, in positive charging OPCs these layers are combined (see Figure 11). Thus, charge generation and charge transport, i.e., electron and hole transport, take place in a single layer. Positive charging OPCs are less common because the photoconductive layer combines all the relevant properties in one layer and is therefore more susceptible to wear. However, as the photons do not need to pass a separate CTL, the achievable resolution of the latent charge image in case of positive charging OPCs is higher [171].

A property of photoconductors which often leads to inaccuracies in electrophotography is the tendency to trap charges. A certain amount of charge is trapped in the photoreceptor after repeated cycling, which cannot be dissipated by incident photons. The trapped charges cause a residual potential U_r inside the photoconductor, which must remain small compared to the potential of the latent charge pattern U_p . Otherwise, the remaining residual potential would dominate the development of powder particles instead of the latent charge pattern, leading to considerable false development. Using the one-dimensional Poisson's equation, the residual potential U_r inside a photoconductor with a thickness d_p for the case of uniform bulk space charge can be written as follows [206]:

$$U_r = \frac{N_b e d_p^2}{2 \epsilon_p} \quad (15)$$

with the number N_b of charges per unit volume of electric charge e in the bulk, the permittivity of free space ϵ_0 and the permittivity of the photoconductor ϵ_p [207]. Using equation (11), (15) can be rewritten to:

$$U_r = \frac{N_b e d_p^2}{2 \epsilon_0 K_p} \quad (16)$$

where ϵ_0 is the permittivity of free space and K_p is the dielectric constant of the photoconductor.

The resolution achievable with electrophotographic toner printers is essentially dependent on the size of the toner particles and the imaging resolution of the exposure device, with a narrow particle size distribution being particularly beneficial for the print quality [208]. The size of toner particles lies in the range of 6 – 20 μm [123]. With 2D electrophotographic toner printers, resolutions of 300 to 1200 dpi (dots per inch) can be obtained [209]. This corresponds to pixel sizes d_{pixel} of $d_{\text{pixel } 300\text{dpi}} \approx 85 \mu\text{m}$ for a resolution of 300 dpi and $d_{\text{pixel } 1200\text{dpi}} \approx 21 \mu\text{m}$ for a resolution of 1200 dpi. Higher resolutions with even smaller pixel sizes can be achieved by using toners with smaller particle sizes. However, particles smaller than 5 μm become increasingly hazardous and require special toners, such as liquid toners [209].

After successful charging of both the powder and the photoconductor in step 1 (cf. Table 6) and the creation of a latent charge pattern by selective exposure of the photoconductor to electromagnetic radiation in step 2, the powder is developed into the charged or discharged areas of the photoconductor in step 3. Depending on the development strategy, either charged area development (CAD) or discharged area development (DAD) can be used to selectively attract powder particles to the photoconductor [169]. In both cases, the electric field force \vec{F}_{el} given by equation (14), dominantly determines the particle motion. However, it should be noted that for DAD the electric development field force is weaker compared to CAD. For powder transfer in step 4, in electrophotographic 2D laser printers, the back of the paper is charged via corona charging with opposite polarity to the charged toner particles. As the toner particles, which mostly consist of thermoplastic polymers, are pressed against the charged paper by the heated photoconductor drum, the powder pattern is transferred to the paper (step 4). Typically, the toner particles are preheated to a temperature above the glass transition temperature (T_g) of the respective thermoplastic polymer to achieve a more rubbery state and thus increase adhesion to the paper [209]. Alternatively, high pressure can be used to deposit them without preheating. Finally, in step 5, the deposited toner particles are fused by surrounding radiant heaters. Step 6, as the last step of an electrophotography

process cycle (cf. Table 6), involves cleaning of the photoconductor, as significant amounts of powder and partially fused toner may still be adhering to the photoconductor drum. This is achieved by mechanical cleaning with blades or brushes, sometimes supported by vacuum. To remove the residual charges from the photoconductor [169], the complete irradiation of the photoconductor by the illumination source already used in step 2 [171] or an alternating current (AC) is employed [210].

2.2.2 First Applications in Powder Bed Fusion and Current Limitations

The first attempts to transfer electrophotography from 2D printing to AM started in 1990 with an advanced SLA process (cf. Figure 1). In this context, electrophotography was used solely as a flexible method for patterning UV exposure by selective deposition of shielding toner particles [16]. In 2001, a first apparatus for using electrophotography as the sole powder application method for powder bed 3D printing was patented [211]. Two years later, in 2003, Kumar and Dutta [162] first published results showing a maximum of 50 layers of polymer toner particles deposited by electrophotography and fused layer by layer.

Essentially, two different strategies can be distinguished for the use of EPA in the context of powder-based AM. The first strategy basically follows strictly the six process steps of conventional 2D toner printing, summarized in Table 6 and discussed in section 2.2.1. In particular, also powder deposition in step 4 and fusion in step 5 are identical to 2D toner printing, but are repeated several times to 3D print more than one layer [171]. This principle has already been successfully applied in a first industrial machine by Evolve Additive Solutions, Inc. using their patented STEP (selective thermoplastic electrophotographic process) technology [212]. However, contact-based deposition uses high contact pressure and preheating of the powder particles to temperatures above the glass transition temperature of the polymer (cf. section 2.2.1) [213]. The photoconductor drum or plate provides both contact pressure and preheating. Since the drum or plate is heated homogeneously to a certain temperature without individual adaptation to a single material with different thermal properties [213], this strategy can only partially overcome the limitations of PBF-LB/P with conventional powder application methods (cf. sections 2.1.2 and 2.1.3) [133]. As stated in Table 7, especially the multi-material capabilities are still limited to powder materials with matching thermal properties and particle size distributions [209]. Although contact-based electrophotography can produce powder layers

consisting of different regions of more than one material, the flexibility to arbitrarily select these materials is limited [162]. First, the thermal properties of the materials need to be similar [213]. In the case of strongly differing glass transition, melting, crystallization and especially degradation temperatures (T_{degrad}), thermal damage can occur to the material with the lowest degradation temperature during contacting deposition [163]. In addition, during contact, consolidated regions of the already generated part will inevitably be prone to the parasitic effect of curling (cf. section 2.1.1) if the photoconductor is not preheated to a temperature above the crystallization temperature of the polymer with the higher crystallization temperature [69]. A further requirement for the powder materials applied by contact-based EPA is the matching particle size distribution [111]. In case of strongly differing particle sizes, the powder layer will be heterogeneously compacted by contact-based deposition leading to inhomogeneous part properties [102]. Finally, contact-based powder deposition – especially when contacting consolidated regions – inherently increases the risk of cross-contamination between the individual materials [214]. In summary, contact-based EPA limits the flexibility to combine powder materials which show strongly differing property profiles in terms of thermal properties and particle size distribution.

It should be noted that this first strategy for applying EPA in 3D printing does not use a laser for consolidating the layers and is therefore different from PBF-LB/P. For this reason, contact-based EPA is not considered in the overview of different powder application methods and new approaches for PBF-LB/P in Table 5.

The second strategy, on the other hand, is EPA with contactless powder deposition. It aims to completely replace conventional powder application methods (see 2.1.2) for PBF-LB/P by EPA (EPA-PBF-LB/P). Thus, in contrast to the first strategy, which strictly follows the six process steps of 2D electrophotography outlined in Table 6, in the second strategy electrophotography is only used to apply powder layers. However, as with conventional PBF-LB/P, the subsequent consolidation is laser-based. This allows the full flexibility of the laser-based energy input to be preserved [215]. By using multiple lasers with different wavelengths, complex temperature fields can be created [60], allowing polymers with strongly differing thermal properties to be simultaneously processed by PBF-LB/P [216]. However, as mentioned in section 2.1.3, EPA as a powder application method for PBF-LB/P only has an MRL of 2 (see Table 5) [133]. To date, only the general feasibility of the concept has been demonstrated on a single-layer basis outside PBF-

LB/P process conditions without consolidation [156]. Moreover, only single-material layers have been developed and deposited so far [157].

In the second strategy for using EPA for AM, in this case more precisely for PBF-LB/P, process steps 1, 2, 3 and to a large extent 6 (see Table 6) are adopted from 2D electrophotography. In contrast, the contactless powder deposition of powder particles in step 4 is new [156] and was first demonstrated in [158] as part of the second strategy for using EPA for AM. The fusion in step 5 has been adopted in principle from conventional PBF-LB/P, but has not yet been demonstrated in the context of EPA-PBF-LB/P [157]. Furthermore, charge accumulation within the generated part is a major challenge of EPA [162]. While in the case of contacting powder deposition, charge accumulation within the generated part leads to inhomogeneities and defects in the deposited layer [209], in the case of contactless powder deposition it renders the deposition of new powder layers impossible [162] or leads to severe geometric inaccuracies [158].

In summary, EPA with contactless powder deposition has great potential to overcome the drawbacks of conventional powder application methods for PBF-LB/P (cf. Table 7) [134]. In particular, even powder materials with strongly differing thermal properties and particle size distributions can be combined within a layer [159]. However, the potential of this flexibility for the additive manufacturing landscape has not yet been explored [133].

Table 7: Comparison between the contacting and contactless strategy for using EPA in AM.

	EPA with contacting powder deposition	EPA with contactless powder deposition
Multi-material capabilities	Combination of different materials only if similar thermal properties ($T_{g \text{ polymer A}} < T_{\text{degrad polymer B}}$) and particle size distributions [213]	Free combination of different materials, even with strongly differing thermal properties and particle size distributions [133]
Consolidation principle	Heat and contact pressure provided by photoconductor drum or plate [213]	Consolidation identical to PBF-LB/P [162]
Utilization in AM	Successful generation of simple [171,209] and complex [212] multi-layer parts	Only demonstration of general feasibility [156] on single-layer basis [158] without consolidation [157]

3 Objective and Methodology

The aim of this thesis is to identify and understand the requirements for the successful utilization of electrophotography as powder application method for PBF-LB/P. As can be concluded from section 2.1.2, by reducing the dependence of the powder layer quality on powder properties, in particular flowability, the variety of polymer materials suitable for PBF-LB/P could be drastically increased [130]. Furthermore, as discussed in sections 2.1.2 and 2.1.3, a major confining factor of conventional powder application methods (cf. Table 5) is the limited number of materials that can be processed simultaneously. As discussed in sections 2.1.3, 2.2.1, and 2.2.2, using EPA with contactless powder deposition offers the potential to overcome the limitations of conventional powder application methods for PBF-LB/P. At the same time, however, EPA with contactless powder deposition is the least understood and developed powder application method for PBF-LB/P (cf. sections 2.1.3 and 2.2.2). This is reflected in the poor MRL of 2 (see Table 5), which results from the fact that so far only single layers have been developed and deposited without consolidation. Although the powder development onto a photoconductive plate was successfully demonstrated in [157], the layers deposited without contact were not suitable for PBF-LB/P. The main reasons for this are poor reproducibility, layer coverage, layer thickness and geometric accuracy of the deposited layers (cf. sections 2.1.3 and 2.2.2). Thus, as shown in section 2.2.2 and summarized in Table 7, a number of challenges make the use of EPA with contactless powder deposition in PBF-LB/P impossible to date. For this reason, the potential to extend the process limits of conventional PBF-LB/P by using this novel powder application method has not yet been investigated.

For this purpose, a bottom-up approach (see Figure 12) is applied in order to determine and utilize influencing factors starting from interparticle interaction mechanisms (sections 4.1 and 4.2) to challenges arising from the formation of layers consisting of charged polymer particles (sections 4.3 and 4.4). Finally, the generation of parts by laser-based consolidation of multiple layers of charged particles is examined. In this context, new opportunities for the additive manufacturing landscape enabled by the usage of EPA for PBF-LB/P are studied (section 4.4 and chapter 5). The full potential of this technology for the manufacturing landscape is demonstrated in particular by the successful processing of pharmaceutical powders in chapter 5. These powders are very difficult to process due to their poor

flowability and relatively low thermal degradation threshold [47], which is challenging for conventional PBF-LB/P (cf. sections 2.1.1 and 2.1.2).

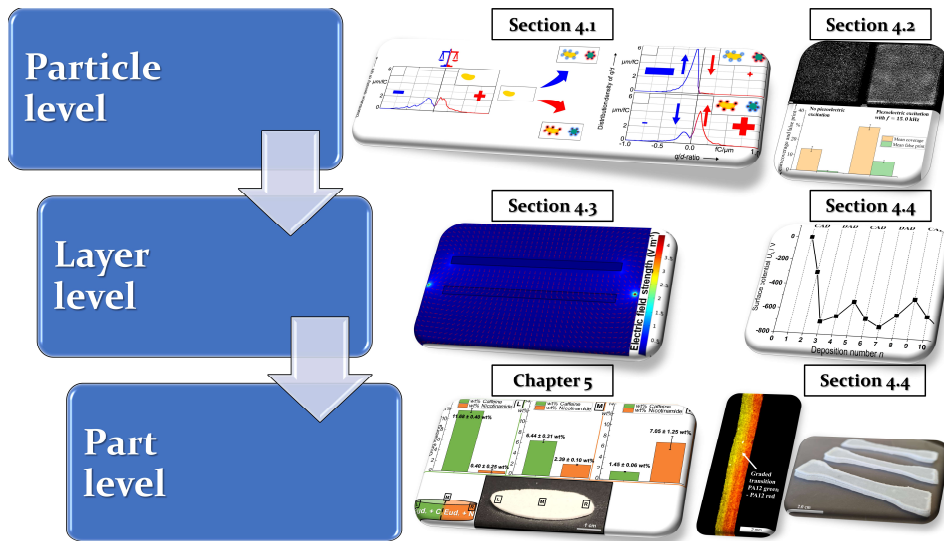


Figure 12: Bottom-up approach for identifying and understanding the requirements for the utilization of electrophotography in the context of PBF-LB/P.

As discussed in sections 2.1.1 and 2.1.2, powder charging is already a challenge with conventional powder application methods. Since for EPA the powder charging behavior needs to be understood in order to adapt the particle charging to the process, a detailed analysis of the powder charging behavior at the particle level is conducted in section 4.1. The aim is to understand the underlying charging phenomena and, in particular, the possibilities for tailoring them (cf. section 4.1). In addition, the interparticle interaction forces are investigated to develop strategies for improving deposition efficiency by exploiting the different distance dependencies of these forces (cf. section 4.2). As shown in sections 2.1.3 and 2.2.2, poor powder deposition efficiency has been one of the major challenges of EPA with contactless powder deposition to date. In particular, the multiple deposition of more than one powder layer including consolidation has not been investigated so far (cf. section 2.2.2 and Table 7).

Based on an in-depth analysis of the charging phenomena and interparticle forces at the particle level, the next step is to understand the processes of EPA with contactless powder deposition at the layer level. Since the motion of charged particles in an electric field is directly dependent on the direction and strength of that field (cf. section 2.2.1 and equation (14)), the effects

of different electric fields on the deposition of powder layers are studied in section 4.3. As shown in section 2.2.2, one of the main challenges of EPA, even in the case of contacting powder deposition where the contact pressure of the photoconductor drum or plate determines powder deposition [171], is the accumulation of charges within the generated part [162]. This effect is even more critical for EPA with contactless powder deposition [209], where powder deposition relies solely on the electrical deposition field, without mechanical assistance from the contact pressure of the photoconductor drum or plate (cf. sections 2.2.1 and 2.2.2) [157]. While in the case of contacting powder deposition, charge accumulation within the generated part leads to inhomogeneities and defects in the deposited layer, in the case of contactless powder deposition it renders the deposition of new powder layers impossible [162] or leads to severe geometric inaccuracies [158] (cf. 2.2.2). For this reason, charge accumulation within the generated part and the resulting homogeneity of the applied layer are investigated in section 4.4. Moreover, based on the understanding of the parasitic effect of charge accumulation, which correlates with an increase in the surface potential of the EPA-PBF-LB/P part, compensation strategies are developed in section 4.4.

Finally, the possibility of overcoming the limitations of conventional powder application methods of PBF-LB/P by EPA-PBF-LB/P is studied in section 4.4 and chapter 5 at part level. In particular, chapter 5 demonstrates the full potential of this new powder application method by simultaneously processing different powder materials that exhibit both poor powder flowability and strongly differing thermal property profiles. As shown in sections 2.1.1, 2.1.2 and 2.1.3 (in particular Table 5), simultaneously processing such powders has not been possible in conventional PBF-LB/P. However, as demonstrated in section 2.1.2, increasing the variety of polymer materials suitable for PBF-LB/P and the ability to apply them at different positions within a powder layer would significantly enhance versatility of PBF-LB/P.

Based on the bottom-up approach to identify and understand the requirements for the successful use of EPA with contactless powder deposition as the sole powder application method for PBF-LB/P, the research questions visualized in Figure 13 can be derived. These underlying research questions are addressed in chapters 4 and 5.

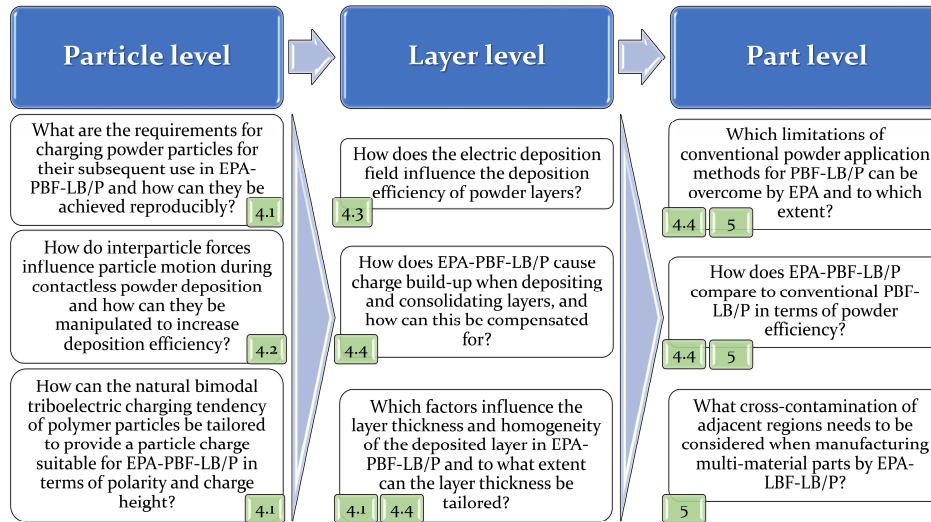


Figure 13: Key research questions and associated sections within this thesis to identify and understand the requirements for the successful substitution of conventional powder application for PBF-LB/P methods with EPA.

4 Requirements for Substituting Conventional Powder Application Methods of PBF-LB/P by EPA

4.1 Achieving a Suitable Particle Charging

Enabling triboelectric charging as a powder charging method for electrophotographic powder application in laser-based powder bed fusion of polymers by triboelectric charge control

Published in Additive Manufacturing 68 (2023), 103531

Sebastian-Paul Kopp^{a,b,c,*}, Björn Düsenberg^{b,d}, Pius Marcellinus Eshun^a, Jochen Schmidt^{b,d}, Andreas Bück^{b,d}, Stephan Roth^{a,b,c}, Michael Schmidt^{a,b,c,e}

^a Bayerisches Laserzentrum GmbH, 91052 Erlangen, Germany

^b Collaborative Research Center (CRC) 814 “Additive Manufacturing”, 91058 Erlangen, Germany

^c Erlangen Graduate School in Advanced Optical Technologies (SAOT), 91052 Erlangen, Germany

^d Friedrich-Alexander-University Erlangen-Nuremberg, Institute of Particle Technology (LFG), 91058 Erlangen, Germany

^e Friedrich-Alexander-University Erlangen-Nuremberg, Institute of Photonic Technologies (LPT), 91052 Erlangen, Germany

*Corresponding author.

Tel.: +49-9131-97790-27; E-mail address: s-p.kopp@blz.org

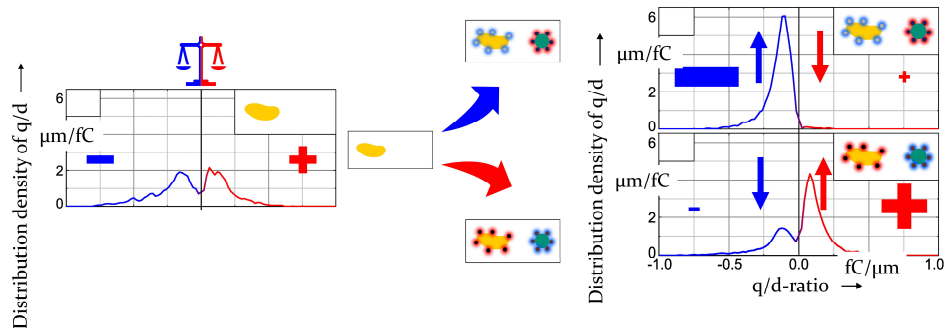


Figure 14: Triboelectric charge control of polymer particles, transforming the natural bimodal particle charging (left) to monomodal charging (right) suitable for EPA-PBF-LB/P.

Achieving a reproducible powder particle charging is one of the key aspects for successful EPA-PBF-LB/P. As discussed in section 2.2.1, the reason for

this is that the charging height and polarity has a direct effect on particle motion in the electric development and deposition fields and is therefore crucial for precise powder application. However, the requirements for charging powder particles for their subsequent use in EPA-PBF-LB/P are unknown.

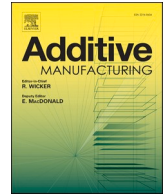
In this study, for the first time, the charging behavior of polymers at the particle level is investigated and correlated with the resulting deposition behavior in EPA-PBF-LB/P. In particular, the resulting layer coverage and layer thickness are analyzed as a function of the surface potential of the powder pattern which arises from the particle charge. Triboelectric charging is shown to be a promising powder charging strategy for electrophotography in PBF-LB/P. However, this powder charging method requires charge control as the natural triboelectric charging of polymers leads to a bimodal charge distribution unsuitable for EPA. Therefore, in this study, the synergy of both surface functionalization of polymer particles with CCAs and the use of suitable ferritic carrier particles known from 2D toner printing is used to develop a charge control method for EPA-PBF-LB/P (cf. Figure 14). This allows to precisely tune the polarity and charge height of the particle charging and thus to use this charging method for electrophotographic PBF-LB/P. The homogeneous and efficient charging of the individual powder particles furthermore enables the adaption of the layer thickness of the deposited powder layers by varying the electric deposition field strength. Further evidence for the higher efficiency of triboelectric charging compared to gas discharge-based powder charging was published in [217]. The half-life of the powder charging created by triboelectric charging was found to be significantly longer than that of corona charging.

The functionalization of the polymer particles with CCAs was parallelly investigated and the results were published in [218].

Highlights:

- Understanding of the requirements for charged powder particles for their subsequent use in EPA
- Knowledge of the relationship between surface potential of a charged powder layer and resulting development and deposition efficiency of EPA
- Understanding of possibilities to tailor the natural triboelectric charging tendency of polymers in terms of polarity and charge height to enable their usage in EPA-PBF-LB/P

- Ability to adjust the thickness of powder layers deposited by EPA from a single particle diameter to up to five times the particle diameter by varying the electric field strength of the deposition field due to the efficient triboelectric charging



Research paper

Enabling triboelectric charging as a powder charging method for electrophotographic powder application in laser-based powder bed fusion of polymers by triboelectric charge control

Sebastian-Paul Kopp^{a,b,c,*}, Björn Düsenberg^{b,d}, Pius Marcellinus Eshun^a, Jochen Schmidt^{b,d}, Andreas Bück^{b,d}, Stephan Roth^{a,b,c}, Michael Schmidt^{a,b,c,e}

^a Bayerisches Laserzentrum GmbH, 91052 Erlangen, Germany

^b Collaborative Research Center (CRC) 814 "Additive Manufacturing", 91058 Erlangen, Germany

^c Erlangen Graduate School in Advanced Optical Technologies (SAOT), 91052 Erlangen, Germany

^d Friedrich-Alexander-University Erlangen-Nuremberg, Institute of Particle Technology (LFG), 91058 Erlangen, Germany

^e Friedrich-Alexander-University Erlangen-Nuremberg, Institute of Photonic Technologies (LPT), 91052 Erlangen, Germany

ARTICLE INFO

Keywords:

Charge control
Electrophotography
Triboelectric charging
Laser powder bed fusion
Polymer particles
Powder application

ABSTRACT

Substituting conventional doctor blade- or roller-based powder application methods for laser-based powder bed fusion of polymers (PBF-LB/P) by electrophotographic powder application (EPA) offers significant advantages. In particular, the selective powder deposition enabled by EPA allows high powder efficiency and the possibility to locally adjust part properties during their fabrication. However, defined charging of powder particles is crucial for achieving an accurate selective deposition of powder layers by means of electrophotography. This is the first comprehensive study on the specific triboelectric charge control of polymer particles for their subsequent use in electrophotographic powder application for PBF-LB/P. For this purpose, approaches for charge control of toner particles in the context of digital (2D) printing technologies are adapted and applied to polypropylene (PP) feedstocks for PBF-LB/P. In order to show transferability to other polymers, the charge control method developed in this paper is also applied to polyamide 12 (PA12) high density polyethylene (HDPE) and polystyrene (PS). For successful EPA, unipolar charging of polymer particles is crucial. However, non-functionalized PP shows a strongly bipolar triboelectric charging, which is unsuitable for EPA. The charge control method developed in this work shifts this strongly bipolar triboelectric charging to a unipolar charging. This is achieved by the synergy of both functionalizing the particle surface with charge control agents (CCAs) and choosing suitable carrier particles known from two-component toners. The developed method allows to control crucial parameters of triboelectric charging, namely polarity, amount of charge and resulting surface potential. Furthermore, the presented results provide new insights into the transfer behavior of charged PP particles in an external electric field. Finally, this enables the triboelectric charging mechanism to be used for electrophotographic powder application in PBF-LB/P.

1. Introduction

Additive manufacturing (AM) processes, such as laser-based powder bed fusion of polymers (PBF-LB/P) have become an integral part of the manufacturing landscape [1]. However, conventional AM technologies lack the possibility of processing more than one material simultaneously. On the one hand, this requires a melting strategy that can be specially adapted to the thermal property profiles of the various materials [2]. On the other hand, the generation of multi-material

components using AM technologies in particular necessitates the ability to selectively deposit powder particles into the build chamber [3,4]. However, for PBF-LB/P, selective powder deposition is not possible with conventional doctor blade- or roller-based powder application processes [5,6]. Therefore, the fabrication of parts with locally adjusted functional properties, such as high wear resistance, high temperature resistance or partially induced elasticity to achieve so-called compliant mechanisms, is not possible with conventional powder application methods [5–7]. Furthermore, as described more in detail in [4], powder efficiency of

* Corresponding author at: Bayerisches Laserzentrum GmbH, 91052 Erlangen, Germany.

E-mail address: s-p.kopp@blz.org (S.-P. Kopp).

<https://doi.org/10.1016/j.addma.2023.103531>

Received 29 December 2022; Received in revised form 13 March 2023; Accepted 27 March 2023

Available online 29 March 2023

2214-8604/© 2023 The Authors. Published by Elsevier B.V. This is an open access article under the CC BY license (<http://creativecommons.org/licenses/by/4.0/>).

conventional PBF-LB/P needs to be further improved in order to decrease the environmental impact of this manufacturing technology.

Using electrophotographic powder application (EPA) instead of conventional doctor blade- or roller-based powder application methods offers great potential to surmount their shortcomings [7–9]. As demonstrated in [3,4,10,11], EPA offers the possibility to apply different powder particles for PBF-LB/P both precisely and selectively. Thus, on the one hand, EPA enables the generation of components with locally adjusted functional properties [3,4], and, on the other hand, the selective powder deposition enabled by EPA significantly increases powder efficiency [4]. As a result, the creation of partcake material and, thus, the need for powder recycling, as described in [4], is completely avoided. EPA in the context of PBF-LB/P (EPA-PBF-LB/P) consists of six process steps [10–12], which are illustrated in Fig. 1 and explained in detail in [3,4].

While – as described in [3,4] – in process step one the photoconductive material of the photoconductive plate (PCP) is charged by gas discharge using a corona charging unit [12,13], both charging by gas discharge as well as triboelectric charging are theoretically possible process variants for charging the powder particles [14–16]. However, triboelectric charging has not yet been used for EPA-PBF-LB/P.

Taking a closer look at the individual process steps it becomes apparent that a key factor for successfully implementing EPA into PBF-LB/P is a reliable, reproducible and homogeneous powder charging. This arises from the fact that the desired movement of powder particles in process steps three (development) and four (deposition) is mainly caused by the electric field force \vec{F}_{el} , which is directly proportional to the charge q of the powder particles and the field strength \vec{E} of the electric development or deposition field [3,4,14,17]. Thus, inhomogeneities of the charge distribution within a powder layer or differences in the charging of powder particles of subsequent layers directly influence the powder development and deposition. This can significantly reduce the efficiency of powder transfer during both, development and deposition, resulting in low dimensional accuracy, inhomogeneous distribution of powder particles within a layer, and limited coverage [3,4,11]. The aforementioned issues are still the main challenges in using EPA for laser-based powder bed fusion [8–12,18]. However, in 2D laser printing of toner particles, EPA, often referred to as xerography in this context, has been the standard powder application method for more than six decades [7,14,19]. Comparing the powder

charging strategies of EPA for 2D laser printing and for PBF-LB/P, it becomes apparent that in case of 2D laser printing the toner particles are typically charged triboelectrically [7], whereas in case of EPA-PBF-LB/P the powder particles are charged by gas discharge using a corona charging unit [10,11]. In general, triboelectric charging of particles is based on charge separation occurring during prolonged contact, collision, or friction between the particles involved. The electron, ion or material transfer model are typically employed in order to explain these effects [20,21]. Although these models are well applicable to conductive materials [20,22], according to [23] there is no model sufficiently describing charge transfer occurring between insulators, such as polymers [24–26]. Since there are no free electrons available in insulators, the so-called surface state model (cf. Fig. 2) was presented in [20,27,28] in order to give a first approach for understanding the charge transfer between insulators. In this model, available energy levels for electrons, referred to as surface states, are only present on the surface of the insulators, not in the bulk. As visualized in Fig. 2, when insulator 1 and insulator 2 contact each other, electrons from the filled surface states of insulator 1 move to empty surface states of the other insulator. This is due to differences in the effective work functions ϕ_1 and ϕ_2 of the surfaces of both insulators [20]. Charge transfer occurs until the Fermi energies of both insulators are the same (cf. Fig. 2 “after contact”), which means that the Fermi energy of insulator 1 has changed by Δ_1 and the Fermi energy of insulator 2 by Δ_2 , respectively. The charge transfer also creates a potential difference E_{pot} between both surfaces.

Finally, an equalization of the Fermi levels of the surfaces is achieved during contact and the energy level can be expressed as (1) [20]:

$$\phi_1 + \Delta_1 + eE_{\text{pot}} = \phi_2 - \Delta_2 \quad (1)$$

In order to obtain a controlled, homogeneous and reproducible triboelectric charging of powder particles, an extensive experimental study and adjustment of suitable materials is required. The main difference between 2D laser printing and PBF-LB/P can therefore be found in the powders used, which in case of triboelectric charging for 2D laser printing require the addition of charge control agents (CCAs). As described in [23], toner particles for 2D laser printing typically consist of a polymer, a pigment and at least one charge control agent. Furthermore [23] states that they have a particle size distribution between 6 and 20 μm [19,29–31]. However, typical materials for PBF-LB/P are polymers, such as polyamide 12 (PA12), polyamide 11 (PA11), polyether ether ketone (PEEK), thermoplastic polyurethane (TPU), polypropylene (PP), and polystyrene (PS) with a particle size distribution between 50 and 130 μm [32–34]. Thus, the toner particles used for 2D laser printing have a narrower and smaller particle size distribution than the particles used for PBF-LB/P. Moreover, unlike the polymer particles used for PBF-LB/P, the toner particles are functionalized by the added CCA in terms of their triboelectric charging behavior.

As already mentioned, a reproducible and homogeneous powder charging is one of the key factors for successful EPA. Although gas discharge-based powder charging offers the possibility of rapidly changing both the polarity and level of charging by modifying the electric charging field and does not require the powder particles to be functionalized [13,35,36], it is rather inefficient in charging the powder particles and furthermore creates high densities of free ions [37,38]. This results from the fact that powder charging due to gas discharge is based on the penetration of electric charges, in this case ions [13,36,39], into the powder surface. More precisely, the electric charges are temporarily stored in traps, which may originate from defects in the polymer structure or even in the boundaries between crystalline and amorphous regions of the polymer [35,40,41]. In order to achieve sufficiently high powder charging for EPA, corona voltages in the range of 3–5 kV or even higher [42–45] have to be applied, primarily depending on the ambient conditions and the material to be charged [35,38,46].

Applying triboelectric charging of powder particles within process step one of EPA-PBF-LB/P offers a number of advantages. Unlike corona

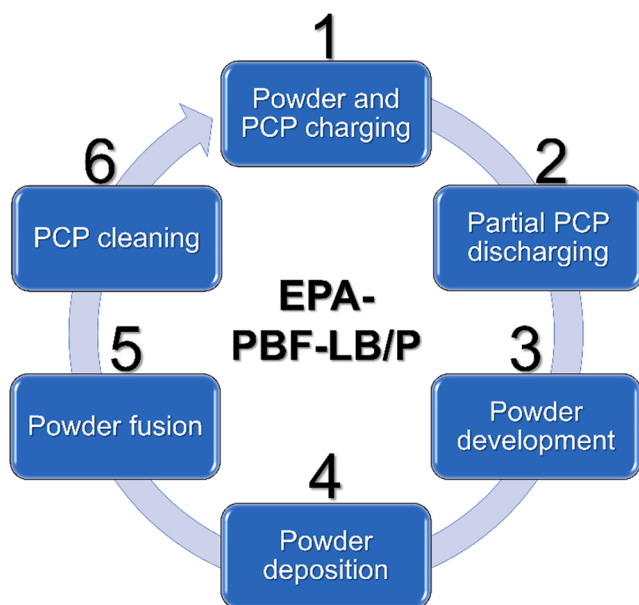


Fig. 1. Schematic overview of main process steps of EPA-PBF-LB/P based on [3,4].

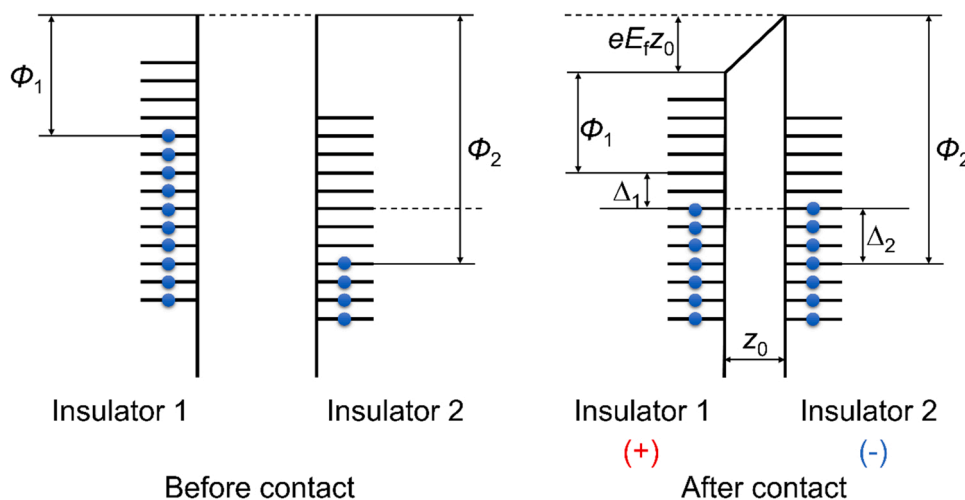


Fig. 2. Energy level diagram for illustrating triboelectric charge transfer in case of insulator-insulator contact with electrons depicted as blue circles; Φ_1 , Φ_2 being the work functions of insulator 1 and insulator 2, respectively; Δ_1 , Δ_2 being the changes of Fermi energy of insulator 1 and insulator 2, respectively; e is the elementary charge, $E_f z_0$ is the potential difference between the surfaces with z_0 being the tunnelling separation distance.

Based on [20,27].

charging, it does not require an external charging field generated by corona voltages in the range of 3–5 kV or even higher [42–44]. Thus, it inherently eliminates all associated disadvantages that come with the accumulation of free ions on the surface of the powder layer on the one hand and the Faraday Cage Effect (FCE) [41,47] on the other. However, as known from 2D laser printing, controlling the triboelectric charging process in terms of polarity, homogeneity and level of the resulting particle charge is essential and one of the major challenges of this charging method [20,30].

In this study, for the first time, the targeted triboelectric charge control of typical PBF-LB/P polymer particles for their usage in EPA-PBF-LB/P is investigated. For this purpose, the triboelectric charging behavior of pure PP, serving as a model polymer, is first analyzed at particle level by charge spectrometry. Based on this analysis, a method for controlling the triboelectric charging of PP particles is adapted from two-component toners [7,48] and applied to PP. A critical aspect of EPA-PBF-LB/P is the transferability of charged polymer particles within the electric development field in process step three and within the electric deposition field in step four, respectively. Thus, the transfer behavior of triboelectrically charged PP within an electric field is investigated in terms of homogeneity and thickness of the resulting powder layer. As shown in [4], regularly changing the polarity of the deposited powder layer is in many cases the key to overcome charge accumulation and thus reducing the efficiency of powder deposition with increasing number of deposited layers. For this reason, the charge control method developed in this work is always considered for positive as well as negative charging.

Finally, the developed charge control method is applied to polyamide 12 (PA12), polystyrene (PS) and high density polyethylene (HDPE) in order to prove its applicability to other materials. To verify the potential of the new charge control method for generating powder layers for additive manufacturing of parts in the context of EPA-PBF-LB/P, PP layers are applied onto the build platform using process steps one to four (cf. Fig. 1).

2. Materials and methods

2.1. Powder preparation

As already discussed in the introduction, for achieving a controlled triboelectric charging of the PBF-LB/P polymer particles to enable their usage in EPA-PBF-LB/P, an approach based on two-component toners

known from toner technology for 2D laser printing [7,48] is chosen and for the first time used for PBF-LB/P polymer particles in this work. For this purpose, ferritic carrier particles are mixed with pure polyamide 12 (PA12), polystyrene (PS), high density polyethylene (HDPE) and polypropylene (PP) as well as with the differently additivated powder formulations of each polymer prepared according to Table 5. Here, the synergy of functionalizing the particle surface with CCAs and selecting suitable carrier particles, as known from two-component toners, is the basis for the charge control method for EPA-PBF-LB/P developed in this work. Two different types of ferritic carrier particles (MF83–100 and MF22–100, Powdertech Co., Ltd., Kashiwa-shi, Chiba, Japan) were used for charge control experiments in this paper. MF83–100 is referred to as carrier(+) due to its tendency to triboelectrically charge itself positively while charging its friction partner negatively. By contrast, MF22–100 is referred to as carrier(-) since it has the tendency to triboelectrically charge itself negatively while charging the friction partner positively. In addition, SEM images of uncoated ferrite carrier particles (MF90–100, Powdertech Co., Ltd., Kashiwa-shi, Chiba, Japan) were taken for comparison. According to the manufacturer and as can be seen in Fig. 6a), the coatings of carrier(-) and carrier(+) consist of nanoparticle surface functionalizations (cf. Table 1) with a thickness in the range of the particle diameter of the nanoparticles. Utilizing the surface state model of triboelectric charging described in the introduction, the surface functionalization of the carrier particles can be said to have the goal of adjusting the effective work functions of the carrier particles with respect to the polymer particles. As a result, the functionalized carrier particles obtain a certain charging tendency given in Table 1.

Table 1

Properties of used carrier particles.

Property	Ferrite carrier (-) MF22-100	Ferrite carrier (+) MF83-100	Uncoated ferrite carrier MF90-100
Charging tendency	Negative	Positive	Not functionalized
Functionalization	Polyvinylidenfluorid-(PDVF-) based	Acrylic resin-based	-
Density / $g\ cm^{-3}$	2.61	2.62	2.70
Mass median diameter $x_{50,3}$ / μm	107.2	114.3	107.5

Both CCAs and carrier particles are used for controlling the triboelectric charging of polymer particles in terms of polarity, charge height and resulting surface potential of the transferred powder layer. While CCAs are directly adhering to the polymer particles and thus act on their surface, the carrier particles (with their own surface functionalization) act as friction partners for the polymer particles inside the charging device (cf. Fig. 4). In Table 1 the relevant properties of the used carrier particles are summarized.

For preparing the two-component mixtures consisting of polymer and carrier particles, a shaking mixer (Type T2f, Willy A. Bachofen AG, Muttenz, Switzerland), with a rotational speed of 49 revolutions per minute (rpm) was utilized. After mixing for 30 min, the powder mixtures were left to rest for 48 h to remove the electrical charges generated by mixing. To find a suitable mixture ratio of polymer and carrier for the charge control experiments in this paper, first different mixtures of pure PP and positively as well as negatively charging carriers were prepared. It is important to mention that a higher amount of carrier within the two-component blend reduces the amount of effectively available polymer for EPA-PBF-LB/P in this blend. Therefore, the most suitable carrier content in the context of this work is defined as the minimum carrier content at which a preferably high coverage and especially layer homogeneity of the powder layer transferred to the transfer drum are achieved for pure PP. At this, the standard deviation of layer coverage is used as an indicator for layer homogeneity. Table 2 gives an overview of the powder blends prepared for identifying the most suitable carrier content for this paper.

For investigating the triboelectric charge control of polymer particles for their usage in EPA-PBF-LB/P, the polymer particles were mixed with charge control agents. For this purpose, a functionalization method, which is described in detail in [23], based on dry coating of polymer particles with charge control substances, was applied. At this, the previously described shaker mixer was utilized.

Two different CCAs, HDK H05XT (hereafter referred to as silica(-), since it increases the negative triboelectric charging tendency of the substance to which it adheres) and HDK H05TA (silica(+)), both Wacker Chemie AG, München, Germany, were used to functionalize the polymer particles with respect to their triboelectric charging behavior. The silica nanoparticles have a mean particle size of 50 nm, whereby silica(-) particles have a surface functionalization with hexamethyldisilazane (HMDS) and polydimethylsiloxane (PDMS) to hydrophobize the surface and enhance negative charging. Silica(+) particles are modified with PDMS for hydrophobation and amide / ammonium groups to increase positive charging. Table 3 gives an overview of the material properties of the additive particles used in this work for functionalizing polymer particles with respect to their triboelectric charging properties.

The coating time was set to 60 min and mixing aids (Type Sili S with 1.3 – 1.65 mm diameter, Sigmund Lindner GmbH, Warmensteinach, Germany) were used to enhance deagglomeration. To ensure reproducibility, each powder mixture was prepared three times. In total, four different polymer types, which are commercially available and widely

Table 2

Overview of powder blend of pure PP and two different carriers. 100 g per mixture.

Powder blend of PP and carrier number:	Content of ferrite carrier (+) MF83-100 / wt%	Content of ferrite carrier (-) MF22-100 / wt%
1	10	-
2	20	-
3	30	-
4	40	-
5	50	-
6	-	10
7	-	20
8	-	30
9	-	40
10	-	50

Table 3

Material properties of the CCAs HDK H05XT and HDK H05TA according to the manufacturer [23].

Property	Silica (-)	Silica (+)
	HDK H05XT	HDK H05TA
Charging tendency	Negative	Positive
Specific surface area (BET) / $\text{m}^2 \text{g}^{-1}$	50 ± 20	50 ± 20
Mean particle size / nm	50	50
Agglomerate particle size / μm	< 20	< 20
Specific charge / $\mu\text{C g}^{-1}$	-450	+ 50
Surface modification	HMDS/PDMS	PDMS/-NR ₂ /-NR ₃

used in conventional PBF-LB/P [49], were functionalized. These include polyamide 12 (PA12, PA2200, EOS GmbH, Krailling, Germany), high density polyethylene (HDPE, Coathylene NC 6454-F, Axalta Coating Systems GmbH, Pratteln, Switzerland), polystyrene (PS, Coathylene SINTPS, Axalta Coating Systems GmbH, Pratteln, Switzerland) and polypropylene (PP, Coathylene PD0580, Axalta Coating Systems GmbH, Pratteln, Switzerland). According to [25,26] the selected polymers are located at significantly different positions in the triboelectric charging series. Therefore, they exhibit strongly differing natural triboelectric charging tendencies and, thus, offer great potential for the investigation of a new method for triboelectric charge control in this work. Although polymers generally tend to attract electrons and, thus, charge negatively after contact with mercury, which serves as a reference for quantifying the triboelectric charging tendency of materials, the triboelectric charge density (TECD) varies significantly (cf. Table 4). Unlike the other polymers used in this work, PA12 (PA2200) already contains a surface functionalization with nano-silica particles, mainly for enhancing the powder flowability [50,51]. This already existing functionalization of PA12 should be considered when interpreting the results with respect to triboelectric charge control using CCAs.

The mass median diameter shown in Table 4 was determined by laser diffractometry (Mastersizer 2000, Malvern, UK). The density is given according to the respective powder supplier.

Each polymer powder was coated with five different weight percentages (wt%) of silica(-) and five different weight percentages of silica(+), respectively. Table 5 provides an overview of the powder functionalizations prepared for each of the polymers described above.

Due to strong interparticle forces, predominantly van der Waals forces as well as electrostatic attraction forces between polymer particles (here acting as host particles) and the respective silica nanoparticles (here acting as guest particles), the surface of the polymer particles is covered with CCAs.

Finally, the most suitable polymer-to-carrier-ratio found from the experiments with the powder blends consisting of pure PP and differently charging carriers shown in Table 2 was used to prepare powder blends consisting of functionalized polymers (cf. Table 5) and the respective carrier particles. For this purpose, the same procedure was applied as for the powder blends presented in Table 2, and 100 g were prepared for each blend.

Fig. 3 shows the symbols for the different polymer and carrier particles used in this work.

Table 4

Selected material properties of polymer powders used in this study; Since TECD of PA12 is not available, the TECD of the molecularly closely related PA6 is given.

Polymer	Mass median diameter $x_{50,3}$ / μm	Density / g cm^{-3}	TECD / $\mu\text{C m}^{-2}$ [25]
PA12	55.9	0.930	-18.35 ± 0.99 (PA6)
PS	58.0	1.060	-103.48 ± 2.48
HDPE	46.0	0.940	-59.91 ± 1.79
PP	98.6	0.907	-27.23 ± 1.31

Table 5
Overview of powder functionalizations for powder transfer experiments. 100 g per mixture.

Powder addition of polymer and silica number:	Silica (-) content / wt%	Silica (+) content / wt%
1	0.05	-
2	0.1	-
3	0.25	-
4	0.5	-
5	1.0	-
6	-	0.05
7	-	0.1
8	-	0.25
9	-	0.5
10	-	1.0

	Non-functionalized polymer
	Polymer functionalized with silica(+)
	Polymer functionalized with silica(-)
	Positively charging carrier MF83-100
	Negatively charging carrier MF22-100

Fig. 3. Symbols for polymer and carrier particles used in this work.

2.2. Scanning electron microscopy

For visualizing the contact between polymer and carrier particles a scanning electron microscope (SEM) Gemini Ultra 55 (Carl Zeiss AG, Oberkochen, Germany) equipped with a trough-the-hole detector was utilized. The acceleration voltage was set to 1 kV.

2.3. Triboelectric charging process of polymer particles

The triboelectric charging experiments were performed using a so-called magnetic brush system (Id-tester, Epping GmbH, Neufahrn bei Freising, Germany). Before polymer particles can be transferred to the transfer drum (cf. Fig. 4) they are charged inside the charging device, where the actual triboelectric charging takes place. The underlying principle of this charging process is to achieve close contact and, thus, efficient friction between polymer and carrier particles inside the charging device accompanied with triboelectric charge transfer. For this purpose, a constant rotation of magnetic and mixing drum provides a uniform movement of the powder blend filled into the charging device and, therefore, friction between polymer and carrier particles. The ferritic magnetic carrier particles align with the magnetic field of the magnets distributed around the circumference of the magnetic drum, thus forming the so-called magnetic brush. However, the ferritic carrier particles are electrically conductive and, moreover – since close to each other within the magnetic brush – mostly connected to the grounded magnetic drum. Hence, they are also responsible for keeping the charging conditions for the polymer particles constant by preventing charge accumulation within the magnetic brush. It is important to note that the ferritic carrier particles adhere to the magnetic drum (cf. Fig. 4) and thus are not transferred to the transfer drum. Thus, they do not influence the final part properties.

After charging of the polymer particles inside the charging device, they are transferred to the transfer drum by applying an electric transfer field between transfer drum and charging device (cf. Fig. 4). The charged polymer particles are then transferred to the transfer drum due to the electric field force \vec{F}_{el} , which is proportional to the polymer particle charge q and the electric transfer field strength $\vec{E}_{transfer}$ [4]. The transfer drum with a diameter of 255 mm and a width of 119 mm rotates as long as the electric transfer field is active and powder transfer is taking place. In the context of this work, the electric transfer field strength was set to $\vec{E}_{transfer} = \pm 192 \text{ kV m}^{-1}$ depending on the polarity of the charged polymer particles. This corresponds to a transfer voltage of $U_{transfer} = \pm 770 \text{ V}$ at a separation distance between transfer drum and charging device of approx. 4 mm. According to the schematic overview of EPA-PBF-LB/P in Fig. 1, the charged particles on the transfer drum can then be developed onto the photoconductive plate and further processed in the new, EPA-based additive manufacturing process [3,4]. The focus of this paper is therefore to characterize the layer of charged polymer particles, which forms on the transfer drum, in order to verify the suitability of triboelectric charging coupled with the

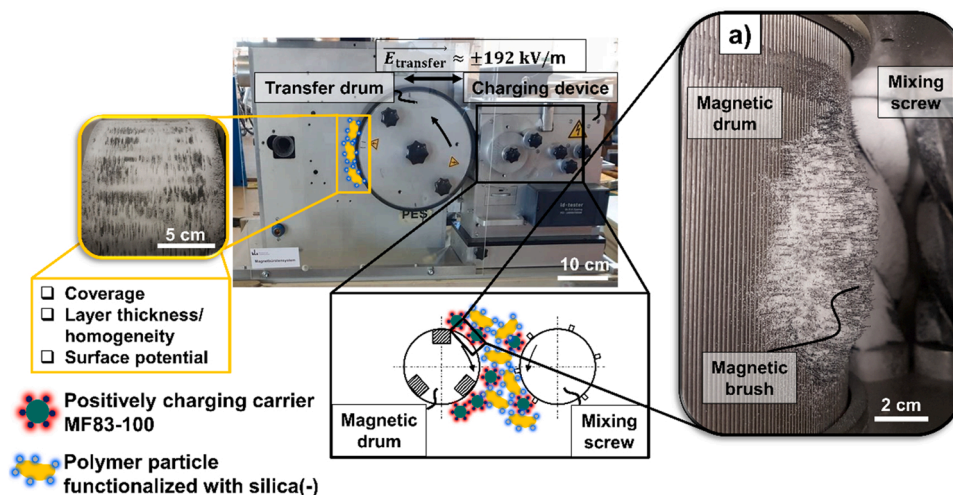


Fig. 4. Triboelectric charging system and experimental design of powder charging experiments with exemplary polymer and carrier particles; a) view into charging device.

inherently necessary triboelectric charge control (cf. Introduction) as new powder charging method for EPA-PBF-LB/P. For this purpose, the powder layer is analyzed with respect to the achieved coverage, layer thickness and homogeneity as well as surface potential.

2.4. Coverage analysis

For determining the powder coverage of the transferred layer an optical measurement procedure based on [3] was applied. For this purpose, videos of the transfer drum were taken during powder transfer from charging device to transfer drum using a camera (Samsung Electronics Co. Ltd., Suwon, South Korea) with a resolution of 3840×2160 pixels and a frame rate of 60 frames per second (fps). The videos were split into single frames and analyzed using the software ImageJ for coverage analysis. According to an image analysis approach reported in [3], the images were turned into 8-bit grayscale images and made binary using the Huang2 [52,53] thresholding method. Finally, comparison of black (no powder) and white (powder) pixels in three equally distributed rectangular areas of the respective images, yielded the corresponding mean coverage value as well as standard deviation.

2.5. Layer thickness and homogeneity analysis

The layer thickness was measured using the depth blade of a precision caliper (Burg-Wächter KG, Wetter-Volmarstein, Germany) with a measurement uncertainty of 0.01 mm after powder transfer from charging device to transfer drum was finished and the transfer drum stopped rotating. The powder layer thickness was determined at 20 different positions, whereby always five measurements were conducted equidistantly in a line ranging from the left to the right edge of the transfer drum with a distance of 23.8 mm to each other. This was repeated four times, at 12, 3, 6 and 9 o'clock position of the transfer drum (cf. Fig. 4). From that, the mean layer thickness as well as standard deviation were calculated. Here, the standard deviation of the 20 measurements was used as an indicator for homogeneity of the polymer powder layer on the transfer drum.

2.6. Surface potential analysis

For measuring the surface potential of the polymer powder layer on the transfer drum, an electrostatic voltmeter type ISOPROBE model 244 A equipped with an electrostatic voltmeter probe model 1017AE (both Monroe Electronics Inc., Lyndonville, NY, USA) was utilized. The separation distance between probe and powder surface was set to 3 mm, and with regard to the measurement positions, the surface potential analysis was carried out analogously to the layer thickness measurement described in 2.5. From that, the mean surface potential as well as standard deviation were calculated. Also in this case, the standard deviation serves as an indicator for showing the homogeneity of the powder charging, which is of great importance for the subsequent EPA-PBF-LB/P-process [4].

2.7. Charge spectrometry

To access the underlying charge at particle level, a charge spectrometry was conducted. By that, charge (q) to diameter (d) ratios can be obtained. In the context of this work, measurements were performed using a q/d -meter (Epping GmbH, Neufahrn bei Freising, Germany). The aim was to understand the effect of charge control and the electrostatic interaction of the functionalized and non-functionalized surfaces of polymer particles with the differently functionalized carrier surfaces. As described in [54], using low pressure, the q/d -meter accelerates a pulsed particle stream into an electric field having static field strength. According to the already mentioned Eq. (2):

$$\vec{F}_{el} = q \cdot \vec{E} \quad (2)$$

where the trajectory of a charged particle with charge q is deflected by \vec{F}_{el} , the force an electric field with electric field strength \vec{E} exerts on it. The force that counteracts this deflection is the drag force described by (3) [54]:

$$F_d = \frac{\rho_F}{2} |\vec{v}_{rel}| \vec{v}_{rel} \frac{\pi}{4} d^2 c_d \quad (3)$$

where \vec{v}_{rel} represents the particle's velocity relative to the surrounding fluid of density ρ_F . Moreover, c_d is the drag coefficient depending on the Reynolds number, and d is the particle diameter. As given in [54], balancing both Eqs. (2) and (3) and gravity, yields the particle trajectories by integrating the balance of forces for their transient motion. According to [54], depending on their charge and polarity, the particles are deposited on different positions on object slides placed in front of capacitor plates, which are used for generating the electric field. Finally, the projection area of the deposited particles is determined, which is used for calculating the charge to diameter (q/d -) ratio [54]. For this purpose, the assumption that the flow conditions and the electric field strength are known, is employed [54,55]. Similar to the triboelectric charging device described in 2.3, the ferritic carrier particles are also retained by a magnetic field to ensure that only polymer particles are characterized with respect to their charge.

2.8. Electrophotographic powder development and deposition of triboelectrically charged polymer particles into the build chamber

For verifying the potential of the new charge control method for generating powder layers for additive manufacturing of parts using EPA-PBF-LB/P, PP layers were applied onto the build platform using process steps one to four (cf. Fig. 1). This experiment is an extension of the triboelectric charging process described in 2.3 and in this case utilizes the layer of charged PP particles on the transfer drum to develop, move and deposit a PP pattern into the build chamber. The subsequent illumination and layer-wise repetition of this procedure in order to additively manufacture parts is not part of this work. However, in [4] the layer-wise deposition, illumination and thus additive manufacturing of parts by EPA-PBF-LB/P already has been successfully shown – but with gas discharge (corona wire) based powder charging instead of triboelectric powder charging.

Fig. 5 gives a schematic overview of the experimental setup. The gray square shows the movable photoconductive plate (PCP) semi-transparent in order to reveal the polymer particles adhering to the undersurface of the PCP. No imaging was performed in this experiment in order to reduce further influencing parameters arising from the imaging step. For conducting the experiment shown in Fig. 5, a thin quadratic, non-conductive plate with a side length of 4.5 cm and a thickness of 0.3 mm was placed on the surface of the transfer drum. After triboelectric charging and powder transfer to the transfer drum (and thus also to the thin plate), the thin plate was transferred to the EPA-PBF-LB/P system, where powder development to the PCP and powder deposition onto the build platform were finally performed.

For showing the applicability of the newly developed charge control method for EPA-PBF-LB/P, a powder blend consisting of 60 wt% of PP powder functionalized with 0.5 wt% silica(-) and 40 wt% positively charging carrier was used. In total, a mass of 100 g of powder blend was filled into the triboelectric charging system for development and deposition experiments.

The moving system as well as high voltage supply of the experimental setup is described in detail in [3]. A 100 μm thick, vapor-deposited arsenic triselenide (As_2Se_3) layer on the undersurface of the PCP was used as photoconductor. The PCP was connected to a high-voltage supply via high-voltage cable, allowing voltages to be applied to the PCP, which established the electric fields between the PCP and powder layer (development field) or PCP and build platform (deposition field). Additionally, the photoconductor was charged by gas

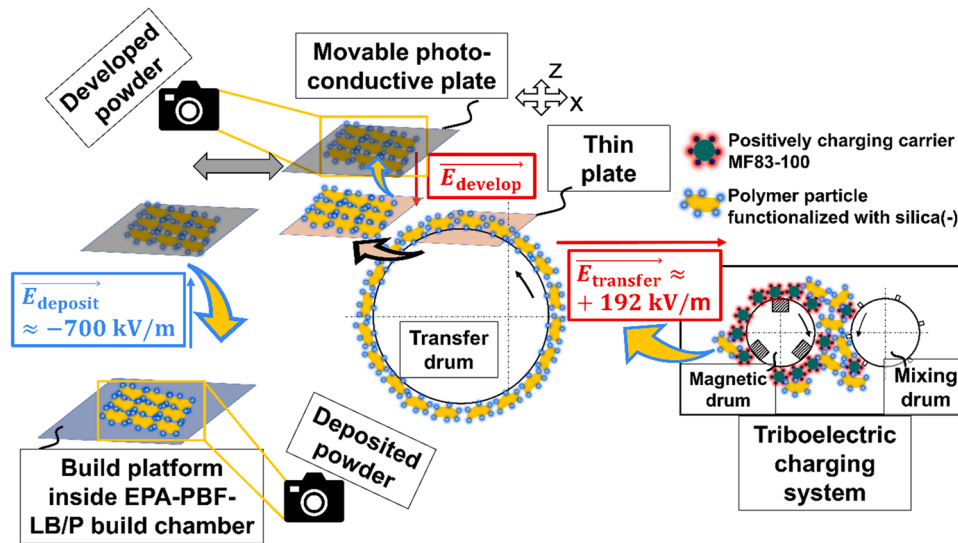


Fig. 5. Schematic overview of experimental setup for triboelectric charging and powder development / deposition into build chamber; red arrows indicate the directions of the respective electric fields using the sign convention that a positive test charge would move in the direction of the field lines [56]; the PCP is shown semi-transparent to reveal the polymer particles adhering to the undersurface of the PCP.

discharge (cf. 1 (Introduction) and Table 6).

For conducting the experiments, the following parameters were utilized (cf. Table 6). None of the applied electric field strengths exceeds the dielectric strength of air at normal conditions (atmospheric pressure $p_0 = 1013$ hPa, temperature $T_0 = 293$ K, relative air humidity = 35%), which is in the range of $\vec{E}_{\text{breakdown}} \approx 3 \bullet 10^6 \text{ V m}^{-1}$ [57,58]. The experiments shown in this work were conducted under normal conditions. However, since charging experiments of polymer particles are known to be temperature-dependent [23,59], it is important to mention that all process steps except for powder deposition in step three and fusion in step four (cf. Fig. 1), take place under normal conditions in the experimental setup developed for EPA-PBF-LB/P. Only for powder deposition in step four, the PCP with the developed powder pattern is exposed to higher temperatures of up to 175 °C, depending on the processed polymer [60]. However, since the time duration in which the PCP is exposed to this high temperature is only a few seconds, no significant heating of the PCP and powder pattern takes place. As shown in [4], the powder deposition efficiencies did not exhibit any significant variations due to elevated temperatures. Thus, the effect of elevated build chamber temperatures is neglected in this work.

The electric field strength for charging the PCP was generated by applying a voltage of + 5 kV at a separation distance of 3 cm to the PCP charging corona wire. In case of the electric transfer field, a voltage of + 770 V was applied to the transfer drum at a separation distance of 4 mm between transfer drum and triboelectric charging system. For powder development the voltage applied to the PCP was varied ranging from + 100 V, + 300 V up to + 700 V at a separation distance of 1.3 mm

Table 6

Parameters for electrophotographic powder development and deposition of triboelectrically charged PP particles into the build chamber (parameters adapted from previous work in [4]).

Parameter	Value
Polarity and charging field strength PCP	+ 167 kV m ⁻¹
Polarity and transfer field strength	+ 192 kV m ⁻¹
Polarity and development field strength	+ 77 kV m ⁻¹ ; + 231 kV m ⁻¹ ;
	+ 538 kV m ⁻¹
Polarity and deposition field strength	-700 kV m ⁻¹
Frequency of sinusoidal signal for piezo excitation	15 kHz
Peak-to-peak voltage of sinusoidal signal	8 V _{p-p}

between PCP and PP powder layer. Finally, for powder deposition, a voltage of - 700 V was applied to the PCP at a separation distance of 1 mm between PCP and build platform.

Pictures were taken from the developed as well as deposited powder patterns utilizing a camera (Samsung Electronics Co. Ltd., Suwon, South Korea) with a resolution of 3840 × 2160 pixels (cf. 2.4). The layer thickness of the powder patterns, which were defined as squares with a side length of 30 mm, was measured according to the procedure described in 2.5 – in this case – however, at five different positions of the square. These include each of the four corners as well as the center of the square.

To increase the powder deposition efficiency in step four (cf. Fig. 1) and to allow comparability of the results obtained in this study with EPA with gas-discharge based powder charging [4], a method based on piezoelectric vibration excitation presented in [3] was applied. A detailed description of the experimental setup can be found in [3,4]. The parameters applied for vibration excitation can be found in Table 6.

3. Results and discussion

3.1. SEM analysis of carrier and polymer particles

The SEM image shown in Fig. 6 visualizes a friction situation between a PP particle functionalized with 0.5 wt% silica(-) and a MF83-100 carrier particle. The PP particle is present in its typical potato shape, whereas the carrier particle has a circular shape.

As can be seen in Fig. 6a), the carrier particles supplied by Powdertech Co., Ltd. also appear to have surface functionalization with nanoparticles, similar to the surface functionalization of the polymer particles (cf. Fig. 6b)). However, the exact weight percentage of nanoparticles used by Powdertech is not specified in detail. According to the manufacturer, an acrylic resin-based functionalization is used for enhancing positive charging and a polyvinylidenefluorid (PDVF) -based functionalization for enhancing negative charging tendency of the carrier particles (cf. Table 1).

Another explanation for the nanometer-sized structures in Fig. 6a), which appear slightly darker compared to the lighter carrier surface, could be abrasion of PP particles adhering to the surface of the carrier particle due to interparticle forces. For investigating this effect more in detail, a SEM of a powder blend consisting of non-functionalized and thus uncoated carrier particles together with PP is shown in Fig. 7.

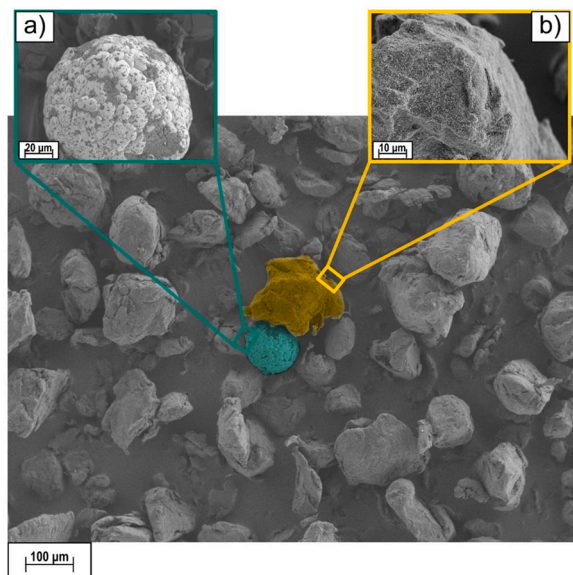


Fig. 6. SEM image of powder blend consisting of 40 wt% carrier MF83-100 and 60 wt% PP functionalized with 0.5 wt% silica(-); a) magnification of carrier MF83-100; b) magnification of PP functionalized with 0.5 wt% silica(-).

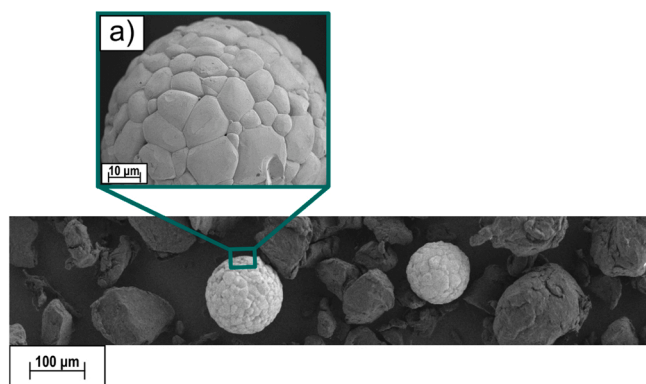


Fig. 7. SEM image of powder blend consisting of 40 wt% uncoated carrier MF90-100 and 60 wt% PP functionalized with 0.5 wt% silica(-); a) magnification of carrier MF90-100.

As can be seen in Fig. 7a), the surface of the non-functionalized carrier particles does not show any additives adhering to the surface of the carrier particle. Therefore, the nanometer-sized structures visible in Fig. 6a) can be attributed to the surface functionalization for achieving a certain charging behavior.

In contrast to conventional two-component toner technology, where the diameter ratio between toner particle and carrier particle is in the range of 1:8 [61], in case of EPA-PBF-LB/P the diameter ratio between PP particle and carrier particle is in the range of 1:1 (cf. particle sizes in Table 1 and Table 4). Thus, for polymer particles typically used in EPA-PBF-LB/P, the surface area of the carrier particles available for triboelectric charging is significantly smaller than in conventional toner technology. This might lead to a less efficient charging process. Therefore, the efficiency of triboelectric charging of polymer particles, which is finally reflected in the achievable surface potential as well as charging homogeneity of the powder layer, is of crucial importance for the following investigations.

3.2. Charge spectrometry of PP

3.2.1. Non-functionalized and functionalized PP without carrier

To gain a better understanding of the charging behavior of PP without carrier particles on particle level, charge spectrometry measurements of non-functionalized and functionalized PP without carrier were performed. The results are shown in Fig. 8.

Independent of the functionalization, PP shows a bimodal charge distribution with almost equal positive and negative charging. Comparing Fig. 8a) – c) it can be observed that the distribution densities of the charge to diameter (q/d -) ratios are not significantly influenced by functionalizing the polymer particles with CCAs. The reason for this behavior is found in the nature of triboelectric charging. In general, it is based on charge separation occurring during prolonged contact, collision, or friction between the particles involved driven by a difference in the work functions of the respective materials [26]. Since similar materials were triboelectrically charged for the results shown in Fig. 8 and also the functionalization is homogeneously distributed over the surface of the polymer particles (cf. Fig. 6c) and [23]), there are no significant differences between the working functions of the friction partners. Small fluctuations in the work functions can thus be considered to be statistically distributed over all particles, so that the probability of the friction partners donating or accepting electrons is equally high.

However, a bimodal charge distribution is unsuitable for EPA-PBF-LB/P. This is due to the fact that the main driving force for powder development in process step three as well as powder deposition in process step four is the electric field force \vec{F}_{el} described in Eq. (2) [4]. Since \vec{F}_{el} is directly dependent on the particle charge q , the presence of nearly equal positive as well as negative charges, as can be seen in Fig. 8 due to the nearly symmetric q/d -ratios, leads to the cancellation of \vec{F}_{el} . Therefore, the goal of the charge control method developed in this work is to transform the strongly bimodal charge distribution of the polymer to a unimodal one.

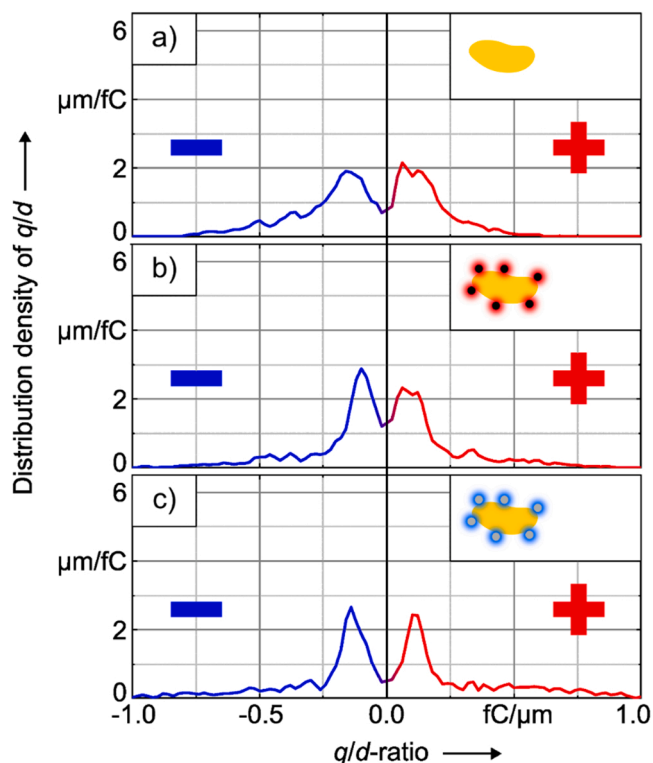


Fig. 8. Charge spectrometry (mean curves) of non-functionalized PP (a), PP functionalized with 0.5 wt% silica(+) (b) and PP functionalized with 0.5 wt% silica(-) (c), without carrier; number of experiments $n = 3$ for each curve.

3.2.2. Non-functionalized PP with carrier

Comparing the results shown in Fig. 9 with the results visualized in Fig. 8, it can be deduced that already in case of non-functionalized PP the charging tendency of the polymer can be manipulated. The charge distribution of PP is shifted towards a rather negative characteristic due to friction with a positively charging ferrite carrier (Fig. 9a), and towards a rather positive characteristic due to friction with a negatively charging ferrite carrier (Fig. 9b)).

Although a charging tendency towards negative (Fig. 9a) or positive (Fig. 9b) charging can be observed, the opposite charging is still present with approximately half the distribution density. Thus, it can be assumed that charged polymer particles, which show a charge distribution density according to Fig. 9 are still not efficiently transferable in EPA-PBF-LB/P. This is further investigated in 3.3.1.

3.2.3. Functionalized PP with carrier

Finally, the synergy of both functionalizing the particle surface with CCAs and choosing suitable carrier particles is applied. The results of the charge spectrometry measurements of functionalized PP particles after triboelectric charging with functionalized carrier particles are shown in Fig. 10.

Especially in case of PP functionalized with 0.5 wt% silica(-) and positively charging carrier MF83-100 a unimodal charge distribution is achieved. Also in case of PP functionalized with 0.5 wt% silica(+) and negatively charging carrier MF22-100 a strong increase of positive charging with an approximately three times higher positive charge distribution density compared to the negative one is obtained. From this, it can be deduced that it is easier for PP, together with the selected CCAs and carrier particles, to suppress positive charging than negative charging. However, it is important to mention that charge spectrometry measurements with PP particles functionalized with more than 0.5 wt% silica(-) or silica(+) together with the respective carrier particles could not be conducted. The reason is that the negative as well as positive triboelectric charging of PP particles in this case exceeded the capability of the used q/d -meter to properly accelerate the charged particles to form a pulsed particulate stream. Therefore, it cannot be excluded that in case of PP functionalized with 1.0 wt% silica(+) and negatively charging ferrite carrier MF22-100, also a positive unimodal triboelectric charging of PP can be obtained, similar to the negative unimodal charging shown in Fig. 10 a). In the next sections, the knowledge gained

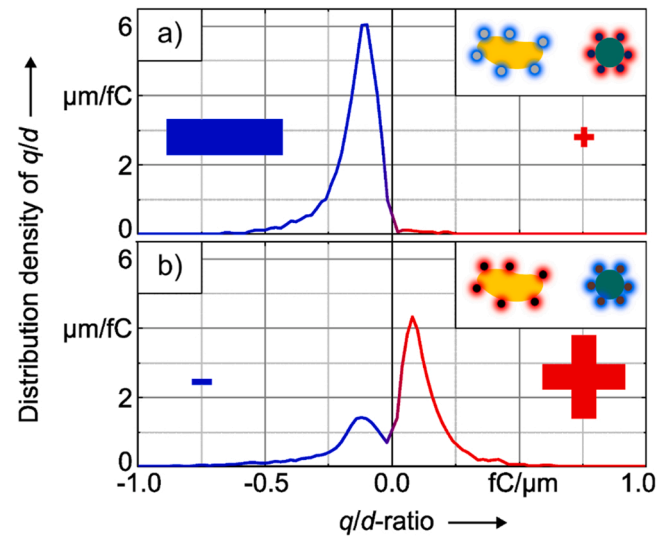


Fig. 10. Charge spectrometry (mean curves) of a powder blend consisting of 60 wt% PP functionalized with 0.5 wt% silica(-) and 40 wt% positively charging ferrite carrier MF83-100 (a), and of a powder blend consisting of 60 wt% PP functionalized with 0.5 wt% silica(+) and 40 wt% negatively charging ferrite carrier MF22-100 (b), respectively; number of experiments $n = 3$ for each curve.

on particle level is applied to EPA-PBF-LB/P.

3.3. Triboelectric charging experiments

3.3.1. Investigation of triboelectric charging of non-functionalized PP as function of carrier content

The goal of the results shown in Fig. 11 and Fig. 12 is to find a suitable carrier content for the further development of a method for triboelectric charge. As described in 2.1, the most suitable carrier content in the context of this work is defined as the minimum carrier content at which a preferably high coverage and especially high layer homogeneity are achieved for pure PP. Generally, it is important to note that the higher the carrier content in the powder blend filled into the triboelectric charging system (cf. Fig. 4), the less polymer powder is available for EPA-PBF-LB/P. Thus, as a first step for developing a charge control strategy, a preferably low carrier content should be chosen at which already for the non-functionalized PP a significant increase of layer

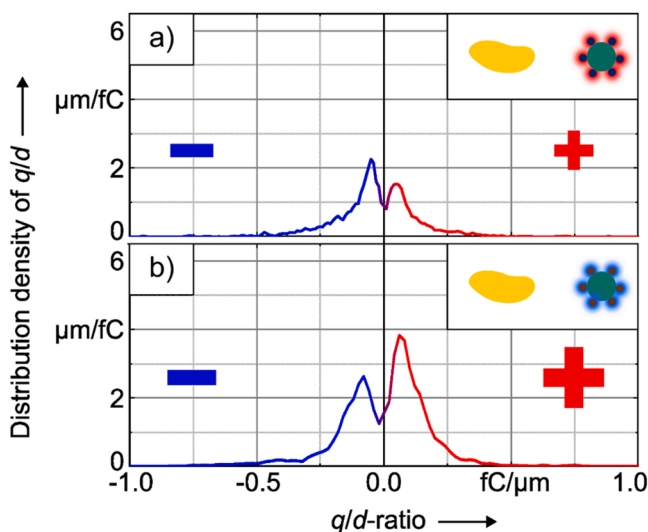


Fig. 9. Charge spectrometry (mean curves) of a powder blend consisting of 60 wt% non-functionalized PP and 40 wt% positively charging ferrite carrier MF83-100 (a), and of a powder blend consisting of 60 wt% non-functionalized PP 40 wt% negatively charging ferrite carrier MF22-100 (b), respectively; number of experiments $n = 3$ for each curve.

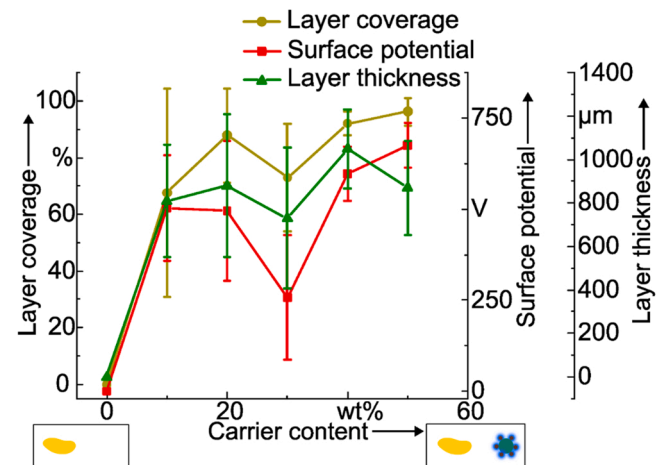


Fig. 11. Layer coverage, surface potential and layer thickness of non-functionalized PP transferred to the transfer drum as function of negatively charging carrier content (MF22-100); number of measurements $n = 20$ for layer thickness and surface potential and $n = 3$ for layer coverage.

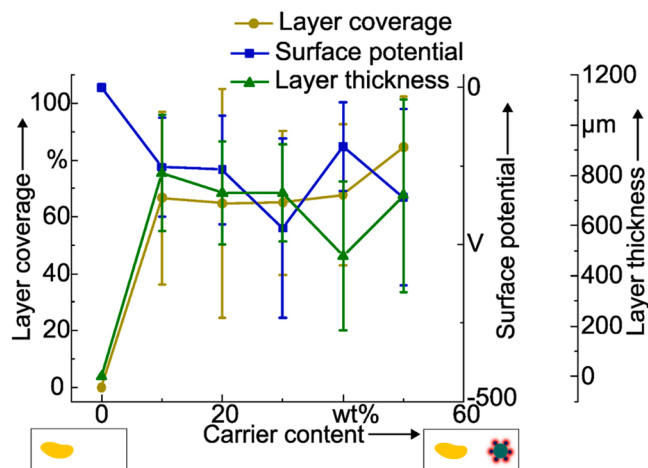


Fig. 12. Layer coverage, surface potential and layer thickness of non-functionalized PP transferred to the transfer drum as function of positively charging carrier content (MF83-100); number of measurements $n = 20$ for layer thickness and surface potential and $n = 3$ for layer coverage.

coverage, thickness, surface potential and homogeneity can be observed.

In Fig. 11 and Fig. 12 the results of two series of triboelectric charging experiments with powder blends consisting of different contents of negatively (MF22-100, Fig. 11) and positively (MF83-100, Fig. 12) charging ferrite carrier and non-functionalized PP are presented. As already expected, based on the charge spectrometry results without carrier (cf. 3.2.1, Fig. 8), the strongly bimodal charge distribution of PP does not allow any powder transfer to the transfer drum in case of 0 wt% carrier content. However, already at 10 wt% carrier content, powder transfer to the transfer drum takes place, and a coverage of approximately 70% in case of negatively charging carrier is achieved. Nevertheless, as the relatively large standard deviation of around $\pm 36\%$ indicates, the coverage is very inhomogeneous, making the layer of charged PP unsuitable for further processing in EPA-PBF-LB/P. In case of negatively charging carrier (Fig. 11), a significant decrease of layer inhomogeneity can be observed at a carrier content of 40 wt%. Here, the layer coverage is above 90% with a standard deviation of 4%. In case of positively charging carrier (Fig. 12), the first slight decrease of layer inhomogeneity is present at 30 wt% carrier with a coverage of approximately 65% and a standard deviation of around 25%. However, as already indicated by the charge distribution on particle level in Fig. 9, without functionalization of PP, the positive triboelectric charging (Fig. 9b) is stronger pronounced than the negative charging tendency shown in Fig. 9a. This matches well with the generally better layer coverage, higher magnitude of surface potential, as well as layer thickness for positively charged PP in Fig. 11 compared to the negative one depicted in Fig. 12.

However, especially in case of positively charged PP (Fig. 11) a significant decrease of layer inhomogeneity with respect to coverage, surface potential and thickness is achieved in case of 40 wt% negatively charging carrier (MF22-100). This carrier content is used for all further experiments. To allow comparability between the positively and negatively charging experiments, also for the positively charging carrier (MF83-100) a content of 40 wt% is defined for the further experiments.

3.3.2. Investigation of triboelectric charging of functionalized PP as function of additive content

In this section, the actual charge control method using the synergy of both functionalizing the particle surface with CCAs and choosing suitable carrier particles is applied to PP and investigated with respect to its applicability to EPA-PBF-LB/P. The requirements of a charged polymer layer for the further process steps three (powder development) and four (powder deposition) (cf. Fig. 1) can be summarized as follows. Firstly,

the layer coverage must be 100%, since surface defects caused, for example, by partially missing powder, are directly transferred to the generated part and, thus, influence its quality. For this reason, also the homogeneity of the powder layer should be preferably high, which is investigated here as standard deviation of the layer coverage. Furthermore, in order to increase process productivity, a charged polymer layer should be suitable for more than one development step. Based on results from gas discharge-based EPA-PBF-LB/P, the layer thickness of a deposited powder layer is in the range of 50 μm in case of PA12 and 100 μm in case of PP [4]. This can be explained by the fact that the ions generated by gas discharge are only capable of penetrating the first powder layer and thus only one layer, consisting of approximately one particle in z-direction with a thickness corresponding to the respective particle diameter, can be developed and deposited. Assuming a comparable layer thickness for triboelectric charging-based EPA-PBF-LB/P investigated in this work, the minimum layer thickness of the prepared polymer layer is defined to be at least 100 μm but should be a multiple of this thickness to achieve the goal of being suitable for more than one powder development step. This means that the layer thickness of the powder layer on the transfer drum exceeds the layer thickness of the powder layer deposited onto the build platform. Thus, more than one layer could be developed from the transfer drum and deposited onto the build platform without the need for new powder transfer to the transfer drum.

Finally, based on results from gas discharge-based EPA-PBF-LB/P [4, 10], the magnitude of the surface potential of the prepared powder layer should be at least 200 V in order to develop a layer with a magnitude of the development field strength of 3846 kV m^{-1} . However, a higher surface potential of the prepared layer would allow the strength of the developing field to be reduced, which would also increase productivity by reducing the time necessary for the high voltage supply to reach the required high voltage. It should be mentioned that increasing the transfer voltage for transferring polymer powder particles from the charging device to the transfer drum could increase layer coverage. However, since in this case polymer particles with a lower triboelectric charging will be transferred, it has to be ensured that the magnitude of surface potential of the powder layer on the transfer drum is still above 200 V.

The results of the triboelectric charging experiments for generating charged PP layers by both, applying functionalization of PP particles with CCAs and using carrier particles, are shown in Fig. 13 for positively charged PP and Fig. 14 for negatively charged PP. In both cases, for additive contents of 0.5 wt% and 1.0 wt% the requirements described above are met. Lower contents of additives in both cases are not suitable

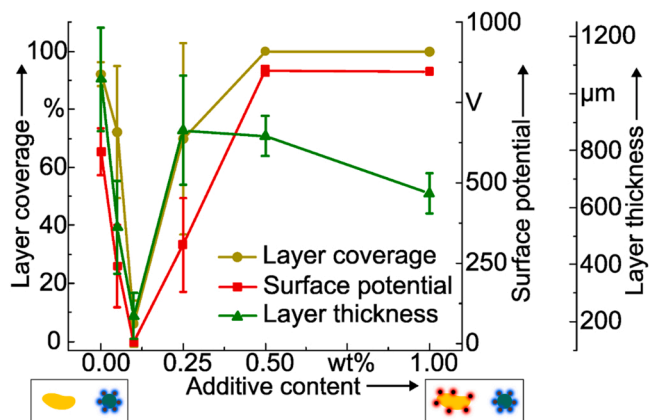


Fig. 13. Layer coverage, surface potential and layer thickness of functionalized PP transferred to the transfer drum as function of silica(+) content after triboelectric charging with 40 wt% negatively charging carrier (MF22-100); number of measurements $n = 20$ for layer thickness and surface potential and $n = 3$ for layer coverage.

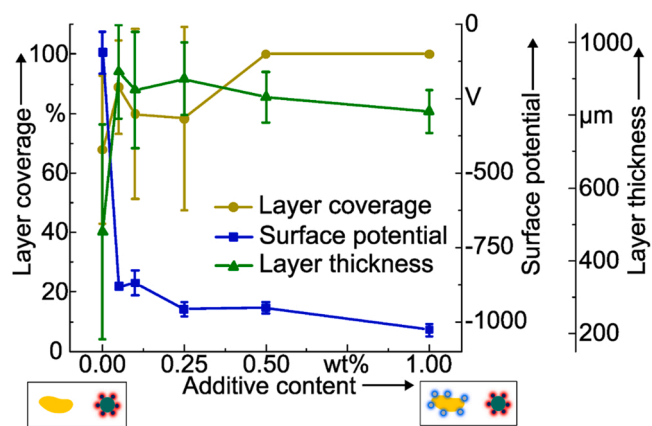


Fig. 14. Layer coverage, surface potential and layer thickness of functionalized PP transferred to the transfer drum as function of silica(-) content after triboelectric charging with 40 wt% positively charging carrier (MF83–100); number of measurements $n = 20$ for layer thickness and surface potential and $n = 3$ for layer coverage.

for EPA-PBF-LB/P, mainly due to insufficient coverage values in combination with high inhomogeneity. As indicated by charge spectrometry measurements of pure PP and positively as well as negatively charging carrier particles (cf. Fig. 9), already the surface functionalization of the carrier particles leads to an enhancement of one charging polarity. Thus, it is not surprising that already in case of 0 wt% additive only due to the charging tendency of the respective carrier particles a limited charge control is achieved leading to powder transfer towards the transfer drum (cf. Fig. 13 and Fig. 14). Interestingly, for both charging polarities (Fig. 13 and Fig. 14), the layer thickness values slightly decrease for additive contents of 1 wt% compared to the thickness values at 0.5 wt%. This can be attributed to the fact that, the opposing field created by the transferred powder on the transfer drum itself, counteracts the powder transfer and, thus, leads to a lower layer thickness on the transfer drum. Especially, in case of negatively charged PP (Fig. 14) this explanation is supported by an increased magnitude of the surface potential of the powder on the transfer drum for 1.0 wt% compared to 0.5 wt%. However, in case of positively charged PP (Fig. 13) this effect of increased surface potential is less pronounced, but still the layer thickness is decreased in case of 1.0 wt% additive content.

Moreover, in case of positively charged PP (Fig. 13), the minimum of surface potential and therefore layer coverage and thickness occurs for an additive content of 0.1 wt% silica(+). However, a similar trend to Fig. 14, where an increasing additive content almost consistently enhances negative charging of PP, would have been expected. This inconsistency shown in Fig. 13 might be explained by the generally strong positive charging tendency of pure PP when in contact with the negatively charging carrier, which is already visibly on particle level (Fig. 9b)). A low amount (below 0.5 wt%) of positively charging CCA silica(+) seems to rather counteract this positive charging tendency of PP. Only at sufficiently high concentrations of silica(+) (above 0.5 wt%), the triboelectric charging between CCAs and carrier leads to an increase of surface potential compared to non-functionalized PP. This comparably weak charge control capability achieved by silica(+) compared to silica(-) might also be attributed to the strongly differing magnitudes of specific charge shown in Table 3, where silica(+) has a specific charge of $+ 50 \mu\text{C g}^{-1}$, whereas silica(-) has a specific charge of $- 450 \mu\text{C g}^{-1}$.

Besides an increase of counteracting opposing field strength in case of 1.0 wt%, the higher particle charge can also lead to stronger attraction forces to the magnetic brush formed by the carrier particles inside the triboelectric charging system (cf. 2.3). Although the conductive ferritic carrier particles conduct the charges generated during triboelectric charging with the polymer particles to ground via magnetic

drum, for a short period of time also the coated surface of the carrier particles is charged. The generally higher charging in case of functionalization of the PP surface with 1.0 wt% additive content may therefore also lead to stronger attractive forces between PP and carrier particles. As a consequence, the layer thickness is decreased. Besides positive effects on powder charging, the usage of silica-based additives may also enhance powder flowability of the polymer powders [23].

3.3.3. Transferability to other polymers

The charge control method developed in 3.3.2 is applied to PA12, PS and HDPE in this section. The results of the triboelectric charging and powder transfer experiments for these polymers are presented in Fig. 15. For all analyzed polymers, functionalization with 0.5 wt% CCA and mixing the polymer with 40 wt% carrier leads to coverage values of 100%. Furthermore, the inhomogeneity of layer coverage is negligible, as evidenced by standard deviation values below 1%.

Thus, the charge control method developed in this work is also applicable for polymers located at significantly different positions in the triboelectric charging series. Although according to Table 4 the TECD of these polymers varies significantly, the coverage of the powder layer transferred to the transfer drum in all cases yields 100%. The aforementioned functionalization of the used PA12 (PA2200) with nano-silica particles for enhancing the powder flowability (cf. 2.1) by the manufacturer does not have any significant influence of the performance of the charge control method developed in this work, when comparing the coverage of PA12 to the other polymers in Fig. 15.

3.4. Electrophotographic powder development and deposition of triboelectrically charged PP particles into build chamber

Finally, the charge control method developed in this work is validated using process steps one to four (cf. Fig. 1). In Fig. 16 the development as well as deposition results of PP functionalized with 0.5 wt% silica(-) are shown. The results prove that triboelectric-based powder charging can completely substitute gas discharge-based powder charging used so far. As can be seen in Fig. 16, both, development and

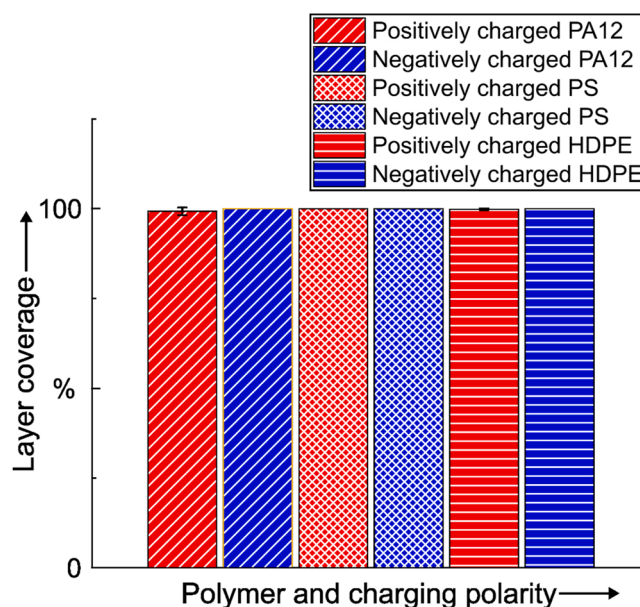


Fig. 15. Layer coverage of functionalized PA12, PS and HDPE transferred to the transfer drum; positively charged polymers functionalized with 0.5 wt% silica(+) and mixed with 40 wt% negatively charging carrier (MF22–100); negatively charged polymers functionalized with 0.5 wt% silica(-) and mixed with 40 wt% positively charging carrier (MF83–100); number of measurements $n = 3$; standard deviations for bars 2,3,4 and 6 are 0%.

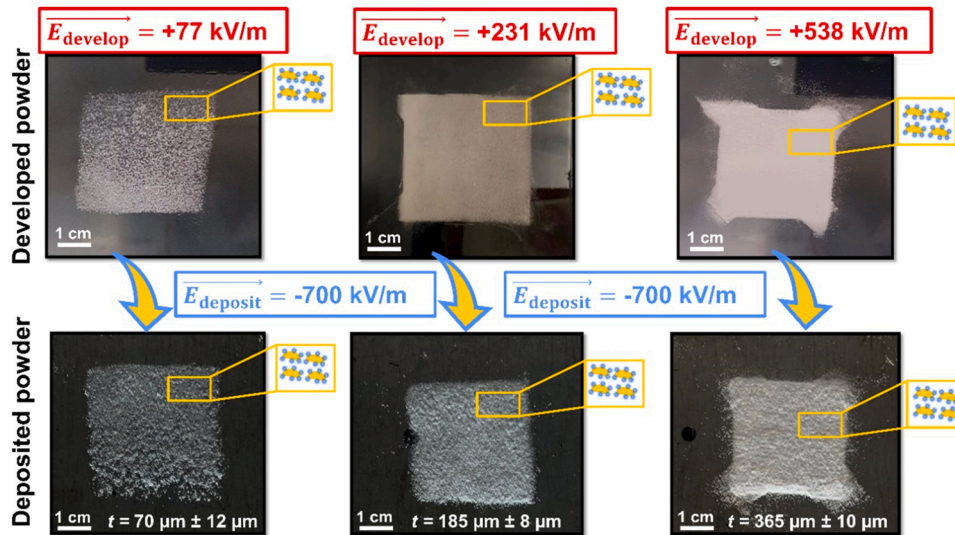


Fig. 16. PP functionalized with 0.5 wt% silica(-) and mixed with 40 wt% positively charging carrier (MF83–100) for triboelectric charging developed to PCP using different electric development field strengths and deposited onto build platform; number of measurements $n = 20$ for layer thickness.

deposition of triboelectrically charged PP work successfully and functional layers of PP are available in the build chamber for further processing according to the conventional PBF-LB/P fusion process. In comparison to gas discharge-based powder charging, the development field strength is decreased by a factor of approximately 50 from 3846 kV m^{-1} [4] to 77 kV m^{-1} in case of the left development result shown in Fig. 16 and by a factor of approximately 7–538 kV m^{-1} . This can be attributed to the significantly more efficient and homogeneous charging process of triboelectric charging in comparison to gas discharge-based powder charging. Also, the deposition field strength is reduced by a factor of approximately 3.6 from 2500 kV m^{-1} in case of gas discharge-based powder charging [4,10] to 700 kV m^{-1} in case of triboelectric powder charging.

Another remarkable advantage of the triboelectric approach is the fact that as can be observed from the different layer thickness values t for the deposited powder layers in Fig. 16, the layer thickness can be adjusted by changing the development field strength. This is due to the fact that not only the upper most powder layer, which in case of gas discharge-based powder charging is charged by incorporated ions, is charged via triboelectric charging. Instead, the entire, several hundreds of micrometers thick powder layer (cf. Fig. 13 and Fig. 14) is homogeneously charged and, therefore, a thicker powder layer can be developed as well as deposited. Taking into account the maximum possible layer thickness with respect to the fusion process considering for example sufficient layer-to-layer interconnection, the fact of adjustable layer thickness values significantly increases the productivity of EPA-PBF-LB/P. In case of conventional doctor blade- or roller-based powder application methods, the layer thickness is typically in the range of 100 – 150 μm and strongly depends on the particle sizes of the used powder [4, 23,60,62]. Considering the different possible layer thickness values shown in Fig. 16, it can be concluded that the use of triboelectric charging in combination with EPA significantly increases the flexibility of adapting the layer thickness of powder layers deposited onto the build platform for PBF-LB/P.

Since for the results shown in Fig. 16, a thin plate was used for transferring the triboelectrically charged particles from the charging device to the EPA-PBF-LB/P system (cf. 2.8), slight distortions of the powder layer can occur. In case of the strong development field in the right image in Fig. 16, also slightly distorted powder particles are still developed and finally deposited onto the build platform, creating the powder pattern surrounding the square.

4. Conclusion and outlook

In this work, a new method for controlling the triboelectric charging of polymer particles for their usage in electrophotographic powder application (EPA) for laser-based powder bed fusion of polymers (PBF-LB/P) was developed and successfully validated. For the first time, triboelectrically charged polymer particles were deposited onto the build platform using EPA for further processing in PBF-LB/P. This was achieved by the synergy of both, functionalizing the particle surface with charge control agents (CCAs) and choosing suitable carrier particles known from two-component toners. This allowed crucial process parameters, such as polarity and resulting surface potential of the charged polymer powder layer to be precisely tuned. Furthermore, the layer thickness of the deposited powder layer could be adjusted with varying the electric development field strength, which was not possible with the gas discharge-based powder charging for EPA-PBF-LB/P used so far. This offers great potential for increasing the productivity of EPA-PBF-LB/P. The homogeneous charging characteristics of triboelectric charging on particle level allowed the electric field strengths used in EPA to be significantly reduced, which increases productivity as well as efficiency of this new powder application method. The developed charge control method was furthermore successfully applied to other polymers with strongly differing triboelectric charging tendencies. In future work, the carrier content may be reduced by finer adjusting it to the additive content of CCA used for functionalizing the polymer particles. Furthermore, the strategy developed in [4] for compensating the accumulation of charges within the generated part needs to be validated for triboelectrically charged polymer particles. The main concept of alternating the polarity of applied powder layers in order to compensate charge accumulation should also work in case of triboelectrically charged particles. Nevertheless, the stronger and more homogenous charging on particle level needs to be further investigated with respect to charge accumulation within the generated part.

CRediT authorship contribution statement

Sebastian-Paul Kopp: Writing – review & editing, Writing – original draft, Visualization, Validation, Supervision, Software, Methodology, Investigation, Formal analysis, Data curation, Conceptualization. **Björn Düsenberg:** Writing – review & editing, Writing – original draft, Validation, Methodology, Investigation, Formal analysis, Data curation, Conceptualization. **Pius Marcellinus Eshun:** Validation, Software,

Investigation, Data curation. **Jochen Schmidt**: Writing – review & editing, Validation, Supervision, Resources, Project administration, Funding acquisition, Formal analysis, Data curation. **Andreas Bück**: Writing – review & editing, Supervision, Resources, Project administration, Funding acquisition, Formal analysis, Conceptualization. **Stephan Roth**: Writing – review & editing, Supervision, Resources, Project administration, Funding acquisition, Formal analysis, Data curation. **Michael Schmidt**: Writing – review & editing, Supervision, Resources, Project administration, Funding acquisition, Formal analysis, Data curation.

Declaration of Competing Interest

The authors declare that they have no known competing financial interests or personal relationships that could have appeared to influence the work reported in this paper.

Data Availability

Data will be made available on request.

Acknowledgements

Funding of the Collaborative Research Center 814 (CRC 814) “Additive Manufacturing”, subprojects B6 and A2, by the German Research Foundation (DFG) – project number 61375930 – is gratefully acknowledged by the authors. Furthermore, the authors gratefully acknowledge funding of the Erlangen Graduate School in Advanced Optical Technologies (SAOT) by the Bavarian State Ministry for Science and Art.

References

- [1] S.H. Huang, P. Liu, A. Moksadar, L. Hou, Additive manufacturing and its societal impact: a literature review, *Int. J. Adv. Manuf. Technol.* 67 (2013) 1191–1203, <https://doi.org/10.1007/s00170-012-4558-5>.
- [2] T. Laumer, T. Stichel, D. Riedlbauer, P. Amend, J. Mergheim, M. Schmidt, Realization of multi-material polymer parts by simultaneous laser beam melting, *JLMN-J. Laser Micro/Nanoeng.* 10 (2015), <https://doi.org/10.2961/jlmn.2015.02.0006>.
- [3] S.-P. Kopp, V. Medvedev, S. Roth, Targeted vibration excitation for increasing the powder deposition efficiency in electrophotographic powder application for laser-based powder bed fusion of polymers, *Procedia CIRP* 111 (2022) 55–60, <https://doi.org/10.1016/j.procir.2022.08.117>.
- [4] S.-P. Kopp, V. Medvedev, T. Frick, S. Roth, Expanding the capabilities of laser-based powder bed fusion of polymers through the use of electrophotographic powder application, *J. Laser Appl.* 34 (2022), 042032, <https://doi.org/10.2351/7.0000774>.
- [5] S. Haeri, Y. Wang, O. Ghita, J. Sun, Discrete element simulation and experimental study of powder spreading process in additive manufacturing, *Powder Technol.* 306 (2017) 45–54, <https://doi.org/10.1016/j.powtec.2016.11.002>.
- [6] H. Chen, Q. Wei, Y. Zhang, F. Chen, Y. Shi, W. Yan, Powder-spreading mechanisms in powder-bed-based additive manufacturing: experiments and computational modeling, *Acta Mater.* 179 (2019) 158–171, <https://doi.org/10.1016/j.actamat.2019.08.030>.
- [7] Lawrence B. Schein, *Electrophotography and Development Physics*, Springer, 1988.
- [8] M. Schneck, M. Horn, M. Schmitt, C. Seidel, G. Schlick, G. Reinhart, Review on additive hybrid- and multi-material-manufacturing of metals by powder bed fusion: state of technology and development potential, *Prog. Addit. Manuf.* 6 (2021) 881–894, <https://doi.org/10.1007/s40964-021-00205-2>.
- [9] C. Wei, L. Li, Recent progress and scientific challenges in multi-material additive manufacturing via laser-based powder bed fusion, *Virtual Phys. Prototyp.* 16 (2021) 347–371, <https://doi.org/10.1080/17452759.2021.1928520>.
- [10] T. Stichel, C. Brachmann, M. Raths, M.A. Dechet, J. Schmidt, W. Peukert, T. Frick, S. Roth, Electrophotographic multilayer powder pattern deposition for additive manufacturing, *Jom* 72 (2020) 1366–1375, <https://doi.org/10.1007/s11837-019-03965-z>.
- [11] S.P. Kopp, T. Stichel, S. Roth, M. Schmidt, Investigation of the electrophotographic powder deposition through a transfer grid for efficient additive manufacturing, *Procedia CIRP* 94 (2020) 122–127, <https://doi.org/10.1016/j.procir.2020.09.024>.
- [12] A. v. Kumar, A. Dutta, J.E. Fay, Electrophotographic printing of part and binder powders, *Rapid Prototyp. J.* 10 (2004) 7–13, <https://doi.org/10.1108/13552540410512480/FULL/XML>.
- [13] M.M. Shahin, Nature of CHarge Carriers in Negative Coronas, *Appl. Opt.* 8 (Issue S1) (1969) 106–110, <https://doi.org/10.1364/AO.8.S1.000106>.
- [14] D.M. Pai, B.E. Springett, Physics of electrophotography, *Rev. Mod. Phys.* 65 (1993) 163–211, <https://doi.org/10.1103/RevModPhys.65.163>.
- [15] S. Matsusaka, H. Masuda, Electrostatics of particles, *Adv. Powder Technol.* 14 (2003) 143–166, <https://doi.org/10.1163/15685203763593958>.
- [16] J.W. Kwek, M. Jayabalasingam, W.K. Ng, J.Y.Y. Heng, R.B.H. Tan, Comparative study of the triboelectric charging behavior of powders using a nonintrusive approach, *Ind. Eng. Chem. Res* 51 (2012) 16488–16494, <https://doi.org/10.1021/IE3016973>.
- [17] E.O. Alt, W. Sandhas, H. Ziegelmann, Coulomb effects in three-body reactions with two charged particles, *Phys. Rev. C* 17 (1978) 1981, <https://doi.org/10.1103/PhysRevC.17.1981>.
- [18] J. Foerster, M. Michatz, M. Binder, A. Frey, C. Seidel, G. Schlick, J. Schilp, Electrostatic powder attraction for the development of a novel recoating system for metal powder bed-based additive manufacturing, *J. Electro* 115 (2022), 103641, <https://doi.org/10.1016/J.ELSTAT.2021.103641>.
- [19] D.A. Hays, Toner adhesion, *J. Adhes.* 51 (1995) 41–48, <https://doi.org/10.1080/00218469508009988>.
- [20] S. Matsusaka, H. Maruyama, T. Matsuyama, M. Ghadiri, Triboelectric charging of powders: a review, *Chem. Eng. Sci.* 65 (2010) 5781–5807, <https://doi.org/10.1016/J.CES.2010.07.005>.
- [21] D.J. Lacks, R.Mohan Sankaran, Contact electrification of insulating materials, *J. Phys. D: Appl. Phys.* 44 (2011), 453001, <https://doi.org/10.1088/0022-3727/44/45/453001>.
- [22] A.T. Ndama, P. Guigon, K. Saleh, A reproducible test to characterise the triboelectric charging of powders during their pneumatic transport, *J. Electro* 3 (2011) 146–156, <https://doi.org/10.1016/J.ELSTAT.2011.03.003>.
- [23] B. Düsenberg, S.-P. Kopp, F. Tischer, S. Schrüfer, S. Roth, J. Schmidt, M. Schmidt, D.W. Schubert, W. Peukert, A. Bück, Enhancing photoelectric powder deposition of polymers by charge control substances, *Polymers* 2022 Vol. 14 (14) (2022) 1332, <https://doi.org/10.3390/POLYM14071332>.
- [24] G. Huber, K.E. Wirth, Electrostatically supported surface coating of solid particles in liquid nitrogen for use in dry-powder-inhalers, *Powder Technol.* 134 (2003) 181–192, [https://doi.org/10.1016/S0032-5910\(03\)00128-1](https://doi.org/10.1016/S0032-5910(03)00128-1).
- [25] H. Zou, Y. Zhang, L. Guo, P. Wang, X. He, G. Dai, H. Zheng, C. Chen, A.C. Wang, C. Xu, Z.L. Wang, Quantifying the triboelectric series, *Nat. Commun.* 10 (2019) 1–9, <https://doi.org/10.1038/s41467-019-09461-x>.
- [26] H. Zou, L. Guo, H. Xue, Y. Zhang, X. Shen, X. Liu, P. Wang, X. He, G. Dai, P. Jiang, H. Zheng, B. Zhang, C. Xu, Z.L. Wang, Quantifying and understanding the triboelectric series of inorganic non-metallic materials, *Nat. Commun.* 11 (2020) 1–7, <https://doi.org/10.1038/s41467-020-15926-1>.
- [27] G. Castle, L. Schein, General Model of Sphere-Sphere Insulator Contact Electrification, (n.d.).
- [28] G.E. J, H.G. C, Triboelectric properties of two-component developers for Xerography, *J. Imaging Sci. Technol.* 36 (1992) 335–349, (https://global.jst.go.jp/en/detail?JGLOBAL_ID=200902091661492543).
- [29] J. Schmidt, M. Sachs, S. Fanselow, M. Zhao, S. Romeis, D. Drummer, K.E. Wirth, W. Peukert, Optimized polybutylene terephthalate powders for selective laser beam melting, *Chem. Eng. Sci.* 156 (2016) 1–10, <https://doi.org/10.1016/J.CES.2016.09.009>.
- [30] J.H. Anderson, The effect of additives on the tribocharging of electrophotographic toners, *J. Electro* 37 (1996) 197–209, [https://doi.org/10.1016/0304-3886\(96\)00017-4](https://doi.org/10.1016/0304-3886(96)00017-4).
- [31] L.A. Bejat, J.E. Johnson, R.O. Jones, B.P. Livengood, K.R. Srinivasan, D.J.V. Strain, Toner Formulations with Tribocharge Control and Stability, US20100040969A1, 2010.
- [32] J.S. Gómez Bonilla, B. Düsenberg, F. Lanyi, P. Schmueki, D.W. Schubert, J. Schmidt, W. Peukert, A. Bück, Improvement of polymer properties for powder bed fusion by combining in situ PECVD nanoparticle synthesis and dry coating, *Plasma Process. Polym.* 18 (2021), <https://doi.org/10.1002/PPAP.202000247>.
- [33] I.M. Kusoglu, C. Donate-buendía, S. Barcikowski, B. Gökce, Laser powder bed fusion of polymers: quantitative research direction indices, *Materials* 2021 Vol. 14 (14) (2021) 1169, <https://doi.org/10.3390/MA14051169>.
- [34] N. Vidakis, M. Petousis, L. Tzounis, A. Maniadi, E. Velidakis, N. Mountakis, J. D. Kechagias, Sustainable additive manufacturing: mechanical response of polyamide 12 over multiple recycling processes, *Materials* 2021 Vol. 14 (14) (2021) 466, <https://doi.org/10.3390/MA14020466>.
- [35] J.A. Giacometti, O.N. Oliveira, Corona charging of polymers, *IEEE Trans. Electr. Insul.* 27 (1992) 924–943, <https://doi.org/10.1109/14.256470>.
- [36] M.M. Shahin, Mass-spectrometric studies of corona discharges in air at atmospheric pressures, *J. Chem. Phys.* 45 (2004) 2600, <https://doi.org/10.1063/1.1727980>.
- [37] J.F. Hughes, *Electrostatic Particle Charging: Industrial and Health Care Applications*, Wiley-Blackwell, 1997, p. 170.
- [38] M.B. Mayr, S.A. Barringer, Corona compared with triboelectric charging for electronic powder coating, *J. Food Sci.* 71 (2006), <https://doi.org/10.1111/J.1750-3841.2006.00024.X>.
- [39] D.K. Brandvold, P. Martinez, D. Dogruel, Polarity dependence of N₂O formation from corona discharge, *Atmos. Environ.* 23 (1989) (1967) 1881–1883, [https://doi.org/10.1016/0004-6981\(89\)90513-1](https://doi.org/10.1016/0004-6981(89)90513-1).
- [40] R.M. Faria, A. Jorge, O.N. Oliveira, A novel space-charge effect in thermally stimulated current measurements on β-PVDF, *J. Phys. D: Appl. Phys.* 23 (1990) 334, <https://doi.org/10.1088/0022-3727/23/3/011>.
- [41] S. Guskov, Electrostatic Charging and Powder Coating with Porcelain Enamels, (2008) 1–15, <https://doi.org/10.1002/9780470294451.CH1>.
- [42] J.A. Giacometti, S. Fedosov, M.M. Costa, Corona charging of polymers: recent advances on constant current charging, *Braz. J. Phys.* 29 (1999) 269–279, <https://doi.org/10.1590/S0103-97331999000200009>.

- [43] C.F. Gallo, Coronas and gas discharges in electrophotography: a review, *IEEE Trans. Ind. Appl. IA* 11 (1975) 739–748, <https://doi.org/10.1109/TIA.1975.349370>.
- [44] C.F. Gallo, Corona—a brief status report, *IEEE Trans. Ind. Appl. IA* 13 (1977) 550–557, <https://doi.org/10.1109/TIA.1977.4503458>.
- [45] P.R. Horinka, Powder particle size: Its effects on coating line performance, (1995) 37.
- [46] Powder coating technology, *J. Electro.* 23 (1989) 3–23, [https://doi.org/10.1016/0304-3886\(89\)90028-4](https://doi.org/10.1016/0304-3886(89)90028-4).
- [47] M.B. Mayr, S.A. Barringer, Corona compared with triboelectric charging for electronic powder coating, *J. Food Sci.* 71 (2006), <https://doi.org/10.1111/J.1750-3841.2006.00024.X>.
- [48] J.H. Anderson, A Comparison of Experimental Data and Model Predictions for Tribocharging of Two-Component Electrophotographic Developers, n.d. <http://www.imaging.org/site/PDFS/Papers/1997/RP-0-68/2292.pdf> (accessed July 28, 2022).
- [49] L.J. Tan, W. Zhu, K. Zhou, Recent progress on polymer materials for additive manufacturing, *Adv. Funct. Mater.* 30 (2020) 2003062, <https://doi.org/10.1002/ADFM.202003062>.
- [50] M. Marschall, C. Heintges, M. Schmidt, Influence of flow aid additives on optical properties of polyamide for laser-based powder bed fusion, *Procedia CIRP* 111 (2022) 51–54, <https://doi.org/10.1016/J.PROCIR.2022.08.114>.
- [51] J. Schmidt, M.A. Dechet, J.S. Gómez Bonilla, N. Hesse, A. Bück, W. Peukert, Characterization of Polymer Powders for Selective Laser Sintering, (2019). <https://doi.org/10.26153/TSW/17314>.
- [52] F. Papadopoulos, M. Spinelli, S. Valente, L. Foroni, C. Orrico, F. Alviano, G. Pasquinelli, Common tasks in microscopic and ultrastructural image analysis using ImageJ, *Ultra Pathol.* 31 (2007) 401–407, <https://doi.org/10.1080/01913120701719189>.
- [53] L. Nichele, V. Persichetti, M. Lucidi, G. Cincotti, Quantitative evaluation of ImageJ thresholding algorithms for microbial cell counting, *OSA Contin.* 3 (2020) 1417, <https://doi.org/10.1364/OSAC.393971>.
- [54] N. Hesse, M.A. Dechet, J.S.G. Bonilla, C. Lübbert, S. Roth, A. Bück, J. Schmidt, W. Peukert, Analysis of tribo-charging during powder spreading in selective laser sintering: Assessment of polyamide 12 powder ageing effects on charging behavior, *Polym. (Basel)* 11 (2019), <https://doi.org/10.3390/polym11040609>.
- [55] R.H. Epping, A. Kuettner, Free air beam in an electric field for determination of the electrostatic charge of powders between 1 and 200 μm , *J. Electro* 55 (2002) 279–288, [https://doi.org/10.1016/S0304-3886\(01\)00210-8](https://doi.org/10.1016/S0304-3886(01)00210-8).
- [56] J.W. Hovick, J.C. Poler, Misconceptions in sign conventions: flipping the electric dipole moment, *J. Chem. Educ.* 82 (2005) 889, <https://doi.org/10.1021/ED082P889>.
- [57] T.W. Dakin, Breakdown of gases in uniform fields, Paschen curves for nitrogen, air and sulphur-hexafluoride, *Electra* 32 (1974) 64–70.
- [58] A. Cserátöny-Hoffer, Über den mechanismus des polaritätseffektes in der durchschlagsspannung von gasen, *Period. Polytech. Electr. Eng. (Arch.)* 5 (1961) 357–372.
- [59] A.G. Bailey, Charging of Solids and Powders, *J. Electro* 30 (1993) 167–180, [https://doi.org/10.1016/0304-3886\(93\)90072-F](https://doi.org/10.1016/0304-3886(93)90072-F).
- [60] J.P. Kruth, X. Wang, T. Laoui, L. Froyen, Lasers and materials in selective laser sintering, *Assem. Autom.* 23 (2003) 357–371, <https://doi.org/10.1108/01445150310698652/FULL/XML>.
- [61] T. Tanigaki, K. Sato, Z. Akase, S. Aizawa, H. Soon Park, T. Matsuda, Y. Murakami, D. Shindo, H. Kawase, Split-illumination electron holography for improved evaluation of electrostatic potential associated with electrophotography, *Appl. Phys. Lett.* 104 (2014), <https://doi.org/10.1063/1.4869830>.
- [62] M.A. Dechet, J.S. Gómez Bonilla, M. Grünwald, K. Popp, J. Rudloff, M. Lang, J. Schmidt, A novel, precipitated polybutylene terephthalate feedstock material for powder bed fusion of polymers (PBF): material development and initial PBF processability, *Mater. Des.* 197 (2021), 109265, <https://doi.org/10.1016/J.MATDES.2020.109265>.

4.2 Enhancing Powder Deposition Efficiency by Reducing Interparticle Attraction Forces

Targeted vibration excitation for increasing the powder deposition efficiency in electrophotographic powder application for Laser-based Powder Bed Fusion of polymers

Published in *Procedia CIRP* 111 (2022), 55-60

Sebastian-Paul Kopp^{a-c,*}, Vadim Medvedev^a, Stephan Roth^{a-c}

^a Bayerisches Laserzentrum GmbH, 91052 Erlangen, Germany

^b Collaborative Research Center (CRC) 814 “Additive Manufacturing”, 91058 Erlangen, Germany

^c Erlangen Graduate School in Advanced Optical Technologies (SAOT), 91052 Erlangen, Germany

*Corresponding author.

Tel.: +49-9131-97790-27; E-mail address: s-p.kopp@blz.org

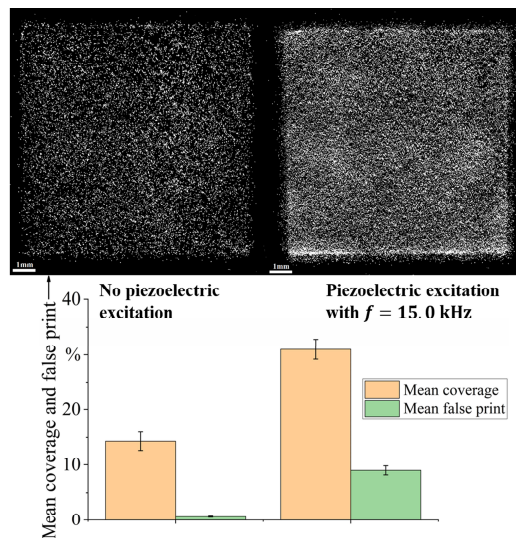


Figure 15: Influence of vibration excitation on the powder deposition result in EPA-PBF-LB/P.

As demonstrated in section 4.1, achieving a homogeneous and reproducible particle charging is crucial for successful EPA. However, EPA with contactless powder deposition requires the detachment of charged particles from the surface of the photoconductor. For this detachment step, the electric field force on the charged powder particles is insufficient to enable efficient

powder deposition. Thus, in this study reducing the strong interparticle attraction forces between the powder particles and the photoconductor is found to be highly beneficial for improving powder deposition efficiency of EPA (cf. Figure 15). Since these attraction forces, in particular the van der Waals force, are strongly dependent on the distance between the particles and the photoconductor, vibration excitation is utilized to increase this distance. This allows the electric field force to become dominant for determining the trajectories of the particles. It is important to note that the local distribution of the direction and strength of the electric deposition field plays an important role for the homogeneity, geometrical accuracy and coverage of the deposited powder layer and is therefore investigated in section 4.3.

Highlights:

- Understanding of the influence of interparticle attraction forces on the powder deposition performance in terms of layer coverage and geometric accuracy
- Strong dependence between the vibrational modes of the mechanical system excited by piezoelectric excitation and increase in powder deposition efficiency of EPA
- Highest increase in deposition efficiency in case of piezoelectric excitation close to resonance frequencies of the mechanical system
- Highest impact of the vibration excitation on deposition result when combined with electric deposition field

12th CIRP Conference on Photonic Technologies [LANE 2022], 4-8 September 2022, Fürth, Germany

Targeted vibration excitation for increasing the powder deposition efficiency in electrophotographic powder application for Laser-based Powder Bed Fusion of polymers

Sebastian-Paul Kopp^{a-c*}, Vadim Medvedev^a, Stephan Roth^{a-c}

^a*Bayerisches Laserzentrum GmbH (blz), Konrad-Zuse-Straße 2-6, 91052 Erlangen, Germany*

^b*Collaborative Research Center 814 – Additive Manufacturing, Am Weichselgarten 9, 91058 Erlangen Germany*

^c*Erlangen Graduate School in Advanced Optical Technologies (SAOT), Paul Gordan Straße 6, 91052 Erlangen, Germany*

* Corresponding author. Tel.: +49-9131-97790-27; fax: +49-9131-97790-11. E-mail address: s-p.kopp@blz.org

Abstract

High efficiency in terms of powder consumption and the ability to generate multi-material parts using additive manufacturing are key features of the electrophotographic powder application for laser-based powder bed fusion of polymers (PBF-LB/P). The reliable deposition of powder particles onto the build platform is one decisive process step. The aim is to achieve a high degree of coverage and, at the same time, maintain an accurate contour of the deposited powder layer.

In addition to the use of a suitable electrical transfer field, which has already been investigated, targeted vibration excitation offers enormous potential for improvement. For this purpose, a mechanical simulation model is set up in this study, which is subsequently validated experimentally. By using the knowledge gained from the simulation, for example with regard to suitable vibration modes, the powder deposition has been significantly improved.

© 2022 The Authors. Published by Elsevier B.V.

This is an open access article under the CC BY-NC-ND license (<https://creativecommons.org/licenses/by-nc-nd/4.0>)

Peer-review under responsibility of the international review committee of the 12th CIRP Conference on Photonic Technologies [LANE 2022]

Keywords: laser-based powder bed fusion; electrophotography; vibration excitation; additive manufacturing; interparticle forces

1. Introduction

Owing to their inherent flexibility and efficiency, additive manufacturing (AM) processes are of great interest for generating highly complex parts [1]. At this, polymer AM technologies, such as laser-based powder bed fusion of polymers (PBF-LB/P), have gained significant influence in recent years, especially in medical, aerospace and automotive industries [2–4].

However, conventional PBF-LB/P employs a layer-by-layer manufacturing manner using doctor blade or roller-based powder application processes [5]. They do not allow to selectively as well as precisely adapt the powder composition and material distribution within a powder layer and thus render

the generation of products with distributed functional properties or even multi-material-parts impossible [6].

A promising approach in order to overcome the aforementioned deficiencies of conventional powder application methods is the usage of electrophotographic powder application (EPA) [7,8]. EPA can be divided into six main process steps [9–11]. In step one the powder and a photoconductive plate (PCP, aluminum plate coated with photoconductive material) are homogeneously charged [12–14]. In step two a latent charge pattern is generated on the PCP by selective illumination. In step three charged powder particles are attracted towards the PCP due to electrostatic forces, which is the so-called development step. In step four the PCP is laterally moved to the build chamber and the powder

particles are deposited onto the build platform, which is located inside the build chamber. In step five a laser beam illuminates the deposited powder particles in order to fuse them. Finally, in step six the PCP is cleaned.

Especially the reliable and reproducible deposition of powder particles onto the build platform leading to dimensionally accurate, homogeneously distributed and highly covered powder layers still needs to be further improved [9,10]. In [11] a significant increase of the powder deposition efficiency could be achieved by using a specially designed transfer frame for adapting and controlling the electric transfer field. It has been shown that by tailoring the spatial electric field distribution of the electric transfer field both the dimensional accuracy as well as the coverage of the deposited powder layer can be improved.

In the context of EPA for PBF-LB/P van der Waals (vdW) forces on the one hand cause the powder particles to very strongly adhere to each other even in case of opposite electrostatic charging. On the other side, vdW forces also lead to a very strong attraction between powder particles and the PCP. Thus, both effects reduce the efficiency of powder deposition since they counteract the electrostatic forces applied by the electric transfer field for powder deposition. From [15,16] it is known that vdW forces occur due to fluctuations in the charge density of molecules. However, they vanish very quickly with increasing distance r between two molecules. Simplified, they exhibit an inverse dependence on the sixth power of the distance [17,18]. Therefore, increasing the distance between powder particles would decrease the vdW attraction forces, which counteract the electrostatic forces applied for powder deposition. For this purpose, in [11] a mechanical excitation caused by a rapid acceleration of the lateral axis has been tested. The results indicate that adapting and controlling the electric transfer field in combination with a mechanical excitation offers an even greater potential for improving the powder deposition. These findings fit well with results obtained in [19], where a piezoelectric excitation system was applied in order to assist the dust particle removal on solar panels in Martian or Lunar surface environments. Although no electric transfer field was applied in the latter case, a mechanical excitation was used in both [11] and [19] to increase the distance between the particles and thus reduce the vdW attractive force. In contrast to axis-induced mechanical excitation, piezoelectric excitation offers a variety of advantages such as adjustable vibration shapes and frequencies [20], making it particularly suitable for its application in EPA.

The aim of this paper is to investigate the potential of a piezo-induced mechanical excitation for EPA in PBF-LB/P in order to improve the dimensional accuracy and degree of coverage of the deposited powder layers. For this purpose, first a modal analysis of the mechanical system is conducted in order to gain a better understanding of its mechanical performance under various excitation conditions. Moreover, this allows to identify particularly advantageous vibration modes for EPA in advance. More specifically, vibration modes which provide a preferably strong acceleration (by excitation at an eigenfrequency (cf. 2.1)) on the powder particles in the desired direction of deposition while keeping the lateral acceleration as low as possible are of special interest. Finally,

EPA with piezo-induced vibration excitation is experimentally investigated with respect to dimensional accuracy and degree of coverage of the deposited powder layers based on the findings of the simulative modal analysis.

2. Materials and methods

2.1. Simulative modal analysis

The simulative modal analysis was conducted using the well-established solid mechanics interface of COMSOL Multiphysics 5.2a, which is based on a finite element analysis (FEA) with various numerical solvers [21]. Mechanical systems are known to exhibit a very strong response with a relatively large amplitude inherently accompanied by strong accelerations when periodically excited with a certain system-dependent frequency, the so-called eigenfrequency [22]. It is important to mention that mechanical systems usually have a multitude of eigenfrequencies which correlate with their respective patterns of motion – their eigenmodes [23]. When excited with a force, which oscillates at a certain frequency (e. g. the eigenfrequency), the entire mechanical system will also begin to oscillate at that frequency resulting in accelerations at each oscillating point of the mechanical system. The PCP as part of the oscillating mechanical system and thus also the powder particles, which directly adhere to the bottom surface of the PCP, are therefore subject to the accelerations caused by the oscillating force. As already discussed, the accelerations caused by the oscillating force are particularly strong in case of the force oscillating at one of the eigenfrequencies of the mechanical system. The design of the simulation model, which is based on the actual experimental setup, is shown in Fig. 1, with the entire mechanical system in the model made of aluminum.

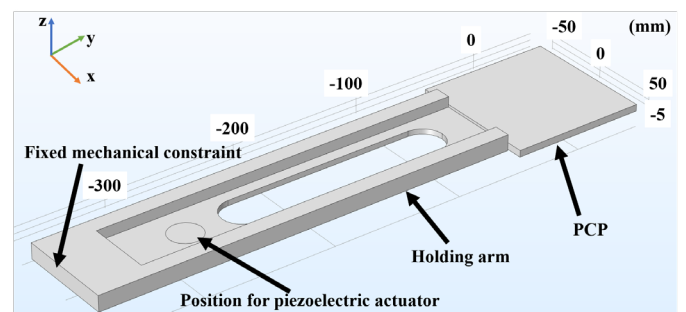


Fig. 1. Design of the simulation model for modal analysis.

Except for the 100 μm thick vapor-deposited photoconductive arsenic triselenide (As_2Se_3) layer at the bottom surface of the PCP and the piezoelectric actuator itself, the mechanical system is also entirely made of aluminum. The backside of the holding arm is modelled as a fixed mechanical constraint, which also corresponds to the mounting of the holding arm in the experimental setup. However, the remaining parts of the simulation model shown in Fig. 1 are free from boundary conditions. In order to account for the mass of the piezoelectric actuator and its mounting, an additional mass of 0.5 kg is added to the position for the piezoelectric actuator. The

dynamic vibration excitation of the actuator is finally introduced using a dynamic force impacting via boundary load at the position for the piezoelectric actuator. At this, the dynamic force can generally be described using the expression:

$$F_z(t) = A \cdot \sin(2\pi ft) \quad (1)$$

where F_z is an oscillating load with amplitude A , frequency f and time duration t . The simulations were conducted for a duration $0 \leq t \leq 0.5$ s. From a practical point of view, it is not necessary to simulate longer durations since the powder deposition almost happens instantaneously when the electric transfer field is applied. Therefore, the duration for which a decrease of vdW attraction forces by applying a piezo-induced mechanical excitation is beneficial, is also very short.

For improving the powder deposition efficiency by increasing the interparticle distance and therefore reducing the vdW attraction forces it is not sufficient to analyze the overall acceleration, which occurs on the bottom surface of the PCP due to vibration excitation. In fact, a spatially resolved determination of the caused acceleration is more reasonable. However, the number of evaluation points should be kept at a low level in order to save computation time. Fig. 2 illustrates five defined point probes for the simulative analysis of the spatially resolved acceleration.

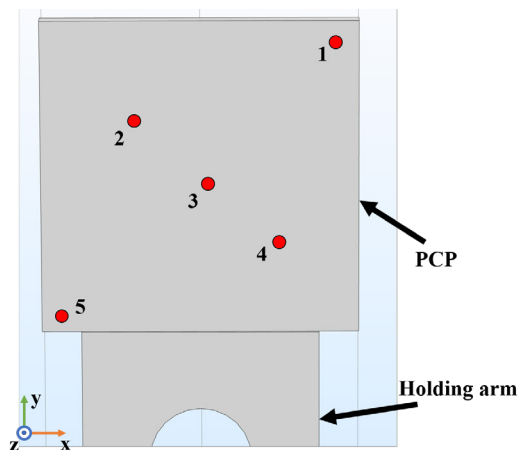


Fig. 2. Positions of the point probes on the bottom surface of the PCP: 1 – top right, 2 – top left shifted, 3 – central, 4 – bottom right shifted, 5 – bottom left.

Utilizing symmetry effects of the square PCP, five representative points are arranged in a way such that the vibration excitation-caused acceleration of powder particles adhering to the bottom surface of the PCP can be estimated. The knowledge gained from the simulative modal analysis is used to predefine particularly suitable vibration frequency ranges for the relatively time-intensive experimental investigations.

2.2. Experimental setup

The two decisive parts of the experimental setup are the development chamber on the one hand and the build chamber on the other. While the process steps (cf. 1) one, two, three and six take place in the development chamber, the steps four and

five are carried out in the build chamber. For moving the holding arm together with the PCP, a positioning system consisting of a direct-drive linear actuator as x-axis and a lift stage as z-axis (both Aerotech Inc., USA) is applied. For high-voltage supply a THQ series (hivolt.de GmbH & Co. KG, Germany) high-voltage power supply is used. In the context of this paper, polyamide PA12 powder (PA2200, EOS GmbH, Germany) with $d_{50} = 55.9 \mu\text{m}$ was charged in an electric charging field with an electric field strength of $\vec{E}_{\text{charging}} \approx 167 \text{ kV/m}$. The electric field strength for powder development was set to $\vec{E}_{\text{develop}} \approx -1077 \text{ kV/m}$ and for powder deposition to $\vec{E}_{\text{deposit}} \approx 400 \text{ kV/m}$. The parameters were adapted from [10,11] with focus on the identification of effects and improvements caused by the various investigated piezoelectric vibration excitations. The powder application unit consisting of the holding arm, which is connected to the positioning system, the PCP and a piezoelectric actuator, is shown in Fig. 3.

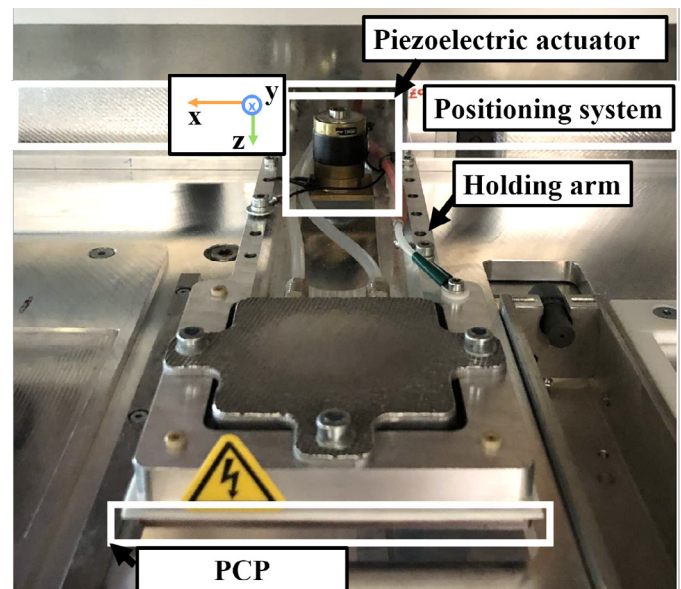


Fig. 3. Detail view of the powder application unit.

For piezoelectric excitation, a signal generator TG1010A (Thurlby Thandar Instruments, UK) is used to generate various types of electrical waveforms over a wide range of frequencies. The amplitude of the electrical signals was set to a peak-to-peak voltage of $U_{p-p} = 8 V_{p-p}$. A Pst 1000/16/20 VS25 (Piezosystem Jena GmbH, Germany) is used as piezoelectric actuator. To amplify the signal of the function generator to sufficiently high input values of the piezoelectric actuator, an analog power amplifier LE 1000/035 (Piezosystem Jena GmbH, Germany) is utilized with an amplification factor of 100.

2.3. Image analysis

For image acquisition, a 12-megapixel f/1.8 (Samsung Electronics Co., Ltd., South Korea) camera was used. The images of the deposited powder patterns were processed with the software ImageJ in order to determine the corresponding coverage and false print values. For this purpose, the images of the deposited powder patterns were split into sections for

investigating the false print (FP) and coverage (C), respectively, as shown in Fig. 4.

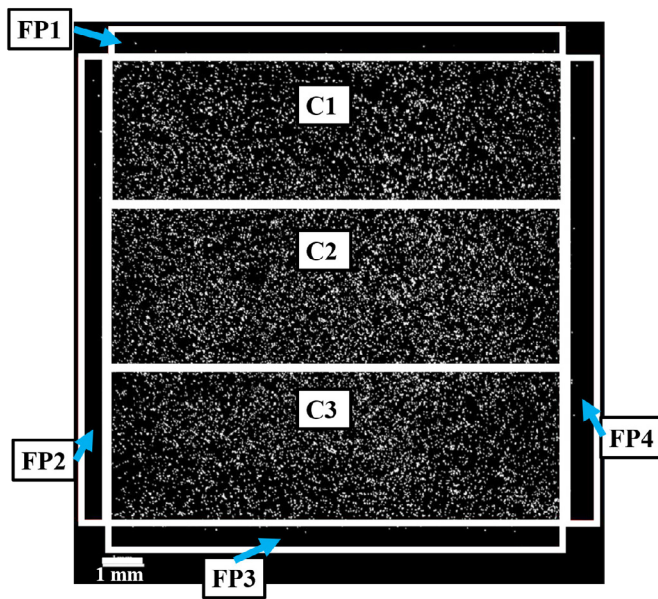


Fig. 4. Sections for coverage (C1-3) and false print (FP1-4) analysis.

After converting the photos to 8-bit grayscale images, the Huang2 [24,25] thresholding method was employed in order to convert them to binary images. By comparing the number of black and white pixels within each of the respective sections (cf. Fig. 4), the false print as well as the coverage can be determined. Finally, for each deposited powder pattern on the one hand the mean coverage and on the other hand the mean false print can be calculated, both with standard deviation.

3. Results and discussion

The simulated average accelerations in longitudinal (z-) and lateral (x-) direction, exemplary depicted for the first five simulated eigenfrequencies of the mechanical simulation model, are visualized in Fig. 5 and Fig. 6. At this, the acceleration in x-direction is chosen as an indicator for the lateral acceleration behavior. When comparing the longitudinal acceleration (Fig. 5) with the lateral acceleration (Fig. 6), it becomes apparent that an increase in longitudinal acceleration is inevitably accompanied by increasing lateral acceleration. For example, an increase of the longitudinal acceleration for point probe 1 (Fig. 5) from $\approx 60 \text{ mm/s}^2$ at $f = 318.2 \text{ Hz}$ to $\approx 135 \text{ mm/s}^2$ at $f = 1949.2 \text{ Hz}$ correlates with an increase of the lateral acceleration for point probe 1 (Fig. 6) from $\approx 3.3 \text{ mm/s}^2$ at $f = 318.2 \text{ Hz}$ to $\approx 6.2 \text{ mm/s}^2$ at $f = 1949.2 \text{ Hz}$. This indicates that in general a higher longitudinal acceleration of the powder particles, and therefore an increase in powder deposition efficiency and hence coverage, will also result in a higher degree of false print.

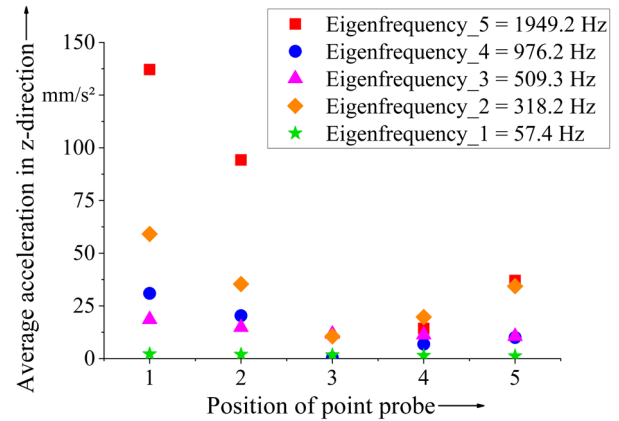


Fig. 5. Simulated average acceleration in z-direction for five selected point probes (cf. Fig. 2): 1 – top right, 2 – top left shifted, 3 – central, 4 – bottom right shifted, 5 – bottom left.

Unlike this relationship between longitudinal and lateral acceleration components, there is no clear trend between excitation frequency and resulting accelerations. Therefore, the individual eigenfrequencies have to be examined in terms of their suitability for EPA.

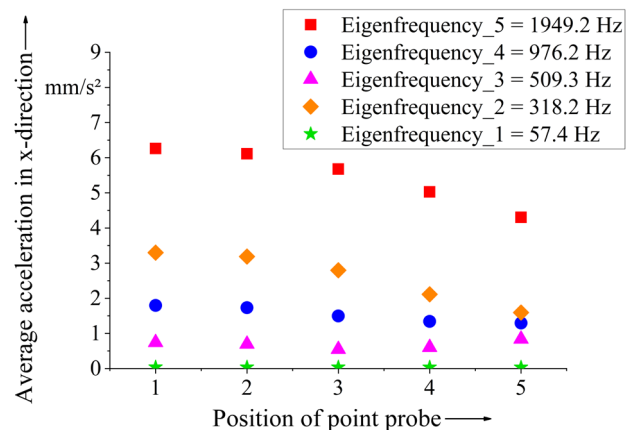


Fig. 6. Simulated average acceleration in x-direction for five selected point probes (cf. Fig. 2): 1 – top right, 2 – top left shifted, 3 – central, 4 – bottom right shifted, 5 – bottom left.

Although slight differences between the simulation model and the experimental setup, e. g. in terms of geometries, joints or materials, cannot be excluded, there is good agreement between the simulation and experimental results. In Fig. 7 on the one hand the simulation result of the total acceleration in z-direction for the simulated eigenfrequency of $f = 10.5 \text{ kHz}$ is shown. On the other hand, the experimental result of powder deposition (PA12), conducted with the same excitation frequency, is visualized. It can be seen that areas with high acceleration values, both for negative (blue) and positive (red) acceleration values, also show higher degrees of coverage in the powder deposition experiment. Thus, especially in the corners as well as two circular areas, which are located below the center of the square, larger values of both acceleration as well as coverage can be observed. This behavior can be explained by the initially introduced hypothesis of decreasing vdW attraction forces due to a piezo-induced acceleration. In

order to enhance the contrast of the correlation between the simulated longitudinal acceleration result (Fig. 7 left) and the experimental result of powder deposition (Fig. 7 right), in this case no electric field for powder deposition was applied. Therefore, the deposited powder pattern (Fig. 7 right) is mainly directly caused by the longitudinal acceleration acting on the powder particles and the reduction of attractive vdW forces, both induced by the piezoelectric excitation.

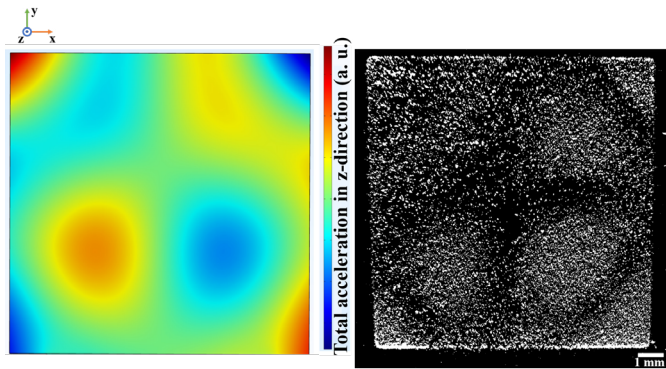


Fig. 7. Correlation between simulated total acceleration in z-direction (left) and the experimental result of powder deposition of PA12 (right), both with an excitation frequency / eigenfrequency $f = 10.5$ kHz (sinusoidal), $E_{\text{charging}} \approx 167$ kV/m, $E_{\text{develop}} \approx -1077$ kV/m and $E_{\text{deposit}} \approx 0$ kV/m.

A particularly suitable eigenfrequency was found at $f = 15.0$ kHz. By applying a piezoelectric vibration excitation at this frequency, the mean coverage was improved from $\approx 15\%$ without piezoelectric excitation to $\approx 30\%$ (cf. Fig. 8).

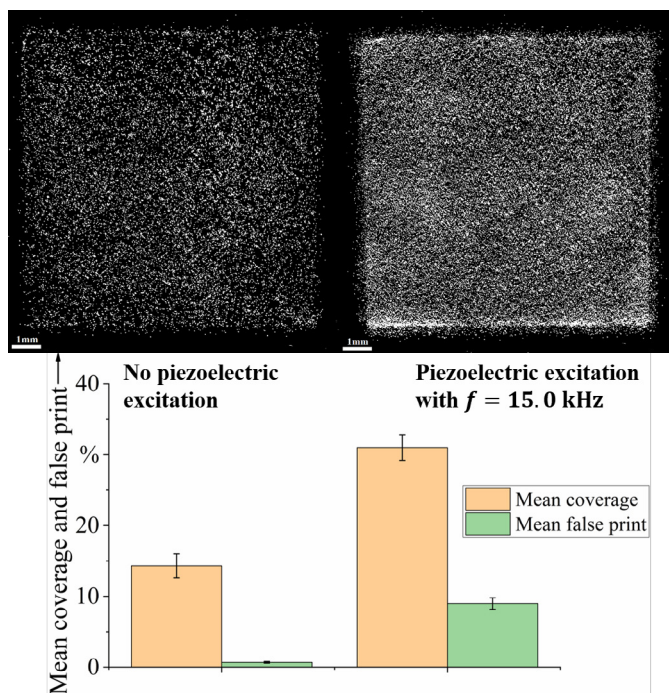


Fig. 8. Comparison between experimental result of powder deposition of PA12 without piezoelectric excitation (left) and with applied piezoelectric excitation (right) with an excitation frequency / eigenfrequency $f = 15.0$ kHz (sinusoidal), $E_{\text{charging}} \approx 167$ kV/m, $E_{\text{develop}} \approx -1077$ kV/m and $E_{\text{deposit}} \approx 400$ kV/m.

However, at the same time the mean false print increased from $\approx 1\%$ without piezoelectric excitation to $\approx 8\%$ with applied piezoelectric excitation at $f = 15.0$ kHz, which can be attributed to the aforementioned unavoidable increase of the lateral acceleration component when enhancing the longitudinal one.

Finally, by applying the particularly suitable excitation frequency of $f = 15.0$ kHz and increasing the electric field strength for powder deposition to $E_{\text{deposit}} \approx 900$ kV/m, the result shown in Fig. 9 was achieved. Here, the coverage is $98.78\% \pm 0.85\%$ and the false print is $4.52\% \pm 0.21\%$. For achieving this result, the electric field strength for powder deposition was increased to $E_{\text{deposit}} \approx 900$ kV/m in order to reach a preferably high coverage. Unlike the previous studies, which were focused on the identification of effects and improvements caused by different piezoelectric vibration excitations, the aim of this experiment was to achieve a preferably high coverage. Interestingly, the increased electric field strength for powder deposition resulted in a reduction of false print (cf. Fig. 8 (right) and Fig. 9). This can be attributed to the fact that the vdW forces, which counteract the electrostatic forces applied by the electric transfer field for powder deposition (cf. 1), are reduced due to the piezoelectric excitation. Therefore, the electrostatic forces become dominant for determining the trajectories of the particles. Since the electric field for powder deposition is aligned perpendicularly between PCP and build platform [11], the particles increasingly follow the straight trajectory determined by the straight electric field lines as the electric field strength increases.

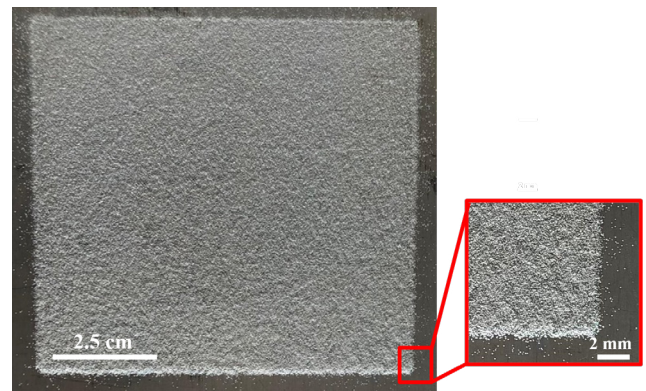


Fig. 9. Final powder deposition result with applied piezoelectric excitation with an excitation frequency / eigenfrequency $f = 15.0$ kHz (sinusoidal), $E_{\text{charging}} \approx 167$ kV/m, $E_{\text{develop}} \approx -1077$ kV/m and $E_{\text{deposit}} \approx 900$ kV/m.

4. Conclusion

Achieving a reliable and reproducible deposition of powder particles onto the build platform leading to dimensionally accurate, homogeneously distributed and highly covered powder layers is one of the key factors for a successful implementation of electrophotographic powder application in laser-based powder bed fusion of polymers. In this work, a method based on a targeted vibration excitation by applying a piezoelectric actuator for improving the powder deposition efficiency was examined. It was shown that a piezoelectric vibration excitation allows the vdW attraction forces to be efficiently reduced in order to enable the applied electric field

forces to determine the motion of the powder particles. For finding particularly suitable excitation frequencies, a simulation model for eigenfrequency studies was established and validated. Mechanical systems are known to exhibit a very strong response with a relatively large amplitude inherently accompanied by strong accelerations when periodically excited at their respective eigenfrequency. The simulation as well as experimental analysis revealed that an increase of the longitudinal acceleration for enhancing the powder deposition efficiency is inevitably accompanied with an increase of the lateral acceleration and therefore false print. However, this effect can be compensated by increasing the electric field strength for powder deposition.

Acknowledgements

The authors gratefully acknowledge funding of the Collaborative Research Center 814 (CRC 814), sub-project B6, by the German Research Foundation (DFG) and of the Erlangen Graduate School in Advanced Optical Technologies (SAOT) by the Bavarian State Ministry for Science and Art.

References

- [1] Huang SH, Liu P, Mokasdar A, Hou L. Additive manufacturing and its societal impact: A literature review. *Int J Adv Manuf Technol* 2013;67:1191–203. <https://doi.org/10.1007/s00170-012-4558-5>.
- [2] Tan LJ, Zhu W, Zhou K. Recent Progress on Polymer Materials for Additive Manufacturing. *Adv Funct Mater* 2020;30:2003062. <https://doi.org/10.1002/ADFM.202003062>.
- [3] Fasel U, Keidel D, Baumann L, Cavolina G, Eichenhofer M, Ermanni P. Composite additive manufacturing of morphing aerospace structures. *Manuf Lett* 2020;23:85–8. <https://doi.org/10.1016/J.MFGLET.2019.12.004>.
- [4] Delic M, Evers DR. The effect of additive manufacturing adoption on supply chain flexibility and performance: An empirical analysis from the automotive industry. *Int J Prod Econ* 2020;228. <https://doi.org/10.1016/J.IJPE.2020.107689>.
- [5] Haeri S, Wang Y, Ghita O, Sun J. Discrete element simulation and experimental study of powder spreading process in additive manufacturing. *Powder Technol* 2017;306:45–54. <https://doi.org/10.1016/J.POWTEC.2016.11.002>.
- [6] Wei C, Li L. Recent progress and scientific challenges in multi-material additive manufacturing via laser-based powder bed fusion. *Virtual Phys Prototyp* 2021;16:347–71. <https://doi.org/10.1080/17452759.2021.1928520>.
- [7] Li Y, Feng Z, Hao L, Huang L, Xin C, Wang Y, et al. A Review on Functionally Graded Materials and Structures via Additive Manufacturing: From Multi-Scale Design to Versatile Functional Properties. *Adv Mater Technol* 2020;5:1900981. <https://doi.org/https://doi.org/10.1002/admt.201900981>.
- [8] Schneck M, Horn M, Schmitt M, Seidel C, Schlick G, Reinhart G. Review on additive hybrid- and multi-material-manufacturing of metals by powder bed fusion: state of technology and development potential. *Prog Addit Manuf* 2021;6:881–94. <https://doi.org/10.1007/s40964-021-00205-2>.
- [9] Kumar A V., Dutta A, Fay JE. Electrophotographic printing of part and binder powders. *Rapid Prototyp J* 2004;10:7–13. <https://doi.org/10.1108/13552540410512480/FULL/XML>.
- [10] Stichel T, Brachmann C, Rath M, Dechet MA, Schmidt J, Peukert W, et al. Electrophotographic Multilayer Powder Pattern Deposition for Additive Manufacturing. *Jom* 2020;72:1366–75. <https://doi.org/10.1007/s11837-019-03965-z>.
- [11] Kopp SP, Stichel T, Roth S, Schmidt M. Investigation of the electrophotographic powder deposition through a transfer grid for efficient additive manufacturing. *Procedia CIRP* 2020;94:122–7. <https://doi.org/10.1016/j.procir.2020.09.024>.
- [12] Pai DM, Springett BE. Physics of electrophotography. *Rev Mod Phys* 1993;65:163. <https://doi.org/10.1103/RevModPhys.65.163>.
- [13] Shahin MM. Nature of Charge Carriers in Negative Coronas. *Appl Opt* Vol 8, Issue S1, Pp 106-110 1969;8:106–10. <https://doi.org/10.1364/AO.8.S1.000106>.
- [14] Matsusaka S, Masuda H. Electrostatics of particles. *Adv Powder Technol* 2003;14:143–66. <https://doi.org/10.1163/156855203763593958>.
- [15] Particle adhesion theory and experiment. *Adv Colloid Interface Sci* 1967;1:111–239. [https://doi.org/10.1016/0001-8686\(67\)80004-6](https://doi.org/10.1016/0001-8686(67)80004-6).
- [16] Gady B, Schleef D, Reifenberger R, Rimai D, DeMejo L. Identification of electrostatic and van der Waals interaction forces between a micrometer-size sphere and a flat substrate. *Phys Rev B* 1996;53:8065. <https://doi.org/10.1103/PhysRevB.53.8065>.
- [17] Castellanos A. The relationship between attractive interparticle forces and bulk behaviour in dry and uncharged fine powders. *Adv Phys* 2005;54:263–376. <https://doi.org/10.1080/17461390500402657>.
- [18] Dzyaloshinskii IE, Lifshitz EM, Pitaevskii LP. The general theory of van der Waals forces. *Adv Phys* 1961;10:165–209. <https://doi.org/10.1080/00018736100101281>.
- [19] Williams RB, Tanimoto R, Simonyan A, Fuerstenau S. Vibration characterization of self-cleaning solar panels with piezoceramic actuation. *Collect Tech Pap - AIAA/ASME/ASCE/AHS/ASC Struct Struct Dyn Mater Conf* 2007;1:512–20. <https://doi.org/10.2514/6.2007-1746>.
- [20] Mishra S, Unnikrishnan L, Nayak SK, Mohanty S. Advances in Piezoelectric Polymer Composites for Energy Harvesting Applications: A Systematic Review. *Macromol Mater Eng* 2019;304. <https://doi.org/10.1002/MAME.201800463>.
- [21] Sharma P, Singh R, Hussain M. On modal analysis of axially functionally graded material beam under hygrothermal effect. *Proc Inst Mech Eng Part C J Mech Eng Sci* 2020;234:1085–101. <https://doi.org/10.1177/0954406219888234>.
- [22] Billah KY, Scanlan RH. Resonance, Tacoma Narrows bridge failure, and undergraduate physics textbooks. *Am J Phys* 1998;59:118. <https://doi.org/10.1119/1.16590>.
- [23] Walker J, Halliday D, Resnick R. *Fundamentals of physics*. Wiley; 2011.
- [24] Papadopoulos F, Spinelli M, Valente S, Foroni L, Orrico C, Alviano F, et al. Common tasks in microscopic and ultrastructural image analysis using ImageJ. *Ultrastruct Pathol* 2007;31:401–7. <https://doi.org/10.1080/01913120701719189>.
- [25] Nichele L, Persichetti V, Lucidi M, Cincotti G. Quantitative evaluation of ImageJ thresholding algorithms for microbial cell counting. *OSA Contin* 2020;3:1417. <https://doi.org/10.1364/OSAC.393971>.

4.3 Forming of the Electric Deposition Field

Investigation of the electrophotographic powder deposition through a transfer grid for efficient additive manufacturing

Published in Procedia CIRP 94 (2020), 122-127

Sebastian-Paul Kopp^{a,b,c,*}, Thomas Stichel^{a,b}, Stephan Roth^{a,b,c}, Michael Schmidt^{a-d}

^a Bayerisches Laserzentrum GmbH, 91052 Erlangen, Germany

^b Collaborative Research Center (CRC) 814 “Additive Manufacturing”, 91058 Erlangen, Germany

^c Erlangen Graduate School in Advanced Optical Technologies (SAOT), 91052 Erlangen, Germany

^d Friedrich-Alexander-University Erlangen-Nuremberg, Institute of Photonic Technologies (LPT), 91052 Erlangen, Germany

*Corresponding author.

Tel.: +49-9131-97790-27; E-mail address: s-p.kopp@blz.org

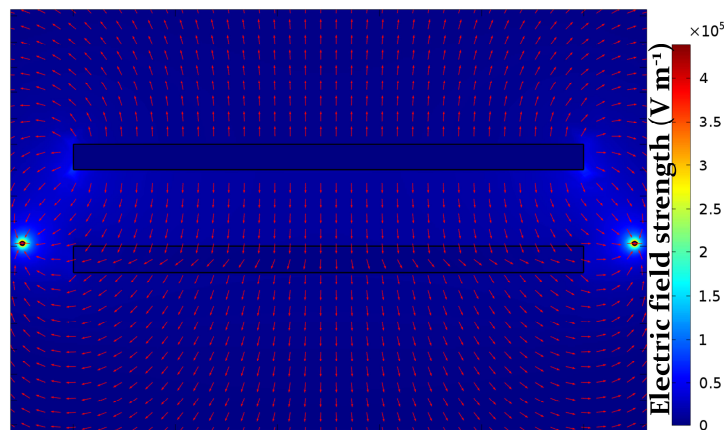


Figure 16: Tailored electric deposition field by using a transfer frame.

After adequate particle charging (cf. section 4.1) and overcoming the strong attraction between the powder particles and the photoconductor (cf. section 4.2), a further crucial aspect for contactless powder deposition is the electric deposition field. It is important to note that due to the low weight of the powder particles, gravitational forces are of minor importance for powder deposition. Rather, the local distribution of the direction and strength of the electric deposition field dominates the particle motion (cf. section 2.2.1 and equation (14)). In this study, the influence of the electric deposition field on the powder deposition result is investigated. Based on

the understanding of this influence, a suitable transfer structure is developed and validated in order to adjust the electric deposition field (cf. Figure 16).

Highlights:

- Understanding of the influence of the electric deposition field on the deposition efficiency of powder particles for EPA-PBF-LB/P in terms of coverage and geometrical accuracy of the deposited layer
- Knowledge of the relationship between shape of the transfer structure, resulting shape of the electric deposition field and powder deposition result
- Identification of a frame-shaped transfer structure as a suitable geometry to obtain a proper local distribution of the electric deposition field strength and direction for EPA-PBF-LB/P

11th CIRP Conference on Photonic Technologies [LANE 2020] on September 7-10, 2020

Investigation of the electrophotographic powder deposition through a transfer grid for efficient additive manufacturing

Sebastian-Paul Kopp^{a,c,d*}, Thomas Stichel^{a,c}, Stephan Roth^{a,c,d}, Michael Schmidt^{a-d}

^a*Bayerisches Laserzentrum GmbH (blz), Konrad-Zuse-Straße 2-6, 91052 Erlangen, Germany*

^b*Institute of Photonic Technologies (LPT), Friedrich-Alexander-Universität Erlangen-Nürnberg, Konrad-Zuse-Straße 3-5, 91052 Erlangen, Germany*

^c*Collaborative Research Center (CRC) 814 “Additive Manufacturing”, 91058 Erlangen, Germany*

^d*Erlangen Graduate School in Advanced Optical Technologies (SAOT), 91052 Erlangen, Germany*

* Corresponding author. Tel.: +49-9131-97790-27; fax: +49-9131-97790-11. E-mail address: s-p.kopp@blz.org

Abstract

Until today, the electrophotographic transfer of toner powders has been applied successfully in common printing technology for many years. Utilizing the electrophotographic principle for the transfer of polymer powders in the context of additive manufacturing can give a variety of advantages like e.g. the possibility of generating multi-material components or a reduced consumption of powder. Here, the multiple depositions of powder particle-layers via electrostatic forces to create 3D objects have turned out to be a major challenge. Therefore, a new strategy based on the usage of a grounded transfer grid is examined. Due to its positioning above the generated layers, it makes the powder deposition independent of the already produced part height. For improving the particle transfer, geometrical properties of the grid are analyzed with respect to their influence on the efficiency of the powder deposition. Here, particular attention is paid to the manipulation of the electric transfer field, which is applied for accelerating the charged powder particles. The aim is to enhance the coverage and dimensional accuracy of the deposited powder layers by finding a new transfer structure.

© 2020 The Authors. Published by Elsevier B.V.

This is an open access article under the CC BY-NC-ND license (<http://creativecommons.org/licenses/by-nc-nd/4.0/>)

Peer-review under responsibility of the Bayerisches Laserzentrum GmbH

Keywords: selective laser melting, electrophotography, polymer powder transfer, multi-material deposition, electric field

1. Introduction

The utilization of additive manufacturing techniques such as selective laser melting of polymer powder enables almost arbitrary design flexibility [1,2]. However, conventional powder application methods do not allow the simultaneous and selective deposition of different materials and thus render the generation of multi-material components impossible [3]. Nevertheless, being able to fabricate multi-material parts by means of additive manufacturing offers a variety of benefits for many different areas such as the medical industry [4].

A promising approach is to use the electrophotographic principle for generating tailored powder layers [5,6]. At this, it becomes apparent that the powder deposition, which must be

reproducible, dimensionally accurate and has to feature a high coverage, remains a major challenge.

Here, the spatial distribution of the electric transfer field, which develops between the photoconductive plate and the respectively applied transfer structure, significantly affects the powder deposition. The influence of an electric field on charged particles is determined by the Coulomb force, which moves the charged particles against the viscous drag air force described by the Stokes law [7]. Depending on the applied charging strategy [8,9], different phenomena lead to the overall charge. In case of the herein presented corona charging, the charge consists of ions as well as induced dipoles, which result from deformation polarization. Apart from that, triboelectric charging merely causes the latter [10].

On the one hand in this paper the manipulation of the electric transfer field by applying different transfer structures is investigated in order to enhance the powder deposition. This is done by employing a simulative analysis of the spatial distribution of the electric transfer field. At this, the simulation allows the evaluation of the ratio between field components, which point into the desired movement direction of the powder particles, and parasitic transversal field components. The latter lead to a distraction of powder particles from their straight movement direction and thus impair the powder deposition.

On the other hand the experimental analysis, which is presented in this paper, is used for validating the simulative results and hence is focused on the behavior of the charged powder particles within the applied electric transfer field. For this purpose the deposited powder layers are studied with respect to their coverage and dimensional accuracy.

The state of the art transfer grid [3] exhibits two major drawbacks. First, the grid wires act as physical barriers at which the powder particles are scattered. Second, these wires introduce substantial transversal field components deflecting the particles from their linear motion. Therefore, a new transfer structure is to be found which does not act as a physical barrier for powder particles being deposited and furthermore features decreased parasitic transversal field components. In order to quantify the ratio between parasitic transversal and the intended longitudinal field component in the direction of particle movement, the spatial field distribution of the transfer grid is first simulated. The thereby obtained quantitative spatial field distribution is subsequently used for designing a new transfer structure which features reduced transversal field components and thus increases the efficiency of the powder deposition. The simulative results are then compared with experimental results utilizing the new transfer structure.

Ultimately, the charge accumulation within the part as a consequence of the multiple depositions of charged powder layers on top of each other also has to be taken into account. That is because the accumulation of charges may lead to a weakening of the electric transfer field [9]. Consequently, this could significantly decrease both the motive forces responsible for the powder transfer and thus the coverage of the deposited powder layers. Therefore, the influence of the part height on the transfer field is simulated.

2. Simulative and experimental investigations

2.1. Methodology

The conducted simulations of the spatial distributions of resulting electric transfer fields for various transfer structures presented in this paper were performed with COMSOL Multiphysics 5.2a. The simulations are based on numerical solutions of Maxwell's equations. Within the conducted simulations the assumption of purely electrostatic processes is made, i.e. excluding any kind of charge flow. This assumption is valid for the investigation of electric transfer fields of different transfer structures because except for the negligibly short (relating to the inertia of the powder particles) duration of the switch-on or switch-off process of the electric transfer field, there is no charge flow present [7]. In case of the analyzed

influence of the part height on the attenuation of the electric transfer field as a matter of fact charge flow might occur within the built part and between the part and surrounding air. However, since the built part consists of dielectric material, this effect most probably is of subordinate importance. Fig. 1 shows the applied layer geometry representing an exemplary test part for the powder deposition both for the simulative as well as experimental examination. Due to comparability with previous work [3], the presented experiments were conducted with a negatively charged powder mixture of 99.0 wt. % of polypropylene PP PD0580 DuPont with a particle size distribution $X_{50} = 113.6 \mu\text{m}$ and 1.0 wt. % of Aerosil (R106, Evonik).

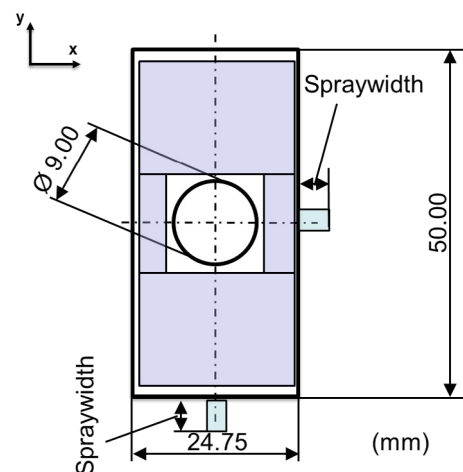


Fig. 1. Utilized test geometry for the simulative and experimental analysis; the four areas for experimental determination of the coverage are colored.

As initially mentioned, the primary quality criteria in the context of powder pattern deposition are reproducibility, dimensional accuracy and a high coverage. The aim is to achieve coverage close to 100 %, which is comparable to conventional powder application methods. Furthermore, the spraywidth should tend to 0 mm for a preferably high dimensional accuracy.

For the experimental analysis regarding coverage and spraywidth the powder is initially charged by applying a distinct powder charge voltage and subsequently developed onto a photoconductive plate [3]. At this, the test geometry depicted in Fig. 1 is used. Hereinafter, an electric transfer field is established between the photoconductive plate and the transfer structure for depositing the powder particles onto the substrate plate.

The determination of the coverage is conducted within the four highlighted areas visualized in Fig. 1. It can be calculated with the number of white pixels n_{white} and the number of black pixels n_{black} using a cut-off threshold of 50 % for the discrimination between white and black pixels as follows:

$$\text{Coverage} = \frac{n_{\text{white}}}{n_{\text{white}} + n_{\text{black}}} 100 \% \quad (1)$$

2.2. Simulative analysis of electric field distributions for different transfer structure geometries

The simulation model for the state of the art transfer grid as well as the transfer frame, which is introduced as a new transfer structure for achieving reduced transversal field components, is visualized in Fig. 2. This transfer frame does not show any physical barrier for the powder particles moving from the photoconductive plate towards the substrate plate anymore. Moreover, due to the absence of grid wires it has reduced parasitic transversal field components. The simulation model is based on the experimental setup, which already has been reported in previous work [3,6].

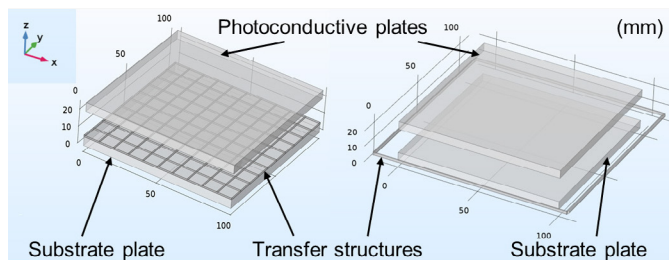


Fig. 2. Simulated transfer structure geometries; grid (left), frame (right).

The simulation setup consists of an aluminum plate representing the photoconductive plate and a polyamide 6 substrate plate on which the powder layers are deposited. Here, the center of the test geometry (cf. Fig. 1) coincides with the center of the substrate plate. Furthermore, the transfer structures are made of copper and are grounded whereas a voltage of 1000 V is assigned to the photoconductive plate. By contrast, no voltage is assigned to the substrate plate enabling the investigation of the influence of the part height on the transfer field. That is possible because the charge of every powder layer is conserved in this way.

Both the transfer grid and the transfer frame are positioned at a z -position directly above the deposited powder layer or the substrate plate in case of the first layer, respectively. In accordance with the state of the art grid [3] a wire diameter of 1 mm with a row spacing of 10 mm and an overall length of 100 mm is chosen for the simulation depicted in Fig. 3. However, it has shown that in case of a transfer frame good results can be achieved with a wire diameter of 1.5 mm and a wire length of 120 mm. This configuration, which is used in the presented paper, gives a reasonable compromise between preferably strong field components of approximately 12500 V/m in negative z -direction and relatively weak parasitic transversal field components of approximately 1500 V/m (cf. Fig. 3). These values are valid when limiting the used area to a square of 25 mm · 25 mm centered in the middle of the photoconductive plate.

Fig. 3 visualizes the spatial distribution of the electric field strength for the used transfer grid along a line directly above the substrate plate at $y = 55$ mm (cf. Fig. 2). This position was chosen for reasons of clarity since here the transversal field components in y -direction cancel out for symmetry reasons within a grid mesh. As opposed to this, the transfer frame was analyzed at $y = 50$ mm since no intermediate grid wires are

present and thus the transversal field components in y -direction cancel out here for symmetry reasons. The mentioned symmetry reasons arise from the fact that at equidistant positions relative to both sides of grid or frame elements, the electric field spreads equally towards these elements and thus cancels out at the center line.

As expected, the grid causes substantial transversal field components, which increase with decreasing distance to the grid wires. The electric field strength in transversal direction reaches up to 25 % of that in z -direction leading to significant spray at the edges of the powder pattern. This is aggravated by the fact that the grid wires serve as physical barriers, which reduce the coverage. Therefore, the maximum coverage with the above-mentioned state of the art transfer grid lies in the range of 70 % [3].

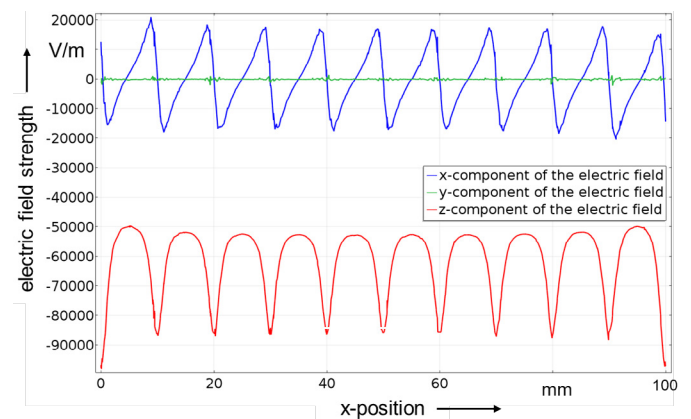


Fig. 3. Simulated electric field strength at $y = 55$ mm directly above the substrate plate in case of a transfer grid.

Since there are no intermediate grid wires present at a transfer frame, it can be expected that in case of the frame the transversal field components are considerably less pronounced than for the transfer grid. In fact, this can be seen in Fig. 4. When limiting the used area to a square of 25 mm · 25 mm centered in the middle of the photoconductive plate (i.e. $37.5 \text{ mm} < x < 62.5 \text{ mm}$ and due to symmetry reasons of the rectangular frame $37.5 \text{ mm} < y < 62.5 \text{ mm}$), the transversal field components can be limited to less than 12 % of those in z -direction. However, because the distance to the framework is maximal in this area, the electric field components in z -direction exhibit a minimum.

Beyond that, the absence of physical barriers should positively influence the achievable coverage. Nevertheless, the electric field strength in z -direction in case of the transfer frame is significantly lower compared to the transfer grid. At this, the experimental analysis has to evince whether the electric field is still strong enough to move the charged particles from the photoconductive plate to the substrate plate.

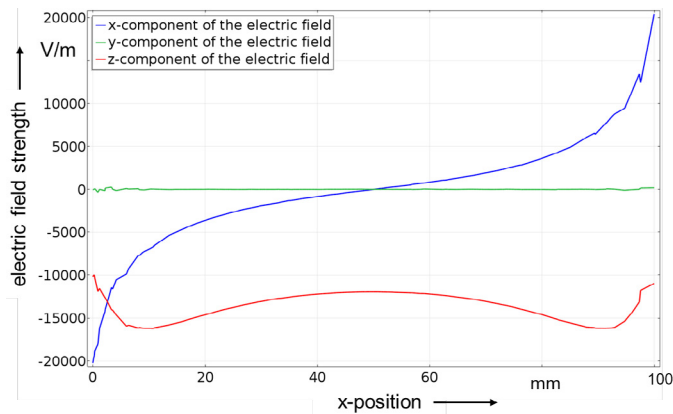


Fig. 4. Simulated electric field strength at $y = 50$ mm directly above the substrate plate in case of a transfer frame.

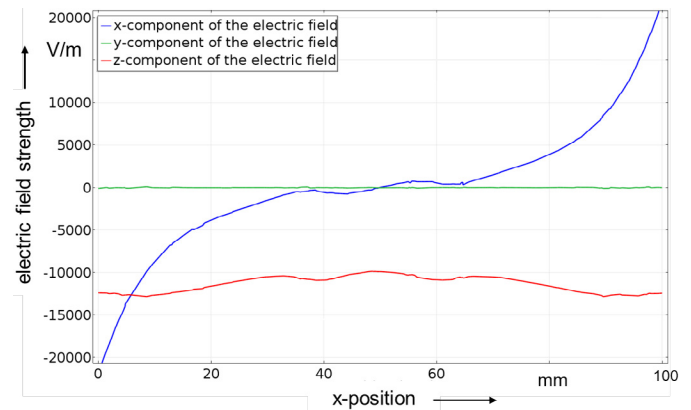


Fig. 5. Simulated electric field strength at $y = 50$ mm directly above a test part with a thickness of 10 mm (100 deposited powder layers) and an accumulated charge of $1.5 \cdot 10^{-10}$ C in case of a transfer frame.

2.3. Simulative analysis of the influence of the part height on the electric transfer field

So far the electric field distribution in case of depositing a powder layer directly onto the substrate plate has been investigated. The simulated electric field distribution only holds true for the first powder layer, though. For including the influence of the part height on the electric transfer field, the accumulation of charges within the part has to be considered. The charge of every single powder layer can be estimated by initially calculating the gravitational force F_g acting on that layer using a density of ca. 1000 kg/m^3 . By knowing the field strength of the electric field E , which is applied for attracting a powder layer to the photoconductive plate during powder development (approx. 660 kV/m) [3], the charge q within a single powder layer can be calculated yielding [7]:

$$q = \frac{F_g}{E} = 1.5 \cdot 10^{-12} \text{ C} \quad (2)$$

Furthermore, for the simulation a particle diameter of $100 \mu\text{m}$ and a relative permittivity of the built part of 2.5 were applied.

According to the Coulomb potential, the potential of a point charge increases with growing charge [7]. Thus, the potential of a part will also increase with growing number of layers due to the accumulation of charges within the part. Since the voltage between two points is defined by their potential difference [11], the voltage between the photoconductive plate and the part surface will therefore decrease with growing number of layers. This results in an attenuation of the electric transfer field. Fig. 5 displays the lateral distribution of electric field strength (in x -direction) directly above 100 powder layers of the test geometry depicted in Fig. 1.

At this, the distance between the part surface and the photoconductive plate is kept constant to 15 mm as is the case with the powder deposition directly to the substrate plate (cf. Fig. 4). Interestingly, according to the simulation, the effect of field attenuation outlined above only weakens the electric field in z -direction by approximately 8 %, which can be compensated by slightly increasing the voltage at the photoconductive plate if necessary.

The small deflections visible in Fig. 5 (contrary to Fig. 4) arise from the fact that there is no potential assigned to the substrate plate whereas the deposited powder layers have a distinct potential originating from their charge and therefore lead to a disturbance of the electric transfer field.

2.4. Experimental results for various transfer structure geometries

The resulting powder layers deposited through a transfer grid and a transfer frame, respectively, can be seen in Fig. 6. However, in case of the transfer frame the electric field strength in z -direction is not sufficient for overcoming the strong adhesive forces like the van der Waals force as long as the powder particles are attached to the photoconductive plate. Only a small mechanical excitation pulse acting on the photoconductive plate, which slightly increases the distance between the single particles and thus decreases the intermolecular interactions, allows the powder particles to follow the electric transfer field.

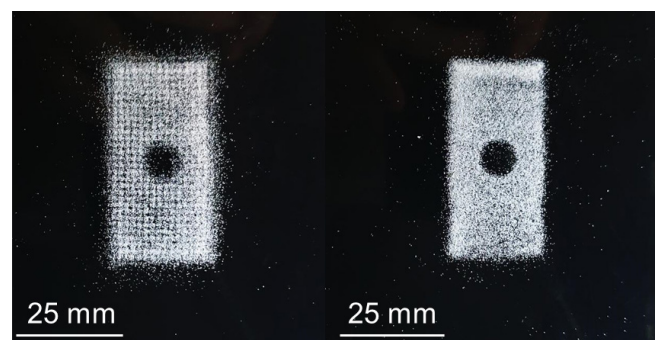


Fig. 6. Single test layers of a powder mixture of 99.0 wt. % PP PD0580 DuPont and 1.0 wt. % Aerosil (R106, Evonik) deposited through a transfer grid (left) and a transfer frame (right).

It is evident from Fig. 6 that the usage of a transfer frame leads to an increased coverage, which is quantitatively depicted in Fig. 7. According to that, the coverage reaches more than 90 % with a distinct reduction in case of a lower powder charge voltage. This behavior can be explained by the relatively weak z -component of the electric transfer field of the transfer frame. By contrast, the powder charging does not have a significant impact on the coverage in case of the grid. For referencing reasons the powder deposition was also conducted without any kind of transfer structure (“blank”). Especially for a transfer voltage of -3.5 kV the coverage values without a transfer structure are comparable to those of the transfer grid. This behavior can be explained by the fact that in the experimental setup the surrounding components like the formwork are grounded for safety reasons.

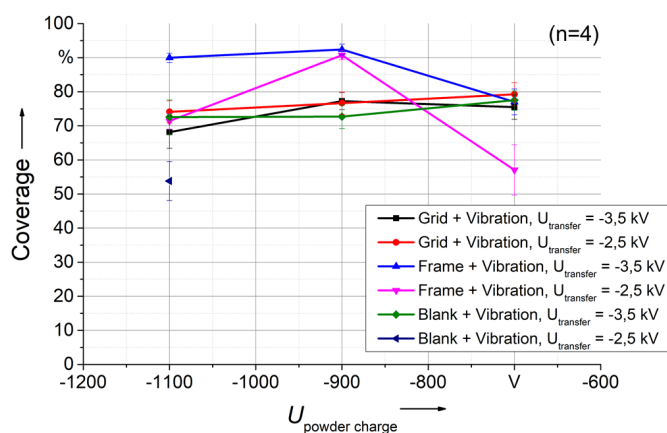


Fig. 7. Coverage values for different powder charge voltages and transfer structure geometries.

However, this also introduces some kind of electric field between the photoconductive plate and the surrounding components. Apparently, this field is strong enough to move the charged powder particles to the substrate plate in the event of a small induced mechanical excitation pulse as long as the powder charge voltage is high enough. Otherwise no measurable powder transfer takes place anymore (cf. missing values for “blank + vibration” at a transfer voltage of -2.5 kV in Fig. 7 and Fig. 8)

Fig. 8 shows that by applying a transfer frame the mean spray can be reduced to approximately 0 mm, which corresponds to a reduction by up to 90 % compared to the state of the art transfer grid. The comparably high spray values of the transfer grid are caused by relatively strong transversal field components and scattering effects, which arise from collisions of powder particles at grid wires.

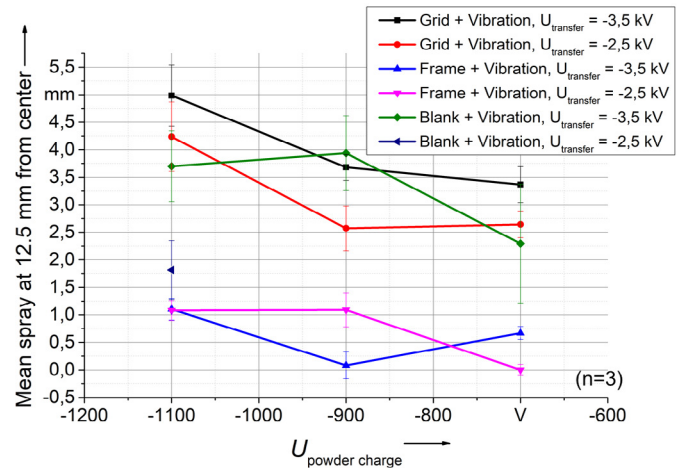


Fig. 8. Mean spray for different powder charge voltages and transfer structure geometries at a distance of 12.5 mm from center.

Interestingly, the mean spray in case of no applied transfer structure is similar to that of the transfer grid. This is most probably caused by the transversal field components of the mentioned electric field between the photoconductive plate and grounded surrounding components.

3. Conclusion

The powder deposition through a state of the art transfer grid exhibits two main drawbacks. These are the existence of grid wires acting as physical barriers and very strong parasitic transversal field components, which deflect the powder particles from their linear motion. By applying the newly introduced improved transfer frame these grid wires are avoided. Furthermore, the transversal field components can be significantly reduced. At this, the simulative investigation reveals that in case of the transfer frame the ratio between transversal field components and field components in z -direction can be reduced by a factor of two compared to the transfer grid. The subsequent experimental analysis has shown that this results in a significant reduction of the spraywidth of up to 90 %. Furthermore, the coverage could be enhanced by approximately 17 % by applying the new transfer frame in combination with an induced mechanical excitation pulse onto the photoconductive plate. For a further improvement of the coverage, future investigations should employ a piezo-induced mechanical excitation and additionally investigate the impact of different particle size distributions on the powder deposition behavior. Since the particle size distribution among others influences the charge distribution [8,9], it might affect the electrophotographic powder pattern deposition and could help to improve the coverage even further.

Moreover, the conducted simulative analysis has shown that the accumulation of charges within deposited powder layers only slightly attenuates the electric transfer field. This can be compensated by slightly adjusting the voltage at the photoconductive plate if necessary.

It has been shown that a detailed analysis of the simulated spatial electric field distribution can help to understand the movement of charged powder particles within an applied electric field. Although the similarly charged particles may

exhibit forces of repulsion to each other, the influence of an external electric field on their behavior can be predicted in a reasonable way. Thus, the transfer frame could be introduced for improving the dimensional accuracy as well as the coverage. Therefore, it helps to advance towards the superior aim of the presented investigations, which is the implementation of the electrophotographic powder deposition into the process of selective laser melting.

Acknowledgements

The authors gratefully acknowledge funding of the Collaborative Research Center 814 (CRC 814), sub-project B6, and of the Erlangen Graduate School in Advanced Optical Technologies (SAOT) by the German Research Foundation (DFG) in the framework of the German excellence initiative.

References

- [1] Kruth JP, Wang X, Laoui T, Froyen L. Lasers and materials in selective laser sintering. *Assembly Automation* 2003;23(4):357-371.
- [2] Kruth JP, Levy G, Klocke F, Childs THC. Consolidation phenomena in laser and powder-bed based layered manufacturing. *CIRP Annals* 2007;56:730-759.
- [3] Stichel T, Brachmann C, Raths M, Dechet MA, Schmidt J, Peukert W, Frick T, Roth S. Electrophotographic Multilayer Powder Pattern Deposition for Additive Manufacturing. *JOM* 2020;72:1366–1375.
- [4] Bandyopadhyay A, Heer B. Additive manufacturing of multi-material structures. *Materials Science and Engineering: R: Reports* 2018;129:1–16.
- [5] Kumar A, Dutta A, Fay J. Electrophotographic printing of part and binder powders. *Rapid Prototyping Journal* 2004;10(1):7-13.
- [6] Stichel T, Brandl T, Hauser T, Geißler B, Roth S. Electrophotographic multi-material powder deposition for additive manufacturing. *Procedia CIRP* 2018;74:249–253.
- [7] Pai DM, Springett BE. Physics of electrophotography. *Reviews of Modern Physics* 1993;65(1):163–211.
- [8] Shahin MM. Nature of Charge Carriers in Negative Coronas. *Appl Opt Suppl Electr Photog* 1969;82:106-110.
- [9] Matsusaka S, Masuda H. Electrostatics of particles. *Advanced Powder Technology* 2003;14(2):143–166.
- [10] Shahin MM. Mass-spectrometric Studies of Corona Discharges in Air at Atmospheric Pressures. *J Chem Phys* 1966;43:2600-2605.
- [11] Itakura T, Masuda H, Ohtsuka C, Matsusaka S. The contact potential difference of powder and the tribo-charge. *Journal of Electrostatics* 1996;38(3):213–226.

4.4 Compensation of Charge Accumulation

Expanding the capabilities of laser-based powder bed fusion of polymers through the use of electrophotographic powder application

Published in Journal of Laser Applications 34 (2022), 042032

Sebastian-Paul Kopp^{a-c,*}, Vadim Medvedev^{a-c}, Thomas Frick^a, Stephan Roth^{a-c}

^a Bayerisches Laserzentrum GmbH, 91052 Erlangen, Germany

^b Collaborative Research Center (CRC) 814 “Additive Manufacturing”, 91058 Erlangen, Germany

^c Erlangen Graduate School in Advanced Optical Technologies (SAOT), 91052 Erlangen, Germany

*Corresponding author.

Tel.: +49-9131-97790-27; E-mail address: s-p.kopp@blz.org

Reprinted with permission from [Expanding the capabilities of laser-based powder bed fusion of polymers through the use of electrophotographic powder application; Journal of Laser Applications 34 (2022), 042032]. Copyright [2022], Laser Institute of America.

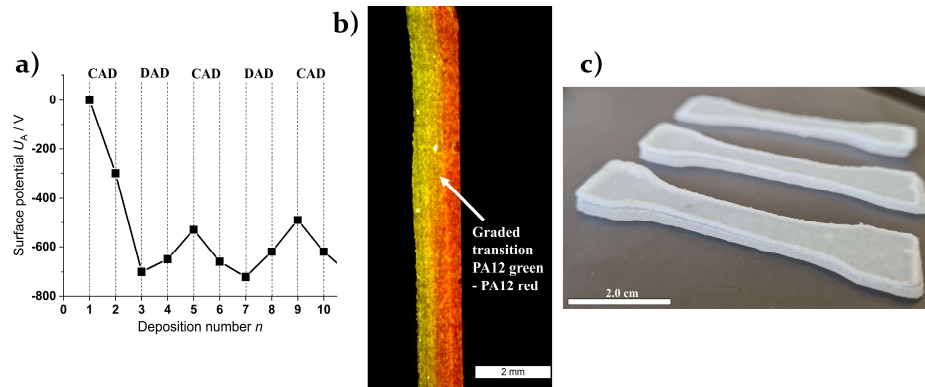


Figure 17: a) Applied charge compensation strategy for limiting the surface potential of the part generated by EPA-PBF-LB/P; b) graded material transition showing the potential of selective multi-material powder deposition by EPA; c) parts manufactured by EPA-PBF-LB/P consisting of a polypropylene (PP) powder which cannot be processed in conventional PBF-LB/P due to poor powder flowability.

The methods developed and investigated in the previous sections 4.1, 4.2 and 4.3 allow the reproducible deposition of single layers by EPA with contactless powder deposition, achieving high layer coverage and geometric accuracy. In addition, the thickness of the individual layers can be tailored. However, as already known from EPA with contacting powder deposition (cf. section 2.2.2), charge accumulation within the generated part is a major

challenge in 3D electrophotography. Therefore, in this study the charge build-up during the deposition and consolidation of layers is investigated. An important relationship between the charge build-up and the electrical volume resistivity (EVR) is proposed and a strategy to compensate for the charge build-up is developed (cf. Figure 17 a)). For the first time, 3D parts can be generated using EPA-PBF-LB/P (cf. Figure 17 c)) and analyzed for mechanical performance and multi-material capability (Figure 17 b)). To manufacture the parts shown in Figure 17 c) a PP powder was used, which is not suitable for conventional PBF-LB/P due to insufficient powder flowability. This demonstrates the ability of EPA to enable new powder materials to be processed in PBF-LB/P, which has been a major limitation of conventional powder application methods (cf. section 2.1.2).

The toolset developed and investigated in sections 4.1, 4.2 and 4.3 and the compensation strategy discussed in this section, form the basis for two patent applications [219,220] in the context of this work.

Highlights:

- Understanding of the charge accumulation behavior during deposition and consolidation of powder layers by EPA-PBF-LB/P
- Dependence of charge accumulation behavior on the polymer used
- Development and investigation of a strategy to compensate for charge accumulation during EPA based on alternating the polarity of the deposited powder layers
- Potential to significantly reduce powder waste with EPA compared to conventional powder application methods due to the selectivity of powder deposition and the elimination of the need to fill the entire PBF-LB/P build platform with powder material
- Possibility to process a PP powder in PBF-LB/P, which could not previously be processed in laser-based powder bed fusion due to insufficient powder flowability
- Possibility to flexibly combine more than one material within a part to allow multi-material PBF-LB/P

RESEARCH ARTICLE | OCTOBER 27 2022

Expanding the capabilities of laser-based powder bed fusion of polymers through the use of electrophotographic powder application

Special Collection: [Proceedings of the International Congress of Applications of Lasers & Electro-Optics \(ICALEO 2022\)](#)

Sebastian-Paul Kopp ; Vadim Medvedev; Thomas Frick; Stephan Roth



J. Laser Appl. 34, 042032 (2022)

<https://doi.org/10.2351/7.0000774>



View
Online



Export
Citation

[CrossMark](#)



Journal of
Laser Applications

[Learn More](#)



RAPID TIME
TO ACCEPTANCE



COMMUNITY
DRIVEN



EXPANSIVE
COVERAGE



PRESTIGIOUS
EDITORIAL BOARD



EXTENSIVE
MARKETING

Expanding the capabilities of laser-based powder bed fusion of polymers through the use of electrophotographic powder application

Cite as: J. Laser Appl. 34, 042032 (2022); doi: 10.2351/7.0000774

Submitted: 24 June 2022 · Accepted: 27 September 2022 ·

Published Online: 27 October 2022



Sebastian-Paul Kopp,^{1,2,3,a)} Vadim Medvedev,^{1,2,3} Thomas Frick,¹ and Stephan Roth^{1,2,3}

AFFILIATIONS

¹Bayerisches Laserzentrum GmbH, Konrad-Zuse-Straße 2-6, 91052 Erlangen, Germany

²Collaborative Research Center (CRC) 814 "Additive Manufacturing," Am Weichselgarten 10, 91058 Erlangen-Tennenlohe, Germany

³Erlangen Graduate School in Advanced Optical Technologies (SAOT), Paul-Gordan-Straße 6, 91052 Erlangen, Germany

Note: Paper published as part of the special topic on Proceedings of the International Congress of Applications of Lasers & Electro-Optics 2022.

^{a)}Electronic mail: s-p.kopp@blz.org

ABSTRACT

Generating multimaterial parts, reaching higher efficiency in powder consumption, and decoupling of powder application behavior from powder properties such as powder flowability are key aspects for using electrophotographic powder application (EPA) in laser-based powder bed fusion of polymers (PBF-LB/P). Moreover, EPA allows the layer thickness to be reduced from around 100–150 μm , depending on respective particle size distribution, in the case of conventional doctor blade or roller-based powder application methods to the diameter of the applied polymer particles (typically between 50 and 130 μm). This can have positive effects on the interlayer connection and, therefore, the mechanical properties of the additively manufactured part because less powder volume has to be fused with the already generated underlying part. Moreover, due to the above-mentioned independence of EPA from powder flowability, the addition of flow aids, such as nano silica, can be reduced to a minimum or even avoided completely. This is the first comprehensive study on resulting properties of parts generated by PBF-LB/P using EPA taking into account both the reduction in layer thickness and reduced addition of flow aids. In addition to improving mechanical properties of generated parts, the independence of powder flowability, in particular, offers the possibility of qualifying currently unsuitable materials for PBF-LB/P. For this purpose, besides widely employed polyamide 12 (PA12), a polypropylene (PP) powder is used that is very difficult to process in conventional PBF-LB/P and can only be applied there with the help of flow aids.

Key words: electrophotography, laser-based powder bed fusion of polymers (PBF-LB/P), additive manufacturing, polypropylene (PP), polyamide 12 (PA12)

Published under an exclusive license by Laser Institute of America. <https://doi.org/10.2351/7.0000774>

INTRODUCTION

Due to their inherent flexibility and efficiency, additive manufacturing (AM) processes particularly demonstrate their strengths in the generation of highly complex parts.¹ Although the applicability of AM processes in mass production is still considered one of the biggest hurdles, a recent study has revealed good potential for the introduction of AM processes in mass production of electrochemical energy systems.^{2,3} Beyond that, polymer AM technologies, such as laser-based powder bed fusion of polymers (PBF-LB/P),

have gained significant importance in recent years in the context of generating highly complex parts, especially in medical, aerospace, and automotive industries.^{4–6}

However, conventional PBF-LB/P uses layer-by-layer manufacturing with doctor blade or roller-based powder application processes, which necessarily involve filling of the complete build chamber.⁷ Moreover, they do not allow powder composition and material distribution within a powder layer to be adjusted in a targeted and precise manner, making them impossible to generate

06 November 2023 17:27:38

products with distributed functional properties or even multimaterial parts.⁸ As already mentioned above, another decisive disadvantage of conventional powder application methods for PBF-LB/P is the fact that they cause a complete filling of the build volume within the build chamber with the material used.^{7,9,10} However, only a certain percentage of powder in the build chamber is used to generate the actual part. The so-called nesting efficiency (weight) ($NE(\text{weight})$) relates the weight of the parts produced to the total weight of powder material used for the build job and is defined as¹¹

$$NE(\text{weight}) = \frac{\text{Build weight}}{\text{Total weight of powder in container}}. \quad (1)$$

Although various strategies for improving the nesting efficiency have been presented,^{11–13} the practically applied weight-based nesting efficiency is in the range of 8%.¹⁴ For this reason, it is not surprising that more than 50% of the environmental impact of the PBF-LB/P process can be attributed to the generation of polymer waste material and the so-called end-of-life treatment of waste powders. Here, high temperatures inside the build chamber in combination with long processing times play a decisive role. These two influencing factors cause chemical and physical aging effects of the powder, which significantly reduce recyclability of powder portions that are not processed into the actual part, the so-called partcake material.¹⁵ Owing to the aforementioned process conditions, the partcake powder must be refreshed with new polymer material for further usage.^{15,16} Depending on the polymer material used, typical refreshing rates lie in the range of 30%–50%.^{15–18} The reuse and recycling of polymer powder materials is undoubtedly an integral part of future-oriented and sustainable PBF-LB/P.^{14,19,20} However, on the one hand, this requires additional process steps such as sieving or mixing. In addition, some application areas and materials do not allow reuse due to very high standards for the materials used, as is often the case in medical or pharmaceutical applications in particular.^{21,22}

One of the most important powder properties for PBF-LB/P is powder flowability, as it has a direct influence on process reliability and part quality.²³ This arises from the fact that conventional doctor blade or roller-based powder application processes require a certain powder flowability in order to generate reproducible and accurate powder layers. Beyond that, the risk of build job abortions or part defects is strongly related to reproducibility and accuracy of the coated powder layers.²⁴ Because a variety of factors such as particle shape, particle size distribution, or the electrochemical properties of the particles can influence flowability, the adjustment of suitable powder flowability has a key role in powder recycling as well as new development of powder materials for PBF-LB/P.²⁵ Therefore, materials successfully applicable for PBF-LB/P are limited. While traditional polymer processing techniques, such as injection molding or extrusion, have access to thousands of different formulations consisting of several dozens of base polymers, only a handful of different formulations are available for PBF-LB/P so far.²³ Consequently, reducing the dependence of the powder application method on powder flowability would offer great potential for PBF-LB/P. On the one hand, effort and, thus, costs in powder production could be reduced. In addition, it would be possible to use a significantly wider

range of powder materials for PBF-LB/P and, thus, significantly increase the possible applications of this manufacturing technique, for example, in the pharmaceutical sector.

A promising approach in order to overcome the aforementioned deficiencies of conventional powder application methods is the usage of electrophotographic powder application (EPA).^{8,26} EPA can be divided into six main process steps.^{27–29} In step one, the powder and a photoconductive plate (PCP, an aluminum plate coated with a photoconductive material) are homogeneously charged.^{30–32} In the second step, a latent charge pattern is generated on the PCP by selective illumination. In step three, charged powder particles are attracted toward the PCP due to electrostatic forces, which is the so-called development step. Depending on the selected polarity for charging the powder particles in step two, charged particles can be either developed into charged (charged area development CAD) or discharged (discharged area development DAD) areas of the PCP. In step four, the PCP is moved laterally to the build chamber and the powder particles are deposited onto the build plate, which is located inside the build chamber. In step five, a laser beam illuminates deposited powder particles in order to fuse them. Finally, in step six, the PCP is cleaned. The general demonstration of the working principle of EPA in the context of PBF-LB/P (EPA-PBF-LB/P) on a single-layer basis was shown in Refs. 28 and 33. By using a specially designed transfer frame for adapting and controlling the electric transfer field, a significant increase in powder deposition efficiency was achieved in Ref. 29. So far, however, only single-layer tests have been carried out, and no melting of the layers has yet taken place. In particular, the accumulation of charges associated with a progressive decrease in the electric transfer field strength has already been identified in Refs. 27 and 34 as a major challenge for successful EPA in the context of PBF-LB/P.

In this paper, for the first time, parts generated using EPA in combination with PBF-LB/P are shown and analyzed. In addition, one focus of the investigations carried out is the charge accumulation during the generation process of the part and a new process strategy, which is developed to compensate it. Finally, the potentials of EPA for PBF-LB/P are highlighted based on the aforementioned deficiencies of conventional PBF-LB/P using the results shown in this paper.

MATERIALS AND METHODS

Experimental setup for EPA in the context of PBF-LB/P

The two decisive parts of the experimental setup are the development chamber, on the one hand, and the build chamber, on the other. While the process steps (cf. Introduction) one, two, three, and six take place in the development chamber, steps four and five are carried out in the build chamber (cf. Fig. 1).

For moving the holding arm together with the PCP, a positioning system consisting of a direct-drive linear actuator as x-axis and a lift stage as z-axis (both Aerotech GmbH, Fürth, Germany) is applied. The holding arm connects the positioning system and PCP. For high-voltage supply, a THQ series (hivolt.de GmbH & Co. KG, Hamburg, Germany) high-voltage power supply is used. The equipment for melting the layers consists of a CO₂-laser with a maximum output power of 60 W (Synrad ti60, Novanta Photonics,

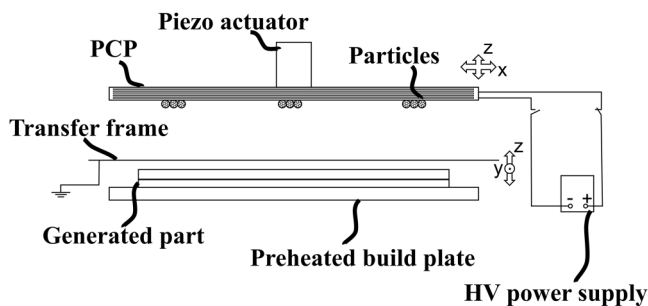


FIG. 1. Schematic overview of decisive parts of the experimental setup inside the build chamber.

Seattle, WA, USA) and a laser scanner (Miniscan II-20, Raylase GmbH, Weßling, Germany) as well as a F-Theta lens with a focal length $f = 420$ mm (Raylase GmbH, Weßling, Germany). As already discussed, EPA offers the possibility of applying only the powder volume necessary for generating the desired part. Thus, only a small amount of powder has to be preheated to the respective preheating temperature of the polymer (cf. Table I), which lies between the upper limit of crystallization and the lower limit of melting temperature.³⁵ For this reason, the time- as well as energy-intensive preheating of the entire build chamber, as is the case with conventional PBF-LB/P, was avoided by applying a local preheating procedure. Therefore, the build plate was placed onto a heating stage (RCT basic, IKA-Werke GmbH, Staufen im Breisgau, Germany), which was preheated to the respective preheating temperature (cf. Table I). In this way, sufficient preheating of the deposited powder was achieved for the parts generated in this paper up to a height of 2 mm. For improving powder deposition,

step four was assisted by piezoelectric excitation. Therefore, a signal generator TG1010A (Thurlby Thandar Instruments, Huntingdon, UK) was used for generating a sinusoidal signal. A PSt 1000/16/20 VS25 (Piezosystem Jena GmbH, Jena, Germany) was used as a piezoelectric actuator. To amplify the signal of the function generator to sufficiently high input values of the piezoelectric actuator, an analog power amplifier LE 1000/035 (Piezosystem Jena GmbH, Jena, Germany) was utilized with an amplification factor of 100.

Experimental investigations in this paper were carried out using polyamide PA12 powder (PA2200, EOS GmbH, Krailling, Germany) with $d_{50 \text{ PA12}} = 55.9 \mu\text{m}$ and polypropylene PP powder (Coathylene PD0580, Axalta Coating Systems GmbH, Pratteln, Switzerland) with $d_{50 \text{ PP}} = 98.6 \mu\text{m}$. To improve powder handling of the used PP, 0.05 wt. % of fumed silica (Aerosil R106, Evonik Industries AG, Essen, Germany) was added. Usually, 0.5–1.0 wt. % of fumed silica is required to sufficiently functionalize polymer powders for conventional doctor blade or roller-based powder application processes.^{36,37} In order to visualize the graded material transition, the PA12 powder was dyed using 0.1 wt. % chrome oxide green (Chromoxidgrün, Kremer Pigmente GmbH & Co. KG, Aichstetten, Germany) and 0.1 wt. % iron oxide red (Eisenoxidrot 110 M, hell, Kremer Pigmente GmbH & Co. KG, Aichstetten, Germany), respectively.

For conducting the experiments, the following parameters were used (cf. Table I).

Measurement of the surface potential and microscopic analysis of generated parts

The measurement of the surface potential was carried out using an electrostatic voltmeter (Monroe 244A, Monroe Electronics Inc., Lyndonville, NY, USA) with a measurement accuracy of 0.1% at a separation distance between the probe and the powder bed surface or the surface of the molten and solidified layer of ≈ 3 mm. A stereo microscope (M80, Leica Microsystems GmbH, Wetzlar, Germany) was used for the microscopic analysis of the generated parts.

Measurement of the mechanical part properties

In order to determine the mechanical properties of the generated PP parts, tensile strength specimens (according to DIN EN ISO 3167—test specimen 1BA) were generated utilizing EPA-PBF-LB/P and tested. Thickness and width of the measuring range of the tensile bars were measured with a micrometer caliper with an accuracy of 0.01 mm. Tensile tests were performed according to DIN EN ISO 527-2 on a universal testing machine (Quasar 100, Cesare Galdabini, Vigevano, Italy) at room temperature with a load cell of 10 kN and a contact extensometer. Young's modulus was measured at a speed of 0.5 mm/min until an elongation of 0.3% was reached, followed by a speed of 20 mm/min to measure ultimate tensile strength and elongation.

RESULTS AND DISCUSSION

Charge accumulation during powder deposition

For a better understanding of the processes involved in powder deposition and in particular challenges arising from

TABLE I. Parameters for generating PA12 and PP parts using EPA-PBF-LB/P.

Parameter	Value
Laserpower	16.2 W (PA12) 18.0 W (PP)
Laser hatching distance	0.1 mm (PA12, PP)
Laser scanning speed	600 mm/s (PA12) 800 mm/s (PP)
Preheating temperature	170 °C (PA12) 160 °C (PP)
Polarity and charging field strength PCP	+167 kV/m
Polarity and charging field strength powder	±167 kV/m (PA12, PP)
Polarity and development field strength	±3846 kV/m (PA12, PP)
Polarity and transfer field strength	±2500 kV/m (PA12, PP)
Frequency of sinusoidal signal for piezo-excitation	15 kHz
Peak-to-peak voltage of sinusoidal signal	8 V _{P-P}

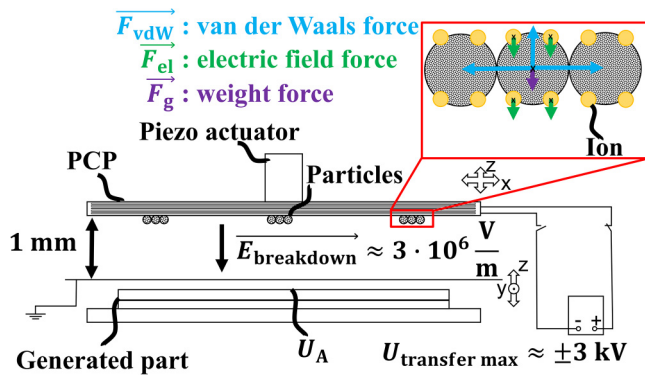


FIG. 2. Modeling of the powder deposition step and charge accumulation.

accumulation of charges within the generated part, a schematic overview of the deposition step is shown in Fig. 2.

In this schematic overview, the already generated exemplary part consists of two molten and solidified layers of a first material. A third layer, consisting of only three distinct powder portions of a second material, is being deposited with a deposition distance of 1 mm between the PCP and the transfer frame,²⁹ which is positioned slightly above the surface of the already generated part. The powder particles are charged via gas discharge in process step one. According to Refs. 38 and 39, this leads to storage of different ions into surface defects or transition zones between crystalline and amorphous polymer regions. The type of ions generated by gas discharge and stored within the polymer layer depends on both polarity and surrounding atmospheric humidity.^{38,39} Polarity and the number of stored ions finally define the resulting particle charge q_{particle} . Since mass and, therefore, gravitational force F_g acting on the powder particles are relatively small, the dominant force for powder deposition is the electric field force F_{el} . It mainly acts on the ions stored within the powder layer³⁰ and consequently on the powder particles. For powder deposition, the electric field force has to overcome the van der Waals force F_{vdW} , which attaches the powder particles to the PCP. F_{el} can be given as^{30,40}

$$\vec{F}_{\text{el}} = q_{\text{particle}} \cdot \vec{E}_{\text{transfer}}, \quad (2)$$

with particle charge q_{particle} and electric field strength of the electric transfer field $\vec{E}_{\text{transfer}}$. From Eq. (2), it becomes clear that in the case of $\vec{E}_{\text{transfer}} = 0$, there is no powder deposition possible. However, assuming a common deposition distance of 1 mm and a dielectric strength of air at normal conditions (atmospheric pressure $p_0 = 1013$ hPa, temperature $T_0 = 293$ K) in the range of $\vec{E}_{\text{breakdown}} \approx 3 \times 10^6 \frac{\text{V}}{\text{m}}$ ^{41,42} the electric transfer field strength $\vec{E}_{\text{transfer}}$ will become zero if the applied voltage is $|U_{\text{transfer max}}| \geq 3$ kV. This is due to the fact that the dielectric strength of air is exceeded in the gap between the PCP and transfer frame. Therefore, the voltage applied to the PCP for powder deposition U_{transfer} must not exceed ± 3 kV. Hence, an increasing

surface potential U_A caused by charge accumulation within the generated part and leading to a weakening of the electric transfer field can only be compensated up to a certain limit by increasing the deposition voltage. As a result, electric transfer field strength $\vec{E}_{\text{transfer}}$ and, thus, electric field force \vec{F}_{el} on powder particles will decrease with increasing U_A . Generally, the surface potential U_A of a powder layer depends on the polarity and the number of stored ions within this layer. This is determined by the applied powder charging parameters, especially charging voltage and, therefore, charging field strength, in process step one (cf. Introduction, Table I). However, for charge accumulation within a generated part, the layer-by-layer storage of ions is crucial. This storage is mainly determined by polarity and the number of ions stored within the respective powder layer and the charge flow inside the generated part toward the grounded build plate (cf. Fig. 1) and charge flow toward the surrounding atmosphere. While the former mainly depends on the density as well as the thickness of the deposited powder layer and of the already generated part and the electrical volume resistivity (EVR) of the used polymer, the latter depends on the environmental conditions (air flow, temperature, and humidity). The effect of increasing magnitude of the surface potential is visible in Fig. 3. Here, in total, four powder layers of PP are deposited and sintered (no more powder deposition takes place during deposition number 5). EPA-PBF-LB/P is used in the CAD operating mode, which means that the powder is charged negatively and a positive electric transfer field (electric field lines point in the positive z-direction) for powder deposition is applied (cf. Table I).

The first powder layer, which is applied directly onto the build plate (zeroth layer) inside the build chamber, has a calculated thickness of $100 \mu\text{m}$ and, therefore, contributes with $100 \mu\text{m}$ to the

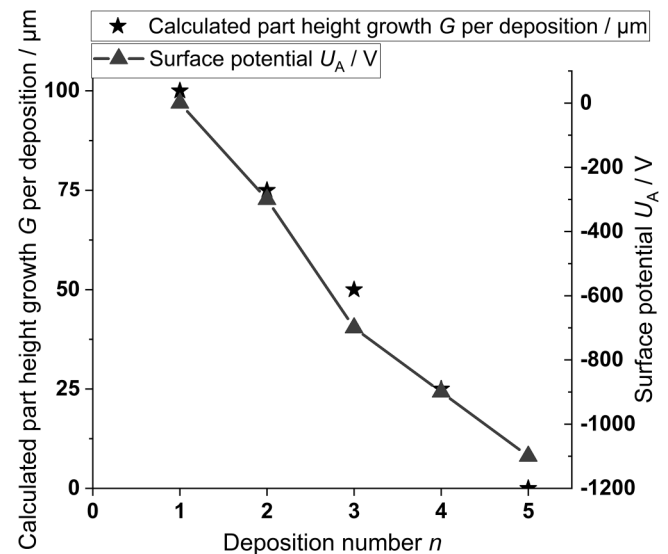


FIG. 3. Resulting surface potential and calculated growth of part height G per deposition for generation of PP tensile test bar using EPA-PBF-LB/P in the CAD operating mode without compensation of charge accumulation [error bars (measurement uncertainty) of surface potential are smaller than symbol size].

06 November 2023 17:27:38

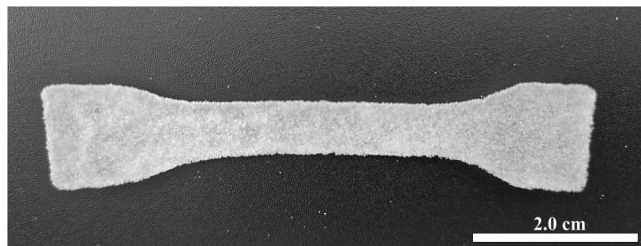


FIG. 4. Generated PP part with tensile test bar geometry and four deposited and solidified layers (part height: $250 \pm 10 \mu\text{m}$) using EPA-PBF-LB/P in the CAD operating mode without compensation of charge accumulation.

height growth of the part. Due to the fact that layer number 1 is deposited directly to the build plate, the measured surface potential is $U_A = 0 \text{ V}$ (ground potential). However, when depositing the second layer, the magnitude of the surface potential for deposition of layer number 2 increases to $|U_A| = 300 \text{ V}$ due to charges within layer 1. The growth G of part height per deposited layer is calculated by dividing the achieved part height of $250 \pm 10 \mu\text{m}$ (see Fig. 4) by the number of layers, which contribute to this part height. In fact, only in the case of the first four layers, powder deposition is observable. Furthermore, parts generated with 5, 10, or 20 layers show the same height of $250 \pm 10 \mu\text{m}$ as long as no compensation strategy to avoid charge accumulation is applied. As a first approximation, it is assumed that the decrease in part height growth is linear and, thus, indirectly proportional to the increase in $|U_A|$. However, to verify this inverse linear dependence between G and $|U_A|$, in future work, the growth of part height after each deposition should be measured, e.g., with a light section sensor.

A strategy for compensating charge accumulation independently of the already generated part thickness and in the case of constant environmental conditions is to achieve a net charge of zero by neutralization of contrarily charged ions. In fact, a deposited powder layer with a certain surface potential caused by stored ions should be followed by a powder layer with contrary charging but the same magnitude of surface potential. Thus, the operating modes of EPA-PBF-LB/P should be regularly changed from CAD to DAD. Although changing the polarity after each powder deposition would be even more efficient regarding compensation of charge accumulation and increasing part height growth, a certain duration is needed for reversion of polarity by the high voltage power supply. It has shown to be a good trade-off between duration for reversion of polarity and still maintaining significant growth of part height to change the operation mode from CAD to DAD after every second powder deposition. According to Fig. 3, significant powder deposition can be achieved up to $|U_A| \leq 750 \text{ V}$, which is reached after two deposited and solidified powder layers. Therefore, for polymer powders, which have similar charge storage and, thus, charge accumulation properties like PP, the polarity of applied powder layers should be changed after every second layer deposition. This has two major benefits for the powder application process. First, as can be seen in Fig. 5, the surface potential is kept between $-750 \text{ V} < U_A < -450 \text{ V}$. This corresponds to values at which, based on Fig. 3, significant powder deposition is achieved for PP.

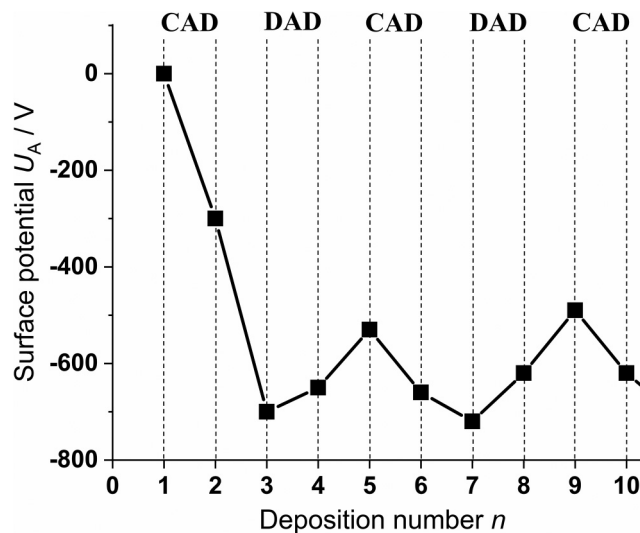


FIG. 5. Resulting surface potential for generation of the PP tensile test bar using EPA-PBF-LB/P with applied compensation strategy to avoid charge accumulation [error bars (measurement uncertainty) of surface potential are smaller than symbol size].

Beyond that, a change from CAD to DAD is particularly beneficial since in the case of DAD positively charged powder particles are deposited in a negative transfer field (electric field lines point in the negative z -direction), which is enhanced by the negative surface potential of the already generated part. In other words, while charge accumulation increasingly inhibits powder deposition in the CAD operating mode, it supports powder deposition in the DAD operating mode. Applying EPA-PBF-LB/P in combination with the developed compensation strategy to avoid charge accumulation, three tensile test bars as shown in Fig. 6 are generated.

06 November 2023 17:27:38

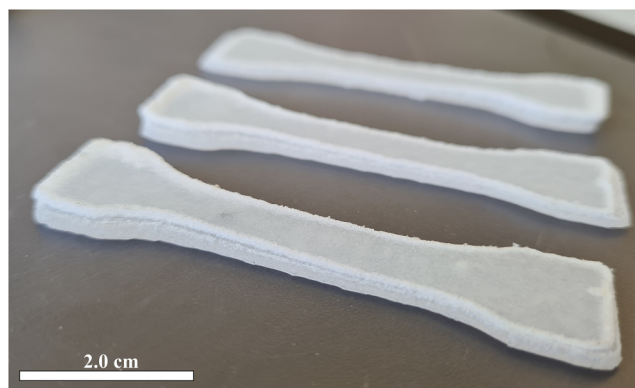


FIG. 6. Generated PP tensile test bars using EPA-PBF-LB/P with applied compensation of charge accumulation consisting of ≈ 35 deposited, fused, and solidified layers (part height: $2.0 \pm 0.01 \text{ mm}$).

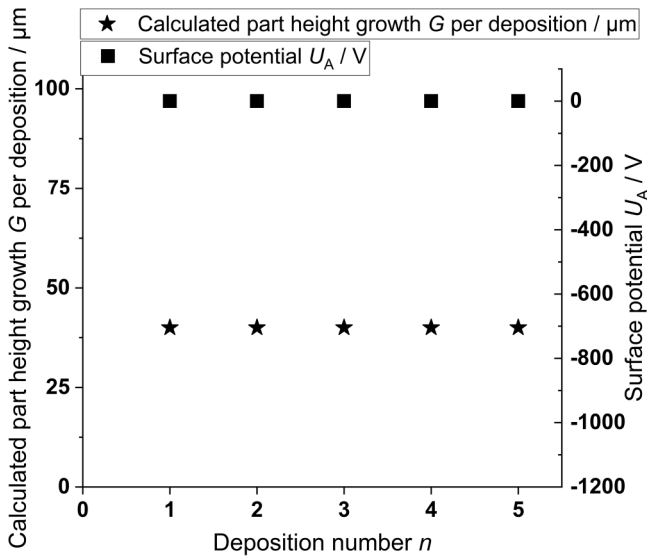


FIG. 7. Resulting surface potential and calculated growth of part height G per deposition for generation of PA12 tensile test bar using EPA-PBF-LB/P in the CAD operating mode without compensation of charge accumulation [error bars (measurement uncertainty) of surface potential are smaller than symbol size].

Comparing the surface potentials for deposition number 5 without compensation strategy (Fig. 3) and in the case of an applied compensation strategy (Fig. 5), it becomes clear that in the first case the surface potential is already at -1100 V due to four deposited layers using the CAD operating mode. In contrast, by applying the described compensation strategy, a decrease in the

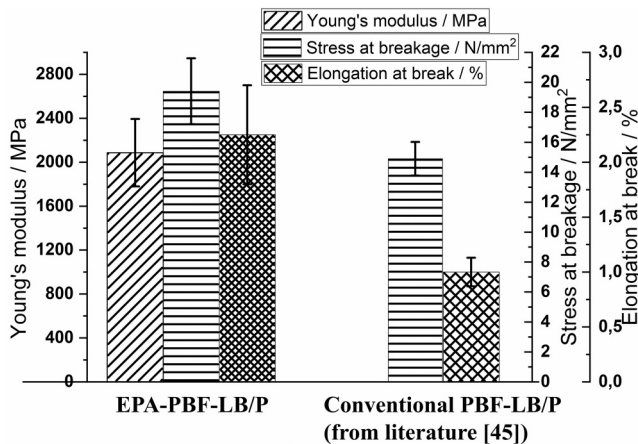


FIG. 8. Mechanical properties of PP tensile test bars generated using EPA-PBF-LB/P with an applied compensation strategy to avoid charge accumulation (error bars indicate standard deviation of three measurements) and conventional PBF-LB/P (values for conventional PBF-LB/P from Ref. 45).

magnitude of the surface potential by 570 to -530 V (cf. Fig. 5) for deposition number 5 is achieved.

Unlike PP, no compensation for accumulated charge is required when processing PA12 with EPA-PBF-LB/P, as indicated in Fig. 7. This behavior is examined in more detail below.

Although the CAD operating mode is used throughout all layer depositions, the surface potential U_A of the deposited, fused,

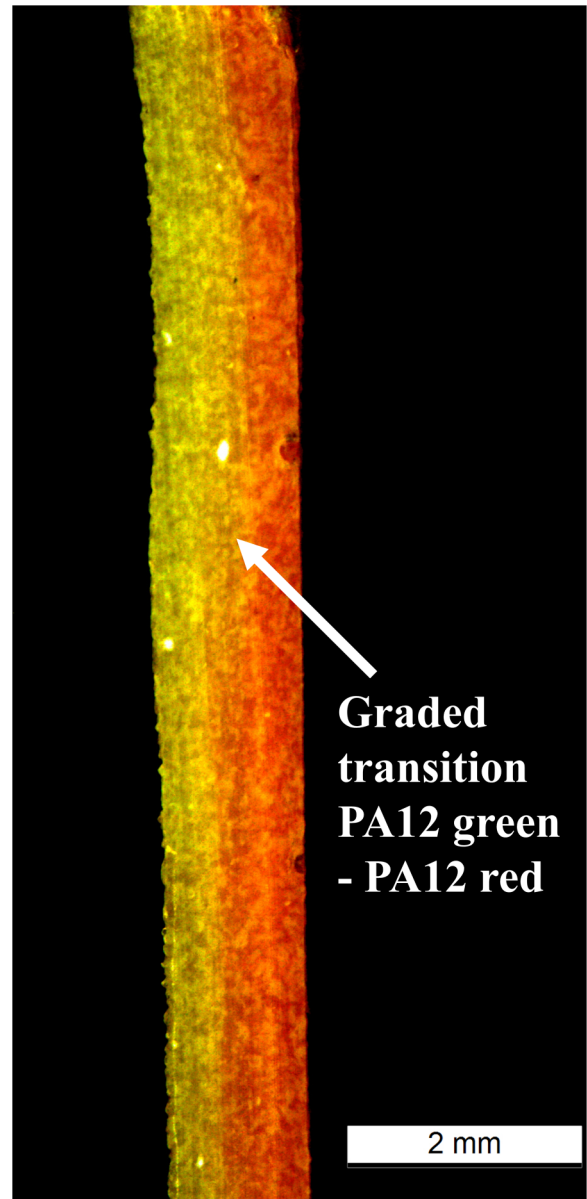


FIG. 9. PA12 part generated using EPA-PBF-LB/P in the CAD operating mode with graded material transition between green and red dyed PA12 consisting of ≈ 45 deposited, fused, and solidified layers (part height: 1.8 ± 0.01 mm) without compensation of charge accumulation.

06 November 2023 17:27:38

and solidified layers is constantly zero for PA12. Therefore, no attenuation of the electric transfer field is taking place, which results in constant G . A possible explanation for this behavior can be found in different EVRs of PA12 and PP.⁴³ While EVR of PP is in the range of $10^{16} \Omega\text{m}$, EVR of PA12 lies around $10^{12} \Omega\text{m}$.⁴⁴ Since PP shows four orders of magnitude larger EVR than PA12, the faster decay of accumulated charges seems plausible. Consequently, EPA-PBF-LB/P of PA12 can be conducted without applying a strategy for compensating the accumulation of charges. As can be seen in Fig. 9, a PA12 part consisting of ≈ 45 deposited, fused, and solidified layers can be generated using EPA-PBF-LB/P without applying a charge accumulation compensation strategy.

Mechanical properties of PP tensile test bars generated using EPA-PBF-LB/P

In Fig. 8, the mechanical properties of the PP tensile test bars as shown in Fig. 6 are visualized.

Although the amount of flow aid is decreased by a factor of 10–20 compared to literature,^{36,37} the parts shown in Fig. 6 display mechanical properties, which are comparable to PP parts generated using conventional PBF-LB/P.⁴⁵ EPA-PBF-LB/P, thus, enables the processing of a powder material that is not printable in conventional PBF-LB/P due to its insufficient functionalization with fumed silica.

Graded material transition

As already discussed at the beginning (cf. Introduction), conventional PBF-LB/P does not allow to adjust powder composition and material distribution within a powder layer. In Fig. 9, a part generated using EPA-PBF-LB/P is shown, which consists of two different PA12 powders, PA12 green and PA12 red. The part consists of ≈ 15 layers of PA12 red and ≈ 15 layers of PA12 green, with a graded, layer-by-layer material transition adjusted in the area marked with an arrow (cf. Fig. 9), followed by ≈ 15 layers of PA12 green. In this case, the overall calculated part height growth G per deposition is around $40 \mu\text{m}$, which corresponds to the calculated height growth in Fig. 7. This indicates that due to the lower EVR of PA12 compared to PP, no significant charge accumulation occurs within the generated part. Therefore, the entire part depicted in Fig. 9 is generated without compensation of charge accumulation using the CAD operating mode throughout all layer depositions.

CONCLUSION

Conventional powder application processes for laser-based powder bed fusion of polymers (PBF-LB/P) essentially exhibit three deficiencies. On the one hand, they cause a complete filling of the build volume with the material used. However, only a small portion of the powder in the build chamber is used to generate the actual part. The remaining powder has to be recycled at great expense. Since electrophotographic powder application (EPA) offers the possibility of applying only the powder volume necessary for generating the desired part, the usage of EPA for PBF-LB/P (EPA-PBF-LB/P) can significantly reduce the environmental impact of this manufacturing technology. Beyond that, the number

of powder materials applicable for PBF-LB/P is limited, mainly due to insufficient powder flowability. In this paper, successful processing of a PP powder, which is unsuitable for conventional PBF-LB/P, by using EPA-PBF-LB/P was shown. The achieved mechanical part properties are comparable to conventional PBF-LB/P using a specially adapted and, thus, suitable PP powder. In this context, the surface potential increase caused by the accumulation of charges within the generated PP part was examined and a strategy to compensate for this effect was developed. Finally, it was shown that by using EPA for PBF-LB/P, the material distribution within a powder layer can be adjusted.

ACKNOWLEDGMENTS

The authors gratefully acknowledge funding of the Collaborative Research Center 814 (CRC 814), sub-project B6, by the German Research Foundation (DFG)—Project No. 61375930—and of the Erlangen Graduate School in Advanced Optical Technologies (SAOT) by the Bavarian State Ministry for Science and Art.

AUTHOR DECLARATIONS

Conflict of Interest

The authors have no conflicts to disclose.

Author Contributions

Sebastian-Paul Kopp: Conceptualization (lead); Data curation (lead); Formal analysis (lead); Investigation (lead); Methodology (lead); Project administration (supporting); Resources (supporting); Software (lead); Validation (lead); Visualization (lead); Writing – original draft (lead); Writing – review & editing (equal). **Vadim Medvedev:** Data curation (supporting); Investigation (supporting). **Thomas Frick:** Methodology (supporting); Validation (supporting); Writing – review & editing (equal). **Stephan Roth:** Funding acquisition (lead); Project administration (lead); Resources (lead); Supervision (lead); Writing – review & editing (equal).

REFERENCES

- ¹S. H. Huang, P. Liu, A. Mokasdar, and L. Hou, “Additive manufacturing and its societal impact: A literature review,” *Int. J. Adv. Manuf. Technol.* **67**, 1191–1203 (2013).
- ²U. M. Dilberoglu, B. Gharehpapagh, U. Yaman, and M. Dolen, “The role of additive manufacturing in the era of industry 4.0,” *Proc. Manuf.* **11**, 545–554 (2017).
- ³S. M. H. Hashemi, U. Babic, P. Hadikhani, and D. Psaltis, “The potentials of additive manufacturing for mass production of electrochemical energy systems,” *Curr. Opin. Electrochem.* **20**, 54–59 (2020).
- ⁴P. Robles-Martinez, X. Xu, S. J. Trenfield, A. Awad, A. Goyanes, R. Telford, A. W. Basit, and S. Gaisford, “3D printing of a multi-layered polypill containing six drugs using a novel stereolithographic method,” *Pharmaceutics* **11**(6), 274 (2019).
- ⁵U. Fasel, D. Keidel, L. Baumann, G. Cavolina, M. Eichenhofer, and P. Ermanni, “Composite additive manufacturing of morphing aerospace structures,” *Manuf. Lett.* **23**, 85–88 (2020).
- ⁶M. Delic and D. R. Evers, “The effect of additive manufacturing adoption on supply chain flexibility and performance: An empirical analysis from the automotive industry,” *Int. J. Prod. Econ.* **228**, 107689 (2020).

- ⁷S. Haeri, Y. Wang, O. Ghita, and J. Sun, "Discrete element simulation and experimental study of powder spreading process in additive manufacturing," *Powder Technol.* **306**, 45–54 (2017).
- ⁸C. Wei and L. Li, "Recent progress and scientific challenges in multi-material additive manufacturing via laser-based powder bed fusion," *Virtual Phys. Prototyp.* **16**, 347–371 (2021).
- ⁹H. Chen, Q. Wei, Y. Zhang, F. Chen, Y. Shi, and W. Yan, "Powder-spreading mechanisms in powder-bed-based additive manufacturing: Experiments and computational modeling," *Acta Mater.* **179**, 158–171 (2019).
- ¹⁰M. Y. Shaheen, A. R. Thornton, S. Luding, and T. Weinhart, "The influence of material and process parameters on powder spreading in additive manufacturing," *Powder Technol.* **383**, 564–583 (2021).
- ¹¹P. Mogno, D. Lepicart, and N. Perry, "Rapid prototyping: Energy and environment in the spotlight," *Rapid Prototyp. J.* **12**, 26–34 (2006).
- ¹²A. S. Gogate and S. S. Pande, "Intelligent layout planning for rapid prototyping," *Int. J. Prod. Res.* **46**, 5607–5631 (2008).
- ¹³S. M. Hur, K. H. Choi, S. H. Lee, and P. K. Chang, "Determination of fabricating orientation and packing in SLS process," *J. Mater. Process. Technol.* **112**, 236–243 (2001).
- ¹⁴K. Kellens, R. Renaldi, W. Dewulf, J. P. Kruth, and J. R. Duflou, "Environmental impact modeling of selective laser sintering processes," *Rapid Prototyp. J.* **20**, 459–470 (2014).
- ¹⁵K. Wudy and D. Drummer, "Aging effects of polyamide 12 in selective laser sintering: Molecular weight distribution and thermal properties," *Addit. Manuf.* **25**, 1–9 (2019).
- ¹⁶K. Dotchev and W. Yusoff, "Recycling of polyamide 12 based powders in the laser sintering process," *Rapid Prototyp. J.* **15**, 192–203 (2009).
- ¹⁷F. M. Mwanja, M. Maringa, and K. Van Der Walt, "A review of methods used to reduce the effects of high temperature associated with polyamide 12 and polypropylene laser sintering," *Adv. Polym. Technol.* **2020**, 1–11.
- ¹⁸R. D. Goodridge, C. J. Tuck, and R. J. M. Hague, "Laser sintering of polyamides and other polymers," *Prog. Mater. Sci.* **57**, 229–267 (2012).
- ¹⁹T. Kigure and T. Niino, "Improvement of recycle rate in laser sintering by low temperature process," in *Collections of International Solid Freeform Fabrication Symposium* (2017).
- ²⁰L. Wang, A. Kiziltas, D. F. Mielewski, E. C. Lee, and D. J. Gardner, "Closed-loop recycling of polyamide12 powder from selective laser sintering into sustainable composites," *J. Cleaner Prod.* **195**, 765–772 (2018).
- ²¹A. Awad, F. Fina, A. Goyanes, S. Gaisford, and A. W. Basit, "3D printing: Principles and pharmaceutical applications of selective laser sintering," *Int. J. Pharm.* **586**, 119594 (2020).
- ²²N. A. Charoo, S. F. Barakh Ali, E. M. Mohamed, M. A. Kuttolamadom, T. Ozkan, M. A. Khan, and Z. Rahman, "Selective laser sintering 3D printing—An overview of the technology and pharmaceutical applications," *Drug Dev. Ind. Pharm.* **46**, 869–877 (2020).
- ²³M. Schmid and K. Wegener, "Additive manufacturing: Polymers applicable for laser sintering (LS)," *Proc. Eng.* **149**, 457–464 (2016).
- ²⁴L. Schelhorn, M. Gosch, L. Debeugny, P. Schröter, and W. Schwarz, "Soller S optimal design and process simulation for additive manufacturing," in *8th European Conference For Aeronautics and Space Sciences (EUCAST)* (2019).
- ²⁵L. J. Tan, W. Zhu, and K. Zhou, "Recent progress on polymer materials for additive manufacturing," *Adv. Funct. Mater.* **30**, 2003062 (2020).
- ²⁶M. Schneck, M. Horn, M. Schmitt, C. Seidel, G. Schlick, and G. Reinhart, "Review on additive hybrid- and multi-material-manufacturing of metals by powder bed fusion: State of technology and development potential," *Prog. Addit. Manuf.* **6**, 881–894 (2021).
- ²⁷V. A. Kumar, A. Dutta, and J. E. Fay, "Electrophotographic printing of part and binder powders," *Rapid Prototyp. J.* **10**, 7–13 (2004).
- ²⁸T. Stichel, C. Brachmann, M. Raths, M. A. Dechet, J. Schmidt, W. Peukert, T. Frick, and S. Roth, "Electrophotographic multilayer powder pattern deposition for additive manufacturing," *JOM* **72**, 1366–1375 (2020).
- ²⁹S. P. Kopp, T. Stichel, S. Roth, and M. Schmidt, "Investigation of the electrophotographic powder deposition through a transfer grid for efficient additive manufacturing," *Proc. CIRP* **94**, 122–127 (2020).
- ³⁰D. M. Pai and B. E. Springett, "Physics of electrophotography," *Rev. Mod. Phys.* **65**, 163–211 (1993).
- ³¹M. M. Shahin, "Mass-spectrometric studies of corona discharges in air at atmospheric pressures," *J. Chem. Phys.* **45**, 2600 (1966).
- ³²S. Matsusaka and H. Masuda, "Electrostatics of particles," *Adv. Powder Technol.* **14**, 143–166 (2003).
- ³³T. Stichel, B. Geißler, J. Jander, T. Laumer, T. Frick, and S. Roth, "Electrophotographic multi-material powder deposition for additive manufacturing," *J. Laser Appl.* **30**, 032306 (2018).
- ³⁴V. A. Kumar and A. Dutta, "Investigation of an electrophotography based rapid prototyping technology," *Rapid Prototyp. J.* **9**, 95–103 (2003).
- ³⁵D. Drummer, S. Greiner, M. Zhao, and K. Wudy, "A novel approach for understanding laser sintering of polymers," *Addit. Manuf.* **27**, 379–388 (2019).
- ³⁶T. Laumer, T. Stichel, P. Amend, and M. Schmidt, "Simultaneous laser beam melting of multimaterial polymer parts," *J. Laser Appl.* **27**, S29204 (2015).
- ³⁷T. Laumer, T. Stichel, D. Riedlbauer, P. Amend, J. Mergheim, and M. Schmidt, "Realization of multi-material polymer parts by simultaneous laser beam melting," *J. Laser Micro/Nanoeng.* **10**, 140–147 (2015).
- ³⁸J. A. Giacometti and O. N. Oliveira, "Corona charging of polymers," *IEEE Trans. Electr. Insul.* **27**, 924–943 (1992).
- ³⁹R. M. Faria, A. Jorge, and O. N. Oliveira, "A novel space-charge effect in thermally stimulated current measurements on β -PVDF," *J. Phys. D: Appl. Phys.* **23**, 334–337 (1990).
- ⁴⁰H. A. Pohl, "The motion and precipitation of suspensoids in divergent electric fields," *J. Appl. Phys.* **22**, 869–871 (1951).
- ⁴¹T. W. Dakin, "Breakdown of gases in uniform fields, Paschen curves for nitrogen, air and sulphur-hexafluoride," *Electra* **32**, 64–70 (1974).
- ⁴²A. Cserátóny-Hoffer, "Über den mechanismus des polaritätseffektes in der durchschlagspannung von gasen," *Period. Polytech. Electron. Eng.* **5**, 357–372 (1961).
- ⁴³A. Rakowska and K. Hajdrowski, "Influence of different test conditions on volume resistivity of polymeric insulated cables and polyethylene samples," *IEEE Conf. Publ.* **281**–284 (2000).
- ⁴⁴A. R. Blythe, "Electrical resistivity measurements of polymer materials," *Polym. Test.* **4**, 195–209 (1984).
- ⁴⁵L. J. Tan, W. Zhu, K. Sagar, and K. Zhou, "Comparative study on the selective laser sintering of polypropylene homopolymer and copolymer: Processability, crystallization kinetics, crystal phases and mechanical properties," *Addit. Manuf.* **37**, 101610 (2021).

5 Application potentials of EPA for PBF-LB/P in Pharmaceutical 3D Printing

Electrophotographic 3D printing of pharmaceutical films

Published in Additive Manufacturing 73 (2023), 103707

Sebastian-Paul Kopp^{a,b,c,*}, Vadim Medvedev^{a,b,c}, Katja Tangermann-Gerk^{a,c}, Natalie Wöltinger^a, Richard Rothfelder^{b,c,d}, Fabian Graßl^e, Markus R. Heinrich^e, Patricija Januskaite^f, Alvaro Goyanes^{f,g,h}, Abdul W. Basit^{f,g}, Stephan Roth^{a,b,c}, Michael Schmidt^{a,b,c,d}

^a Bayerisches Laserzentrum GmbH, 91052 Erlangen, Germany

^b Collaborative Research Center (CRC) 814 “Additive Manufacturing”, 91058 Erlangen, Germany

^c Erlangen Graduate School in Advanced Optical Technologies (SAOT), 91052 Erlangen, Germany

^d Friedrich-Alexander-University Erlangen-Nuremberg, Institute of Photonic Technologies (LPT), 91052 Erlangen, Germany

^e Friedrich-Alexander-University Erlangen-Nuremberg, Department of Chemistry and Pharmacy, Pharmaceutical Chemistry, 91058 Erlangen, Germany

^f University College London, Department of Pharmaceutics, UCL School of Pharmacy, London WC1N 1AX, United Kingdom

^g FabRx Ltd., Ashford TN24 8DH, United Kingdom

^h Universidade de Santiago de Compostela (USC), Departamento de Farmacología, Farmacia y Tecnología Farmacéutica, I+D Farma Group (GI-1645), Facultad de Farmacia, iMATUS and Health Research Institute of Santiago de Compostela (IDIS), Santiago de Compostela 15782, Spain

*Corresponding author.

Tel.: +49-9131-97790-27; E-mail address: s-p.kopp@blz.org

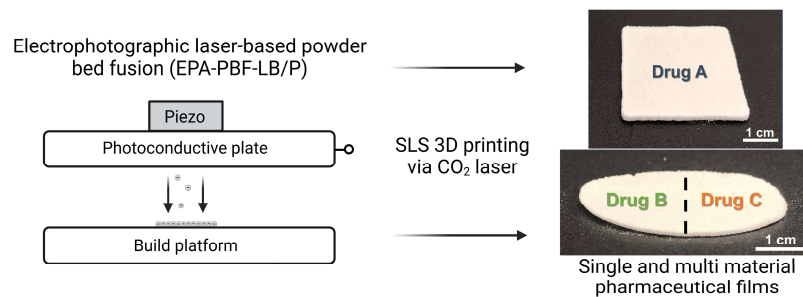


Figure 18: Manufacturing multi-material pharmaceutical parts by EPA-PBF-LB/P.

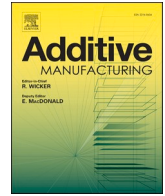
It has already been shown in section 4.4 that EPA has the potential to overcome some of the limitations of conventional PBF-LB/P (cf. section 2.1.2). In particular, it can be used to process powder materials with poor flow properties, significantly reduce the powder waste of PBF-LB/P and enable the production of multi-material parts. In this study, the full potential of EPA-PBF-LB/P is investigated by processing powder materials with strongly differing thermal property profiles, in particular different thermal degradation temperatures. Furthermore, the flow properties of the powders are not adapted to the needs of conventional application methods. The pharmaceutical powders and in particular the drugs processed in this study require a reduction of the layer thickness to a minimum, i.e., to the diameter of the particles used. This is due to the fact that by reducing the layer thickness, the laser energy required for consolidating a layer is also reduced, thus avoiding thermal damage to the drug with the lowest thermal degradation threshold.

The ability to accurately measure drug content by high performance liquid chromatography (HPLC) allows accurate determination of cross-contamination caused by EPA-PBF-LB/P. In addition, the effect of electrostatic separation, which is attributed to varying particle properties, is revealed and investigated.

The findings of this study serve as the basis for a further patent application [221].

Highlights:

- Understanding of the powder transfer behavior in EPA as a function of particle size and shape
- Possibility to fabricate pharmaceutical multi-material parts by laser-based powder bed fusion using a CO₂ laser for the first time without thermal damage to the active pharmaceutical ingredients (APIs)
- Elimination of the need to increase the laser absorption of the pharmaceutical powders by adding dyes or absorbing particles due to the ability to use PBF-LB/P with a CO₂ laser without thermal damage to the APIs
- Knowledge of the cross-contamination caused by EPA resulting from false print and insufficient particle adhesion to the photoconductor



Electrophotographic 3D printing of pharmaceutical films

Sebastian-Paul Kopp^{a,b,c,*}, Vadim Medvedev^{a,b,c}, Katja Tangermann-Gerk^{a,c},
Natalie Wöltinger^a, Richard Rothfelder^{b,c,d}, Fabian Graßl^e, Markus R. Heinrich^e,
Patricija Januskaite^f, Alvaro Goyanes^{f,g,h}, Abdul W. Basit^{f,g}, Stephan Roth^{a,b,c},
Michael Schmidt^{a,b,c,d}

^a Bayerisches Laserzentrum GmbH, 91052 Erlangen, Germany

^b Collaborative Research Center (CRC) 814 "Additive Manufacturing", 91058 Erlangen, Germany

^c Erlangen Graduate School in Advanced Optical Technologies (SAOT), 91052 Erlangen, Germany

^d Friedrich-Alexander-University Erlangen-Nuremberg, Institute of Photonic Technologies (LPT), 91052 Erlangen, Germany

^e Friedrich-Alexander-University Erlangen-Nuremberg, Department of Chemistry and Pharmacy, Pharmaceutical Chemistry, 91058 Erlangen, Germany

^f University College London, Department of Pharmaceutics, UCL School of Pharmacy, London WC1N 1AX, United Kingdom

^g FabRx Ltd., Ashford TN24 8DH, United Kingdom

^h Universidade de Santiago de Compostela (USC), Departamento de Farmacología, Farmacia y Tecnología Farmacéutica, I+D Farma Group (GI-1645), Facultad de Farmacia, iMATUS and Health Research Institute of Santiago de Compostela (IDIS), Santiago de Compostela 15782, Spain

ARTICLE INFO

Keywords:

Additive manufacturing
Electrophotography
Printed pharmaceuticals
Laser powder bed fusion
Laser sintering
Multi-material printing

ABSTRACT

The usage of three-dimensional (3D) printing in pharmaceutical applications offers significant advantages compared to conventional manufacturing approaches such as tableting or encapsulation. Laser sintering (LS), also referred to as powder bed fusion – laser beam (PBF-LB), formerly also known as selective laser sintering (SLS), offers the production of pharmaceuticals directly from a powder mixture with high geometrical flexibility and adjustable release profiles. However, due to limitations of conventional powder application methods for PBF-LB, neither the material composition nor the material distribution can be tailored within a printed layer. To overcome these restrictions, electrophotographic powder application (EPA), a novel method for selective powder application, was utilized in this study. EPA allows the deposited layer thickness to be reduced to values between 12 and 76 μm , depending on the used pharmaceutical powder blend. Thus, the laser energy input required for interlayer connection can be reduced, enabling the use of a CO₂ laser. In this study, for the first time, EPA in combination with powder bed fusion – laser beam of polymers (EPA-PBF-LB/P) was utilized to successfully deposit and print three different model drugs: paracetamol, nicotinamide, and caffeine, mixed with Eudragit L 100–55, a pharmaceutical grade polymer. Through the use of EPA, thin layers of powder blends were successfully deposited in the build chamber, leading to no thermal degradation of the polymer or drugs from the use of a CO₂ laser. Single- and multi-material pharmaceutical films were successfully printed via EPA-PBF-LB, utilizing EPA to selectively as well as precisely apply different powders within a single layer into the build chamber. This introduces a novel method of printing pharmaceuticals using SLS with a CO₂ laser and without the use of additional colorants.

1. Introduction

Additive manufacturing (AM) processes, often referred to as three-dimensional (3D) printing (3DP), involve the layer-by-layer deposition of material to generate objects from computer aided design (CAD) files [1]. This innovative technology has become indispensable in a wide range of industries today, from aerospace [2] to automotive [3] and

medical [4] applications as well as in construction [5–7], offering a high degree of flexibility and the possibility to generate parts with complex geometries, from a variety of materials [8]. Driven by the demand for smarter and more personalized medicines and treatment, 3DP of pharmaceuticals has emerged and developed significantly in recent years [9–12]. An important milestone in the evolution of 3D printed pharmaceuticals was marked by the successful approval of the world's first

* Corresponding author at: Bayerisches Laserzentrum GmbH, 91052 Erlangen, Germany.

E-mail address: s-p.kopp@blz.org (S.-P. Kopp).

<https://doi.org/10.1016/j.addma.2023.103707>

Received 2 March 2023; Received in revised form 25 June 2023; Accepted 21 July 2023

Available online 26 July 2023

2214-8604/© 2023 The Author(s). Published by Elsevier B.V. This is an open access article under the CC BY license (<http://creativecommons.org/licenses/by/4.0/>).

Table 1
Composition overview of powder blends; 30 g per mixture.

Powder blend number:	Eudragit content / wt%	Theoretical drug loading P / wt%	Theoretical drug loading N / wt%	Theoretical drug loading C / wt%
1	95	5	-	-
2	90	10	-	-
3	85	15	-	-
4	95	-	5	-
5	90	-	10	-
6	85	-	15	-
7	95	-	-	5
8	90	-	-	10
9	85	-	-	15

3D printed drug product, an orodispersible epilepsy treatment under the name of Spritam®, by the U.S. Food and Drug Administration (FDA) in 2015 [13,14]. Research into pharmaceutical 3DP has developed at a rapid rate, with the technology being used to manufacture pediatric friendly chewable dosage forms [15], multi-layered polypills [16], LEGO like compartmental tablets for tailored drug release [17], drug-loaded contact lenses [18], and transdermal microneedles [19].

Based on the American Society for Testing and Materials (ASTM) International, the vast number of 3DP technologies have been classified into seven broad categories: binder jetting, vat polymerization, powder bed fusion, material extrusion, material jetting, directed energy deposition, and sheet lamination [20]. Laser sintering (LS), often referred to as powder bed fusion – laser beam (PBF-LB) or formerly as selective laser sintering (SLS) [21,22], involves the selective consolidation of powder particles via a laser source to form a 3D object [23]. This is particularly beneficial in the field of pharmaceutical AM, since most of the materials, excipients and drugs, are available as powders. On the contrary, in other 3DP technologies such as FDM, they need to be further processed into filaments [23–25]. PBF-LB has been extensively investigated in pharmaceutical research due to its solvent free process and high resolution obtained from the laser source and is capable of manufacturing orally disintegrating Printlets™ (3D printed tablets) [22], tablets with braille and moon patterns for patients with visual impairment [26], and miniprintlets for dose personalization [27].

In conventional PBF-LB, powder application is carried out by doctor blade- or roller-based application methods, associated with strict requirements concerning powder flowability [28,29]. Therefore, particle shape [30], interparticle distance and particle size distribution [31], which should lie in the range of 70 – 120 µm [32,33], play a decisive role. Thus, many powder materials are not suitable for PBF-LB with conventional powder application or need to be functionalized with flow aids [34]. A further limitation attributable to conventional powder application methods in PBF-LB is the minimum layer thickness. With doctor blade- or roller-based powder application, the minimum layer thickness in the field of pharmaceutical PBF-LB is between 100 and 200 µm [35–38]. Due to the resulting large powder volume and thus high laser energy required to achieve interlayer connection, the use of carbon dioxide (CO₂) lasers has exceeded the degradation threshold of drugs in previous studies [22,38]. This is mainly due to high absorptance above 80% of polymer powders at CO₂ laser emission wavelength of 10.6 µm [39–43], leading to strong heating of the powder surface and therefore drug degradation. Although conventional PBF-LB of polymer powders mainly employs CO₂ lasers [44–49], pharmaceutical PBF-LB is conducted using diode lasers in the visible spectral range to decrease the energy input [22,47]. This, however, requires the addition of absorbing particles, such as pharmaceutical grade colorants to the powders, to ensure sufficient absorptance [22,47]. Beyond that, doctor blade- or roller-based powder application methods do not allow the material composition to be modified within a powder layer [50]. This strongly limits the capabilities of PBF-LB to generate multi-material parts, and in case of pharmaceutical AM, multi-drug pharmaceuticals [22,24,27,51].

However, being able to flexibly tailor the material composition and distribution in PBF-LB within one layer and from layer to layer would significantly increase the potential of personalizing and adapting medicines to patients' needs [52,53].

A promising new powder deposition approach for overcoming the aforementioned limitations is electrophotographic powder application (EPA) [33,54–59]. EPA can be divided into six main process steps: 1 – charging of the powder and a plate coated with a photoconductive layer, the so-called photoconductive plate (PCP), 2 – partial discharging of the PCP to create a latent charge image, 3 – electrostatic attraction of powder particles to the PCP, the so-called development step, 4 – powder deposition into the build chamber, 5 – selective powder fusion by laser radiation, and finally 6 – cleaning of the PCP [55,56]. Applying EPA to PBF-LB (EPA-PBF-LB) makes powder application independent of the powder flowability [33,56], which is particularly beneficial for pharmaceutical PBF-LB. Unlike conventional powder application methods [60–62], EPA does not require the entire build volume within the build chamber to be filled with powder [54–56,63,64]. Instead, EPA precisely as well as selectively applies powder portions only at positions required for the respective parts to be built [54–56]. This allows different drugs to be combined within one layer, at the same time significantly increasing the powder efficiency [56]. This avoids thermal stress of partcake material, i.e., powder portions which are not directly processed to generate the actual part [56,65]. Thus, exposure times of powder materials to elevated temperatures within the build chamber [65,66] can be reduced to a minimum. This is crucial for pharmaceutical PBF-LB to reduce thermal stress of the respective drugs [24,67].

In this study, for the first time, EPA was applied to pharmaceutical PBF-LB in order to generate drug loaded films. For this purpose, all six process steps of EPA, which are described in detail in [55–57,64], were employed. The main focus was to gain knowledge about the electrophotographic powder application behavior of powder blends consisting of a pharmaceutical grade polymer and different weight percentages of various drugs, giving insights to decisive properties such as coverage, thickness, homogeneity and surface potential of the deposited powder layers and possible separation effects of the powder blend components. Based on this, the applicability of EPA for pharmaceutical 3DP was validated by generating single- and multi-drug films. The possibility of EPA to deposit significantly thinner layers compared to conventional powder application processes [55,56] was utilized to reduce the CO₂ laser energy input required during PBF-LB. Therefore, the potential of applying a CO₂ laser, which is still the standard laser source for PBF-LB of polymers (PBF-LB/P) [44–49], in combination with EPA to avoid thermal degradation [22,38,47,49,68] of the drugs was investigated.

2. Materials and methods

2.1. Materials

Eudragit L 100–55 (molecular weight (MW) 320.000 g/mol), a copolymer of methacrylic acid and ethyl acrylate (1:1 ratio), was purchased from Evonik Röhm GmbH, Darmstadt, Germany. All three model drugs, caffeine (MW 194.19 g/mol), paracetamol (MW 151.16 g/mol), and nicotinamide (MW 122.12 g/mol), were obtained from Sigma-Aldrich, Dorset, UK. Acetonitrile (ACN) (LC-MS grade) and formic acid (LC-MS grade) for drug quantification were obtained from Fisher Scientific GmbH (Schwerte, Germany). Ultra-pure water was taken from a MilliQ® Reference A+ system (Merck KGaA, Darmstadt, Germany).

2.2. Powder preparation

Powder blends consisting of polymer and drug were prepared in a shaking mixer (Type T2f, Willy A. Bachofen AG, Muttenz, Switzerland) with a rotational speed of 49 revolutions per minute (rpm). Mixing time was set to 30 min for each powder blend whereas decay time for charges generated during mixing was set to 48 h. For weighing the respective

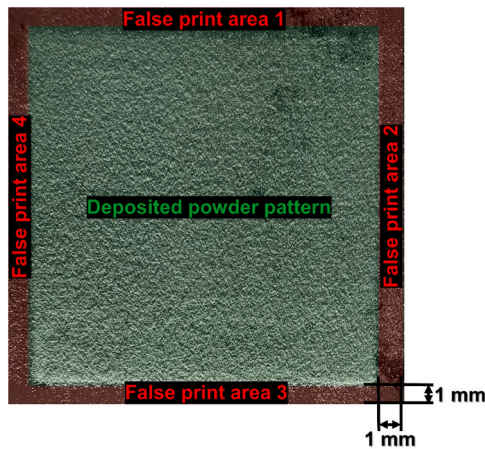


Fig. 1. Overview of different areas for coverage analysis; green: geometry of deposited powder pattern; red: four rectangular areas defined for determining the false print surrounding the actual powder pattern.

constituents of the powder blends, a high precision balance (XS 105, Mettler Toledo Inc., Columbus, OH, USA) with a reproducibility of $\leq \pm 0.02$ mg, according to the manufacturer [69], was utilized.

Eudragit L 100–55, which has already been printed successfully by PBF-LB [47,51,70], was used as the excipient in this work. Eudragit L 100–55 is a thermoplastic pharmaceutical grade polymer and dissolves at pH 5.5 and above [51]. The excipient was blended with three different model drugs, caffeine (C), nicotinamide (N) and paracetamol (P), respectively (Table 1).

2.3. Particle size analysis

Particle size distributions of the polymer and all model drugs used in this study was assessed by laser diffractometry, using a Mastersizer 3000 fitted with an Aero S feeding system for dry samples (Malvern Scientific, Worcestershire, UK). Analysis was carried out at a gauge pressure of 2 bar and a feed rate of 50%. Three replicates of each sample were analyzed to find the average for $x_{10,3}$, $x_{50,3}$ (mass median diameter), and $x_{90,3}$ parameters. Measurements were analyzed and plotted using the Mastersizer 3000 software, v3.62 (Malvern Scientific, Worcestershire, UK).

2.4. Differential scanning calorimetry (DSC)

For analyzing the thermal properties of pure Eudragit L 100–55 as well as of the respective powder blends, differential scanning calorimetry (DSC) analysis was performed non-isothermally with a DSC 822e (Mettler Toledo Inc., Columbus, OH, USA). 10 mg of each sample were placed in standardized, covered 40 μ l aluminum pans. The heating as well as cooling rates were set to 10 K/min and nitrogen with a flow rate of 40 ml/min was used as a purge gas. The DSC measurement was performed in a temperature range between 25 $^{\circ}$ C and 230 $^{\circ}$ C without preliminary heating. For statistical analysis, the number n of measurements was $n = 3$. Data evaluation was conducted with Mettler Toledo STARE Evaluation software version 17.00 employing baselines of type line and integral tangential (for evaluating the endothermic degradation peak at around 200 $^{\circ}$ C) for calculating the relevant enthalpies by integration of the heat flow curves [71,72]. The enthalpies were normalized by sample mass.

2.5. Scanning electron microscopy (SEM)

The surface and microstructure of the powder particles were examined by a scanning electron microscope (SEM) (Zeiss Merlin, Carl Zeiss AG, Oberkochen, Germany). The powders were applied on double-sided

adhesive carbon pads and sputtered with a thin gold layer to ensure electrical conductivity. The powder particles were then examined by SEM using the secondary electron detector (SE) with an acceleration voltage of 10 kV, a probe current of 1.1 nA and a working distance of 10 mm.

2.6. Electrostatic surface potential

The measurement of the surface potential of the powder layers after deposition into the build chamber was conducted using an electrostatic voltmeter type ISOPROBE model 244 A equipped with a probe model 1017AE (both Monroe Electronics Inc., Lyndonville, NY, USA). The probe was placed at a separation distance of 3 mm above the deposited powder layer to be analyzed. To analyze the powder application behavior of EPA with pharmaceutical powder materials, powder layers with a square geometry of 100 mm \times 100 mm were deposited. The surface potential of each deposited powder layer was measured at nine equidistant positions, homogeneously distributed over the deposited square powder layer. From this, the mean surface potential and the standard deviation were calculated.

2.7. Determination of the effective layer thickness (ELT) using a 3D laser scanner

The layer thickness of the deposited powder layers was determined with a 3D laser scanner (scanCONTROL 2900–50, Micro-Epsilon Messtechnik GmbH & Co. KG, Ortenburg, Germany), offering a resolution of 4 μ m according to the manufacturer [73]. A comparable approach was already reported in [74]. The separation distance between powder layer and measurement device was set to 100 mm to fit the 1280 measurement points of one laser line [73] into the deposited square powder layer geometry. The utilized 3D laser scanner measures an absolute height profile line by line. Therefore, first the absolute height profile of the build platform was determined at three equidistant lines for referencing, yielding h_{R1abs} , h_{R2abs} , h_{R3abs} . After electrophotographic application of a powder layer, the absolute height profile of the deposited layer was measured using the positions of the three equidistant reference lines h_{L1abs} , h_{L2abs} , h_{L3abs} . Subtracting the absolute reference height profiles from the respective absolute height profiles of the deposited powder layer and calculating the mean value for three lines yielded the mean effective layer thickness \overline{ELT} (1):

$$\overline{ELT} = \frac{|(h_{L1abs} - h_{R1abs}) + (h_{L2abs} - h_{R2abs}) + (h_{L3abs} - h_{R3abs})|}{3} \quad (1)$$

2.8. Measurement of part dimensions

The dimensions of the printed parts were measured with a precision caliper (Burg-Wächter KG, Wetter-Volmarstein, Germany), which had a measurement uncertainty of 0.01 mm.

2.9. Coverage analysis

For access to the powder coverage values of the deposited powder layers, an optical measurement procedure, which is based on [55], was applied. Images of the deposited layers were taken with a Basler ace 2 camera (type a2A2448–75ucBAS, Basler AG, Ahrensburg, Germany) with an optical resolution of 2472 \times 2064 pixels. As described in [55], the images were first transformed into 8-bit grayscale images. After, in this case – due to lighting conditions – the triangle thresholding method [75–77] was applied to make the images binary. Finally, three equally distributed rectangular areas were selected within the deposited powder patterns and a comparison of black (no powder) and white (pixels) was conducted, yielding the respective coverage values. From that, the mean coverage and standard deviation were calculated for each powder layer deposited. Furthermore, the false print was determined analogously,

Table 2

Experimental parameters of EPA-PBF-LB for generating pharmaceutical test samples.

Parameter	Value
Laser power	18.3 W (paracetamol) 24.0 W (nicotinamide) 18.9 W (caffeine)
Laser hatching distance	0.1 mm
Laser scanning speed	900 mm/s
Preheating temperature	125 °C
Polarity and charging field strength PCP	+167 kV/m
Polarity and charging field strength powder	±167 kV/m
Polarity and development field strength	±2461 kV/m
Polarity and deposition field strength	±2900 kV/m
Frequency of sinusoidal signal for piezo excitation	15 kHz
Peak-to-peak voltage of sinusoidal signal	8 V _{p-p}

whereby false print, based on previous work in [55], is defined here as powder coverage within four rectangular areas with a width of 1 mm surrounding the actual deposited powder pattern (cf. Fig. 1).

2.10. Laser-based powder bed fusion using electrophotographic powder application

EPA-PBF-LB can be divided into six main process steps [54,58], which are described in detail in [55,56]. Essentially, EPA uses the principle of electrostatic attraction and repelling forces to selectively attract powder particles, in this context also called powder development, or to deposit powder particles. An aluminum plate coated with a photoconductive layer, in this context referred to as photoconductive plate (PCP), is used to transfer the developed powder layers from an area where the various powder reservoirs are located at room temperature, to the actual build chamber. The surface temperature of the PCP can be tailored by internal fluid channels using a heat transfer fluid as described in detail in [78]. This allows to keep the temperature of the transferred particles relatively constant during the EPA process independently of the temperature of the build chamber. Powder charging was performed using the gas discharge-based charging method [54–56,64], which does not require functionalization of powder particles for tailoring their

charging behavior as is the case with triboelectric charging [33]. The experimental setup including a piezo for increasing the powder deposition efficiency by piezoelectric excitation (excitation parameters are given in Table 2) of the PCP is described in [55]. As extensively discussed in [55], for the powder deposition step a piezoelectric excitation together with an electric deposition field $\vec{E}_{\text{deposition}}$ was applied between PCP and the build platform or the grounded transfer frame, respectively [54]. This is also described in detail in [78]. Especially in case of growing part height, the transfer frame, which is movable in z-direction, becomes crucial for maintaining a sufficiently strong deposition field strength and thus powder deposition efficiency [54,56]. Combining the electric deposition field with the piezoelectric excitation, which allows to reduce the van der Waals attraction forces between the particles and the PCP, the electric deposition field determines the motion of the particles [55]. Besides the transfer frame for tailoring and maintaining the electric transfer field and the piezoelectric excitation for enhancing powder deposition efficiency, a third strategy was applied for ensuring high deposition efficiency in case of growing part height. This strategy is based on alternating the charging polarity of the deposited powder layers in order to avoid parasitic charge accumulation inside the generated part. This strategy is described and validated in detail in [56, 78]. An overview of the EPA-PBF-LB/P setup is shown in Fig. 2.

For efficient local preheating, the EPA-PBF-LB build chamber was equipped with a preheating setup consisting of a heating stage (RCT basic, IKA-Werke GmbH, Staufen im Breisgau, Germany) according to [56]. Based on the theory of quasi-isothermal PBF-LB [66], the preheating was set to a temperature between melting onset and crystallization onset of the polymer to avoid premature recrystallization associated with curling [56,66]. Since the crystallization onset temperature of Eudragit L 100–55 was measured by DSC in this study to be at 123.44 ± 0.20 °C, the preheating temperature was set to 125 °C. In case of part thicknesses $\gg 1$ mm, local preheating using a heating stage would need to be supported / replaced by a global preheating strategy, comparable to conventional PBF-LB/P machines.

Furthermore, for fusing the layers, an optical setup consisting of a CO₂-laser providing a maximum output power of 60 W (Synrad ti60, Novanta Photonics, Seattle, WA, USA), a laser scanner Miniscan II-20 and a F-Theta lens, which has a focal length of $f = 420$ mm

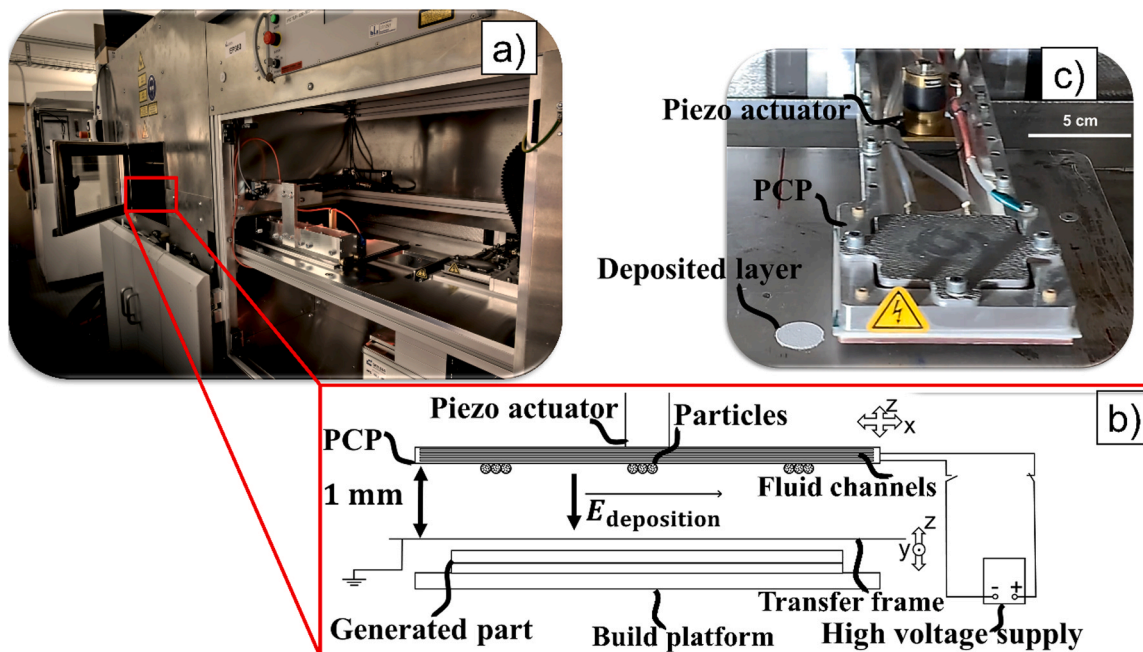


Fig. 2. a) image of the EPA-PBF-LB/P setup; b) schematic overview of the powder deposition (printing) step; c) image of PCP after depositing one layer onto the EPA-PBF-LB/P build platform.

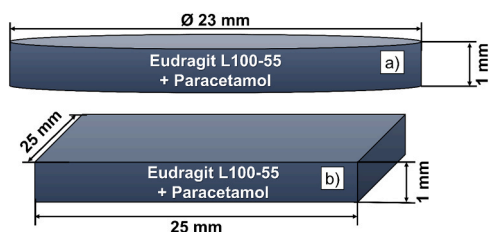


Fig. 3. Dimensions of a) cylindrical and b) cuboidal mono-drug test samples; both printed using powder blend number 3 (85 wt% Eudragit L 100–55 and 15 wt% paracetamol).

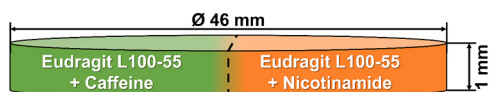


Fig. 4. Dimensions of cylindrical multi-drug test sample; printed using powder blends number 5 (90 wt% Eudragit L 100–55 and 10 wt% nicotinamide) and number 8 (90 wt% Eudragit L 100–55 and 10 wt% caffeine).

Table 3
Calibration curves of drug standards.

Drug	Retention time / min	Detection wavelength / nm	Linear equation	R ²
Nicotinamide	1.92	247	$y = 6113.2x - 2.3554$	1
Paracetamol	4.70	247	$y = 20725x + 16.515$	0.9999
Caffeine	5.45	275	$y = 14714x + 12.165$	0.9999

(both Raylase GmbH, Weßling, Germany), was utilized. A summary of the parameters used for conducting the experiments is given in Table 2.

Two different geometries referring to [79] were used for generating mono-drug samples within this study. Fig. 3 shows the dimensions of a cylindrical and a cuboidal test sample, respectively. Both samples were printed using powder blend number 3 (cf. Table 1).

For investigating the capability of EPA-PBF-LB to generate multi-drug objects, the dimensions visualized in Fig. 4 with a transition area between the caffeine and nicotinamide loaded parts were applied. For this purpose, powder blends number 5 and 8 (cf. Table 1) were selectively developed and deposited by EPA and fused for printing the multi-

drug test samples.

2.11. Quantitative analysis of drug loading of powder mixtures and printed test samples

The powder blends and 3D printed samples were analyzed on an Agilent 1200 high-performance liquid chromatography (HPLC) system equipped with a G1315B DAD (both Agilent Technologies, Santa Clara, CA, USA) and a Phenomenex Gemini NX-C18 110 Å column (250 mm × 4.6 mm, particle size 5 μm) (Phenomenex Inc. Torrance, CA, USA). Mobile phase A consisted of 0.1% v/v formic acid in water and mobile phase B of 0.1% v/v formic acid in ACN. The column was operated at 25 °C with the following gradient (min/%B): – 5.0/0, 0.0/0, 15.0/90, 18.0/90, flow rate: 2.0 ml / min, injection volume: 10 μl. All samples were dissolved in water:ACN 50:50 (v/v) + 0.1% formic acid and filtered (pore size 0.45 μm) (VWR International GmbH, Darmstadt, Germany) before measurement. For the determination of calibration curves, serial dilutions of the respective standards with concentrations ranging from 0.01 mg / ml – 0.4 mg / ml for nicotinamide and 0.01 mg / ml – 0.2 mg / ml for paracetamol and caffeine were measured. In the case of the 3D printed films, small samples weighing roughly 10 mg were broken off and dissolved in 10 ml of solvent. For powder samples approximately 10 mg powder mix was dissolved in 10 ml of solvent. All measurements of 3D printed films and powder blends were done in triplicate. The calibration curves of drug standards are given in Table 3. More details about the determination of the linear equations are given in the appendix.

3. Results and discussion

3.1. Microstructural analysis of pure polymer and powder blends by SEM

As can be seen in Fig. 5a), pure Eudragit L 100–55 consists of spherical particles. They have no visible nanoparticle-based surface functionalization, as is often the case with polymer powders typically used for PBF-LB [33,80–82]. Compared to the drug particles visible in Fig. 5b), c) and d), the nearly perfectly spherical Eudragit particles do not show surface defects such as craters or holes. This decreases the probability for ions, which serve as charge carriers for the gas discharge-based powder charging method applied in this study, to be stored on the particle surface [83,84]. Thus, the microstructural differences between Eudragit L 100–55 and the three investigated drugs suggest the particle charging during powder application to vary. Since the powder transfer behavior of EPA strongly depends on the respective particle charging, an electrostatic separation between polymer and the three investigated drugs may occur.

However, this may be partially compensated by the fact that small-sized Eudragit particles with diameters of around 10 μm adhere to the

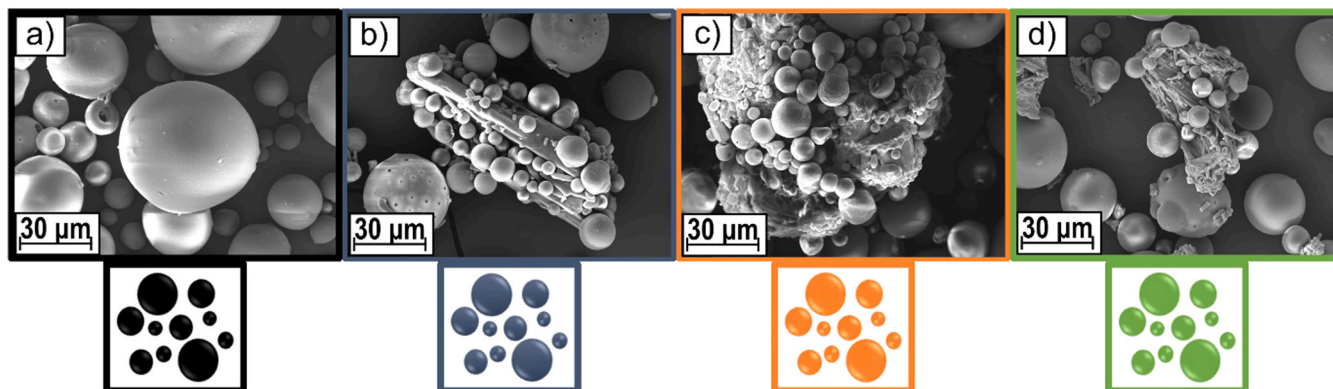


Fig. 5. SEM images of a) pure Eudragit L 100–55 particles; SEM images of b) paracetamol, c) nicotinamide and d) caffeine taken from the respective drug particles after mixing 15 wt% of the drug with 85 wt% of Eudragit L 100–55.

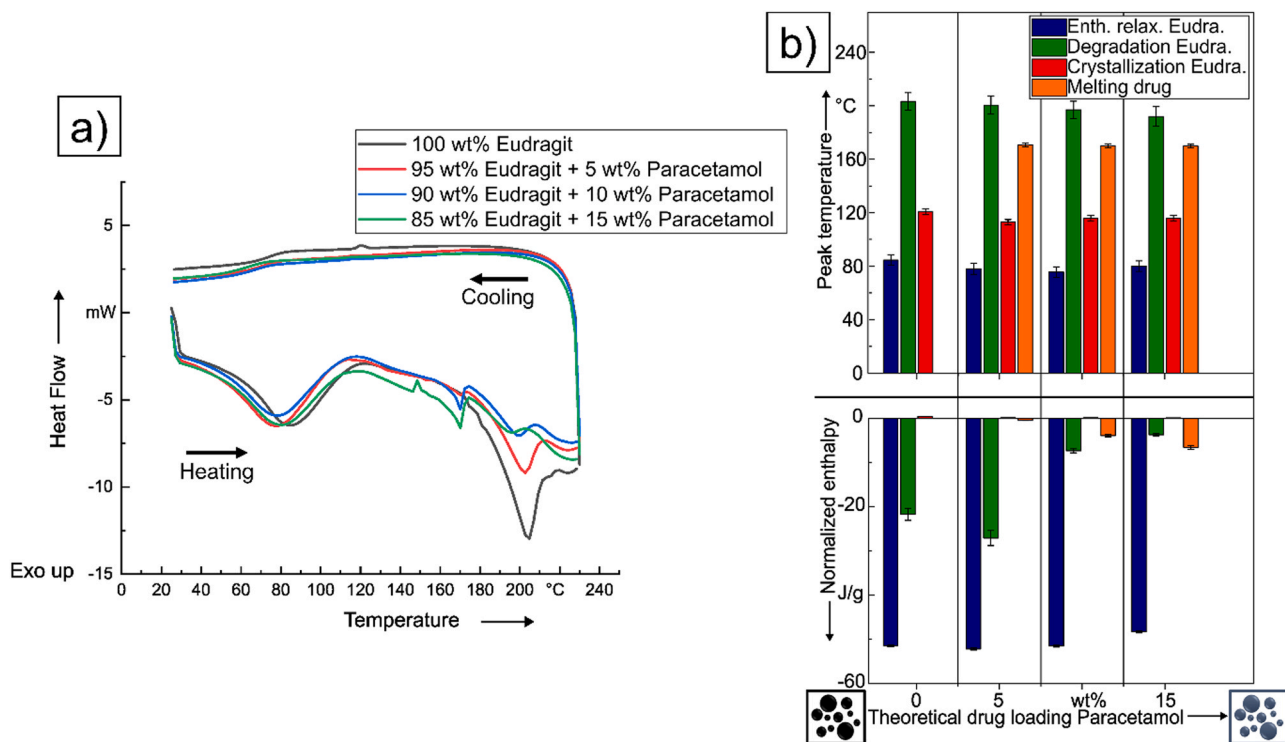


Fig. 6. a) DSC curves of powder blends consisting of Eudragit L 100–55 and paracetamol; b) selected peak temperatures and normalized enthalpy values of powder blends consisting of Eudragit L 100–55 and paracetamol as a function of paracetamol content; number of measurements $n = 3$.

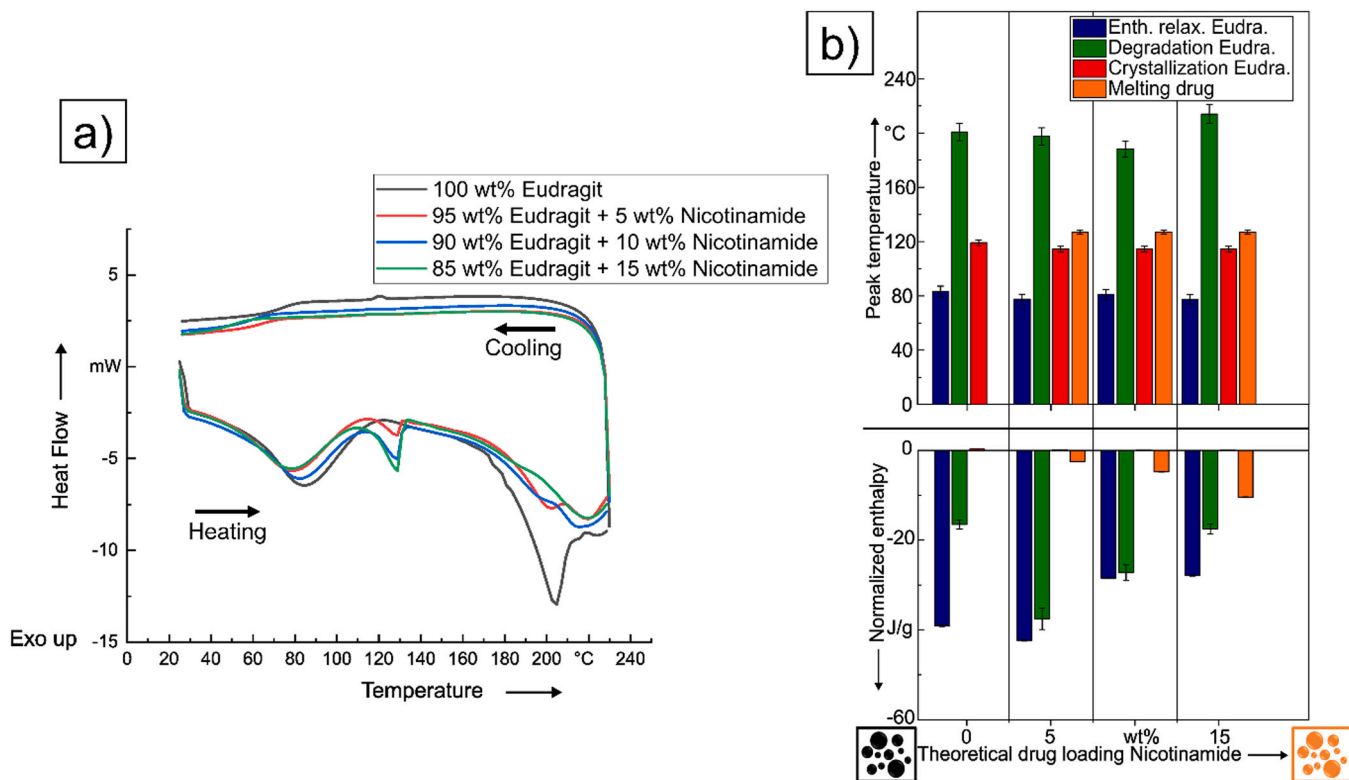


Fig. 7. a) DSC curves of powder blends consisting of Eudragit L 100–55 and nicotinamide; b) selected peak temperatures and normalized enthalpy values of powder blends consisting of Eudragit L 100–55 and nicotinamide as a function of nicotinamide content; number of measurements $n = 3$.

surface of the respective drugs (cf. Fig. 5b), c) and d)). This is most likely due to van der Waals and electrostatic attraction forces, causing the smaller polymer particles to adhere to the larger drug particles [33].

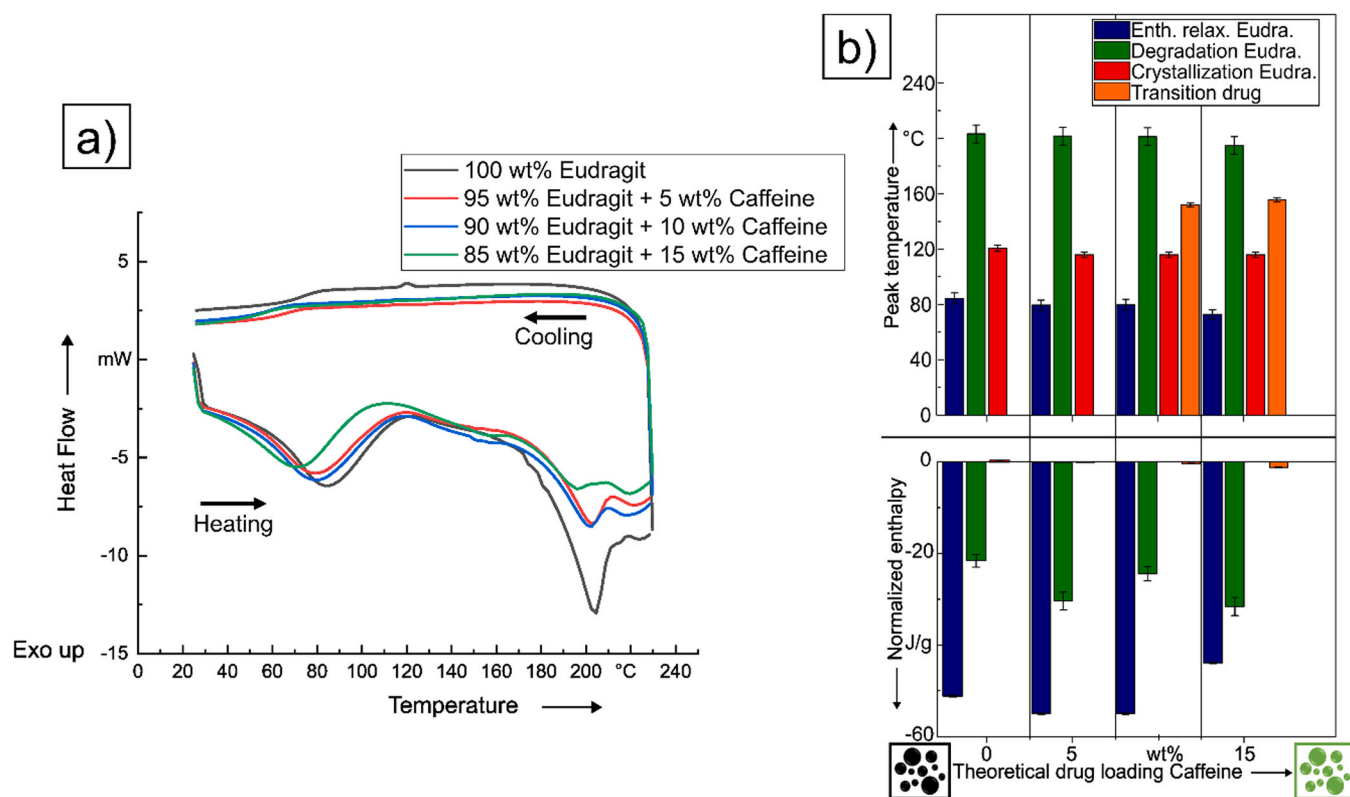


Fig. 8. a) DSC curves of powder blends consisting of Eudragit L 100–55 and caffeine; b) selected peak temperatures and normalized enthalpy values of powder blends consisting of Eudragit L 100–55 and caffeine as function of caffeine content; number of measurements $n = 3$.

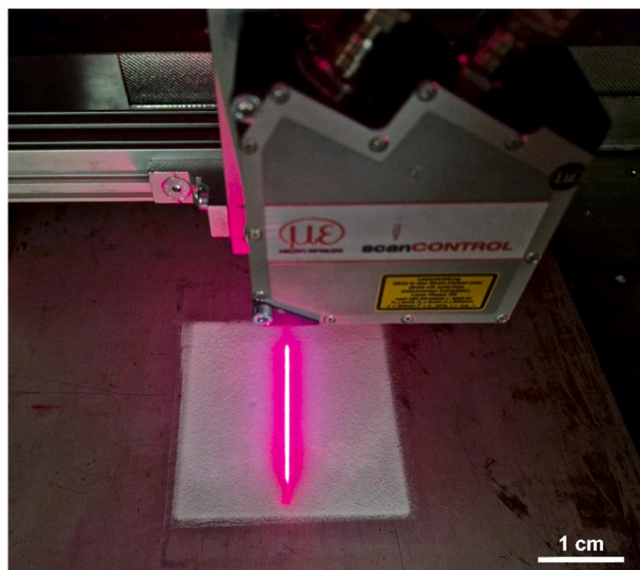


Fig. 9. Exemplary powder layer (in this case consisting of 95 wt% Eudragit L100–55 and 5 wt% paracetamol (powder blend no. 1) deposited into the EPA-PBF-LB/P build chamber during measurement of the layer thickness.

3.2. Thermal analysis of pure Eudragit L 100–55 and drug loaded powder blends

The aim of this section was to determine a suitable PBF-LB processing window for preheating the powder blends used in this study. Selected thermal properties of Eudragit L 100–55 and the powder blends listed in Table 1 are visualized in Figs. 6, 7, and 8. Here, the most relevant

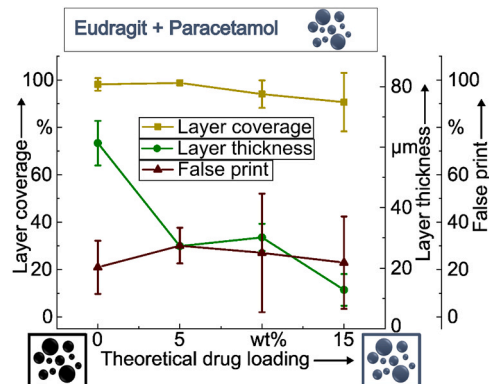


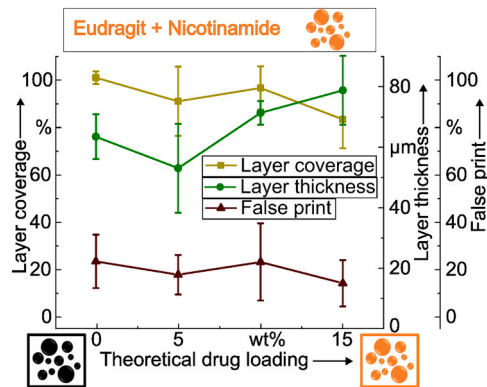
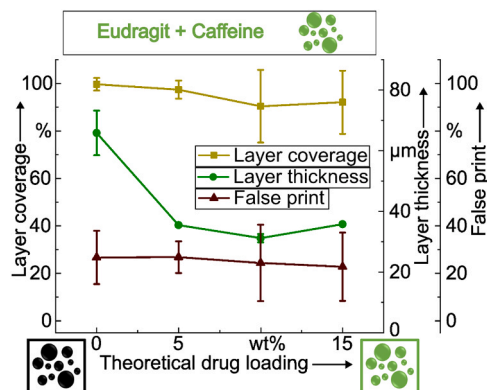
Fig. 10. Layer coverage, layer thickness and false print of powder blends consisting of Eudragit L 100–55 and different weight percentages of paracetamol as a function of the drug loading; number of measurements $n = 3$ for layer coverage and layer thickness, and $n = 4$ for false print.

thermal properties with respect to processability in PBF-LB were selected. For finding suitable PBF-LB process parameters, i.e., a suitable preheating temperature and appropriate laser parameters (laser power, hatching distance and scanning speed), the melting as well as recrystallisation temperatures of the polymer or individual constituents of the polymer blend are crucial.

The broad endothermic peak present in all DSC results around 80 – 100 °C is attributed to the enthalpy relaxation of Eudragit L 100–55 as an amorphous polymer, which is described elaborately in [89,90]. As specified and validated via thermogravimetric analysis (TGA) in [91, 92], methacrylic acids begin to form anhydrides at around 170 °C by structural rearrangement and water loss. Most probably, the peak temperature at around 200 °C visible in Figs. 6, 7, and 8 can be attributed to

Table 4Particle size and density values of the powders used in this work; number of measurements $n = 3$.

Powder	Diameter $x_{10,3} / \mu\text{m}$	Mass median diameter $x_{50,3} / \mu\text{m}$	Diameter $x_{90,3} / \mu\text{m}$	Density / g cm^{-3}
Eudragit L 100–55	18.1 \pm 1.12	46.0 \pm 1.19	88.5 \pm 4.43	0.821 – 0.840[85]
Caffeine	5.48 \pm 0.33	35.4 \pm 3.89	126 \pm 17.6	1.23[86]
Nicotinamide	30.2 \pm 3.99	113 \pm 6.72	203 \pm 26.0	1.40[87]
Paracetamol	6.76 \pm 0.243	40.6 \pm 3.46	175 \pm 44.5	1.293[88]

**Fig. 11.** Layer coverage, layer thickness and false print of powder blends consisting of Eudragit L 100–55 and different weight percentages of nicotinamide as a function of the drug loading; number of measurements $n = 3$ for layer coverage and layer thickness, and $n = 4$ for false print.**Fig. 12.** Layer coverage, layer thickness and false print of powder blends consisting of Eudragit L 100–55 and different weight percentages of caffeine as a function of the drug loading; number of measurements $n = 3$ for layer coverage and layer thickness, and $n = 4$ for false print.

the degradation of Eudragit L 100–55 (according to [93,94] starting at around 176 °C determined by thermogravimetric analysis (TGA)). However, in [91] this temperature range is also predicted to be suitable for melt extrusion as it is at this temperature that the polymer exhibits a viscosity above 10000 Pa \cdot s. However, Eudragit L 100–55 without the addition of excipients is evaluated as not processable by melt extrusion due to an overlap of a suitable extrusion temperature and degradation regime [91]. Nevertheless, as known from [95], the high laser-induced heating and cooling rates of several 1000 K/s [95–97] and the time-dependency of degradation processes allow degradation temperatures of materials processed by PBF-LB to be exceeded.

Based on the theory of quasi-isothermal PBF-LB (cf. 2.10 and [66]), the processing window for the powders analyzed in Figs. 6, 7 and 8 is defined between crystallization onset (cf. 2.10) at 123.44 °C \pm 0.20 °C and the beginning of the degradation / melt extrudable region starting at around 170 °C [91,92] with its peak at around 200 °C (cf. Figs. 6, 7 and

8). However, although a slight crystallization with its peak at around 120 °C could be observed, the crystallization enthalpy of Eudragit L 100–55 (crystallization enthalpy $\Delta H_c \approx 0.5\text{Jg}^{-1}$) and the different powder blends is approximately 100 times lower than the crystallization enthalpy of a typical PBF-LB polymer such as polyamide 12 (PA12, crystallization enthalpy $\Delta H_c \approx 56\text{Jg}^{-1}$) [98]. Nevertheless, curling (cf. 2.10) occurred in this study during PBF-LB without preheating the powder materials above crystallization temperature.

As can be seen from Figs. 6 and 7, the melting temperature of paracetamol is around 168 °C whereas that of nicotinamide is in the range of 125 °C. This fits well with data of the manufacturer as well as literature values [51,99]. In contrast, no melting peak occurred for caffeine, since according to literature, caffeine melts in the range of 235 °C [100,101], which is above the temperature range of the present study. However, the reported transition of caffeine into a new polymorph at approximately 150 °C (α to β transition) [101] is also shown in Fig. 8 in the case of 10 wt% and 15 wt% drug loading. For a drug loading of 5 wt% caffeine, the transition could not be detected. Since no significant shift of the crystallization temperature of Eudragit L 100–55 could be observed as function of the respective drug loadings, the pre-heating temperature for EPA-PBF-LB was set to 125 °C. This lies slightly above the crystallization onset of Eudragit L 100–55 (123.44 °C \pm 0.20 °C).

3.3. Analysis of powder layers deposited into build chamber

The electrophotographic powder application behavior of powder blends consisting of Eudragit L 100–55 as excipient and different weight percentages of three different drugs, paracetamol, nicotinamide, and caffeine was investigated. The goal was to deposit powder layers with preferably high coverage close to 100% as partially missing powder negatively influences part quality. Inadequate coverage would require a second, time consuming powder application step for compensating areas with missing powder. The layer thickness is an important value to estimate the laser energy required for properly fusing a powder layer with sufficient interlayer connection to the underlying part without thermally damaging the materials. The false print (cf. Fig. 1) also gives information about the accuracy of powder deposition and describes the powder contamination within a rectangular area with a width of 1 mm surrounding the deposited powder pattern (cf. 2.9). In the case of pharmaceutical EPA-PBF-LB, the false print needs to be considered when planning the printing process, for instance by slightly decreasing the size of the powder pattern to avoid drug cross-contamination. Moreover, according to [56] the residual surface potential of powder layers deposited by EPA plays an important role. Thus, a strategy for compensating the accumulation of charges needs to be applied in case of residual surface potential. However, in case of all pharmaceutical powders investigated in the present study, the surface potential after powder deposition was measured to be 0 V. This behavior can be attributed to the fact that Eudragit has an electric volume resistivity (EVR) in the range of $10^{10} \Omega\text{m} - 10^{13} \Omega\text{m}$ [102], which is comparable to the EVR of PA12 (around $10^{12} \Omega\text{m}$ [56,103]). Also, in case of PA12, no residual surface potential is present after electrophotographic powder application obviating the need for a compensation strategy against charge accumulation [56]. Fig. 9 shows an exemplary powder layer after deposition into the EPA-PBF-LB/P build chamber during measurement of the layer thickness.

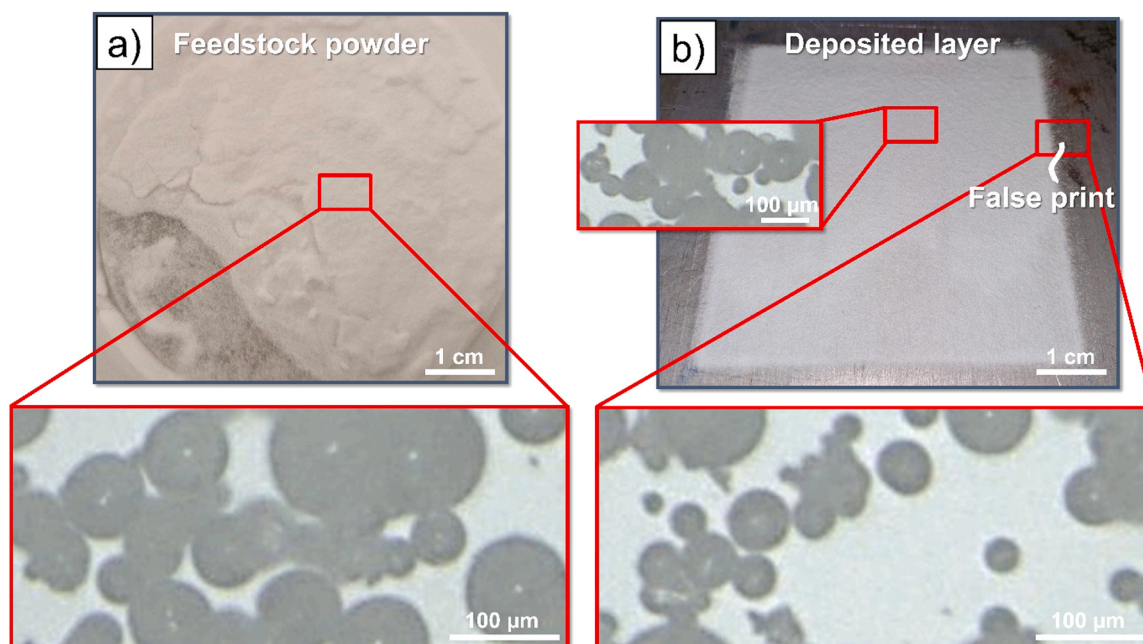


Fig. 13. Comparison of particle sizes between a) feedstock powder and b) powder layer deposited by EPA of powder blend consisting of 85 wt% Eudragit L 100–55 and 15 wt% of paracetamol (powder blend no. 3).

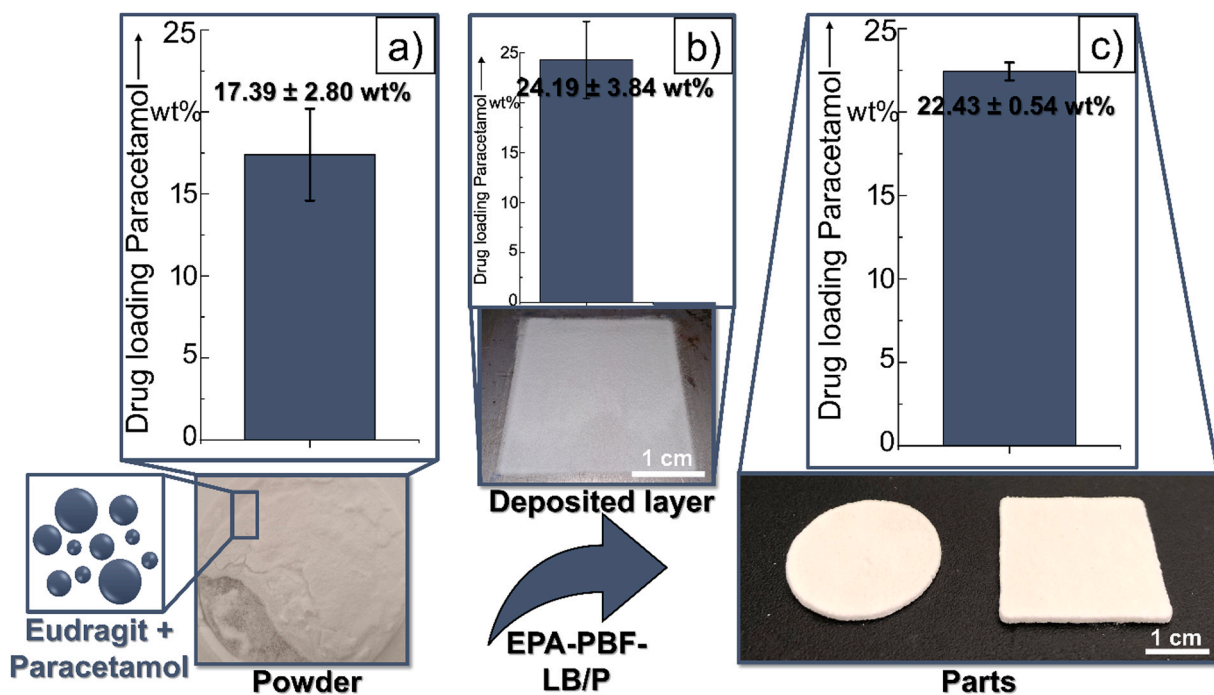


Fig. 14. a) actual drug loading measured by HPLC of a powder blend consisting of Eudragit L 100–55 and a theoretical drug loading of 15 wt% (powder blend no. 3); b) drug loading measured by HPLC of a deposited powder layer (powder blend no. 3); c) two pharmaceutical parts generated by EPA-PBF-LB and the corresponding actual drug loading of the parts measured by HPLC.

For a powder blend consisting of Eudragit and paracetamol (Fig. 10), a theoretical drug loading of 5 wt%, and a layer coverage of 100% was achieved.

At a paracetamol content of 5 wt% and 10 wt% the layer thickness is only about half that of pure Eudragit L 100–55. In case of 15 wt% paracetamol it even decreases to below 20 μm (cf. Fig. 10). Despite the layer thickness decreasing significantly, the layer coverage still remains above 90%. This can be explained by the fact that in this case only fine, i.

e., very small sized particles, were deposited, forming the thinner powder layer with a high coverage above 90%. The chosen gas discharge-based powder charging method (cf. 2.10) generates ions, which are deposited into the powder layer and temporarily stored in traps, mostly defects in the polymer surface or boundaries between crystalline and amorphous regions [83,84]. Gas discharge-based powder charging is often referred to as corona charging. Comparing the smooth microstructure of Eudragit L 100–55 particles (Fig. 5a)) with the rather

Table 5
Comparison of theoretical drug loading versus drug loading measured by HPLC of powder blends used for generating single- and multi-drug 3D printed parts.

Powder blend number	Theoretical drug loading	Measured drug loading / wt%	Localization
3	15 wt% paracetamol	17.39 ± 2.80	Single-drug film (cf. Fig. 14)
5	10 wt% nicotinamide	7.76 ± 1.58	Middle (M) – Right (R) (cf. Fig. 15)
8	10 wt% caffeine	11.13 ± 1.55	Middle (M) – Left (L) (cf. Fig. 15)

rough paracetamol (Fig. 5b)), it can be assumed that the probability of ions trapped on the surface of paracetamol is higher compared to Eudragit. Thus, the acicular paracetamol particles covered with small sized Eudragit particles (cf. 3.1) can be assumed to store more charges for a longer time period and hence are preferably transferred by EPA. Beyond that, as described in [104], transferability of a charged particle within an external electric field generally depends on the charge height of the particle, its aerodynamic diameter [105] and its mass. Although larger particles have more surface area for storing charge carriers as ions in case of gas discharge-based powder charging, particle mass also increases with their size. However, depending on the specific growth of particle charge versus an increase in particle mass, a material-specific optimum particle diameter is obtained, which is preferably transferred in an external electric field [104]. In the case of paracetamol (cf.

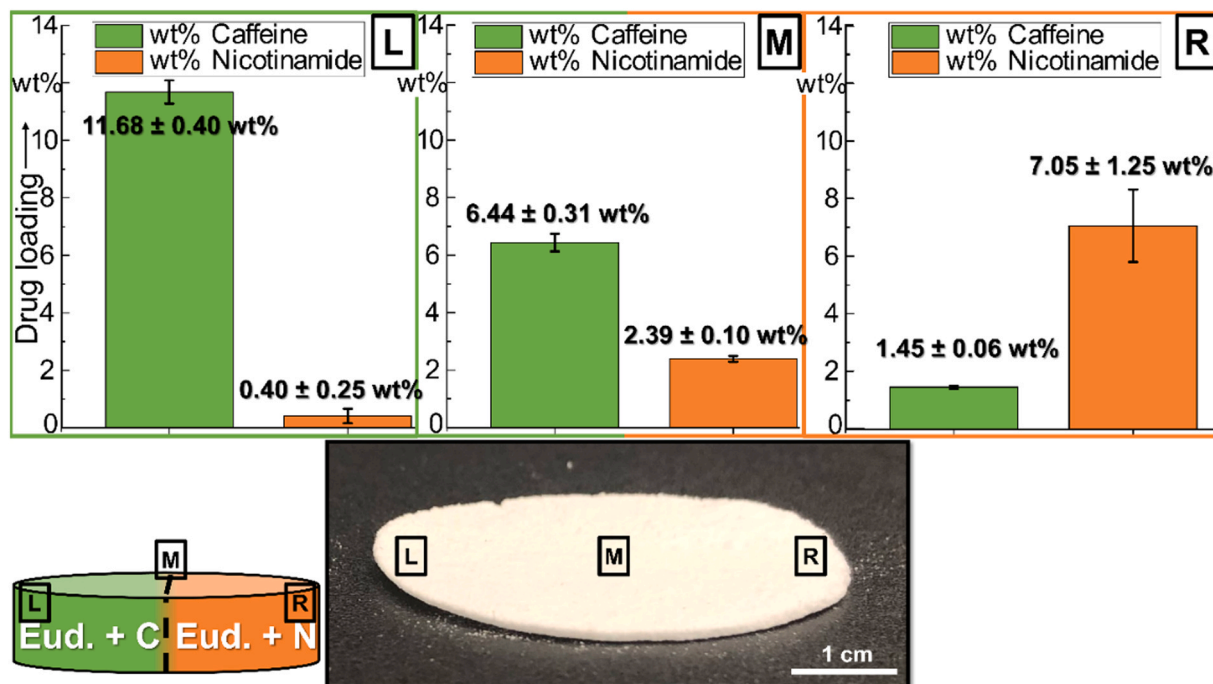


Fig. 15. Position-dependent actual drug loading measured by HPLC of multi-drug 3D printed film.

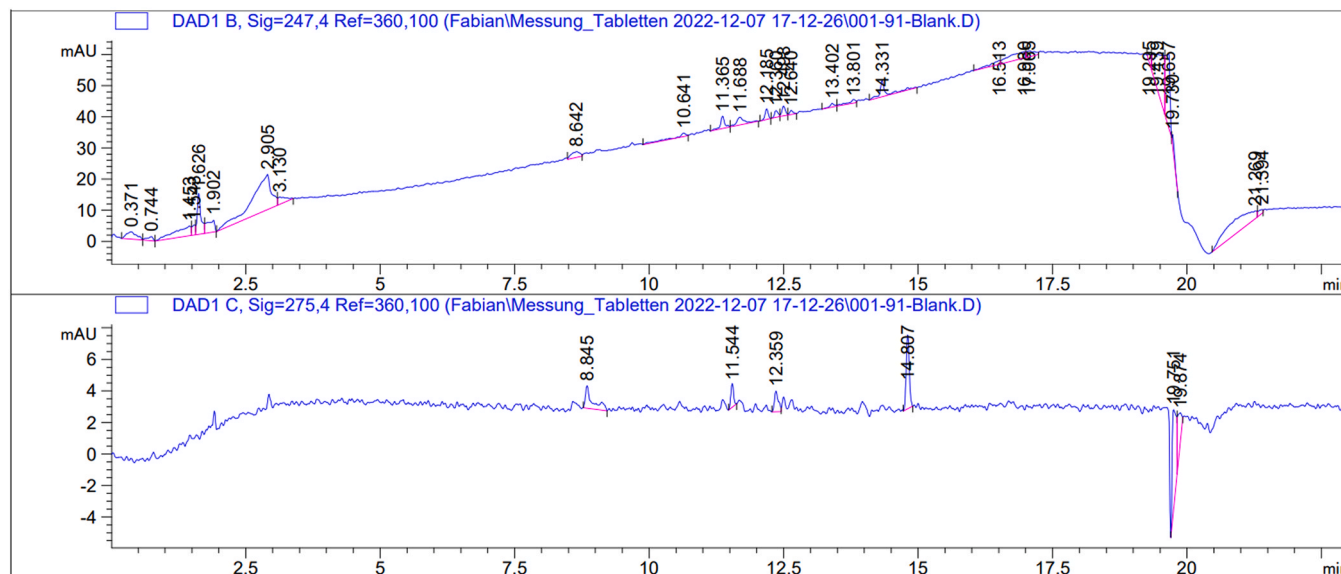


Fig. A1. Blank HPLC chromatogram; absorbance at 247 nm (upper chromatogram) and at 275 nm (lower chromatogram).

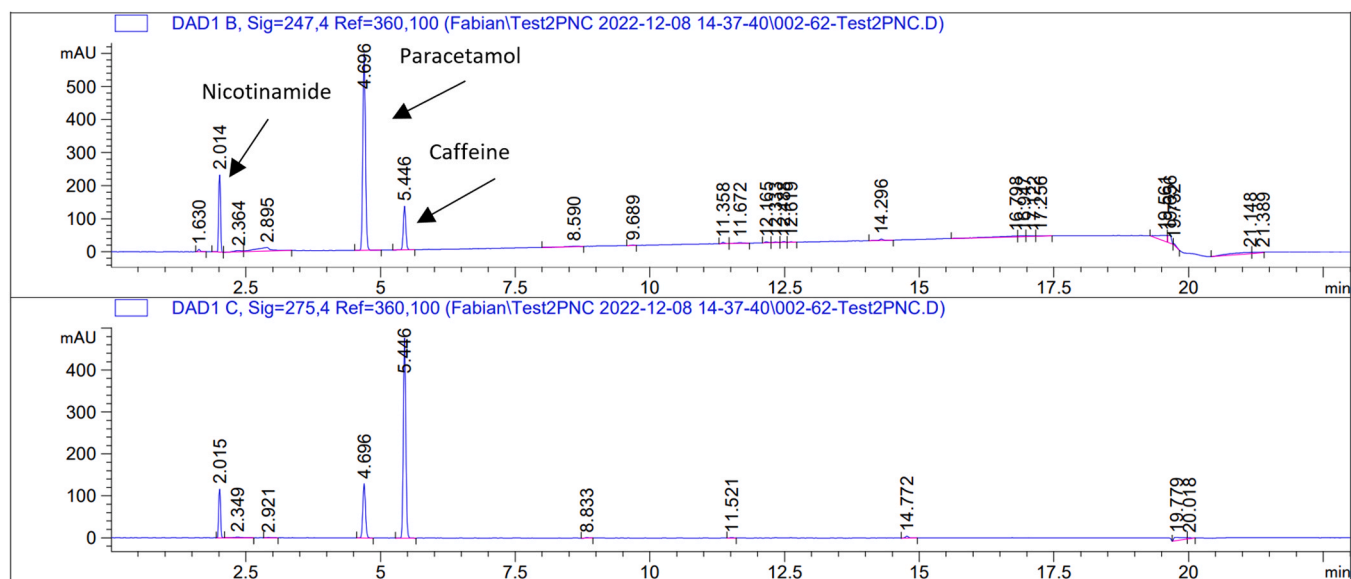


Fig. A2. HPLC chromatograms of reference substances; absorbance at 247 nm (upper chromatogram) and at 275 nm (lower chromatogram).

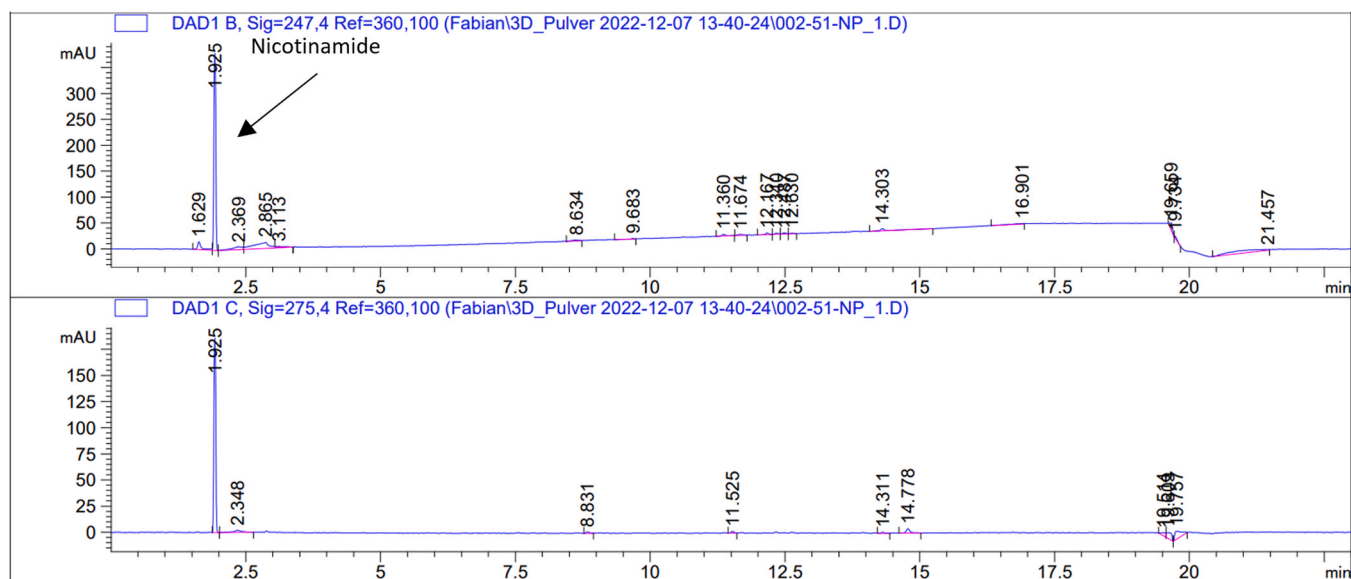


Fig. A3. HPLC chromatograms of powder blend loaded with nicotinamide; absorbance at 247 nm (upper chromatogram) and at 275 nm (lower chromatogram).

Fig. 10), predominantly the small sized particles are transferred within the development and deposition fields of EPA and deposited into the build chamber, which explains the decreasing layer thickness for higher paracetamol loadings. At this it is important to note that paracetamol has a diameter $x_{10,3} = 6.76 \pm 0.243 \mu\text{m}$ (cf. Table 4).

The powder deposition results of a powder blend consisting of Eudragit L 100–55 and different weight percentages of nicotinamide are shown in Fig. 11. In contrast to the results of the powder blend loaded with paracetamol (Fig. 10), the layer thickness increases with increasing content of nicotinamide whereas coverage decreases at a drug loading of 15 wt%. Analogous to paracetamol, the increase in layer thickness with increasing drug load suggests a predominant electrostatic transfer of nicotinamide instead of Eudragit. However, in this case, larger particles are deposited, which is attributed to the significantly larger particles of nicotinamide compared to paracetamol (cf. Table 4). This also explains the slightly decreased layer coverage, since especially fine particles can fill gaps between larger particles. Hence, EPA of powder blends consisting of Eudragit, and paracetamol or caffeine show higher coverage

values than the blend loaded with nicotinamide.

EPA of a powder blend consisting of Eudragit L 100–55 and caffeine (Fig. 12) shows a similar behavior to the powder blend loaded with paracetamol. However, although the particle sizes of both drugs are comparable (cf. Table 4), the resulting layer thickness at 15 wt% drug loading is about two times higher for caffeine with almost similar layer coverage. This can be attributed to a larger material-specific optimum particle diameter of caffeine for electrophotographic powder transfer in the present study.

The false print of around 20% for all three pharmaceutical powder blends is around two times higher than in case of PA12 or PP [55,56]. This means that the powder coverage within four rectangular areas with a width of 1 mm surrounding the actual deposited powder pattern (cf. Fig. 1) is at roughly 20%. This can mainly be attributed to the significantly larger number of fine particles in the pharmaceutical powder blends used in the present study. While PA12 (PA2200, EOS GmbH, Krailling, Germany) has a diameter $x_{10,3} = 53.66 \pm 0.03 \mu\text{m}$ [106], all powders used in this work, have significantly smaller $x_{10,3}$

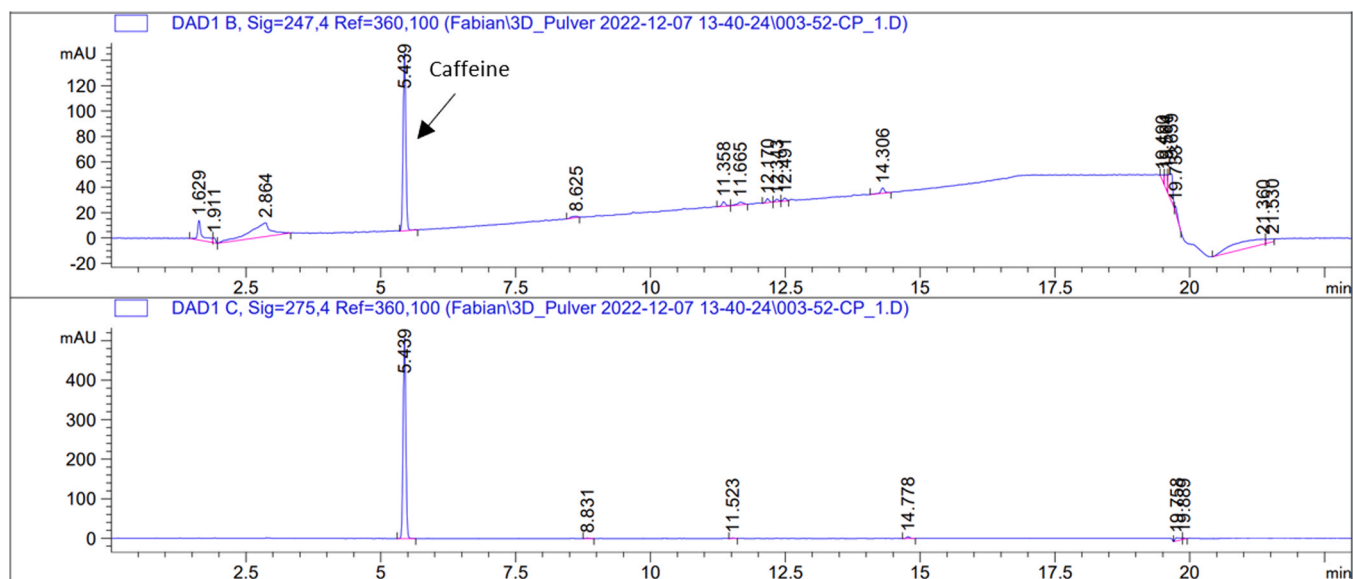


Fig. A4. HPLC chromatograms of powder blend loaded with caffeine; absorbance at 247 nm (upper chromatogram) and at 275 nm (lower chromatogram).

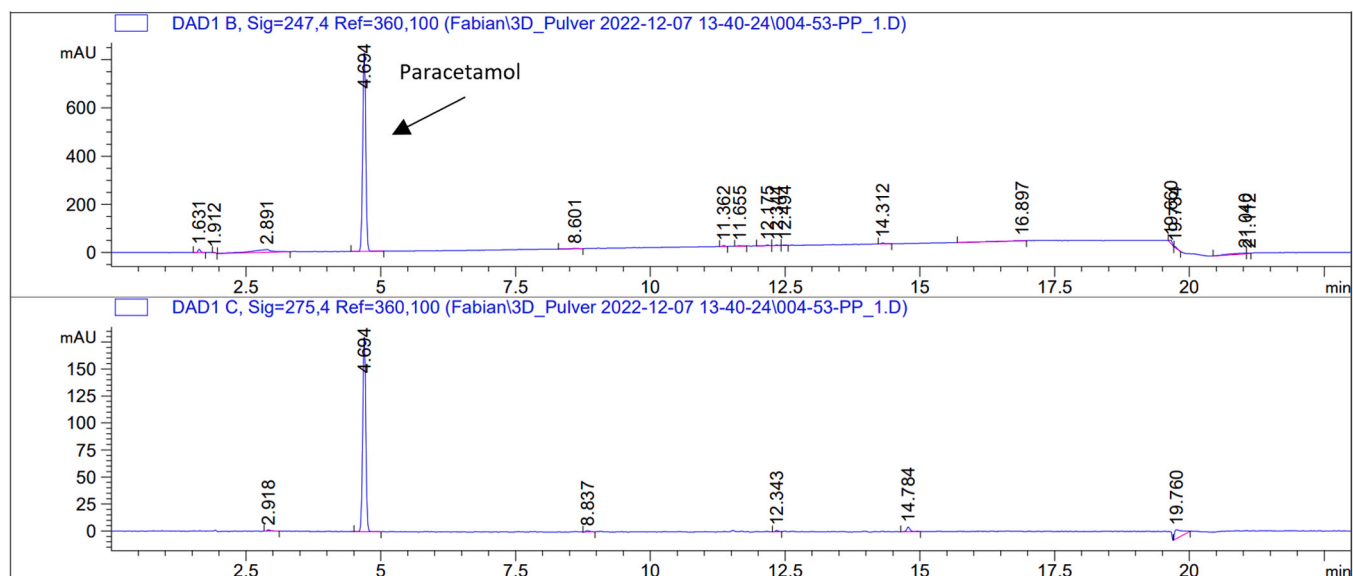


Fig. A5. HPLC chromatograms of powder blend loaded with paracetamol; absorbance at 247 nm (upper chromatogram) and at 275 nm (lower chromatogram).

values (cf. Table 4). Especially small particles are prone to deviations from their straight trajectory due to turbulences for instance [104]. Fig. 13 shows optical microscopy images of particles of the feedstock powder (a) and of particles from different positions of the powder layer deposited by EPA (b)). When comparing the particle sizes in Fig. 13, the described tendency of smaller particles being deposited in the false print region is plausible. The slightly decreased false print in case of the powder blend loaded with nicotinamide (Fig. 11) compared to the powder blends loaded with paracetamol (Fig. 10) and caffeine (Fig. 12) also suggests that a larger amount of fine particles enhances false print.

3.4. Drug loading of test samples printed using EPA-PBF-LB/P

Before generating 3D printed samples, the individual drug loadings of the powder blends used for EPA-PBF-LB were analyzed by HPLC. As can be seen in Fig. 14 and Table 5, the calculated drug loadings of the prepared powder blends differ from the theoretical values, which were targeted by mixing the respective weight percentages (cf. 2.2). In case of

paracetamol (Fig. 14 a) and Table 5 first row) and caffeine (Table 5 third row) the actual drug loading is higher than the theoretical loading and in case of nicotinamide the actual drug loading is lower (Table 5 second row). The deviations from the target values can be attributed to different physical properties of the powders, i.e., particle size and shape, and inaccuracies during powder handling, weighing, and mixing. By applying and fusing 50 layers using the parameters shown in Table 2, the films depicted in Fig. 14 were generated.

The cylindrical part has a diameter of 23.01 ± 0.02 mm and a thickness of 0.98 ± 0.01 mm whereas the cuboidal part has a thickness of 0.98 ± 0.01 mm and an edge length of 25.01 ± 0.01 mm. As already indicated by the layer deposition results in 3.3, a predominant electrostatic transfer of paracetamol is taking place. Hence, the drug loading of the pharmaceutical parts (Fig. 14 c)) increases compared to the drug loading of the powder (Fig. 14 a)). This effect is already visible when looking at the drug loading of the deposited layer (Fig. 14 b)), which is significantly higher than the drug loading of the powder before deposition (Fig. 14 a)).

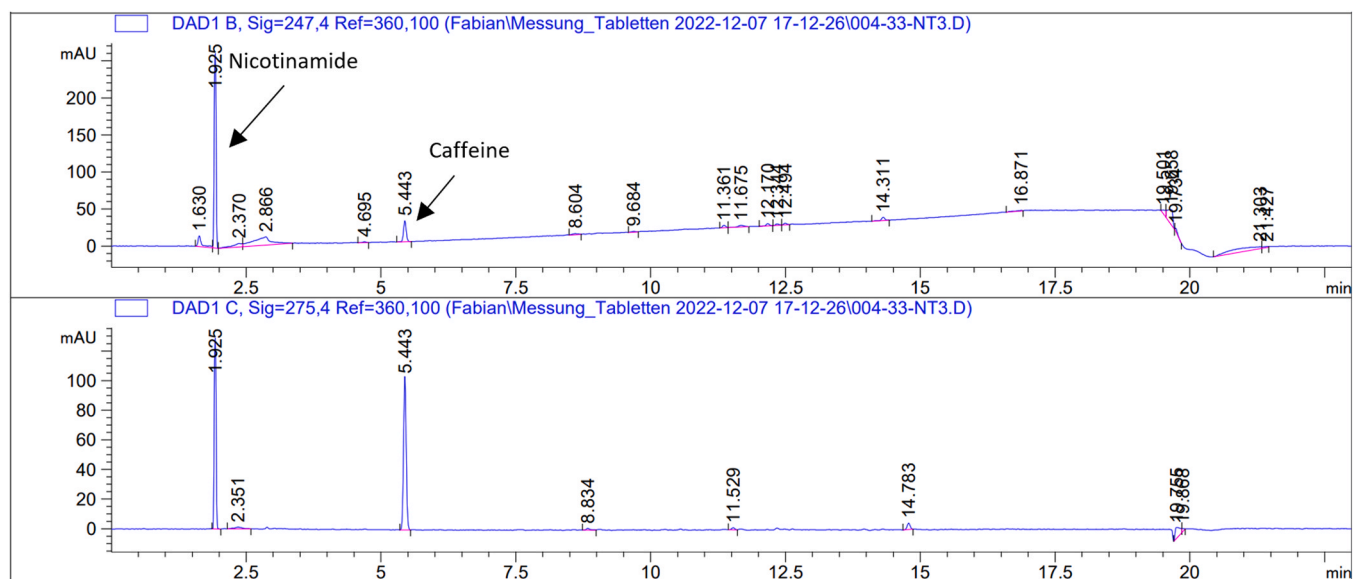


Fig. A6. HPLC chromatograms of multi-drug Printlet™ - nicotinamide loaded region; absorbance at 247 nm (upper chromatogram) and at 275 nm (lower chromatogram).

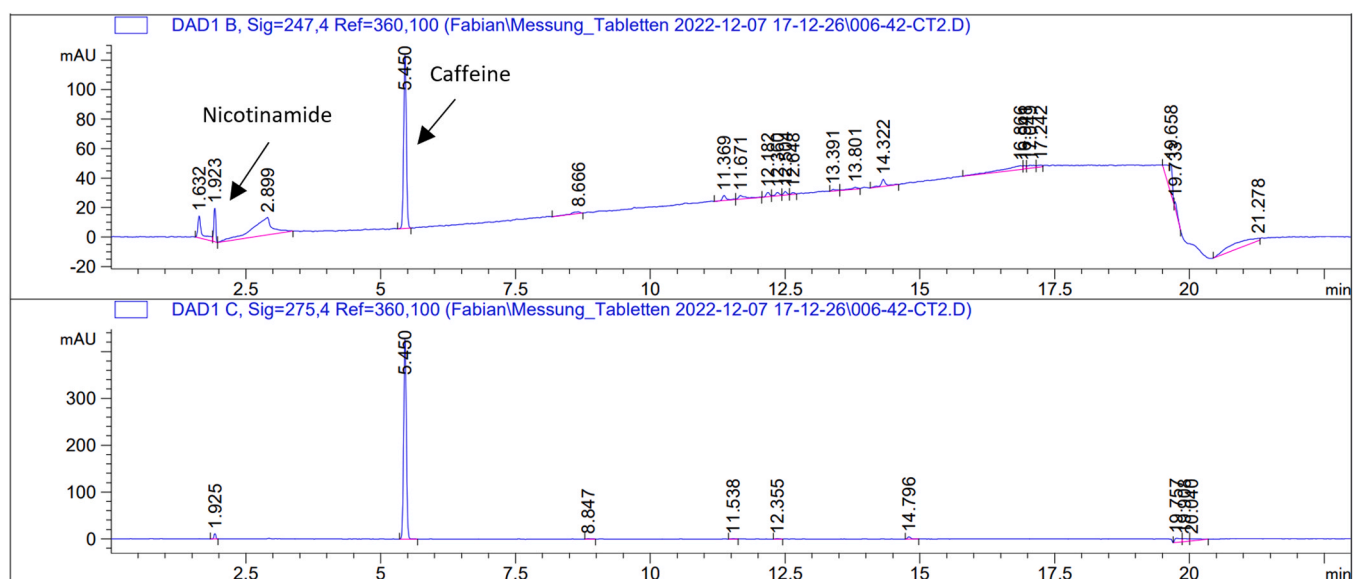


Fig. A7. HPLC chromatograms of multi-drug Printlet™ - caffeine loaded region; absorbance at 247 nm (upper chromatogram) and at 275 nm (lower chromatogram).

Interestingly, the drug loading slightly decreases in case of the generated parts (Fig. 14 c) compared to the first deposited layer shown in Fig. 14 b). This suggests that with an increasing number of layer depositions from the same powder reservoir (Fig. 14 a) the amount of Eudragit L 100–55 particles starts rising again. Furthermore, the standard deviation decreases for the generated parts, indicating that statistically distributed deviations of the drug loading within a deposited layer average out with increasing number of deposited and fused layers. The predominant electrostatic transfer of paracetamol, which is induced by differences of the microstructure and size of the drug particles compared to Eudragit L 100–55 (cf. 3.3), may lead to unacceptable deviations of the achieved drug content compared to the required one within the final part. Although this effect seems to weaken with an increasing number of layer depositions from the same powder feedstock, the drug loading of the feedstock powder has to be carefully adjusted to the specific electrostatic separation effect of the respective powder blend. For avoiding the electrostatic separation, another approach for incorporating drug

particles could be promising. Instead of using a dry blend of polymer and drug particles, so-called supraparticles [107] might solve this issue. Supraparticles offer the opportunity to incorporate drug particles directly into the polymer, which reduces the risk of being separated by EPA. However, this necessitates the generation of suitable supraparticles and furthermore an extensive study on EPA-PBF-LB/P using such particles.

The multi-drug part shown in Fig. 15 has a diameter of 46.07 ± 0.09 mm and a thickness of 1.04 ± 0.03 mm. According to the different layer thickness values (cf. Figs. 11 and 12) it consists of 15 layers of the powder blend loaded with nicotinamide and 25 layers of the caffeine loaded powder blend. The calculated drug loadings in three different areas, left (L), middle (M), and right (R) are given in Fig. 15. The individual drug contents of the respective regions of the multi-drug part correspond well to the drug loadings of the respective powder blends (cf. caffeine loading in Fig. 15 L and nicotinamide loading in Fig. 15 R compared to drug loadings of the powders given in Table 5.

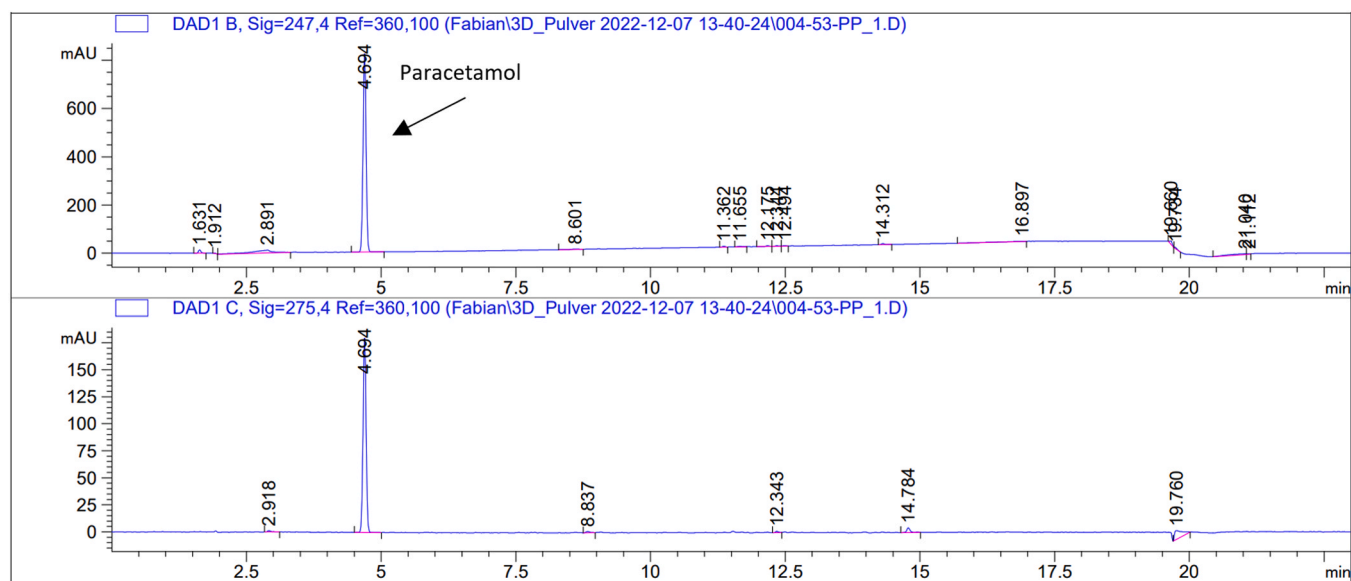


Fig. A8. HPLC chromatograms of mono-drug Printlet™ - loaded with paracetamol; absorbance at 247 nm (upper chromatogram) and at 275 nm (lower chromatogram).

However, especially in the middle region, a higher caffeine than nicotinamide loading is present, which can be explained by the higher actual drug loading of caffeine in the used powder blend compared to the nicotinamide blend. Furthermore, a slight inaccuracy in locating the exact transition area between caffeine and nicotinamide loaded regions for preparing the HPLC samples may also have caused the difference in drug loadings.

While there is no significant content of nicotinamide within the left region of the multi-drug part, some contamination of the right region with caffeine is measured. This can be explained by the fact that each caffeine loaded powder portion adhering to the PCP had to pass across the right region of the 3D printed film during EPA-PBF-LB in order to reach the left region because the movement of the PCP was from right to left. All powder reservoirs are located to the right of the build chamber of the EPA-PBF-LB setup. Thus, it cannot be excluded that some particles of the caffeine loaded powder blend were lost during PCP movement and therefore increased the caffeine loading of the right region. The total mass of the multi-drug film shown in Fig. 15 was roughly 2 g. Thus, to obtain a contamination of around 1.45 wt% caffeine in the right region of the part after 25 depositions of caffeine loaded powder to the left region, roughly 500 µg of caffeine needed to fall off the PCP per deposition during its movement. This corresponds to around 10% of the caffeine loaded powder adhering to the PCP. Since the axis is already slowing down while the caffeine loaded powder moves across the right region of the part, slight vibrations may occur, which are known to decrease interparticle attraction forces and thus increase the probability for particles falling off the PCP [55]. However, as described in detail in [56], mainly the van der Waals force and the electric field force are responsible for adhesion of the powder particles to the PCP. During movement a holding voltage of ± 100 V was applied to the PCP in order to establish an electric holding field similar to [64]. There are mainly two options for enhancing the electrostatic adhesion of the powder particles to the PCP and thus decrease the tendency for powder particles falling off the PCP during movement. Firstly, the holding voltage could be increased and secondly the powder charging could be enhanced by either applying a stronger electric charging field or choosing triboelectric charging as powder charging method. This has been shown to be a promising approach for achieving a more efficient particle charging in the context of EPA-PBF-LB/P [33,59].

The printed samples did not show any evidence of degradation such as color change of the initially white powders. Additionally, no evidence

of degradation could be found by the HPLC analysis of the films. The chromatograms of all HPLC measurements can be found in the appendix. As can be seen from the representative chromatograms of the powder blends and printed parts, no other peaks, which would indicate possible degradation products, except for the three drug-related peaks, were visible.

4. Conclusion

In the present study, electrophotographic powder application (EPA) for powder bed fusion – laser beam (PBF-LB) was applied for generating pharmaceutical parts loaded with three different model drugs. For this purpose, powder blends consisting of an excipient, Eudragit L 100–55, and different concentrations of paracetamol, nicotinamide, and caffeine, respectively, were prepared and successfully deposited into the build chamber by EPA. However, electrostatic separation of the drug particles from the polymer particles was observed, leading to a shift of the achievable layer thickness towards the mass median diameter of the respective drug powder. The reason for the electrostatic separation could be attributed to the microstructure of the individual drugs, which is more suitable for trapping charges from the gas discharge-based powder charging process applied in this work. When utilizing EPA, thin layers up to 5 times thinner than in the case of conventional doctor blade- or roller-based powder application methods for PBF-LB, could be successfully deposited into the build chamber. This allowed a CO₂ laser to be employed for generating pharmaceutical test samples with no evidence of thermal degradation according to the performed high-performance liquid chromatography (HPLC) measurements. Finally, a multi-drug film was successfully printed via EPA-PBF-LB, opening the possibility of EPA to selectively as well as precisely apply different powders within one layer into the build chamber.

CRedit authorship contribution statement

Fabian Graf: Writing – review & editing, Writing – original draft, Visualization, Validation, Software, Methodology, Investigation, Formal analysis, Data curation, Conceptualization. **Markus R. Heinrich:** Writing – review & editing, Supervision, Resources, Project administration, Funding acquisition. **Medvedev Vadim:** Writing – review & editing, Conceptualization, Data curation, Formal analysis, Investigation, Validation. **Katja Tangermann-Gerk:** Writing – review & editing,

Visualization, Validation, Investigation. **Natalie Wöltinger:** Investigation. **Richard Rothfelder:** Conceptualization. **Alvaro Goyanes:** Writing – review & editing, Validation, Supervision, Resources, Project administration, Methodology, Formal analysis, Conceptualization. **Abdul W. Basit:** Writing – review & editing, Supervision, Resources, Project administration, Methodology. **Roth Stephan:** Writing – review & editing, Supervision, Resources, Project administration, Funding acquisition. **Michael Schmidt:** Writing – review & editing, Supervision, Resources, Project administration, Funding acquisition. **Sebastian-Paul Kopp:** Writing – review & editing, Writing – original draft, Visualization, Validation, Supervision, Software, Methodology, Investigation, Formal analysis, Data curation, Conceptualization. **Patricija Januskaite:** Writing – review & editing, Writing – original draft, Visualization, Validation, Methodology, Investigation, Formal analysis, Data curation, Conceptualization.

Declaration of Competing Interest

Alvaro Goyanes and Abdul W. Basit are founders of FabRx Ltd., and as indicated in the Author Contribution section, they took part in the design of the study, in the data curation, manuscript writing and editing, supervision, project administration and in the decision to publish the results. Other authors have no conflict of interest.

Data availability

Data will be made available on request.

Acknowledgements

The authors gratefully acknowledge funding of the Collaborative Research Center 814 (CRC 814) “Additive Manufacturing”, subproject B6, by the German Research Foundation (DFG) – project number 61375930 – and of the Erlangen Graduate School in Advanced Optical Technologies (SAOT) by the Bavarian State Ministry for Science and Art. This research was partially funded by the Engineering and Physical Sciences Research Council (EPSRC) UK grant number EP/S023054/1.

Appendix

Determination of the linear equations given in [Table 3](#):

A calibration curve allows the correlation of an analyte signal obtained from a HPLC measurement to the concentration of analyte present in the sample. To produce a calibration curve, the analyte in question is measured at several known concentrations (serial dilution) and the chromatograms at a defined wavelength (detection wavelength) are analyzed. The area under curve (AUC) of the analyte peak (y-Axis) is then plotted against the applied concentration (x-Axis) for all applied concentrations. A linear trendline is fitted through the data points (calibration curve) and the linear equation is extracted. For quantification, one can now insert the analyte AUC (y) into the linear equation to calculate the concentration (x). The retention time is unique for every analyte and is used to pair signals in the chromatogram with their respective analyte. [Fig. A1](#), [Fig. A2](#), [Fig. A3](#), [Fig. A4](#), [Fig. A5](#), [Fig. A6](#), [Fig. A7](#), [Fig. A8](#).

References

- [1] F. Calignano, D. Manfredi, E.P. Ambrosio, S. Biamino, M. Lombardi, E. Atzeni, A. Salmi, P. Minetola, L. Iuliano, P. Fino, Overview on additive manufacturing technologies, *Proc. IEEE* 105 (2017) 593–612, <https://doi.org/10.1109/JPROC.2016.2625098>.
- [2] U. Fasel, D. Keidel, L. Baumann, G. Cavolina, M. Eichenhofer, P. Ermanni, Composite additive manufacturing of morphing aerospace structures, *Manuf. Lett.* 23 (2020) 85–88, <https://doi.org/10.1016/J.MFGLET.2019.12.004>.
- [3] M. Delic, D.R. Evers, The effect of additive manufacturing adoption on supply chain flexibility and performance: an empirical analysis from the automotive industry, *Int. J. Prod. Econ.* 228 (2020), <https://doi.org/10.1016/J.IJPE.2020.107689>.
- [4] C. Culmone, G. Smit, P. Breedveld, Additive manufacturing of medical instruments: a state-of-the-art review, *Addit. Manuf.* 27 (2019) 461–473, <https://doi.org/10.1016/J.ADDMA.2019.03.015>.
- [5] S.H. Ghaffar, J. Corker, M. Fan, Additive manufacturing technology and its implementation in construction as an eco-innovative solution, *Autom. Constr.* 93 (2018) 1–11, <https://doi.org/10.1016/J.AUTCON.2018.05.005>.
- [6] D. Delgado Camacho, P. Clayton, W.J. O'Brien, C. Seepersad, M. Juenger, R. Ferron, S. Salamone, Applications of additive manufacturing in the construction industry – A forward-looking review, *Autom. Constr.* 89 (2018) 110–119, <https://doi.org/10.1016/J.AUTCON.2017.12.031>.
- [7] A. Paolini, S. Kollmannsberger, E. Rank, Additive manufacturing in construction: a review on processes, applications, and digital planning methods, *Addit. Manuf.* 30 (2019), 100894, <https://doi.org/10.1016/J.ADDMA.2019.100894>.
- [8] R. Kumar, M. Kumar, J.S. Chohan, The role of additive manufacturing for biomedical applications: a critical review, *J. Manuf. Process* 64 (2021) 828–850, <https://doi.org/10.1016/J.JMAPRO.2021.02.022>.
- [9] M. Elbadawi, L.E. McCoubrey, F.K.H. Gavins, J.J. Ong, A. Goyanes, S. Gaisford, A. W. Basit, Harnessing artificial intelligence for the next generation of 3D printed medicines, *Adv. Drug Deliv. Rev.* 175 (2021), <https://doi.org/10.1016/J.ADDR.2021.05.015>.
- [10] A. Goyanes, P. Robles Martinez, A. Buanz, A.W. Basit, S. Gaisford, Effect of geometry on drug release from 3D printed tablets, *Int. J. Pharm.* 494 (2015) 657–663, <https://doi.org/10.1016/J.IJPHARM.2015.04.069>.
- [11] M. Trivedi, J. Jee, S. Silva, C. Blomgren, V.M. Pontinha, D.L. Dixon, B. van Tassel, M.J. Bortner, C. Williams, E. Gilmer, A.P. Haring, J. Halper, B.N. Johnson, Z. Kong, M.S. Halquist, P.F. Rocheleau, T.E. Long, T. Roper, D.S. Wijesinghe, Additive manufacturing of pharmaceuticals for precision medicine applications: a review of the promises and perils in implementation, *Addit. Manuf.* 23 (2018) 319–328, <https://doi.org/10.1016/J.ADDMA.2018.07.004>.
- [12] A.M. Vargason, A.C. Anselmo, S. Mitragotri, The evolution of commercial drug delivery technologies, *Nature Biomedical Engineering* 2021 5:9. 5 (2021) 951–967, <https://doi.org/10.1038/s41551-021-00698-w>.
- [13] J. Norman, R.D. Madurawe, C.M.V. Moore, M.A. Khan, A. Khairuzzaman, A new chapter in pharmaceutical manufacturing: 3D-printed drug products, *Adv. Drug Deliv. Rev.* 108 (2017) 39–50, <https://doi.org/10.1016/J.ADDR.2016.03.001>.
- [14] K. Sen, T. Mehta, S. Sansare, L. Sharifi, A.W.K. Ma, B. Chaudhuri, Pharmaceutical applications of powder-based binder jet 3D printing process – a review, *Adv. Drug Deliv. Rev.* 177 (2021), 113943, <https://doi.org/10.1016/J.ADDR.2021.113943>.
- [15] A. Goyanes, C.M. Madla, A. Umerji, G. Duran Piñeiro, J.M. Giraldez Montero, M. J. Lamas Diaz, M. Gonzalez Barcia, F. Taherali, P. Sánchez-Pintos, M.-L. Couce, S. Gaisford, A.W. Basit, Automated therapy preparation of isoleucine formulations using 3D printing for the treatment of MSUD: first single-centre, prospective, crossover study in patients, *Int. J. Pharm.* 567 (2019), 118497, <https://doi.org/10.1016/J.IJPHARM.2019.118497>.
- [16] P. Robles-Martinez, X. Xu, S.J. Trenfield, A. Awad, A. Goyanes, R. Telford, A.W. Basit, S. Gaisford, 3D Printing of a Multi-Layered Polypill Containing Six Drugs Using a Novel Stereolithographic Method, *Pharmaceutics* 2019, Vol. 11, Page 274. 11 (2019) 274, <https://doi.org/10.3390/PHARMACEUTICS11060274>.
- [17] A.G. Tabriz, M.S. Mithu, M.D. Antonijevic, L. Vilain, Y. Derrar, C. Grau, A. Morales, O.L. Katsamenis, D. Douroumis, 3D printing of LEGO® like designs with tailored release profiles for treatment of sleep disorder, *Int. J. Pharm.* 632 (2023), 122574, <https://doi.org/10.1016/J.IJPHARM.2022.122574>.
- [18] T.D. Pollard, I. Seoane-Viano, J.J. Ong, P. Januskaite, S. Awwad, M. Orlu, M. F. Bande, A.W. Basit, A. Goyanes, Inkjet drug printing onto contact lenses: deposition optimisation and non-destructive dose verification, *Int. J. Pharm.* X 5 (2023), 100150, <https://doi.org/10.1016/J.IJPH.2022.100150>.
- [19] C. Caudill, J.L. Perry, K. Iliadis, A.T. Tessema, B.J. Lee, B.S. Mecham, S. Tian, J. M. DeSimone, Transdermal vaccination via 3D-printed microneedles induces potent humoral and cellular immunity, *Proc. Natl. Acad. Sci. USA* 118 (2021), e2102595118, https://doi.org/10.1073/PNAS.2102595118/SUPPL_FILE/PNAS.2102595118.SAPP.PDF.
- [20] ISO/ASTM DIS 52910(en), Additive manufacturing — Design — Requirements, guidelines and recommendations, (n.d.). <https://www.iso.org/obp/ui/#iso:std:iso-astm:52910:dis:ed-2:v1:en> (accessed February 20, 2023).
- [21] F. Fina, S. Gaisford, A.W. Basit, Powder bed fusion: the working process, current applications and opportunities, *AAPS Adv. Pharm. Sci. Ser.* 31 (2018) 81–105, https://doi.org/10.1007/978-3-319-90755-0_5.
- [22] N. Allahham, F. Fina, C. Marcuta, L. Kraschew, W. Mohr, S. Gaisford, A.W. Basit, A. Goyanes, Selective Laser Sintering 3D Printing of Orally Disintegrating Printlets Containing Ondansetron, *Pharmaceutics* 2020, Vol. 12, Page 110. 12 (2020) 110, <https://doi.org/10.3390/PHARMACEUTICS12020110>.
- [23] A. Awad, F. Fina, A. Goyanes, S. Gaisford, A.W. Basit, Advances in powder bed fusion 3D printing in drug delivery and healthcare, *Adv. Drug Deliv. Rev.* 174 (2021) 406–424, <https://doi.org/10.1016/J.ADDR.2021.04.025>.
- [24] Y.A. Gueche, N.M. Sanchez-Ballester, S. Cailleaux, B. Bataille, I. Soulaïrol, Selective laser sintering (SLS), a new chapter in the production of solid oral forms (SOFs) by 3D printing, *Pharmaceutics* 13 (2021), <https://doi.org/10.3390/PHARMACEUTICS13081212>.
- [25] B. Shaqour, A. Samaro, B. Verleije, K. Beyers, C. Vervae, P. Cos, Production of Drug Delivery Systems Using Fused Filament Fabrication: A Systematic Review, *Pharmaceutics* 2020, Vol. 12, Page 517. 12 (2020) 517, <https://doi.org/10.3390/PHARMACEUTICS12060517>.
- [26] A. Awad, A. Yao, S.J. Trenfield, A. Goyanes, S. Gaisford, A.W. Basit, 3D Printed Tablets (Printlets) with Braille and Moon Patterns for Visually Impaired Patients,

- Pharmaceutics 2020, Vol. 12, Page 172. 12 (2020) 172. <https://doi.org/10.3390/PHARMACEUTICS12020172>.
- [27] A. Awad, F. Fina, S.J. Trenfield, P. Patel, A. Goyanes, S. Gaisford, A.W. Basit, 3D Printed Pellets (Miniprintlets): A Novel, Multi-Drug, Controlled Release Platform Technology, *Pharmaceutics* 2019, Vol. 11, Page 148. 11 (2019) 148. <https://doi.org/10.3390/PHARMACEUTICS11040148>.
- [28] R. Dogea, X.T. Yan, R. Millar, Additive manufacturing process design for complex aircraft components, *Int. J. Adv. Manuf. Technol.* 123 (2022) 4195–4211, <https://doi.org/10.1007/S00170-022-10413-X/FIGURES/23>.
- [29] M. Schmid, K. Wegener, Additive manufacturing: polymers applicable for laser sintering (LS), *Procedia Eng.* 149 (2016) 457–464, <https://doi.org/10.1016/J.PROENG.2016.06.692>.
- [30] W. Nan, M. Pasha, T. Bonakdar, A. Lopez, U. Zafar, S. Nadimi, M. Ghadiri, Jamming during particle spreading in additive manufacturing, *Powder Technol.* 338 (2018) 253–262, <https://doi.org/10.1016/J.POWTEC.2018.07.030>.
- [31] H. Rumpf, Die wissenschaft des agglomerierens, *Chem. Ing. Tech.* 46 (1974) 1–11, <https://doi.org/10.1002/CFTE.330460102>.
- [32] I.M. Kusoglu, C. Doñate-buendía, S. Barcikowski, B. Gökce, Laser Powder Bed Fusion of Polymers: Quantitative Research Direction Indices, *Materials* 2021, Vol. 14, Page 1169. 14 (2021) 1169. <https://doi.org/10.3390/MA14051169>.
- [33] B. Düsenberg, S.-P. Kopp, F. Fischer, S. Schrüfer, S. Roth, J. Schmidt, M. Schmidt, D.W. Schubert, W. Peukert, A. Bück, Enhancing Photoelectric Powder Deposition of Polymers by Charge Control Substances, *Polymers* 2022, Vol. 14, Page 1332. 14 (2022) 1332. <https://doi.org/10.3390/POLYM14071332>.
- [34] M.A. Dechet, J.S. Gómez Bonilla, M. Grünewald, K. Popp, J. Rudloff, M. Lang, J. Schmidt, A novel, precipitated polybutylene terephthalate feedstock material for powder bed fusion of polymers (PBF): material development and initial PBF processability, *Mater. Des.* 197 (2021), 109265, <https://doi.org/10.1016/J.MATDES.2020.109265>.
- [35] U. Gbureck, E. Vorndran, F.A. Müller, J.E. Barralet, Low temperature direct 3D printed bioceramics and bio-composites as drug release matrices, *J. Control Release* 122 (2007) 173–180, <https://doi.org/10.1016/J.JCONREL.2007.06.022>.
- [36] K.H. Low, K.F. Leong, C.K. Chua, Z.H. Du, C.M. Cheah, Characterization of SLS parts for drug delivery devices, *Rapid Prototyp. J.* 7 (2001) 262–267, <https://doi.org/10.1108/13552540110410468>.
- [37] K.F. Leong, K.K.S. Phua, C.K. Chua, Z.H. Du, K.O.M. Teo, Fabrication of porous polymeric matrix drug delivery devices using the selective laser sintering technique, *Proc. Inst. Mech. Eng. H* 215 (2001) 191–201, <https://doi.org/10.1243/0954411011533751>.
- [38] M.A. Alhnan, T.C. Okwuosa, M. Sadia, K.W. Wan, W. Ahmed, B. Arafat, Emergence of 3D Printed Dosage Forms: Opportunities and Challenges, *Pharm. Res* 33 (2016) 1817–1832, <https://doi.org/10.1007/S11095-016-1933-1>.
- [39] R.D. Goodridge, C.J. Tuck, R.J.M. Hague, Laser sintering of polyamides and other polymers, *Prog. Mater. Sci.* 57 (2012) 229–267, <https://doi.org/10.1016/J.PMATSCI.2011.04.001>.
- [40] T. Schuffenhauer, T. Stichel, M. Schmidt, Employment of an extended double-integrating-sphere system to investigate thermo-optical material properties for powder bed fusion, *J. Mater. Eng. Perform.* 30 (2021) 5013–5019, <https://doi.org/10.1007/S11665-021-05586-7>.
- [41] C.A. Chatham, T.E. Long, C.B. Williams, A review of the process physics and material screening methods for polymer powder bed fusion additive manufacturing, *Prog. Polym. Sci.* 93 (2019) 68–95, <https://doi.org/10.1016/J.PROGPOLYMSCI.2019.03.003>.
- [42] M. Heintz, T. Laumer, F. Bayer, T. Hausotte, Temperature-dependent optical material properties of polymer powders regarding in-situ measurement techniques in additive manufacturing, *Polym. Test.* 71 (2018) 378–383, <https://doi.org/10.1016/J.POLYMERTESTING.2018.09.016>.
- [43] M. Marschall, C. Heintges, M. Schmidt, Influence of flow aid additives on optical properties of polyamide for Laser-Based Powder Bed Fusion, *Procedia CIRP* 111 (2022) 51–54, <https://doi.org/10.1016/J.PROCIR.2022.08.114>.
- [44] J.P. Kruth, X. Wang, T. Laoui, L. Froyen, Lasers and materials in selective laser sintering, *Assem. Autom.* 23 (2003) 357–371, <https://doi.org/10.1108/01445150310698652/FULL/XML>.
- [45] M. George, K.R. Aroom, H.G. Hawes, B.S. Gill, J. Love, 3D printed surgical instruments: the design and fabrication process, *World J. Surg.* 41 (2017) 314–319, <https://doi.org/10.1007/S00268-016-3814-5>.
- [46] G. de, A.P. di Giacomo, P.R. Cury, A.M. da Silva, J.V.L. da Silva, S.A. Ajzen, A selective laser sintering prototype guide used to fabricate immediate interim fixed complete arch prostheses in flapless dental implant surgery: technique description and clinical results, *J. Prosthet. Dent.* 116 (2016) 874–879, <https://doi.org/10.1016/J.PROSDENT.2016.04.018>.
- [47] A. Awad, F. Fina, A. Goyanes, S. Gaisford, A.W. Basit, 3D printing: principles and pharmaceutical applications of selective laser sintering, *Int J. Pharm.* 586 (2020), 119594, <https://doi.org/10.1016/J.IJPHARM.2020.119594>.
- [48] H. Lee, C.H.J. Lim, M.J. Low, N. Tham, V.M. Murukeshan, Y.J. Kim, Lasers in additive manufacturing: a review, *Int. J. Precis. Eng. Manuf. - Green. Technol.* 4 (2017) 307–322, <https://doi.org/10.1007/S40684-017-0037-7>.
- [49] Y.A. Gueche, N.M. Sanchez-Ballester, B. Bataille, A. Aubert, L. Leclercq, J.C. Rossi, I. Soulaïrol, Selective Laser Sintering of Solid Oral Dosage Forms with Copovidone and Paracetamol Using a CO₂ Laser, *Pharmaceutics* 2021, Vol. 13, Page 160. 13 (2021) 160. <https://doi.org/10.3390/PHARMACEUTICS13020160>.
- [50] C. Wei, L. Li, Recent progress and scientific challenges in multi-material additive manufacturing via laser-based powder bed fusion, *Virtual Phys. Prototyp.* 16 (2021) 347–371, <https://doi.org/10.1080/17452759.2021.1928520>.
- [51] F. Fina, A. Goyanes, S. Gaisford, A.W. Basit, Selective laser sintering (SLS) 3D printing of medicines, *Int J. Pharm.* 529 (2017) 285–293, <https://doi.org/10.1016/J.IJPHARM.2017.06.082>.
- [52] A. Mohammed, A. Elshaer, P. Sareh, M. Elsayed, H. Hassanin, Additive manufacturing technologies for drug delivery applications, *Int J. Pharm.* 580 (2020), 119245, <https://doi.org/10.1016/J.IJPHARM.2020.119245>.
- [53] P. Kulinski, P. Malczewski, E. Pesta, M. Łaszcz, A. Mendyk, S. Polak, P. Dorożyński, Selective laser sintering (SLS) technique for pharmaceutical applications—development of high dose controlled release printlets, *Addit. Manuf.* 38 (2021), 101761, <https://doi.org/10.1016/J.ADDMA.2020.101761>.
- [54] S.P. Kopp, T. Stichel, S. Roth, M. Schmidt, Investigation of the electrophotographic powder deposition through a transfer grid for efficient additive manufacturing, *Procedia CIRP* 94 (2020) 122–127, <https://doi.org/10.1016/j.procir.2020.09.024>.
- [55] S.-P. Kopp, V. Medvedev, S. Roth, Targeted vibration excitation for increasing the powder deposition efficiency in electrophotographic powder application for Laser-based Powder Bed Fusion of polymers, *Procedia CIRP* 111 (2022) 55–60, <https://doi.org/10.1016/j.procir.2022.08.117>.
- [56] S.-P. Kopp, V. Medvedev, T. Frick, S. Roth, Expanding the capabilities of laser-based powder bed fusion of polymers through the use of electrophotographic powder application, *J. Laser Appl.* 34 (2022), 042032, <https://doi.org/10.2351/7.0000774>.
- [57] A. v Kumar, A. Dutta, J.E. Fay, Electrophotographic printing of part and binder powders, *Rapid Prototyp. J.* 10 (2004) 7–13, <https://doi.org/10.1108/13552540410512480/FULL/XML>.
- [58] A. v Kumar, A. Dutta, Investigation of an electrophotography based rapid prototyping technology, *Rapid Prototyp. J.* 9 (2003) 95–103, <https://doi.org/10.1108/13552540310467095/FULL/XML>.
- [59] S.-P. Kopp, B. Düsenberg, P.M. Eshun, J. Schmidt, A. Bück, S. Roth, M. Schmidt, Enabling triboelectric charging as a powder charging method for electrophotographic powder application in laser-based powder bed fusion of polymers by triboelectric charge control, *Addit. Manuf.* 68 (2023), 103531, <https://doi.org/10.1016/J.ADDMA.2023.103531>.
- [60] S. Haeri, Y. Wang, O. Ghita, J. Sun, Discrete element simulation and experimental study of powder spreading process in additive manufacturing, *Powder Technol.* 306 (2017) 45–54, <https://doi.org/10.1016/J.POWTEC.2016.11.002>.
- [61] H. Chen, Q. Wei, Y. Zhang, F. Chen, Y. Shi, W. Yan, Powder-spreading mechanisms in powder-bed-based additive manufacturing: Experiments and computational modeling, *Acta Mater.* 179 (2019) 158–171, <https://doi.org/10.1016/J.ACTAMAT.2019.08.030>.
- [62] M.Y. Shaheen, A.R. Thornton, S. Luding, T. Weinhart, The influence of material and process parameters on powder spreading in additive manufacturing, *Powder Technol.* 383 (2021) 564–583, <https://doi.org/10.1016/J.POWTEC.2021.01.058>.
- [63] J. Foerster, M. Michatz, M. Binder, A. Frey, C. Seidel, G. Schlick, J. Schilp, Electrostatic powder attraction for the development of a novel recoating system for metal powder bed-based additive manufacturing, *J. Electro* 115 (2022), 103641, <https://doi.org/10.1016/J.JELSTAT.2021.103641>.
- [64] T. Stichel, C. Brachmann, M. Raths, M.A. Dechet, J. Schmidt, W. Peukert, T. Frick, S. Roth, Electrophotographic multilayer powder pattern deposition for additive manufacturing, *Jom* 72 (2020) 1366–1375, <https://doi.org/10.1007/s11837-019-03965-z>.
- [65] K. Wudy, D. Drummer, Aging effects of polyamide 12 in selective laser sintering: molecular weight distribution and thermal properties, *Addit. Manuf.* 25 (2019) 1–9, <https://doi.org/10.1016/J.ADDMA.2018.11.007>.
- [66] D. Drummer, S. Greiner, M. Zhao, K. Wudy, A novel approach for understanding laser sintering of polymers, *Addit. Manuf.* 27 (2019) 379–388, <https://doi.org/10.1016/J.ADDMA.2019.03.012>.
- [67] N.A. Charoo, S.F. Barakh Ali, E.M. Mohamed, M.A. Kuttolamadom, T. Ozkan, M. A. Khan, Z. Rahman, Selective laser sintering 3D printing – an overview of the technology and pharmaceutical applications, *https://doi.org/10.1080/03639045.2020.1764027*. 46 (2020) 869–877. <https://doi.org/10.1080/03639045.2020.1764027>.
- [68] D.G. Yu, L.M. Zhu, C.J. Branford-White, X.L. Yang, Three-dimensional printing in pharmaceuticals: promises and problems, *J. Pharm. Sci.* 97 (2008) 3666–3690, <https://doi.org/10.1002/JPS.21284>.
- [69] Balance XSR105 - Overview - METTLER TOLEDO, (n.d.). https://www.mt.com/de/en/home/products/Laboratory_Weighing_Solutions/analytical-balances/XSR105-30355059.html (accessed January 29, 2023).
- [70] F. Fina, A. Goyanes, C.M. Madla, A. Awad, S.J. Trenfield, J.M. Kuek, P. Patel, S. Gaisford, A.W. Basit, 3D printing of drug-loaded gyroid lattices using selective laser sintering, *Int J. Pharm.* 547 (2018) 44–52, <https://doi.org/10.1016/J.IJPHARM.2018.05.044>.
- [71] A. Sommereyns, S. Gann, J. Schmidt, A.B. Chehreh, A. Lüddecke, F. Walther, B. Gökce, S. Barcikowski, M. Schmidt, How colloidal surface addition of polyamide 12 powders with well-dispersed silver nanoparticles influences the crystallization already at low 0.01 vol%, *Addit. Manuf.* 14 (2020) <https://doi.org/10.3390/MA14185322>.
- [72] C. Schick, Differential scanning calorimetry (DSC) of semicrystalline polymers, *Anal. Bioanal. Chem.* 395 (2009) 1589–1611, <https://doi.org/10.1007/S00216-009-3169-Y>.
- [73] H.D.R., Betriebsanleitung scanCONTROL 29xx, (n.d.). www.micro-epsilon.de (accessed January 30, 2023).
- [74] F. Sillani, E. MacDonald, J. Villela, M. Schmid, K. Wegener, In-situ monitoring of powder bed fusion of polymers using laser profilometry, *Addit. Manuf.* 59 (2022), 103074, <https://doi.org/10.1016/J.ADDMA.2022.103074>.

- [75] G.W. Zack, W.E. Rogers, S.A. Latt, Automatic measurement of sister chromatid exchange frequency, *J. Histochem Cytochem* 25 (1977) 741–753, <https://doi.org/10.1177/25.7.70454>.
- [76] F. Papadopoulos, M. Spinelli, S. Valente, L. Foroni, C. Orrico, F. Alviano, G. Pasquinelli, Common tasks in microscopic and ultrastructural image analysis using ImageJ, *Ultra Pathol.* 31 (2007) 401–407, <https://doi.org/10.1080/01913120701719189>.
- [77] L. Nichele, V. Persichetti, M. Lucidi, G. Cincotti, Quantitative evaluation of ImageJ thresholding algorithms for microbial cell counting, *OSA Contin.* 3 (2020) 1417. <https://doi.org/10.1364/OSAC.393971>.
- [78] S.-P. Kopp, F.ürth, De, Verfahren und Vorrichtung zur additiven Fertigung eines Bauteils sowie entsprechend gefertigtes Bauteil, (n.d.).
- [79] A. Goyanes, F. Fina, A. Martorana, D. Sedough, S. Gaisford, A.W. Basit, Development of modified release 3D printed tablets (printlets) with pharmaceutical excipients using additive manufacturing, *Int J. Pharm.* 527 (2017) 21–30, <https://doi.org/10.1016/J.IJPHARM.2017.05.021>.
- [80] Y. Chen, J. Yang, A. Mujumdar, R. Dave, Fluidized bed film coating of cohesive Geldart group C powders, *Powder Technol.* 189 (2009) 466–480, <https://doi.org/10.1016/J.POWTEC.2008.08.002>.
- [81] J. Yang, A. Sliva, A. Banerjee, R.N. Dave, R. Pfeffer, Dry particle coating for improving the flowability of cohesive powders, (2005). <https://doi.org/10.1016/j.powtec.2005.04.032>.
- [82] R. Pfeffer, R.N. Dave, D. Wei, M. Ramlakhan, Synthesis of engineered particulates with tailored properties using dry particle coating, *Powder Technol.* 117 (2001) 40–67, [https://doi.org/10.1016/S0032-5910\(01\)00314-X](https://doi.org/10.1016/S0032-5910(01)00314-X).
- [83] J.A. Giacometti, S. Fedosov, M.M. Costa, Corona charging of polymers: recent advances on constant current charging, *Braz. J. Phys.* 29 (1999) 269–279, <https://doi.org/10.1590/S0103-97331999000200009>.
- [84] R.M. Faria, A. Jorge, O.N. Oliveira, A novel space-charge effect in thermally stimulated current measurements on β -PVDF, *J. Phys. D. Appl. Phys.* 23 (1990) 334, <https://doi.org/10.1088/0022-3727/23/3/011>.
- [85] L.E. Aguilar, A.R. Unnithan, A. Amarjargal, A.P. Tiwari, S.T. Hong, C.H. Park, C. S. Kim, Electrospun polyurethane/Eudragit® L100-55 composite mats for the pH dependent release of paclitaxel on duodenal stent cover application, *Int J. Pharm.* 478 (2015) 1–8, <https://doi.org/10.1016/J.IJPHARM.2014.10.057>.
- [86] GESTIS-Stoffdatenbank, (n.d.). <https://gestis.dguv.de/data?name=014120> (accessed February 1, 2023).
- [87] 98–92-0 - Nicotinamide, 99% - Niacinamide - Pyridine-3-carboxamide - A15970 - Alfa Aesar, (n.d.). <https://www.alfa.com/de/catalog/A15970/> (accessed February 1, 2023).
- [88] GESTIS-Stoffdatenbank, (n.d.). <https://gestis.dguv.de/data?name=024840> (accessed February 1, 2023).
- [89] R. Zekó, Á. Orbán, J. Nagy, G. Csóka, I. Rác, Coating polymer-plasticizer interaction in relation to the enthalpy relaxation of polymer, *J. Therm. Anal. Calor.* 68 (2004) 531–537, <https://doi.org/10.1023/A:1016095904226>.
- [90] I.M. Hodge, Enthalpy relaxation and recovery in amorphous materials, *J. Non Cryst. Solids* 169 (1994) 211–266, [https://doi.org/10.1016/0022-3093\(94\)90321-2](https://doi.org/10.1016/0022-3093(94)90321-2).
- [91] T. Parikh, S.S. Gupta, A. Meena, A.T.M. Serajuddin, Investigation of thermal and viscoelastic properties of polymers relevant to hot melt extrusion - III: Polymethacrylates and polymethacrylic acid based polymers, *J. Excip. Food Chem.* 5 (2016).
- [92] S.Y. Lin, C.M. Liao, G.H. Hsiue, A reflectance FTIR/DSC microspectroscopic study of the nonisothermal kinetics of anhydride formation in Eudragit L-100 films, *Polym. Degrad. Stab.* 47 (1995) 299–303, [https://doi.org/10.1016/0141-3910\(94\)00129-V](https://doi.org/10.1016/0141-3910(94)00129-V).
- [93] J.R. Hughey, J.C. Di Nunzio, R.C. Bennett, C. Brough, D.A. Miller, H. Ma, R. O. Williams, J.W. McGinity, Dissolution enhancement of a drug exhibiting thermal and acidic decomposition characteristics by fusion processing: a comparative study of hot melt extrusion and kinetisol® dispersing, *AAPS PharmSciTech* 11 (2010) 760, <https://doi.org/10.1208/S12249-010-9431-Y>.
- [94] S.S. Gupta, N. Solanki, A.T.M. Serajuddin, Investigation of thermal and viscoelastic properties of polymers relevant to hot melt extrusion, IV: Affinisol™ HPMC HME polymers, *AAPS PharmSciTech* 17 (2016) 148–157, <https://doi.org/10.1208/S12249-015-0426-6>.
- [95] K. Wudy, M. Drexler, L. Lanzl, Analysis of time dependent thermal properties for high rates in selective laser sintering, *Rapid Prototyp. J.* 24 (2018) 894–900, <https://doi.org/10.1108/RPJ-01-2017-0013/FULL/XML>.
- [96] J.E.K. Schawe, Influence of processing conditions on polymer crystallization measured by fast scanning DSC, *J. Therm. Anal. Calor.* 116 (2014) 1165–1173, <https://doi.org/10.1007/S10973-013-3563-8>.
- [97] V. Mathot, M. Pyda, T. Pijpers, G. vanden Poel, E. van de Kerkhof, S. van Herwaarden, F. van Herwaarden, A. Leenaers, The Flash DSC 1, a power compensation twin-type, chip-based fast scanning calorimeter (FSC): First findings on polymers, *Thermochim. Acta* 522 (2011) 36–45, <https://doi.org/10.1016/J.TCA.2011.02.031>.
- [98] A. el Magri, S.E. Bencaid, H.R. Vanaei, S. Vaudreuil, Effects of Laser Power and Hatch Orientation on Final Properties of PA12 Parts Produced by Selective Laser Sintering, *Polymers* 2022, Vol. 14, Page 3674. 14 (2022) 3674. <https://doi.org/10.3390/POLYM14173674>.
- [99] H. Zhou, Y. Wang, S. Li, M. Lu, Improving chemical stability of resveratrol in hot melt extrusion based on formation of eutectic with nicotinamide, *Int J. Pharm.* 607 (2021), 121042, <https://doi.org/10.1016/J.IJPHARM.2021.121042>.
- [100] E. v. Agafonova, Y. v. Moshchenskii, M.L. Tkachenko, Determining the main thermodynamic parameters of caffeine melting by means of DSC, *Russ. J. Phys. Chem. A* 86 (2012) 1035–1037, <https://doi.org/10.1134/S0036024412060027/METRICS>.
- [101] A. Cesàro, Thermodynamic properties of caffeine crystal forms, *J. Phys. Chem.* 84 (1980) 1345–1346, https://doi.org/10.1021/J100448A011/ASSET/J100448A011.FP.PNG_V03.
- [102] M. Qiao, L. Zhang, Y. Ma, J. Zhu, K. Chow, A novel electrostatic dry powder coating process for pharmaceutical dosage forms: Immediate release coatings for tablets, *Eur. J. Pharm. Biopharm.* 76 (2010) 304–310, <https://doi.org/10.1016/J.EJPB.2010.06.009>.
- [103] A.R. Blythe, Electrical resistivity measurements of polymer materials, *Polym. Test.* 4 (1984) 195–209, [https://doi.org/10.1016/0142-9418\(84\)90012-6](https://doi.org/10.1016/0142-9418(84)90012-6).
- [104] M.B. Mayr, S.A. Barringer, Corona compared with triboelectric charging for electronic powder coating, *J. Food Sci.* 71 (2006), <https://doi.org/10.1111/J.1750-3841.2006.00024.X>.
- [105] A.G. Bailey, The science and technology of electrostatic powder spraying, transport and coating, *J. Electro* 45 (1998) 85–120, [https://doi.org/10.1016/S0304-3886\(98\)00049-7](https://doi.org/10.1016/S0304-3886(98)00049-7).
- [106] C. Mielicki, B. Gronhoff, J. Wortberg, Effects of laser sintering processing time and temperature on changes in polyamide 12 powder particle size, shape and distribution, *AIP Conf. Proc.* 1593 (2015) 728, <https://doi.org/10.1063/1.4873880>.
- [107] S. Wintzheimer, T. Granath, M. Oppmann, T. Kister, T. Thai, T. Kraus, N. Vogel, K. Mandel, Supraparticles: functionality from Uniform Structural Motifs, *ACS Nano* 12 (2018) 5093–5120, https://doi.org/10.1021/ACS.NANO.8B00873/ASSET/IMAGES/MEDIUM/NN-2018-008732_0013.GIF.

6 Conclusion

In this work, the key aspects for enabling the complete substitution of conventional powder application methods for PBF-LB/P by EPA have been systematically identified, investigated and finally applied. A bottom-up approach was used, covering all relevant levels from the charging of individual particles to the formation of layers consisting of charged particles, and finally to parts generated by laser-based fusion of charged powder layers.

As discussed in section 2.1.3 and shown in Table 5, PBF-LB/P using EPA with contactless powder deposition has an MRL of 2 according to the state of the art. By applying the methods developed and investigated in this work, functional parts have been successfully manufactured with EPA-PBF-LB/P. Following the MRL classification of [166] summarized in Figure 7, EPA-PBF-LB/P has therefore been shown to perform at MRL 4 to MRL 5.

The key findings of this thesis are summarized in the following:

1. The natural bimodal charge distribution of triboelectrically charged polymer particles can be transformed into a monomodal distribution suitable for EPA-PBF-LB/P by functionalization of the polymer particles with CCAs in combination with the use of suitable ferritic carrier particles
2. The incorporation of ions into the surface of the powder particles in the case of gas discharge-based powder charging is shown to depend on the particle shape, resulting in different particle charging and consequently in a separation effect caused by EPA
3. In the case of homogeneously charged powder particles, the layer thickness of the applied powder layer can be tailored between a single particle diameter and several times the particle diameter by adjusting the electric deposition field strength
4. The local distribution of the strength and direction of the electric deposition field is crucial for the coverage and geometric accuracy of the deposited powder layer and can be tailored by adapting the geometry of a transfer structure inserted into the gap between the photoconductor and the build platform
5. By reducing the interparticle attraction forces of charged particles within an external electric field, e.g., by vibrational excitation, the motion of the mechanically excited charged particles is dominated by the electric field force, which can be used to increase the deposition efficiency in EPA-PBF-LB/P

6. Accumulation of charges within a part manufactured by EPA-PBF-LB/P:
 - a. Increasing charge accumulation with each deposited and consolidated layer
 - b. Charge accumulation is a function of the electrical volume resistivity of the material
 - c. Direct increase of the surface potential on top of the manufactured part by charge accumulation, resulting in a decrease in powder deposition efficiency
 - d. Alternating the polarity of the deposited powder layers as a suitable strategy to compensate for the charge accumulation within a part manufactured with EPA-PBF-LB/P
7. EPA with contactless powder deposition is shown to overcome the limitations of conventional powder application methods for PBF-LB/P by:
 - a. Significantly reducing the strong dependence on the powder flowability and thus increasing the number of powder materials suitable for PBF-LB/P, in particular if triboelectric powder charging is used for EPA
 - b. Enabling highly selective powder application, providing the flexibility to tailor the material composition and distribution within a layer and from layer to layer
 - c. Enabling the deposition of multiple materials and thus the fabrication of multi-material parts by PBF-LB/P
 - d. Minimizing powder waste by only applying the amount of powder to the build chamber required to produce the part

7 Zusammenfassung

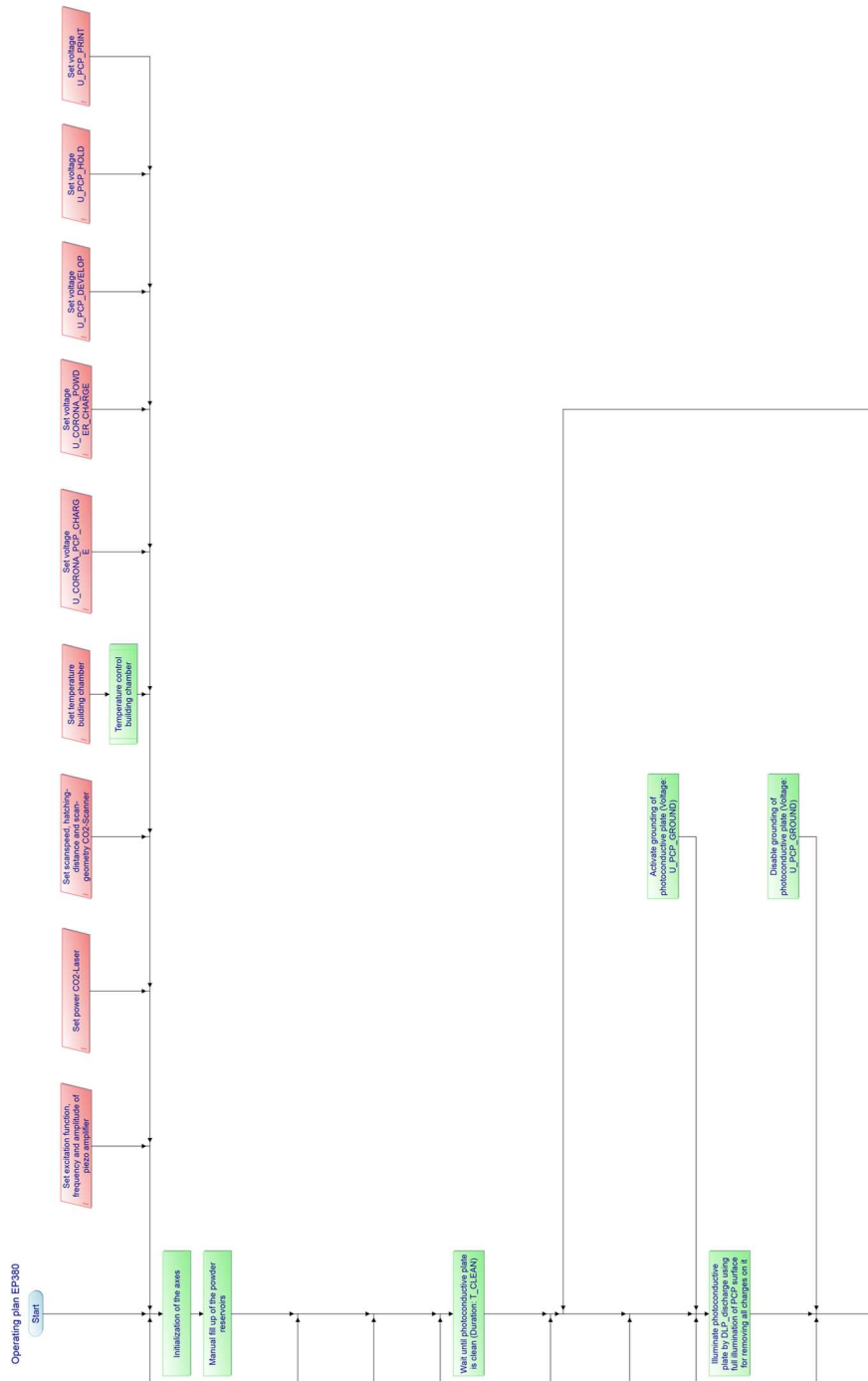
In der vorliegenden Arbeit wurden die Schlüsselaspekte, welche für den Einsatz des EPA anstelle konventioneller Pulverauftragsmethoden für das PBF-LB/P erforderlich sind, systematisch identifiziert, untersucht und angewendet. Dabei wurde ein ganzheitlicher Ansatz verfolgt, der alle relevanten Ebenen von der Aufladung einzelner Pulverpartikel über die Bildung von Schichten bestehend aus geladenen Pulverpartikeln, bis hin zu fertigen Bauteilen, welche mittels EPA-PBF-LB/P gefertigt wurden, umfasst.

Wie in Abschnitt 2.1.3 erörtert und in Table 5 gezeigt, hat PBF-LB/P unter Verwendung von EPA als Pulverauftragsverfahren bisher einen MRL von 2. Mithilfe der in dieser Arbeit entwickelten Methoden konnten mittels EPA-PBF-LB/P funktionale Bauteile hergestellt werden. Demnach kann – basierend auf der MRL-Klassifizierung aus [166], welche in Figure 7 zusammengefasst ist, ein MRL von 4 bis 5 geschlussfolgert werden.

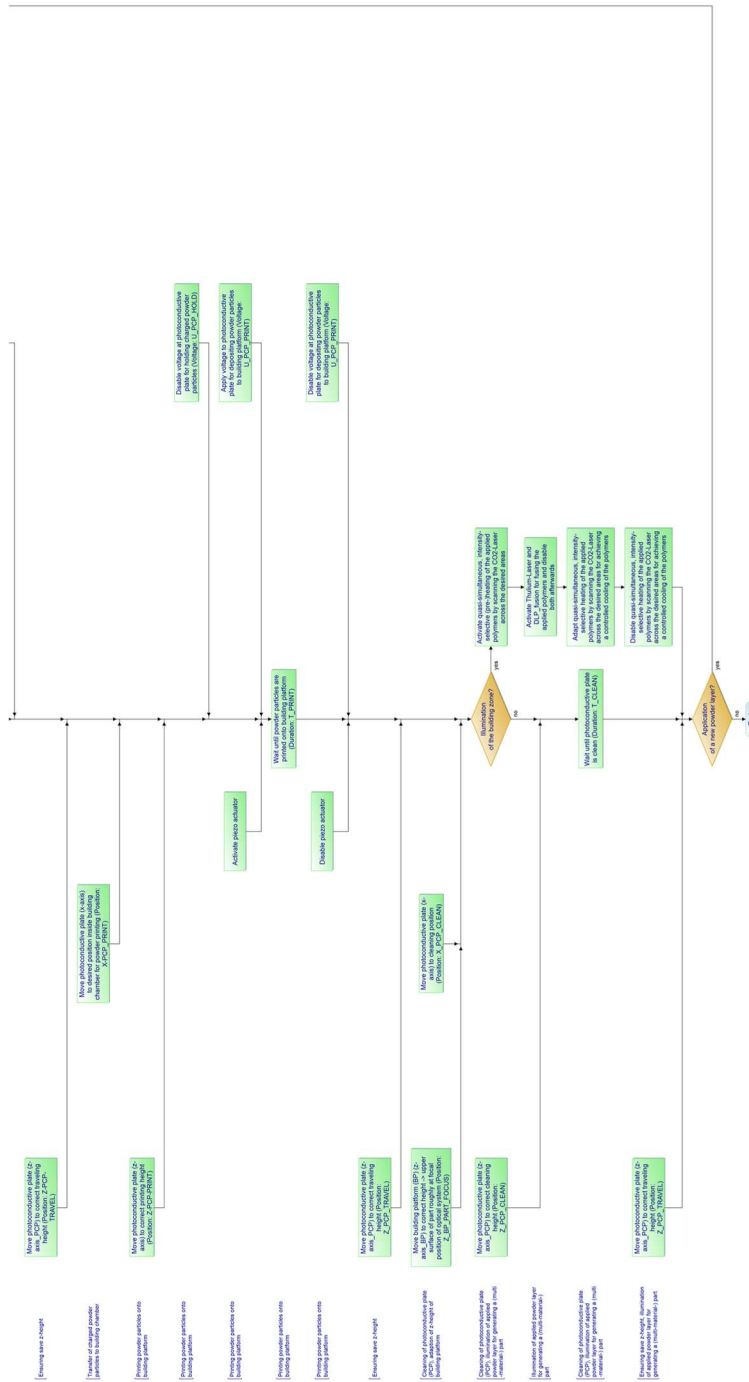
Die Schlüsselerkenntnisse dieser Arbeit werden im Folgenden zusammengefasst:

1. Die natürliche bimodale Ladungsverteilung von triboelektrisch geladenen Polymerpartikeln kann durch Funktionalisierung der Polymerpartikel mit CCAs in Kombination mit der Verwendung geeigneter ferritischer Carrierpartikel zu einer für EPA-PBF-LB/P geeigneten monomodalen Verteilung verschoben werden
2. Die Einlagerung von Ionen in die Oberfläche der Pulverpartikel im Falle der gasentladungs-basierten Pulveraufladung hängt wesentlich von der Partikelform ab, was letztlich eine inhomogene Ladungsverteilung nach sich zieht und zu einem Separationseffekt beim EPA führt
3. Bei homogen aufgeladenen Pulverpartikeln kann die Schichtdicke der aufgetragenen Pulverschicht durch Veränderung der elektrischen Feldstärke des Ablagefeldes zwischen der Dicke eines Partikeldurchmessers und einem Vielfachen des Partikeldurchmessers angepasst werden
4. Die lokale Verteilung der Stärke und Richtung des elektrischen Ablagefeldes ist entscheidend für den Bedeckungsgrad und die geometrische Genauigkeit der abgelegten Pulverschicht und kann in Abhängigkeit der Geometrie einer sich zwischen Fotoleiter und Bauplatzform eingebrachten Transferstruktur modifiziert werden

5. Durch Verringerung der Anziehungskräfte zwischen geladenen Teilchen in einem äußeren elektrischen Feld, z. B. durch Schwingungsanregung, wird die Bewegung der mechanisch angeregten geladenen Teilchen durch die Kraft des elektrischen Feldes dominiert, was zur Erhöhung der Ablageeffizienz im Rahmen von EPA-PBF-LB/P genutzt werden kann
6. Ladungsakkumulation innerhalb eines mittels EPA-PBF-LB/P hergestellten Bauteils:
 - a. Zunahme der Ladungsakkumulation mit jeder applizierten Schicht
 - b. Abhängigkeit der Akkumulation vom elektrischen Volumenwiderstands des jeweiligen Materials
 - c. Direkte Erhöhung des Oberflächenpotenzials des Bauteils, einhergehend mit einer verringerten Pulverablageeffizienz
 - d. Kompensation der Ladungsakkumulation im Bauteil während des EPA-PBF-LB/P durch Alternierung der Polarität der abgelegten Pulverschichten
7. Mithilfe von EPA mit berührungsloser Pulverablage können die Prozessgrenzen des konventionellen PBF-LB/P wie folgt erweitert werden:
 - a. Deutliche Verringerung der Abhängigkeit von der Fließfähigkeit des Pulvers und damit Erhöhung der Anzahl der für PBF-LB/P geeigneten Pulvermaterialien, insbesondere wenn für EPA das Pulver triboelektrisch geladen wird
 - b. Ermöglichung eines selektiven Pulverauftrags mit der Flexibilität, die Materialzusammensetzung und -verteilung innerhalb einer Schicht und von Schicht zu Schicht anzupassen
 - c. Ermöglichung von Multi-Material-Bauteilen mittels PBF-LB/P
 - d. Minimierung des Pulverabfalls, indem nur die für die Herstellung des Teils erforderliche Menge an Pulver in die Baukammer eingebracht wird



Appendix 2: Developed and implemented operation plan for using EPA in a PBF-LB/P machine - part 2.



Appendix 4: Developed and implemented operation plan for using EPA in a PBF-LB/P machine - part 4.

Bibliography

- [1] Carlson C.F. Electrophotography U. S. Patents No. 2,297,691, April 4, 1939.
- [2] Carlson C.F. Electrophotographic Apparatus U. S. Patents No. 2,357,809, November 16, 1940.
- [3] SCHAFFERT, R. M.; OUGHTON, C. D. Xerography: A New Principle of Photography and Graphic Reproduction. *JOSA*, Vol. 38, Issue 12, pp. 991-998 1948, 38 (12), 991-998. <https://doi.org/10.1364/JOSA.38.000991>.
- [4] Lawrence, G. D.; Fishelson, S. Blueprint Photography by the Cyanotype Process. *J Chem Educ* 1999, 76 (9), 1216A. <https://doi.org/10.1021/ED076P1216>.
- [5] Bourell, D. L.; Beaman, J. J.; Wohlers, T. History and Evolution of Additive Manufacturing. *Additive Manufacturing Processes* 2020, 11-18. <https://doi.org/10.31399/ASM.HB.V24.A0006548>.
- [6] Kruth, J. P.; Wang, X.; Laoui, T.; Froyen, L. Lasers and Materials in Selective Laser Sintering. *Assembly Automation* 2003, 23 (4), 357-371. <https://doi.org/10.1108/01445150310698652>.
- [7] Kellens, K.; Renaldi, R.; Dewulf, W.; Kruth, J. P.; Duflou, J. R. Environmental Impact Modeling of Selective Laser Sintering Processes. *Rapid Prototyp J* 2014, 20 (6), 459-470. <https://doi.org/10.1108/RPJ-02-2013-0018>.
- [8] Northon, K. NASA Tests Limits of 3-D Printing with Powerful Rocket Engine Check. 2013. <https://doi.org/10.2/UI/MINIFIED/JQUERY-UI.MIN.JS>.
- [9] Fasel, U.; Keidel, D.; Baumann, L.; Cavolina, G.; Eichenhofer, M.; Ermanni, P. Composite Additive Manufacturing of Morphing Aerospace Structures. *Manuf Lett* 2020, 23, 85-88. <https://doi.org/10.1016/J.MFGLET.2019.12.004>.
- [10] Delic, M.; Eyers, D. R. The Effect of Additive Manufacturing Adoption on Supply Chain Flexibility and Performance: An Empirical Analysis from the Automotive Industry. *Int J Prod Econ* 2020, 228. <https://doi.org/10.1016/J.IJPE.2020.107689>.

- [11] Nouri, A.; Rohani Shirvan, A.; Li, Y.; Wen, C. Additive Manufacturing of Metallic and Polymeric Load-Bearing Biomaterials Using Laser Powder Bed Fusion: A Review. *J Mater Sci Technol* **2021**, *94*, 196–215. <https://doi.org/10.1016/J.JMST.2021.03.058>.
- [12] Allahham, N.; Fina, F.; Marcuta, C.; Kraschew, L.; Mohr, W.; Gaisford, S.; Basit, A. W.; Goyanes, A. Selective Laser Sintering 3D Printing of Orally Disintegrating Printlets Containing Ondansetron. *Pharmaceutics* **2020**, *Vol. 12*, Page 110 **2020**, *12* (2), 110. <https://doi.org/10.3390/PHARMACEUTICS12020110>.
- [13] Fina, F.; Gaisford, S.; Basit, A. W. Powder Bed Fusion: The Working Process, Current Applications and Opportunities. *AAPS Advances in the Pharmaceutical Sciences Series* **2018**, *31*, 81–105. https://doi.org/10.1007/978-3-319-90755-0_5.
- [14] Kusoglu, I. M.; Doñate-buendía, C.; Barcikowski, S.; Gökce, B. Laser Powder Bed Fusion of Polymers: Quantitative Research Direction Indices. *Materials* **2021**, *Vol. 14*, Page 1169 **2021**, *14* (5), 1169. <https://doi.org/10.3390/MA14051169>.
- [15] Wudy, K.; Drummer, D. Aging Effects of Polyamide 12 in Selective Laser Sintering: Molecular Weight Distribution and Thermal Properties. *Addit Manuf* **2019**, *25*, 1–9. <https://doi.org/10.1016/J.ADDMA.2018.11.007>.
- [16] Cohen-Sabban, J.; Bieber, A.; Kamir, J.; Katz, M.; Nagler, M.; Aviv, T. Three Dimensional Modelling Apparatus U. S. Patents No. 4,961,154, June 2, 1990.
- [17] Bynum, D. K. Apparatus for Forming a Three-Dimensional Reproduction of an Object from Laminations U. S. Patent 5,127,037, 1992.
- [18] Schmidt, M.; Merklein, M.; Bourell, D.; Dimitrov, D.; Hausotte, T.; Wegener, K.; Overmeyer, L.; Vollertsen, F.; Levy, G. N. Laser Based Additive Manufacturing in Industry and Academia. *CIRP Annals* **2017**, *66* (2), 561–583. <https://doi.org/10.1016/j.cirp.2017.05.011>.
- [19] DIN 8580:2022-12 Fertigungsverfahren - Begriffe, Einteilung; Manufacturing Processes - Terms and Definitions, Division. Beuth-Verlag, Berlin, 2022.
- [20] DIN EN ISO 17296-2:2016-12 Additive Manufacturing - General Principles - Part 2: Overview of Process Categories and Feedstock (ISO 17296-2:2015); German Version EN ISO 17296-2:2016. Beuth-Verlag, Berlin, 2016.

- [21] ASTM F2792-12a Standard Terminology for Additive Manufacturing Technologies, (Withdrawn 2015) , 2012.
- [22] DIN EN ISO/ASTM 52900:2022-03 Additive Manufacturing - General Principles - Fundamentals and Vocabulary (ISO/ASTM 52900:2021); German Version EN ISO/ASTM 52900:2021. Beuth-Verlag, Berlin, 2022.
- [23] Hupfeld, T. Nanoparticle-Functionalized Polymers for Laser Powder Bed Fusion, Dissertation of University of Duisburg-Essen, 2021. <https://doi.org/10.17185/dupublico/74518>.
- [24] Bourell, D.; Kruth, J. P.; Leu, M.; Levy, G.; Rosen, D.; Beese, A. M.; Clare, A. Materials for Additive Manufacturing. *CIRP Annals* **2017**, *66* (2), 659–681. <https://doi.org/10.1016/J.CIRP.2017.05.009>.
- [25] Culmone, C.; Smit, G.; Breedveld, P. Additive Manufacturing of Medical Instruments: A State-of-the-Art Review. *Addit Manuf* **2019**, *27*, 461–473. <https://doi.org/10.1016/J.ADDMA.2019.03.015>.
- [26] Fayazfar, H.; Salarian, M.; Rogalsky, A.; Sarker, D.; Russo, P.; Paserin, V.; Toyserkani, E. A Critical Review of Powder-Based Additive Manufacturing of Ferrous Alloys: Process Parameters, Microstructure and Mechanical Properties. *Mater Des* **2018**, *144*, 98–128. <https://doi.org/10.1016/J.MATDES.2018.02.018>.
- [27] Yuan, S.; Shen, F.; Chua, C. K.; Zhou, K. Polymeric Composites for Powder-Based Additive Manufacturing: Materials and Applications. *Prog Polym Sci* **2019**, *91*, 141–168. <https://doi.org/10.1016/J.PROG-POLYMSCI.2018.11.001>.
- [28] Deckers, J.; Vleugels, J.; Kruth, J. P. Additive Manufacturing of Ceramics: A Review. *Journal of Ceramic Science and Technology* **2014**, *5* (4), 245–260. <https://doi.org/10.4416/JCST2014-00032>.
- [29] Florio, K.; Puccio, D.; Viganò, G.; Pfeiffer, S.; Verga, F.; Grasso, M.; Colosimo, B. M.; Graule, T.; Wegener, K. Process Characterization and Analysis of Ceramic Powder Bed Fusion. *International Journal of Advanced Manufacturing Technology* **2021**, *117* (7–8), 2105–2116. <https://doi.org/10.1007/S00170-021-07625-Y/FIGURES/15>.
- [30] Schmid, M. *Selektives Lasersintern (SLS) Mit Kunststoffen - Technologie, Prozesse Und Werkstoffe*; Carl Hanser Verlag: Munich, 2015.

- [31] Salmi, M. Additive Manufacturing Processes in Medical Applications. *Materials* 2021, Vol. 14, Page 191 2021, 14 (1), 191. <https://doi.org/10.3390/MA14010191>.
- [32] Hieu, L. C.; Bohez, E.; Vander Sloten, J.; Phien, H. N.; Vatcharaporn, E.; Binh, P. H.; An, P. V.; Oris, P. Design for Medical Rapid Prototyping of Cranioplasty Implants. *Rapid Prototyp J* 2003, 9 (3), 175–186. <https://doi.org/10.1108/13552540310477481>.
- [33] Bourell, D. L.; Watt, T. J.; Leigh, D. K.; Fulcher, B. Performance Limitations in Polymer Laser Sintering. *Phys Procedia* 2014, 56 (C), 147–156. <https://doi.org/10.1016/J.PHPRO.2014.08.157>.
- [34] Kellens, K.; Mertens, R.; Paraskevas, D.; Dewulf, W.; Duflou, J. R. Environmental Impact of Additive Manufacturing Processes: Does AM Contribute to a More Sustainable Way of Part Manufacturing? *Procedia CIRP* 2017, 61, 582–587. <https://doi.org/10.1016/J.PROCIR.2016.11.153>.
- [35] Greiner, S. Bedeutung Der Geometrieabhängigen Belichtungstemperaturen Für Das Lasersintern von Kunststoffen, Dissertation der Friedrich-Alexander-Universität Erlangen-Nürnberg (FAU), 2023.
- [36] Eggers, T.; Rackl, H.; Lacroix, F. von. Investigation of the Influence of the Mixing Process on the Powder Characteristics for Cyclic Reuse in Selective Laser Sintering. *Powders* 2023, Vol. 2, Pages 32-46 2023, 2 (1), 32–46. <https://doi.org/10.3390/POWDERS2010003>.
- [37] Gebhardt, A. Grundlagen Des Rapid Prototyping: Eine Kurzdarstellung Der Rapid Prototyping Verfahren. 2004. <https://doi.org/https://doi.org/10.21269/136>.
- [38] Cui, X.; Yan, D. Preparation, Characterization and Crystalline Transitions of Odd-Even Polyamides 11,12 and 11,10. *Eur Polym J* 2005, 41 (4), 863–870. <https://doi.org/10.1016/J.EURPOLYMJ.2004.10.045>.
- [39] Laumer, T.; Stichel, T.; Nagulin, K.; Schmidt, M. Optical Analysis of Polymer Powder Materials for Selective Laser Sintering. *Polym Test* 2016, 56, 207–213. <https://doi.org/10.1016/J.POLYMERTESTING.2016.10.010>.
- [40] Cross, L. H.; Richards, R. B.; Willis, H. A. The Infra-Red Spectrum of Ethylene Polymers. *Discuss Faraday Soc* 1950, 9 (0), 235–245. <https://doi.org/10.1039/DF9500900235>.

- [41] *Fine Detail Resolution 3D Printing | EOS GmbH*. <https://www.eos.info/en/innovations/3d-printing-of-the-future/fine-detail-resolution> (accessed 2023-07-09).
- [42] Chatham, C. A.; Long, T. E.; Williams, C. B. A Review of the Process Physics and Material Screening Methods for Polymer Powder Bed Fusion Additive Manufacturing. *Prog Polym Sci* **2019**, *93*, 68–95. <https://doi.org/10.1016/J.PROGPOLYMSCI.2019.03.003>.
- [43] Awad, A.; Fina, F.; Goyanes, A.; Gaisford, S.; Basit, A. W. Advances in Powder Bed Fusion 3D Printing in Drug Delivery and Healthcare. *Adv Drug Deliv Rev* **2021**, *174*, 406–424. <https://doi.org/10.1016/J.ADDR.2021.04.025>.
- [44] *EOS LaserProFusion für den werkzeuglosen Spritzguss | EOS GmbH*. <https://www.eos.info/de/innovationen/3d-druck-der-zukunft/laserpro-fusion> (accessed 2023-07-09).
- [45] Hupfeld, T.; Doñate-Buendía, C.; Krause, M.; Sommereyns, A.; Wegner, A.; Sinnemann, T.; Schmidt, M.; Gökce, B.; Barcikowski, S. Scaling up Colloidal Surface Additivation of Polymer Powders for Laser Powder Bed Fusion. *Procedia CIRP* **2020**, *94*, 110–115. <https://doi.org/10.1016/j.procir.2020.09.022>.
- [46] Goodridge, R. D.; Tuck, C. J.; Hague, R. J. M. Laser Sintering of Polyamides and Other Polymers. *Prog Mater Sci* **2012**, *57* (2), 229–267. <https://doi.org/10.1016/J.PMATSCI.2011.04.001>.
- [47] Awad, A.; Fina, F.; Goyanes, A.; Gaisford, S.; Basit, A. W. 3D Printing: Principles and Pharmaceutical Applications of Selective Laser Sintering. *Int J Pharm* **2020**, *586*, 119594. <https://doi.org/10.1016/J.IJPHARM.2020.119594>.
- [48] Yu, D. G.; Zhu, L. M.; Branford-White, C. J.; Yang, X. L. Three-Dimensional Printing in Pharmaceuticals: Promises and Problems. *J Pharm Sci* **2008**, *97* (9), 3666–3690. <https://doi.org/10.1002/JPS.21284>.
- [49] Gueche, Y. A.; Sanchez-Ballester, N. M.; Cailleaux, S.; Bataille, B.; Soulairol, I. Selective Laser Sintering (SLS), a New Chapter in the Production of Solid Oral Forms (SOFs) by 3D Printing. *Pharmaceutics* **2021**, *13* (8). <https://doi.org/10.3390/PHARMACEUTICS13081212>.
- [50] Alhnan, M. A.; Okwuosa, T. C.; Sadia, M.; Wan, K. W.; Ahmed, W.; Arafat, B. Emergence of 3D Printed Dosage Forms: Opportunities

- and Challenges. *Pharm Res* **2016**, *33* (8), 1817–1832. <https://doi.org/10.1007/S11095-016-1933-1>.
- [51] Fina, F.; Goyanes, A.; Gaisford, S.; Basit, A. W. Selective Laser Sintering (SLS) 3D Printing of Medicines. *Int J Pharm* **2017**, *529* (1–2), 285–293. <https://doi.org/10.1016/J.IJPHARM.2017.06.082>.
- [52] Goodridge, R.; Ziegelmeier, S. Powder Bed Fusion of Polymers. *Laser Additive Manufacturing: Materials, Design, Technologies, and Applications* **2017**, 181–204. <https://doi.org/10.1016/B978-0-08-100433-3.00007-5>.
- [53] Kruth, J.; Levy, G.; Klocke, F.; annals, T. C.-C.; 2007, undefined. Consolidation Phenomena in Laser and Powder-Bed Based Layered Manufacturing. *Elsevier* **56** (2). <https://doi.org/10.1016/j.cirp.2007.10.004>.
- [54] Li, X.; Van Hooreweder, B.; Lauwers, W.; Follon, B.; Witvrouw, A.; Geebelen, K.; Kruth, J. P. Thermal Simulation of the Cooling down of Selective Laser Sintered Parts in PA12. *Rapid Prototyp J* **2018**, *24* (7), 1117–1123. <https://doi.org/10.1108/RPJ-10-2016-0176/FULL/HTML>.
- [55] Kruth, J. P.; Levy, G.; Klocke, F.; Childs, T. H. C. Consolidation Phenomena in Laser and Powder-Bed Based Layered Manufacturing. *CIRP Annals* **2007**, *56* (2), 730–759. <https://doi.org/10.1016/J.CIRP.2007.10.004>.
- [56] Ehrenstein, G. W.; Riedel, G.; Trawiel, P. Praxis Der Thermischen Analyse von Kunststoffen. *Hanser Verlag* **2003**, 2. Auflage.
- [57] Schmachtenberg, E.; Seul, T. Model of Isothermic Laser-Sintering. *Plastics, virtual gold : conference proceedings ; annual technical conference / ANTEC 2002, May 5 - 9, 2002, San Francisco, CA. Society of Plastics Engineers 0-9716435-0-4* **2002**, 4100.
- [58] Wudy, K.; Drexler, M.; Lanzl, L.; Drummer, D. Analysis of Time Dependent Thermal Properties for High Rates in Selective Laser Sintering. *Rapid Prototyp J* **2018**, *24* (5), 894–900. <https://doi.org/10.1108/RPJ-01-2017-0013/FULL/XML>.
- [59] Gabriele Alscher. Das Verhalten Teilkristalliner Thermoplaste Beim Lasersintern, Vom Fachbereich 12 - Maschinenwesender Universität-GH Essen, Essen, 2000.

- [60] Laumer, T.; Stichel, T.; Amend, P.; Schmidt, M. Simultaneous Laser Beam Melting of Multimaterial Polymer Parts. *J Laser Appl* **2015**, *27* (S2), S29204. <https://doi.org/10.2351/1.4906303>.
- [61] Medvedev, V.; Kopp, S.-P.; Roth, S. *Advanced Laser Irradiation Strategies for Tailoring Temperature Profiles for Laser-Based Powder Bed Fusion (PBF-LB/P) of Highly Absorbing Polymers; Lasers in Manufacturing (LiM) Conference 2023, Munich 2023*.
- [62] Schlicht, S.; Greiner, S.; Drummer, D. Low Temperature Powder Bed Fusion of Polymers by Means of Fractal Quasi-Simultaneous Exposure Strategies. *Polymers* **2022**, Vol. 14, Page 1428 **2022**, *14* (7), 1428. <https://doi.org/10.3390/POLYM14071428>.
- [63] Schmid, M.; Amado, A.; Wegener, K. Polymer Powders for Selective Laser Sintering (SLS). *AIP Conf Proc* **2015**, *1664* (1), 160009. <https://doi.org/10.1063/1.4918516/822390>.
- [64] Soe, S. P. Quantitative Analysis on SLS Part Curling Using EOS P700 Machine. *J Mater Process Technol* **2012**, *212* (11), 2433–2442. <https://doi.org/10.1016/J.JMATPROTEC.2012.06.012>.
- [65] Rietzel, D. Werkstoffverhalten Und Prozessanalyse Beim Laser-Sintern von Thermoplasten: Technisch-Wissenschaftlicher Bericht, Dissertation der Friedrich-Alexander-Universität Erlangen-Nürnberg, 2011.
- [66] Drummer, D.; Rietzel, D.; Kühnlein, F. Selektives Lasersintern von Teilkristallinen Thermoplasten. *RT- eJournal - Forum für Rapid Technologie* **2009**, *6*, 1–14.
- [67] Marschall, M.; Cholewa, S.; Kopp, S.-P.; Drummer, D.; Schmidt, M. Holistic Characterization of PBF-LB/P Powder Regarding Isothermal Crystallization, Rheology and Optical Properties Under Process Conditions; Springer, Cham, 2024; pp 43–52. https://doi.org/10.1007/978-3-031-37671-9_5.
- [68] Rietzel, D.; Kühnlein, F.; Drummer, D. Characterization of New Thermoplastics for Additive Manufacturing by Selective Laser Sintering. *68th Annual Technical Conference of the Society of Plastics Engineers 2010, SPE Proceedings (ANTEC), Orlando, Florida 2010*, 2247–2253.
- [69] Drummer, D.; Greiner, S.; Zhao, M.; Wudy, K. A Novel Approach for Understanding Laser Sintering of Polymers. *Addit Manuf* **2019**, *27*, 379–388. <https://doi.org/10.1016/J.ADDMA.2019.03.012>.

- [70] Kandis, M.; Bergman, T. L. A Simulation-Based Correlation of the Density and Thermal Conductivity of Objects Produced by Laser Sintering of Polymer Powders. *J Manuf Sci Eng* **2000**, *122* (3), 439–444. <https://doi.org/10.1115/1.1286558>.
- [71] Childs, T. H. C.; Tontowi, A. E. Selective Laser Sintering of a Crystalline and a Glass-Filled Crystalline Polymer: Experiments and Simulations. *Proc Inst Mech Eng B J Eng Manuf* **2001**, *215* (11), 1481–1495. <https://doi.org/10.1243/0954405011519330>.
- [72] Greco, A.; Maffezzoli, A. Polymer Melting and Polymer Powder Sintering by Thermal Analysis. *J Therm Anal Calorim* **2003**, *72* (3), 1167–1174. <https://doi.org/10.1023/A:1025096432699/METRICS>.
- [73] Launhardt, M.; Drummer, D. Determination of the Fundamental Dimension Development in Building Direction for Laser-Sintered Parts. *Journal of Polymer Engineering* **2019**, *39* (2), 197–206. <https://doi.org/https://doi.org/10.1515/polyeng-2018-0204>.
- [74] Osmanlic, F.; Wudy, K.; Laumer, T.; Schmidt, M.; Drummer, D.; Körner, C. Modeling of Laser Beam Absorption in a Polymer Powder Bed. *Polymers (Basel)* **2018**, *10* (7), 784. <https://doi.org/10.3390/polym10070784>.
- [75] Beitz, S.; Uerlich, R.; Bokelmann, T.; Diener, A.; Vietor, T.; Kwade, A. Influence of Powder Deposition on Powder Bed and Specimen Properties. *Materials (Basel)* **2019**, *12* (2). <https://doi.org/10.3390/MA12020297>.
- [76] Wang, L.; Yu, A.; Li, E.; Shen, H.; Zhou, Z. Effects of Spreader Geometry on Powder Spreading Process in Powder Bed Additive Manufacturing. *Powder Technol* **2021**, *384*, 211–222. <https://doi.org/10.1016/J.POWTEC.2021.02.022>.
- [77] Yao, D.; An, X.; Fu, H.; Zhang, H.; Yang, X.; Zou, Q.; Dong, K. Dynamic Investigation on the Powder Spreading during Selective Laser Melting Additive Manufacturing. *Addit Manuf* **2021**, *37*, 101707. <https://doi.org/10.1016/J.ADDMA.2020.101707>.
- [78] Miao, G.; Du, W.; Pei, Z.; Ma, C. A Literature Review on Powder Spreading in Additive Manufacturing. *Addit Manuf* **2022**, *58*, 103029. <https://doi.org/10.1016/J.ADDMA.2022.103029>.
- [79] Moghadasi, M.; Miao, G.; Li, M.; Pei, Z.; Ma, C. Combining Powder Bed Compaction and Nanopowders to Improve Density in Ceramic

- Binder Jetting Additive Manufacturing. *Ceram Int* **2021**, *47* (24), 35348–35355. <https://doi.org/10.1016/J.CERAMINT.2021.09.077>.
- [80] Cao, S.; Qiu, Y.; Wei, X. F.; Zhang, H. H. Experimental and Theoretical Investigation on Ultra-Thin Powder Layering in Three Dimensional Printing (3DP) by a Novel Double-Smoothing Mechanism. *J Mater Process Technol* **2015**, *220*, 231–242. <https://doi.org/10.1016/J.JMATPROTEC.2015.01.016>.
- [81] Barker, G. C.; Mehta, A. Vibrated Powders: Structure, Correlations, and Dynamics. *Phys Rev A (Coll Park)* **1992**, *45* (6), 3435. <https://doi.org/10.1103/PhysRevA.45.3435>.
- [82] Soldner, D.; Greiner, S.; Burkhardt, C.; Drummer, D.; Steinmann, P.; Mergheim, J. Numerical and Experimental Investigation of the Isothermal Assumption in Selective Laser Sintering of PA12. *Addit Manuf* **2021**, *37*, 101676. <https://doi.org/10.1016/J.ADDMA.2020.101676>.
- [83] Greiner, S.; Jaksch, A.; Cholewa, S.; Drummer, D. Development of Material-Adapted Processing Strategies for Laser Sintering of Polyamide 12. *Advanced Industrial and Engineering Polymer Research* **2021**, *4* (4), 251–263. <https://doi.org/10.1016/J.AIEPR.2021.05.002>.
- [84] Drexler, M.; Greiner, S.; Lexow, M.; Lanzl, L.; Wudy, K.; Drummer, D. Selective Laser Melting of Polymers: Influence of Powder Coating on Mechanical Part Properties. *Journal of Polymer Engineering* **2018**, *38* (7), 667–674. <https://doi.org/10.1515/POLYENG-2017-0133>.
- [85] Shaheen, M. Y.; Thornton, A. R.; Luding, S.; Weinhart, T. The Influence of Material and Process Parameters on Powder Spreading in Additive Manufacturing. *Powder Technol* **2021**, *383*, 564–583. <https://doi.org/10.1016/J.POWTEC.2021.01.058>.
- [86] Haeri, S.; Wang, Y.; Ghita, O.; Sun, J. Discrete Element Simulation and Experimental Study of Powder Spreading Process in Additive Manufacturing. *Powder Technol* **2017**, *306*, 45–54. <https://doi.org/10.1016/J.POWTEC.2016.11.002>.
- [87] Parteli, E. J. R.; Pöschel, T. Particle-Based Simulation of Powder Application in Additive Manufacturing. *Powder Technol* **2016**, *288*, 96–102. <https://doi.org/10.1016/J.POWTEC.2015.10.035>.

- [88] Chen, H.; Wei, Q.; Zhang, Y.; Chen, F.; Shi, Y.; Yan, W. Powder-Spreading Mechanisms in Powder-Bed-Based Additive Manufacturing: Experiments and Computational Modeling. *Acta Mater* **2019**, *179*, 158–171. <https://doi.org/10.1016/J.ACTAMAT.2019.08.030>.
- [89] Schiochet Nasato, D.; Briesen, H.; Pöschel, T. Influence of Vibrating Recoating Mechanism for the Deposition of Powders in Additive Manufacturing: Discrete Element Simulations of Polyamide 12. *Addit Manuf* **2021**, *48*, 102248. <https://doi.org/10.1016/J.ADDMA.2021.102248>.
- [90] Marschall, M.; Heintges, C.; Schmidt, M. Influence of Flow Aid Additives on Optical Properties of Polyamide for Laser-Based Powder Bed Fusion. *Procedia CIRP* **2022**, *111*, 51–54. <https://doi.org/10.1016/J.PROCIR.2022.08.114>.
- [91] Pal, S.; Gubeljak, N.; Bončina, T.; Hudák, R.; Toth, T.; Zivcak, J.; Lobjen, G.; Leben, N.; Drstvenšek, I. The Effects of Locations on the Build Tray on the Quality of Specimens in Powder Bed Additive Manufacturing. *International Journal of Advanced Manufacturing Technology* **2021**, *112* (3–4), 1159–1170. <https://doi.org/10.1007/S00170-020-06563-5/FIGURES/8>.
- [92] Ali, U.; Mahmoodkhani, Y.; Imani Shahabad, S.; Esmailizadeh, R.; Liravi, F.; Sheydaei, E.; Huang, K. Y.; Marzbanrad, E.; Vlasea, M.; Toyserkani, E. On the Measurement of Relative Powder-Bed Compaction Density in Powder-Bed Additive Manufacturing Processes. *Mater Des* **2018**, *155*, 495–501. <https://doi.org/10.1016/J.MATDES.2018.06.030>.
- [93] Phua, A.; Smith, J.; Davies, C. H. J.; Cook, P. S.; Delaney, G. W. Understanding the Structure and Dynamics of Local Powder Packing Density Variations in Metal Additive Manufacturing Using Set Voronoi Analysis. *Powder Technol* **2023**, *418*, 118272. <https://doi.org/10.1016/J.POWTEC.2023.118272>.
- [94] Körner, C.; Bauereiß, A.; Attar, E. Fundamental Consolidation Mechanisms during Selective Beam Melting of Powders. *Model Simul Mat Sci Eng* **2013**, *21* (8), 085011. <https://doi.org/10.1088/0965-0393/21/8/085011>.
- [95] Körner, C.; Attar, E.; Heintges, P. Mesoscopic Simulation of Selective Beam Melting Processes. *J Mater Process Technol* **2011**, *211* (6), 978–987. <https://doi.org/10.1016/J.JMATPROTEC.2010.12.016>.

- [96] Greiner, S.; Lanzl, L.; Wudy, K.; Drexler, M.; Drummer, D. Untersuchungen Zum Potential Der Pulververdichtung Durch Den Pulverauftrag Beim Selektiven Laserstrahlschmelzen von Kunststoffen. *Rapid.Tech – International Trade Show & Conference for Additive Manufacturing* **2017**, *406–418*. <https://doi.org/10.3139/9783446454606.029>.
- [97] Haeri, S. Optimisation of Blade Type Spreaders for Powder Bed Preparation in Additive Manufacturing Using DEM Simulations. *Powder Technol* **2017**, *321*, 94–104. <https://doi.org/10.1016/J.POWTEC.2017.08.011>.
- [98] Meyer, L.; Wegner, A.; Witt, G. Influence of the Ratio between the Translation and Contra-Rotating Coating Mechanism on Different Laser Sintering Materials and Their Packing Density. In *2017 International Solid Freeform Fabrication Symposium*; University of Texas at Austin, 2017.
- [99] Zhang, J.; Tan, Y.; Bao, T.; Xu, Y.; Xiao, X.; Jiang, S. Discrete Element Simulation of the Effect of Roller-Spreading Parameters on Powder-Bed Density in Additive Manufacturing. *Materials* **2020**, *13* (10). <https://doi.org/10.3390/MA13102285>.
- [100] Oropeza, D.; Penny, R. W.; Gilbert, D.; Hart, A. J. Mechanized Spreading of Ceramic Powder Layers for Additive Manufacturing Characterized by Transmission X-Ray Imaging: Influence of Powder Feedstock and Spreading Parameters on Powder Layer Density. *Powder Technol* **2022**, *398*. <https://doi.org/10.1016/J.POWTEC.2021.117053>.
- [101] Wang, L.; Li, E. L.; Shen, H.; Zou, R. P.; Yu, A. B.; Zhou, Z. Y. Adhesion Effects on Spreading of Metal Powders in Selective Laser Melting. *Powder Technol* **2020**, *363*, 602–610. <https://doi.org/10.1016/J.POWTEC.2019.12.048>.
- [102] Niino, T.; Sato, K. Effect of Powder Compaction in Plastic Laser Sintering Fabrication. In *2009 International Solid Freeform Fabrication Symposium*; University of Texas at Austin, 2009.
- [103] Zhang, J.; Tan, Y.; Xiao, X.; Jiang, S. Comparison of Roller-Spreading and Blade-Spreading Processes in Powder-Bed Additive Manufacturing by DEM Simulations. *Particuology* **2022**, *66*, 48–58. <https://doi.org/10.1016/J.PARTIC.2021.07.005>.

- [104] Yamamoto, H.; Scarlett, B. Triboelectric Charging of Polymer Particles by Impact. *Particle & Particle Systems Characterization* **1986**, *3* (3), 117–121. <https://doi.org/10.1002/PPSC.19860030305>.
- [105] Hesse, N.; Dechet, M. A.; Bonilla, J. S. G.; Lübbert, C.; Roth, S.; Bück, A.; Schmidt, J.; Peukert, W. Analysis of Tribo-Charging during Powder Spreading in Selective Laser Sintering: Assessment of Polyamide 12 Powder Ageing Effects on Charging Behavior. *Polymers (Basel)* **2019**, *11* (4). <https://doi.org/10.3390/polym11040609>.
- [106] Chen, H.; Wei, Q.; Wen, S.; Li, Z.; Shi, Y. Flow Behavior of Powder Particles in Layering Process of Selective Laser Melting: Numerical Modeling and Experimental Verification Based on Discrete Element Method. *Int J Mach Tools Manuf* **2017**, *123*, 146–159. <https://doi.org/10.1016/J.IJMACHTOOLS.2017.08.004>.
- [107] Du, W.; Ren, X.; Pei, Z.; Ma, C. Ceramic Binder Jetting Additive Manufacturing: A Literature Review on Density. *Journal of Manufacturing Science and Engineering, Transactions of the ASME* **2020**, *142* (4). <https://doi.org/10.1115/1.4046248/1074276>.
- [108] Utela, B. R.; Storti, D.; Anderson, R. L.; Ganter, M. Development Process for Custom Three-Dimensional Printing (3DP) Material Systems. *J Manuf Sci Eng* **2010**, *132* (1), 0110081–0110089. <https://doi.org/10.1115/1.4000713/468586>.
- [109] Ziaee, M.; Hershman, R.; Mahmood, A.; Crane, N. B. Fabrication of Demineralized Bone Matrix/Polycaprolactone Composites Using Large Area Projection Sintering (LAPS). *Journal of Manufacturing and Materials Processing* *2019*, *Vol. 3*, *Page 30* **2019**, *3* (2), 30. <https://doi.org/10.3390/JMMP3020030>.
- [110] Nan, W.; Pasha, M.; Ghadiri, M. Numerical Simulation of Particle Flow and Segregation during Roller Spreading Process in Additive Manufacturing. *Powder Technol* **2020**, *364*, 811–821. <https://doi.org/10.1016/J.POWTEC.2019.12.023>.
- [111] Budding, A.; Vaneker, T. H. J. New Strategies for Powder Compaction in Powder-Based Rapid Prototyping Techniques. *Procedia CIRP* **2013**, *6*, 527–532. <https://doi.org/10.1016/J.PROCIR.2013.03.100>.
- [112] Meier, C.; Weissbach, R.; Weinberg, J.; Wall, W. A.; Hart, A. J. Critical Influences of Particle Size and Adhesion on the Powder Layer

Uniformity in Metal Additive Manufacturing. *J Mater Process Technol* **2019**, *266*, 484–501. <https://doi.org/10.1016/J.JMATPROTEC.2018.10.037>.

- [113] Chen, H.; Chen, Y.; Liu, Y.; Wei, Q.; Shi, Y.; Yan, W. Packing Quality of Powder Layer during Counter-Rolling-Type Powder Spreading Process in Additive Manufacturing. *Int J Mach Tools Manuf* **2020**, *153*, 103553. <https://doi.org/10.1016/J.IJMACHTOOLS.2020.103553>.
- [114] Gregorski, S. J. High Green Density Metal Parts by Vibrational Compaction of Dry Powder in Three Dimensional Printing Process, Massachusetts Institute of Technology. Department of Mechanical Engineering. Doctoral Thesis, 1996.
- [115] Du, W.; Roa, J.; Hong, J.; Liu, Y.; Pei, Z.; Ma, C. Binder Jetting Additive Manufacturing: Effect of Particle Size Distribution on Density. *Journal of Manufacturing Science and Engineering, Transactions of the ASME* **2021**, *143* (9). <https://doi.org/10.1115/1.4050306/1100582>.
- [116] Mersch, E.; Lumay, G.; Boschini, F.; Vandewalle, N. Effect of an Electric Field on an Intermittent Granular Flow. *Phys Rev E Stat Nonlin Soft Matter Phys* **2010**, *81* (4), 041309. <https://doi.org/10.1103/PHYSREVE.81.041309/FIGURES/10/MEDIUM>.
- [117] Fiscina, J. E.; Lumay, G.; Ludewig, F.; Vandewalle, N. Compaction Dynamics of Wet Granular Assemblies. *Phys Rev Lett* **2010**, *105* (4), 048001. <https://doi.org/10.1103/PHYSREVLETT.105.048001/FIGURES/4/MEDIUM>.
- [118] Landi, G.; Barletta, D.; Poletto, M. Modelling and Experiments on the Effect of Air Humidity on the Flow Properties of Glass Powders. *Powder Technol* **2011**, *207* (1–3), 437–443. <https://doi.org/10.1016/J.POWTEC.2010.11.033>.
- [119] Kudrolli, A. Sticky Sand. *Nature Materials* **2008**, *7* (3), 174–175. <https://doi.org/10.1038/nmat2131>.
- [120] Emery, E.; Oliver, J.; Pugsley, T.; Sharma, J.; Zhou, J. Flowability of Moist Pharmaceutical Powders. *Powder Technol* **2009**, *189* (3), 409–415. <https://doi.org/10.1016/J.POWTEC.2008.06.017>.
- [121] Valverde, J. M.; Castellanos, A. Random Loose Packing of Cohesive Granular Materials. *Europhys Lett* **2006**, *75* (6), 985. <https://doi.org/10.1209/EPL/I2006-10208-4>.

- [122] Blümel, C.; Sachs, M.; Laumer, T.; Winzer, B.; Schmidt, J.; Schmidt, M.; Peukert, W.; Wirth, K. E. Increasing Flowability and Bulk Density of PE-HD Powders by a Dry Particle Coating Process and Impact on LBM Processes. *Rapid Prototyp J* **2015**, *21* (6), 697–704. <https://doi.org/10.1108/RPJ-07-2013-0074/FULL/XML>.
- [123] Schmidt, J.; Sachs, M.; Fanselow, S.; Zhao, M.; Romeis, S.; Drummer, D.; Wirth, K. E.; Peukert, W. Optimized Polybutylene Terephthalate Powders for Selective Laser Beam Melting. *Chem Eng Sci* **2016**, *156*, 1–10. <https://doi.org/10.1016/J.CES.2016.09.009>.
- [124] Zhou, H.; Götzinger, M.; Peukert, W. The Influence of Particle Charge and Roughness on Particle–Substrate Adhesion. *Powder Technol* **2003**, *135–136*, 82–91. <https://doi.org/10.1016/J.POWTEC.2003.08.007>.
- [125] Chen, H.; Zhu, W.; Tang, H.; Yan, W. Oriented Structure of Short Fiber Reinforced Polymer Composites Processed by Selective Laser Sintering: The Role of Powder-Spreading Process. *Int J Mach Tools Manuf* **2021**, *163*, 103703. <https://doi.org/10.1016/J.IJMACHTOOLS.2021.103703>.
- [126] Lumay, G.; Francqui, F.; Detrembleur, C.; Vandewalle, N. Influence of Temperature on the Packing Dynamics of Polymer Powders. *Advanced Powder Technology* **2020**, *31* (10), 4428–4435. <https://doi.org/10.1016/J.APT.2020.09.019>.
- [127] Salmoria, G. V.; Leite, J. L.; Vieira, L. F.; Pires, A. T. N.; Roesler, C. R. M. Mechanical Properties of PA6/PA12 Blend Specimens Prepared by Selective Laser Sintering. *Polym Test* **2012**, *31* (3), 411–416. <https://doi.org/10.1016/J.POLYMERTESTING.2011.12.006>.
- [128] Cappella, B.; Stark, W. Adhesion of Amorphous Polymers as a Function of Temperature Probed with AFM Force–Distance Curves. *J Colloid Interface Sci* **2006**, *296* (2), 507–514. <https://doi.org/10.1016/J.JCIS.2005.09.043>.
- [129] Ziegelmeier, S.; Christou, P.; Wöllecke, F.; Tuck, C.; Goodridge, R.; Hague, R.; Krampe, E.; Wintermantel, E. An Experimental Study into the Effects of Bulk and Flow Behaviour of Laser Sintering Polymer Powders on Resulting Part Properties. *J Mater Process Technol* **2015**, *215* (1), 239–250. <https://doi.org/10.1016/J.JMATPROTEC.2014.07.029>.

- [130] Schmid, M.; Wegener, K. Additive Manufacturing: Polymers Applicable for Laser Sintering (LS). *Procedia Eng* **2016**, *149*, 457–464. <https://doi.org/10.1016/J.PROENG.2016.06.692>.
- [131] Grey, R. O.; Beddow, J. K. On the Hausner Ratio and Its Relationship to Some Properties of Metal Powders. *Powder Technol* **1969**, *2* (6), 323–326. [https://doi.org/10.1016/0032-5910\(69\)80024-0](https://doi.org/10.1016/0032-5910(69)80024-0).
- [132] *VDI-Richtlinie 3405: Additive Fertigungsverfahren, Rapid Manufacturing - Laser-Sintern von Kunststoffbauteilen - Güteüberwachung*; 2013.
- [133] Schneck, M.; Horn, M.; Schmitt, M.; Seidel, C.; Schlick, G.; Reinhart, G. Review on Additive Hybrid- and Multi-Material-Manufacturing of Metals by Powder Bed Fusion: State of Technology and Development Potential. *Progress in Additive Manufacturing* **2021**, *6* (4), 881–894. <https://doi.org/10.1007/s40964-021-00205-2>.
- [134] Wei, C.; Li, L. Recent Progress and Scientific Challenges in Multi-Material Additive Manufacturing via Laser-Based Powder Bed Fusion. *Virtual Phys Prototyp* **2021**, *16* (3), 347–371. <https://doi.org/10.1080/17452759.2021.1928520>.
- [135] Laumer, T.; Meisenbach KG. Erzeugung von Thermoplastischen Werkstoffverbunden Mittels Simultanem, Intensitätsselektivem Laserstrahlschmelzen, Dissertation der Friedrich-Alexander-Universität Erlangen-Nürnberg (FAU), 2017. <https://doi.org/10.25593/978-3-87525-428-0>.
- [136] Andriani, C.; Chua, C. K.; Liu, Z. H.; Zhang, D. Q.; Sing, S. L. Review on Melting of Multiple Metal Materials in Additive Manufacturing. *Proceedings of the International Conference on Progress in Additive Manufacturing* **2014**, *0*, 170–175. https://doi.org/10.3850/978-981-09-0446-3_134.
- [137] Anstaett, C.; Seidel, C.; Reinhart, G. Herstellung von 3-D-Multimaterialbauteilen Aus Kupfer-Chrom-Zirkonium Und Werkzeugstahl 1.2709. *Rapid. Tech+ FabCon* **2018**, *3*, 330–344.
- [138] Mahamood, R. M.; Akinlabi, E. T. Laser Metal Deposition of Functionally Graded Ti6Al4V/TiC. *Mater Des* **2015**, *84*, 402–410. <https://doi.org/10.1016/J.MATDES.2015.06.135>.
- [139] Li, Y.; Feng, Z.; Hao, L.; Huang, L.; Xin, C.; Wang, Y.; Bilotti, E.; Essa, K.; Zhang, H.; Li, Z.; Yan, F.; Peijs, T. A Review on Functionally Graded Materials and Structures via Additive Manufacturing: From

- Multi-Scale Design to Versatile Functional Properties. *Adv Mater Technol* **2020**, *5* (6), 1900981. <https://doi.org/https://doi.org/10.1002/admt.201900981>.
- [140] Scaramuccia, M. G.; Demir, A. G.; Caprio, L.; Tassa, O.; Previtali, B. Development of Processing Strategies for Multigraded Selective Laser Melting of Ti6Al4V and IN718. *Powder Technol* **2020**, *367*, 376–389. <https://doi.org/10.1016/J.POWTEC.2020.04.010>.
- [141] Jackson, B.; Wood, K.; Beaman, J. J. Discrete Multi-Material Selective Laser Sintering (M₂ SLS): Development for an Application in Complex Sand Casting Core Arrays. In *2000 International Solid Freeform Fabrication Symposium*; 2000.
- [142] Wu, W.; Yongqiang, Y.; Mao Guisheng, D. W.; Song, C. Free Manufacturing of Heterogeneous Materials Part by Selective Laser Melting. *Optics and Precision Engineering* **2019**, *27* (3), 517–526.
- [143] Pegna, J.; Pattofatto, S.; Berge, R.; Bangalan, C.; Herring, H.; LeSaux, M.; Engler, J. The Sand Painter: Two Dimensional Powder Deposition. In *Proceedings on the Solid Freeform Fabrication Symposium, Austin, TX; 1999*; pp 695–709.
- [144] Schuffenhauer, T.; Stichel, T.; Kopp, S.-P.; Roth, S.; Schmidt, M. Process Route Adaption to Generate Multi-Layered Compounds Using Vibration-Controlled Powder Nozzles in Selective Laser Melting of Polymers. *Lasers in Manufacturing (LiM) Conference 2019, Munich 2019*.
- [145] Stichel, T.; Laumer, T.; Baumüller, T.; Amend, P.; Roth, S. Powder Layer Preparation Using Vibration-Controlled Capillary Steel Nozzles for Additive Manufacturing. *Phys Procedia* **2014**, *56*, 157–166. <https://doi.org/10.1016/j.phpro.2014.08.158>.
- [146] Rothfelder, R.; Lanzl, L.; Selzam, J.; Drummer, D.; Schmidt, M. Vibrational Microfeeding of Polymer and Metal Powders for Locally Graded Properties in Powder-Based Additive Manufacturing. *J Mater Eng Perform* **2021**, *30* (12), 8798–8809. <https://doi.org/10.1007/S11665-021-06271-5/FIGURES/15>.
- [147] Girnth, S.; Koopmann, J.; Klawitter, G.; Waldt, N.; Niendorf, T. 3D Hybrid-Material Processing in Selective Laser Melting: Implementation of a Selective Coating System. *Progress in Additive Manufacturing 2019 4:4* **2019**, *4* (4), 399–409. <https://doi.org/10.1007/S40964-019-00082-W>.

- [148] Wei, C.; Sun, Z.; Chen, Q.; Liu, Z.; Li, L. Additive Manufacturing of Horizontal and 3D Functionally Graded 316L/Cu10Sn Components via Multiple Material Selective Laser Melting. *Journal of Manufacturing Science and Engineering, Transactions of the ASME* **2019**, *141* (8). <https://doi.org/10.1115/1.4043983/956043>.
- [149] Wei, C.; Li, L.; Zhang, X.; Chueh, Y. H. 3D Printing of Multiple Metallic Materials via Modified Selective Laser Melting. *CIRP Annals* **2018**, *67* (1), 245–248. <https://doi.org/10.1016/J.CIRP.2018.04.096>.
- [150] Wei, C.; Gu, H.; Sun, Z.; Cheng, D.; Chueh, Y. H.; Zhang, X.; Huang, Y.; Li, L. Ultrasonic Material Dispensing-Based Selective Laser Melting for 3D Printing of Metallic Components and the Effect of Powder Compression. *Addit Manuf* **2019**, *29*, 100818. <https://doi.org/10.1016/J.ADDMA.2019.100818>.
- [151] Glasschroeder, J.; Prager, E.; Zaeh, M. F. Powder-Bed-Based 3D-Printing of Function Integrated Parts. *Rapid Prototyp J* **2015**, *21* (2), 207–215. <https://doi.org/10.1108/RPJ-12-2014-0172>.
- [152] Lanzl, L.; Wudy, K.; Greiner, S.; Drummer, D. Selective Laser Sintering of Copper Filled Polyamide 12: Characterization of Powder Properties and Process Behavior. *Polym Compos* **2019**, *40* (5), 1801–1809. <https://doi.org/10.1002/PC.24940>.
- [153] Bedoret A.; Hick M.; Eckes K. Belgium Patent No. BE1024613B1 - Device and Method for Creating a Particle Structure, September 29, 2016.
- [154] Marchal M.; Hick M.; Mercelis P. Belgium Patent No. BE1027856B1 - Leveling System and Method, December 13, 2019.
- [155] *How multi-powder deposition will transform industrial 3D printing - Aerosint.* <https://aerosint.com/powder-deposition-multimaterial-printing/> (accessed 2023-08-12).
- [156] Stichel, T.; Brandl, T.; Hauser, T.; Geißler, B.; Roth, S. Electrophotographic Multi-Material Powder Deposition for Additive Manufacturing. *Procedia CIRP* **2018**, *74*, 249–253. <https://doi.org/10.1016/J.PROCIR.2018.08.104>.
- [157] Stichel, T.; Brachmann, C.; Raths, M.; Dechet, M. A.; Schmidt, J.; Peukert, W.; Frick, T.; Roth, S. Electrophotographic Multilayer Powder Pattern Deposition for Additive Manufacturing. *Jom* **2020**, *72* (3), 1366–1375. <https://doi.org/10.1007/s11837-019-03965-z>.

- [158] Stichel, T.; Geißler, B.; Jander, J.; Laumer, T.; Frick, T.; Roth, S. Electrophotographic Multi-Material Powder Deposition for Additive Manufacturing. *J Laser Appl* **2018**, *30* (3), 032306. <https://doi.org/10.2351/1.5040619>.
- [159] Setter, R.; Stichel, T.; Schuffenhauer, T.; Kopp, S. P.; Roth, S.; Wudy, K. Additive Manufacturing of Multi-Material Polymer Parts Within the Collaborative Research Center 814. *Lecture Notes in Mechanical Engineering* **2021**, 142–152. https://doi.org/10.1007/978-3-030-70332-5_13.
- [160] Anstaett, C.; Seidel, C. Multi-Material Processing. *Laser Technik Journal* **2016**, *13* (4), 28–31. <https://doi.org/10.1002/LATJ.201600027>.
- [161] van der Eijk, C.; Mugaas, T.; Karlsen, R.; Åsebø, O.; Kolnes, Ø.; Skjevda, R. Metal Printing Process - Development of a New Rapid Manufacturing Process for Metal Parts. *Proceedings of the International Powder Metallurgy Congress & Exhibition (Euro PM2004) Volume 5* **2004**, 133–138.
- [162] Kumar, A. V.; Dutta, A. Investigation of an Electrophotography Based Rapid Prototyping Technology. *Rapid Prototyp J* **2003**, *9* (2), 95–103. <https://doi.org/10.1108/13552540310467095/FULL/XML>.
- [163] Kumar, A. V.; Dutta, A.; Fay, J. E. Electrophotographic Printing of Part and Binder Powders. *Rapid Prototyp J* **2004**, *10* (1), 7–13. <https://doi.org/10.1108/13552540410512480/FULL/XML>.
- [164] Sauser, B.; Verma, D.; Ramirez-Marquez, J.; Gove, R. From TRL to SRL: The Concept of Systems Readiness Levels. In *Conference on Systems Engineering Research*; Citeseer, 2006; Vol. 5.
- [165] *About AIM Photonics — AIM Photonics*. <https://www.aimphotonics.com/about-us> (accessed 2023-08-12).
- [166] *DoD Manufacturing Readiness Levels*. <https://www.dodmrl.com/> (accessed 2023-08-12).
- [167] Bejat, L. A.; Johnson, J. E.; Jones, R. O.; Livengood, B. P.; Srinivasan, K. R.; Strain, D. J. V. Toner Formulations with Tribocharge Control and Stability. US20100040969A1, 2010.
- [168] Hays, D. A. Toner Adhesion*. *J Adhes* **1995**, *51* (1–4), 41–48. <https://doi.org/10.1080/00218469508009988>.

- [169] Schein, L. B. *The Electrophotographic Process*; Schein, L. B., Ed.; Springer Berlin Heidelberg: Berlin, Heidelberg, 1992. https://doi.org/10.1007/978-3-642-77744-8_2.
- [170] Hecht, E. *Optics*; Pearson Education, Incorporated, 2017.
- [171] Benning, M. J. Development of a Novel Electrophotographic Additive Layer Manufacturing Machine. Doctoral Thesis, School of Mechanical and Systems Engineering - University of Newcastle upon Tyne, Newcastle upon Tyne, United Kingdom, 2012.
- [172] Shahin, M. M. Nature of Charge Carriers in Negative Coronas. *Applied Optics*, Vol. 8, Issue 51, pp. 106-110 **1969**, 8 (101), 106-110. <https://doi.org/10.1364/AO.8.S1.000106>.
- [173] Shahin, M. M. Mass-Spectrometric Studies of Corona Discharges in Air at Atmospheric Pressures. *J Chem Phys* **2004**, 45 (7), 2600. <https://doi.org/10.1063/1.1727980>.
- [174] Gallo, C. F. Corona—A Brief Status Report. *IEEE Trans Ind Appl* **1977**, IA-13 (6), 550-557. <https://doi.org/10.1109/TIA.1977.4503458>.
- [175] Gallo, C. F. Coronas and Gas Discharges in Electrophotography: A Review. *IEEE Trans Ind Appl* **1975**, IA-11 (6), 739-748. <https://doi.org/10.1109/TIA.1975.349370>.
- [176] Giacometti, J. A.; Oliveira, O. N. Corona Charging of Polymers. *IEEE Transactions on Electrical Insulation* **1992**, 27 (5), 924-943. <https://doi.org/10.1109/14.256470>.
- [177] Giacometti, J. A.; Fedosov, S.; Costa, M. M. Corona Charging of Polymers: Recent Advances on Constant Current Charging. *Brazilian Journal of Physics* **1999**, 29 (2), 269-279. <https://doi.org/10.1590/S0103-97331999000200009>.
- [178] Faria, R. M.; Jorge, A.; Oliveira, O. N. A Novel Space-Charge Effect in Thermally Stimulated Current Measurements on β -PVDF. *J Phys D Appl Phys* **1990**, 23 (3), 334. <https://doi.org/10.1088/0022-3727/23/3/011>.
- [179] Dakin, T. W. Breakdown of Gases in Uniform Fields, Paschen Curves for Nitrogen, Air and Sulphur-Hexafluoride. *Electra* **1974**, 32, 64-70.
- [180] Cserátony-Hoffer, A. ÜBER DEN MECHANISMUS DES POLARITÄTSEFFEKTES IN DER DURCHSCHLAGSPANNUNG VON GASSEN. *Periodica Polytechnica Electrical Engineering (Archives)* **1961**, 5 (4), 357-372.

- [181] Trichel, G. W. The Mechanism of the Negative Point to Plane Corona near Onset. *Physical Review* **1938**, *54* (12), 1078–1084. <https://doi.org/10.1103/PhysRev.54.1078>.
- [182] Trichel, G. W. The Mechanism of the Positive Point-to-Plane Corona in Air at Atmospheric Pressure. *Physical Review* **1939**, *55* (4), 382. <https://doi.org/10.1103/PhysRev.55.382>.
- [183] Hayne, T. F. Screen Controlled Corona Device (Scorotron) for Charging in a Xerographic Copier. *IEEE Trans Ind Appl* **1976**, No. 1, 63–67.
- [184] Jones, J. E.; Cohen, A. M. Chebyshev Comparisons of Current Laws for Point-Plane DC Coronae in Air. *J Electrostat* **1997**, *39* (2), 111–128. [https://doi.org/10.1016/S0304-3886\(96\)00045-9](https://doi.org/10.1016/S0304-3886(96)00045-9).
- [185] Weinberg, Z. A.; Matthies, D. L.; Johnson, W. C.; Lampert, M. A. Measurement of the Steady-State Potential Difference across a Thin Insulating Film in a Corona Discharge. *Review of Scientific Instruments* **1975**, *46* (2), 201–203. <https://doi.org/10.1063/1.1134166>.
- [186] Goetsch, D. L.; Ozon, G. *Occupational Safety and Health for Technologists, Engineers, and Managers*; Prentice Hall Upper Saddle River, 2011; Vol. 5.
- [187] Pai, D. M.; Springett, B. E. Physics of Electrophotography. *Rev Mod Phys* **1993**, *65* (1), 163. <https://doi.org/10.1103/RevModPhys.65.163>.
- [188] Pohl, H. A. The Motion and Precipitation of Suspensoids in Divergent Electric Fields. *J Appl Phys* **1951**, *22* (7), 869–871. <https://doi.org/10.1063/1.1700065>.
- [189] Matsusaka, S.; Maruyama, H.; Matsuyama, T.; Ghadiri, M. Triboelectric Charging of Powders: A Review. *Chem Eng Sci* **2010**, *65* (22), 5781–5807. <https://doi.org/10.1016/J.CES.2010.07.005>.
- [190] Anderson, J. H. The Effect of Additives on the Tribocharging of Electrophotographic Toners. *J Electrostat* **1996**, *37* (3), 197–209. [https://doi.org/10.1016/0304-3886\(96\)00017-4](https://doi.org/10.1016/0304-3886(96)00017-4).
- [191] Zou, H.; Zhang, Y.; Guo, L.; Wang, P.; He, X.; Dai, G.; Zheng, H.; Chen, C.; Wang, A. C.; Xu, C.; Wang, Z. L. Quantifying the Triboelectric Series. *Nat Commun* **2019**, *10* (1), 1–9. <https://doi.org/10.1038/s41467-019-09461-x>.

- [192] Matsusaka, S.; Maruyama, H.; Matsuyama, T.; Ghadiri, M. Triboelectric Charging of Powders: A Review. *Chem Eng Sci* **2010**, *65* (22), 5781–5807. <https://doi.org/10.1016/J.CES.2010.07.005>.
- [193] Lacks, D. J.; Mohan Sankaran, R. Contact Electrification of Insulating Materials. *J Phys D Appl Phys* **2011**, *44* (45), 453001. <https://doi.org/10.1088/0022-3727/44/45/453001>.
- [194] Zou, H.; Guo, L.; Xue, H.; Zhang, Y.; Shen, X.; Liu, X.; Wang, P.; He, X.; Dai, G.; Jiang, P.; Zheng, H.; Zhang, B.; Xu, C.; Wang, Z. L. Quantifying and Understanding the Triboelectric Series of Inorganic Non-Metallic Materials. *Nat Commun* **2020**, *11* (1), 1–7. <https://doi.org/10.1038/s41467-020-15926-1>.
- [195] Thourson, T. L. Xerographic Development Processes: A Review. *IEEE Trans Electron Devices* **1972**, *19* (4), 495–511. <https://doi.org/10.1109/T-ED.1972.17447>.
- [196] Epping, R. H.; Mehlin, M.; Muenz, M. Standardized Measurements Methods for Analyzing Electrostatically Charged Toners. In *Hard Copy and Printing Technologies*; SPIE, 1990; Vol. 1252, pp 123–131.
- [197] Epping, R. H.; Kuettner, A. Free Air Beam in an Electric Field for Determination of the Electrostatic Charge of Powders between 1 and 200 Mm. *J Electrostat* **2002**, *55* (3–4), 279–288. [https://doi.org/10.1016/S0304-3886\(01\)00210-8](https://doi.org/10.1016/S0304-3886(01)00210-8).
- [198] Weiss, D. S.; Abkowitz, M. Advances in Organic Photoconductor Technology. *Chem Rev* **2010**, *110* (1), 479–526. https://doi.org/10.1021/CR900173R/ASSET/CR900173R.FP.PNG_V03.
- [199] SCHAFFERT RM. New High- Sensitivity Organic Photoconductor for Electrophotography. *IBM J Res Dev* **1971**, *15* (1), 75–89. <https://doi.org/10.1147/RD.151.0075>.
- [200] Pai, D. M. Organic Photoconductors in Electrophotography. *J Non Cryst Solids* **1983**, *59–60* (PART 2), 1255–1263. [https://doi.org/10.1016/0022-3093\(83\)90396-4](https://doi.org/10.1016/0022-3093(83)90396-4).
- [201] Petritz, R. L. Theory of Photoconductivity in Semiconductor Films. *Physical Review* **1956**, *104* (6), 1508–1516. <https://doi.org/10.1103/PHYSREV.104.1508>.

- [202] Crandall, R. S. Chapter 8 Photoconductivity. *Semiconductors and Semimetals* **1984**, 21 (PB), 245–297. [https://doi.org/10.1016/S0080-8784\(08\)62916-6](https://doi.org/10.1016/S0080-8784(08)62916-6).
- [203] Foerster, J.; Michatz, M.; Binder, M.; Frey, A.; Seidel, C.; Schlick, G.; Schilp, J. Electrostatic Powder Attraction for the Development of a Novel Recoating System for Metal Powder Bed-Based Additive Manufacturing. *J Electrostat* **2022**, 115, 103641. <https://doi.org/10.1016/J.ELSTAT.2021.103641>.
- [204] Hsu, C. Y.; Chen, Y. C.; Lin, R. Y. Y.; Ho, K. C.; Lin, J. T. Solid-State Dye-Sensitized Solar Cells Based on Spirofluorene (Spiro-OMeTAD) and Arylamines as Hole Transporting Materials. *Physical Chemistry Chemical Physics* **2012**, 14 (41), 14099–14109. <https://doi.org/10.1039/C2CP41326D>.
- [205] Poplavskyy, D.; Nelson, J. Nondispersive Hole Transport in Amorphous Films of Methoxy-Spirofluorene-Arylamine Organic Compound. *J Appl Phys* **2003**, 93 (1), 341–346. <https://doi.org/10.1063/1.1525866>.
- [206] Genovese, L.; Deutsch, T.; Neelov, A.; Goedecker, S.; Beylkin, G. Efficient Solution of Poisson's Equation with Free Boundary Conditions. *Journal of Chemical Physics* **2006**, 125 (7). <https://doi.org/10.1063/1.2335442/898596>.
- [207] Kanemitsu, Y.; Funada, H.; Imamura, S. Xerographic Studies of Charge Trapping in Layered Organic Photoconductors. *J Appl Phys* **1990**, 67 (9), 4152–4158. <https://doi.org/10.1063/1.344977>.
- [208] Rubin, B. J.; Ware, R. E.; Kamp, D. Measurement of Particle Size and Electrostatic Charge Distributions on Toners Using E-SPART Analyzer. *IEEE Trans Ind Appl* **1991**, 27 (4), 611–619. <https://doi.org/10.1109/28.85472>.
- [209] Jones, J. B. Investigation of Laser Printing for 3D Printing and Additive Manufacturing. Doctoral Thesis, The University of Warwick, Coventry, United Kingdom, 2013.
- [210] Benning, M. J.; Dalgarno, K. Proof of Concept of a Novel Combined Consolidation and Transfer Mechanism for Electrophotographic 3D Printing. *Rapid Prototyp J* **2018**, 24 (6), 1040–1048. <https://doi.org/10.1108/RPJ-04-2018-0111/FULL/HTML>.

- [211] Grenda, E. P. Apparatus of Fabricating 3 Dimensional Objects by Means of Electrophotography, Ionography or a Similar Process U. S. Patents No. 6,206,672 B1, 2001.
- [212] *Technology — Evolve Additive Solutions*. <https://evolve-additive.com/products/technology/> (accessed 2023-08-17).
- [213] Martin, T. I. Method for Printing 3D Parts and Support Structures with Electrophotography - Based Additive Manufacturing U. S. Patents No. 10,065,371 B2, September 4, 2018.
- [214] Malliaris, A.; Turner, D. T. Influence of Particle Size on the Electrical Resistivity of Compacted Mixtures of Polymeric and Metallic Powders. *J Appl Phys* **2003**, *42* (2), 614. <https://doi.org/10.1063/1.1660071>.
- [215] Stichel, T.; Laumer, T.; Schmidt, M. Simulation Des (Quasi-)Simultanen Laserstrahlschmelzens Zur Herstellung von Multi-Material-Bauteilen Aus Polymeren. *Rapid.Tech + FabCon 3.D – International Trade Show + Conference for Additive Manufacturing* **2018**, 312–329. <https://doi.org/10.3139/9783446458123.020>.
- [216] Laumer, T.; Stichel, T.; Riedlbauer, D.; Amend, P.; Mergheim, J.; Schmidt, M. Realization of Multi-Material Polymer Parts by Simultaneous Laser Beam Melting. *JLMN-Journal of Laser Micro/Nanoengineering* **2015**, *10* (2). <https://doi.org/10.2961/jlmn.2015.02.0006>.
- [217] Setter, R.; Hafenecker, J.; Rothfelder, R.; Kopp, S.-P.; Roth, S.; Schmidt, M.; Merklein, M.; Wudy, K. Innovative Process Strategies in Powder-Based Multi-Material Additive Manufacturing. *Journal of Manufacturing and Materials Processing* **2023**, *7* (4), 133. <https://doi.org/10.3390/jmmp7040133>.
- [218] Düsenberg, B.; Kopp, S.-P.; Tischer, F.; Schrüfer, S.; Roth, S.; Schmidt, J.; Schmidt, M.; Schubert, D. W.; Peukert, W.; Bück, A. Enhancing Photoelectric Powder Deposition of Polymers by Charge Control Substances. *Polymers* **2022**, *Vol. 14*, Page 1332 **2022**, *14* (7), 1332. <https://doi.org/10.3390/POLYM14071332>.
- [219] Kopp, S.-P.; Düsenberg, B.; Bück, A.; Schmidt, M. Method and Device for the Additive Manufacture of a Component, and Component Manufactured in Accordance with the Method. WO2023066674A1, October 6, 2022.

- [220] Kopp, S.-P.; Düsenberg, B.; Bück, A.; Schmidt, M. Process and Device for the Additive Manufacturing of a Component and Correspondingly Manufactured Component . DE102021211871A1, October 21, 2021.
- [221] Kopp, S.-P.; Medvedev, V.; Schmidt, M. Verfahren Zur Additiven Fertigung Eines Medizinischen Und/Oder Pharmazeutischen Produkts Sowie Entsprechendes Produkt. P221341DE, January 12, 2023.

Own publications referring to this work

- [P1] Kopp, S.-P.; Düsenberg, B.; Eshun, P. M.; Schmidt, J.; Bück, A.; Roth, S.; Schmidt, M.: *Enabling Triboelectric Charging as a Powder Charging Method for Electrophotographic Powder Application in Laser-Based Powder Bed Fusion of Polymers by Triboelectric Charge Control*. *Addit Manuf* 2023, 68, 103531. <https://doi.org/10.1016/J.ADDMA.2023.103531>.
- [P2] Kopp, S.-P.; Stichel, T.; Roth, S.; Schmidt, M.: *Investigation of the Electrophotographic Powder Deposition through a Transfer Grid for Efficient Additive Manufacturing*. *Procedia CIRP* 2020, 94, 122–127. <https://doi.org/10.1016/j.procir.2020.09.024>.
- [P3] Kopp, S.-P.; Medvedev, V.; Roth, S.: *Targeted Vibration Excitation for Increasing the Powder Deposition Efficiency in Electrophotographic Powder Application for Laser-Based Powder Bed Fusion of Polymers*. *Procedia CIRP* 2022, 111, 55–60. <https://doi.org/10.1016/j.procir.2022.08.117>.
- [P4] Kopp, S.-P.; Medvedev, V.; Frick, T.; Roth, S.: *Expanding the Capabilities of Laser-Based Powder Bed Fusion of Polymers through the Use of Electrophotographic Powder Application*. *J Laser Appl* 2022, 34 (4), 042032. <https://doi.org/10.2351/7.0000774>.
- [P5] Kopp, S.-P.; Medvedev, V.; Tangermann-Gerk, K.; Wöltinger, N.; Rothfelder, R.; Graßl, F.; Heinrich, M. R.; Januskaite, P.; Goyanes, A.; Basit, A. W.; Roth, S.; Schmidt, M.: *Electrophotographic 3D Printing of Pharmaceutical Films*. *Addit Manuf* 2023, 103707. <https://doi.org/10.1016/J.ADDMA.2023.103707>.
- [P6] Kopp, S.-P.; Stichel, T.; Schuffenhauer, T.; Roth, S.; Schmidt, M.: *Herausforderungen der additiven Fertigung von Multi-Material-Bauteilen*. Tagungsband des 7. Industriekolloquiums des Sonderforschungsbereichs 814 – Additive Fertigung (ISBN 978-3-931864-81-1) 2019.

- [P7] Kopp, S.-P.; Düsenberg, B.; Bück, A.; Schmidt, M.: *Method and Device for the Additive Manufacture of a Component, and Component Manufactured in Accordance with the Method*. WO2023066674A1, October 6, 2022.
- [P8] Kopp, S.-P.; Düsenberg, B.; Bück, A.; Schmidt, M.: *Process and Device for the Additive Manufacturing of a Component and Correspondingly Manufactured Component*. DE102021211871A1, October 21, 2021.
- [P9] Kopp, S.-P.; Medvedev, V.; Schmidt, M.: *Verfahren Zur Additiven Fertigung Eines Medizinischen Und/Oder Pharmazeutischen Produkts Sowie Entsprechendes Produkt*. P221341DE, January 12, 2023.

Students' theses referring to this work

- [S1] Eshun, Pius Marcellinus: *Research on the triboelectric charging process of polymer powders with focus on its usability in the context of electrophotographic powder application for laser-based powder bed fusion of polymers*. Projektarbeit (2021), Erlangen
- [S2] Eshun, Pius Marcellinus: *Comparison of different powder charging strategies for their usage in electrophotographic laser-based powder bed fusion of polymers*. Masterarbeit (2022), Erlangen
- [S3] Medvedev, Vadim: *Optimization potentials for the deposition process of polymer particles in the context of electrophotographic powder application for laser-based powder bed fusion of polymers*. Masterarbeit (2022), Erlangen
- [S4] Ly Huynh, Cindy: *From particles to powder layers to parts: Characterization of electrophotographic powder application for laser-based additive manufacturing*. Masterarbeit (2023), Erlangen
- [S5] Ebert, Niklas: *Efficient generation of bactericidal properties on additively manufactured parts by electrophotographic powder application*. Masterarbeit (2024), Erlangen

Kurzzusammenfassung

Additive Fertigungsverfahren wie das laserbasierte Pulverbettsschmelzen von Polymeren (PBF-LB/P) zeichnen sich durch ihre hohe Flexibilität aus und sind aus der modernen Fertigungslandschaft nicht mehr wegzudenken. Jedoch schränken herkömmliche Pulverauftragsverfahren diese Flexibilität bedeutend ein.

Aus diesem Grund wird in dieser Arbeit ein neuartiger Ansatz für den Pulverauftrag verfolgt, der im Wesentlichen auf dem seit Jahrzehnten bekannten und dank des Laserdruckers weit verbreiteten Prinzip der Elektrofotografie beruht. Bisher ist der erfolgreiche Einsatz der Elektrofotografie in der laserbasierten additiven Fertigung jedoch noch nicht gelungen.

Im Rahmen dieser Arbeit wird der elektrofotografische Pulverauftrag (EPA) im Kontext des PBF-LB/P systematisch untersucht, wobei ein ganzheitlicher Ansatz von der Aufladung einzelner Pulverpartikel über die Erzeugung geladener Pulverschichten bis hin zu fertigen Bauteilen, die mittels PBF-LB/P mit EPA hergestellt wurden. Hierdurch können wesentliche Limitationen herkömmlicher Pulverauftragsverfahren beseitigt werden. Insbesondere verringert der Einsatz des EPA die Abhängigkeit des Pulverauftrags von der Fließfähigkeit, was die bisher stark eingeschränkte Materialvielfalt für das PBF-LB/P signifikant erweitert. Zudem können mithilfe von EPA Multi-Material-Bauteile mittels PBF-LB/P hergestellt werden. Nicht zuletzt wird die Pulvereffizienz und damit die Umweltbilanz des PBF-LB/P deutlich verbessert, da durch die Selektivität des Pulverauftrags lediglich so viel Pulvermaterial in den Bauraum eingebracht wird, wie zur Herstellung des Bauteils tatsächlich erforderlich ist.

Abstract

Additive manufacturing processes such as laser-based powder bed fusion of polymers (PBF-LB/P) are characterized by their high flexibility and have become an indispensable part of the modern manufacturing landscape. Conventional powder application processes, however, limit this flexibility considerably.

For this reason, a novel approach to powder application is pursued in this work, which is essentially based on the principle of electrophotography, which has been known for decades and is widely used due to the laser printer. However, the successful use of electrophotography in laser-based additive manufacturing has not yet been achieved.

In this thesis, electrophotographic powder deposition (EPA) is systematically investigated in the context of PBF-LB/P, taking a holistic approach from the charging of individual powder particles, through the generation of charged powder layers, to finished components produced by PBF-LB/P with EPA. In this way, significant limitations of conventional powder application processes can be eliminated. In particular, the use of EPA reduces the dependency of powder application on flowability, which significantly expands the previously severely limited material variety for PBF-LB/P. In addition, multi-material parts can be produced using PBF-LB/P with the aid of EPA. Last but not least, the powder efficiency and thus the environmental balance of PBF-LB/P is significantly improved, since the selectivity of the powder application means that only as much powder material is applied to the build chamber as is actually required to produce the individual part.